UNIVERSITAT DE BARCELONA
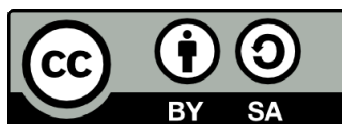
Dynamical characterisation of the Magellanic Clouds with Gaia data and the KRATOS simulations

Óscar Jiménez Arranz

DYNAMICAL CHARACTERISATION OF THE MAGELLANIC CLOUDS WITH GAIA DATA AND THE KRATOS SIMULATIONS

ÓSCAR JIMÉNEZ ARRANZ

SUPERVISORS
DR. MERCÈ ROMERO GÓMEZ
DR. XAVIER LURI CARRASCOSO

UNIVERSITAT DE BARCELONA

Dynamical characterisation of the Magellanic Clouds with Gaia data and the KRATOS simulations

Memòria presentada per optar al grau de
doctor per la Universitat de Barcelona

Programa de doctorat en Física

AUTOR
Óscar Jiménez Arranz

DIRECTORS
Dr. Mercè Romero Gómez
Dr. Xavier Luri Carrascoso

TUTOR
Dr. Alberto Manrique Oliva

DEPARTAMENT DE FÍSICA QUÀNTICA I ASTROFÍSICA
Barcelona, 12 de gener de 2024

UNIVERSITAT DE
BARCELONA

This thesis is presented following the regulations of the University of Barcelona (Approved by the CdG in the session of 16 March 2012 and modified by the CdG on 9 May and 19 July 2012, 29 May and 3 October 2013, 17 July of 2014, 16 July 2015, 15 June and 21 November 2016, 5 December 2017, 4 May 2018, 15 May and 22 July 2019, 7 of October 2020, and 14 of July 2021). The listed regulations allow for the presentation of a PhD thesis as a compendium of published articles. According to the regulations, the thesis must contain a minimum of three published or accepted articles. This thesis contains the published version of three articles, which is sufficient to allow its presentation.

Barcelona, 12 January 2024

———————————————
Óscar Jiménez Arranz

ACKNOWLEDGMENTS

Primer de tot vull agrair als meus directors de tesi, els Drs. Mercè Romero-Gómez i Xavier Luri, haver compartit amb mi el seu temps i coneixement durant els últims tres anys. Gràcies, Mercè, per tantes estones de discussió que m'han ensenyat a ser un millor investigador. De tu he après a com s'ha de fer recerca. Gràcies, Xavi, per haver-me introduït un món tan apassionant com el de l'anàlisi de dades i per haver acceptat a un "particulero" com al teu estudiant de tesi, no molta gent ho hagués fet. Valoro molt la independència que tots dos m'heu donat a l'hora de fer recerca, sense mai perdre ull del què feia i estant allà sempre que he necessitat ajuda i assessorament. Gràcies a tots dos per haver aconseguit que la meva època predoctoral sigui inmillorable. Sempre diré amb orgull qui han sigut els meus directors de tesi.

I would also like to thank all the collaborators I have had during the past years. Without them this thesis would have not been possible. Me gustaría empezar agradeciéndole al Dr. Ángel Berihuete su eterna paciencia conmigo. De Cádiz no sólo me llevé un código que funcionaba (que, creedme, ya era muchísimo), sino también el haber podido conocer mejor a una maravillosa persona e investigador. Ángel, eso sí, te tomo la palabra. La próxima vez cuadramos mejor las fechas y te visito para Carnavales.

I would like to express my gratitude to Dr. Laurent Chemin for the opportunity to lead such a personal and ambitious project when I was literally "no one", just a first-year PhD student with o publications on his record. Our laboral temporal intersection was quite narrow, since I was in Barcelona and Laurent in Chile. However, the many-hours time difference did not prevent us from working hand in hand with (I think) excellent results enabling me to absorb a wealth of knowledge on his expertise on bar dynamics. Thanks Laurent for your charisma and for being so nice with me.

I want to express my thankfulness to Dr. Paul McMillan for always having THE comment. When starting a conversation with Paul I always knew that a problem was going to be solved or that an excellent idea would come up from that talk. I will always remember your hospitality and care when visiting you and Santi in Lund. Thanks Paul for sharing your wisdom and kindness with me.

Menció especial al Dr. Santi Roca-Fàbrega per haver traspassat la part laboral i haver-se convertit en tot un amic. Abans d'anar a Lund ja tenia la sospita que ens podríem entendre bé, tot i això, has superat tot tipus d'expectativa. La meva "bojeria" va entrar ràpidament en ressonància amb la teva. Amb tu he après molt de ciència i natura

durant les llargues xerrades que hem tingut durant les encara més llargues rutes per Skåne. T'estic especialment agraït per haver carregat la tenda i el meu sac de dormir. Prometo que el pròxim cop que et visiti a Lund portaré una motxilla més gran.

Gràcies també als Drs. Teresa Antoja, Eduard Masana, Paul Adamczyk, Alfred Castro-Ginard i Maria-Rosa Cioni per tot el que heu aportat a la meva recerca.

Aquesta feina tampoc hagués sigut possible sense l'entorn de treball tan sa i agradable que he tingut, des del meus companys de despatx: Marcel, Julien i Judith; els companys de doctorat: Ana, Andreu, Arnau, Carlos, Bruno, Dani del Ser, Dani M., Edgar, Elena, Emanuele, Elina, Helena, Jordi, Josep, Juan, Judith A., Judit D., Julien, Lucía, Mar, Marcel, Marie, Marc, Pablo, Quim, Sergi, Toni i Xiying; fins al grup de GaiaUB: Cesca, Carme, Chloé, Xavi, Mercè, Teresa, Marc, Maria, Marie, Eduard, Èlia, Josep Manel, Michael, Lola, Friedrich, Juan, Marcel, Jordi, Judith A., Judit D., Albert M., Sergi, Javi, Claus, Albert S., Ferran i Víctor.

D'aquestes llistes, hi ha un grup de persones de qui vull afegir un parell de coses més. Començo amb el Marcel, que podreu notar que el seu nom apareix en totes tres. Això pot donar una pista de la gran quantitat de temps que hem passat junts. Gràcies, Marcel, per tantes bones estones i pels bons consells que sempre m'has donat dins i fora de la oficina. Sense cap mena de dubte ets el millor company de despatx que un pot tenir. Trobaré a faltar que algú es tregui els auriculars i digui "Buah, idea loca, a veure què en penseu". Agrair a la Cesca el tracte tan proper que ha tingut amb els més joves del grup, a més dels comentaris tan certers que sempre m'ha donat en benefici de la nostra investigació. Gràcies, Carme, per les converses que hem tingut sobre com es feia astronomia en el passat, quina és la història de Gaia i totes aquestes coses que un només pot aprendre parlant amb gent que ha estat allà. Agrair al Jordi i a l'Albert M. que hagin aguantat tota la feinada que els hi he donat amb el Cloud. Als companys de tesi, el ja mític Balcón Milenario, donar-vos les més sinceres gràcies per tantes bones estones a l'hora de dinar, per les excursions per la muntanya i els caps de setmana a Begur. Ha sigut un plaer compartir aquest viatge amb tots vosaltres, on ho heu fet que tot sigui molt més fàcil. Amb el dipòsit (i posterior defensa) d'aquesta tesi deixareu de ser els meus companys de doctorat, però us conservaré com amics.

No vull deixar de donar les gràcies al JR per sempre ajudar-me a lidiar amb la burocràcia amb la millor de les actituds i somriures. També agraïr al professorat amb el que he compartit multitud de viatges a Àger on he pogut aprendre molt tant d'astronomia, com de la vida acadèmica, com de vosaltres.

During my thesis I had the privilege of meeting the wonderful group of people working at Lund Observatory: Álvaro, Corentin, Rebecca, Johan, Bibi, Santi, Paul, Nerea, Viktor, Madeleine, Nich, Anatole,

Simon, Oscar, Thomas, Colin, Ross, Dainis, David, Jens, Eva, Judith, Lennart, Alex, Michal, Florent, Katrin and Nils, among others. You made me feel less far away from home. Eternamente agradecido a Álvaro por haber puesto tanto esfuerzo en que me integrara rápidamente en el grupo y en la ciudad. Sin duda lo consiguió. Thanks Corentin for all the chats we had during lunch time. Thanks Rebecca for not letting me run the Backyard Ultra alone. Thanks Johan for the delicious meal, I will always remember that apple pie. Thanks Bibi for making the Astrolympics possible. I am grateful to Lund for the amazing three-month period I had there.

Gràcies a l'Arnau Muros i al Jan Strunk per tot el que he après amb ells. Supervisar estudiants no és una tarea fàcil, per això vull donar un altre cop les gràcies al Xavi per haver confiat en mi i haver-me donat la possibilitat de co-supervisar amb ell dos treballs de final de grau. Observant com ell treballa he après a ser un millor supervisor.

Con esta tesis, que materializa el trabajo de estos últimos años, probablemente logre doctorarme y con ello nazca el "Óscar investigador". Sin embargo, para descubrir dónde y cuándo nació el "Óscar físico" debemos remontarnos más de diez años atrás, antes de entrar a la universidad. En el IES Baldiri Guilera, un humilde instituto público del Prat de Llobregat, mis compañeros de clase y yo tuvimos la suerte de coincidir en espacio y tiempo con Emilio Llorente, nuestro profesor de Física. La percepción que teníamos todos los estudiantes sobre el instituto era que este tenía un presupuesto bastante limitado, pero al entrar a clase de Física sabíamos que cada día haríamos un experimento nuevo. No sabíamos cómo lo conseguía. ¿De dónde sacaría todos estos aparatos?, nos preguntábamos. Durante los dos años que estuvimos con él pudimos ver con nuestros propios ojos como una corriente eléctrica genera un campo magnético, los rayos catódicos, jugamos con infinidad de rampas y bolas e ¡incluso llegamos a hacer una cámara de niebla! Imaginaos la sensación de alucine que teníamos nosotros, sus estudiantes, al ver las trazas de las partículas que provenían del espacio sobre hielo seco. Años más tarde, en la universidad, al hablar con mis compañeros y compañeras de carrera pude darme cuenta de lo (por desgracia) inusual que es tener un profesor así. Emilio era atento y sabía cómo motivarnos, siempre empujando a sus alumnos a aprender de manera la más divertida, pero sin nunca perder el rigor. Emilio, quiero agradecerte que hicieras la elección sobre a qué quería dedicar mi vida fuera tan fácil. De mi promoción nadie más acabó haciendo carrera científica pero, sin duda alguna, todos coincidíamos en que la clase de Física era la mejor del día. Con ello te ganaste el respeto y cariño de toda una generación.

Finalmente, quiero agradecer el apoyo que he recibido de todo mi entorno fuera de la universidad. Gracias a mis amigos más cercanos, que llevan acompañándome media vida: Alba, Alta, Antonio, Ávila, Balboa, Cris, Dani, Javi, Laura, Maria, Pablo, Santi, Sonia y Víctor. Con

vosotros he vivido y crecido tanto que siempre llevo algo de vosotros dentro de mí.

Durante la tesis decidí vivir la experiencia de irme a vivir con algunos de mis mejores amigos de toda la vida: Ávila, Javi y Víctor. Decidir vivir en el House of Pleasure durante gran parte de mi tesis fue todo un acierto. Allí hemos vivido (y seguimos viviendo) infinidad de buenos momentos que en el futuro recordaremos con todavía mucho más cariño. En unos años pondremos en contexto todo lo vivido y lo felices que fuimos.

No querría dejar sin mencionar a Miguel Ángel, que cada vez que coincidimos parece cómo si no hubiera pasado el tiempo, a Joseba, por tantas aventuras que hemos compartido en la montaña y por aquellos "Fiebre de martes noche" junto a Martí, y a Juanillo, por instruirme en la constancia y el esfuerzo en edad temprana, dos valores que me he han acompañado toda la vida.

Esta tesis está dedicada a mi familia, con mis padres y hermano a la cabeza, por haberme empujado a ser la persona que soy a día de hoy. De mi padre llevo el interés por la ciencia, el gustarme hacer de "manitas", cómo diría mi madre, y la parte más aventurera de mi personalidad. De mi madre, en cambio, llevo su eterna sonrisa, su buen humor contagioso y el dar siempre de manera desinteresada. Con mi hermano he compartido un sinfín de momentos de todo tipo: comidas familiares, conciertos, viajes, fiestas con amigos y un largo etcétera. Además, cómo buen hermano pequeño que soy, a él le debo gran parte mis gustos. De no haber sido por él seguramente no escucharía la música que escucho, ni vería las pelis que veo. Qué suerte he tenido de tener un hermano con tan buen criterio. Habiendo compartido todas estas vivencias, lo más importante que he aprendido de él es que, no importa cuantas veces falles, hay que seguir persiguiendo tu sueño. Con esta tesis, no sé si empieza o acaba el mío, ya que a la vez cierro y abro una nueva etapa. De lo que sí que estoy seguro es de que algún día cumplirás el tuyo, Sergi.

Quiero acabar estos agradecimientos dirigiéndome a Ana. Intentaré ser breve ya que, si digo todo lo que siento, la sección de agradecimientos sería más larga que el propio manuscrito. Si me decidiera a hacerlo, no podría expresar todo lo que siento, entregándote mucho menos de lo que mereces. Apoyo, alegría y amor son palabras que me has enseñado y que me han acompañado durante esta aventura. No sentirse sólo durante el doctorado es algo esencial para afrontar los momentos más difíciles y/o de más dudas. Contigo no es que no me haya sentido nunca sólo, contigo he sentido que cuando estamos juntos somos más que la suma de nuestras partes. Ana, gracias por cada día decidir compartir conmigo tu vida.

Les galàxies més clarament visibles a ull nu en el cel nocturn són els Núvols de Magalhães, les galàxies més grans al voltant de la Via Làctia (MW). Per la seva proximitat, el Gran i el Petit Núvol de Magalhães (LMC i SMC, respectivament) proporcionen als astrònoms una finestra única sobre les complexitats dels sistemes galàctics, essent un cas ideal per estudiar les interaccions galàctiques, l'evolució estel·lar i els principis fonamentals que regeixen la formació i dinàmica de les galàxies.

El LMC és tan peculiar que dona nom a un tipus de galàxia, les espirals barrades magallàniques. Aquesta galàxia nana presenta un disc sense bulb, amb un sol braç espiral i una barra estel·lar asimètrica i descentrada. És una galàxia rica en gas caracteritzada per un disc inclinat i deformat que es troba a uns 50 kpc de la nostra galàxia. Durant molt de temps, s'ha considerat que el SMC és un satèl·lit del LMC degut a la seva proximitat. Aquesta es troba a uns 62 kpc de la MW i a una distància de 20-25 kpc del LMC. El SMC és una galàxia nana irregular rica en gas.

El satèl·lit *Gaia* es va llançar el 19 de desembre de 2013 i es troba actualment en funcionament (a gener del 2024). Aquesta missió espacial mesura amb precisió les posicions, moviments i distàncies (mitjançant la seva paral·laxi) de les estrelles, observant-les repetidament al llarg del temps. *Gaia* és l'empresa científica principal de l'Agència Espacial Europea (ESA) per mapejar i estudiar les estrelles de la nostra galàxia. Tot i això, *Gaia* recull llum de totes les fonts: asteroides, binàries no resoltes, quàsars i altres fonts que entren al pla focal. Entre els objectes que travessen el pla focal de *Gaia*, es troben les estrelles dels Núvols de Magalhães. Aquestes galàxies estan prou a prop perquè *Gaia* sigui capaç de resoldre individualment moltes de les seves estrelles.

Aquesta tesi es centra en l'anàlisi cinemàtica del disc del LMC. Per fer-ho, vam aplicar una estratègia de selecció basada en xarxes neuronals per distingir les estrelles del LMC del fons de la MW fent servir la major part de la informació disponible de *Gaia*. Amb les mostres netes del LMC, vam generar mapes i perfils de velocitat 3D obtinguts a partir dels moviments propis i les velocitats en la línia de visió de *Gaia* DR3. Aquesta va ser la primera vegada que es generava un conjunt homogeni de dades (d'una galàxia que no és la MW) amb informació de velocitats 3D, resultant en un catàleg de més de vint mil estrelles. Vam fer servir aquests mapes cinemàtics per definir noves restriccions sobre la corrotació i la velocitat de rotació de la barra estel·lar del LMC. Seguint l'èxit del classificador LMC/MW,

vam entrenar i usar una xarxa neuronal per separar també les estrelles del SMC del fons de la MW.

No obstant això, l'estudi de la formació i evolució del sistema LMC-SMC no es pot dur a terme únicament amb dades observacionals. Les observacions només ens donen una imatge estàtica de tot el procés, i per això la majoria dels investigadors les complementen amb simulacions numèriques. En els darrers anys, aquests estudis s'han centrat a intentar recrear la distribució de gas neutre i la posició i propietats dels corrents fent servir simulacions hidrodinàmiques, i no en la cinemàtica interna dels Núvols. En aquest context presentem KRATOS, una suite d'accés lliure de 28 simulacions de tipus N-cossos de galàxies semblants al LMC i a galàxies amb massa similar al SMC, tant de manera aïllada com interaccionant. Amb aquests models és possible estudiar la formació de subestructures en un disc semblant al LMC després de la interacció amb un sistema de massa similar al SMC i comparar-les amb les observacions (com ara els mapes cinemàtics i la velocitat de rotació de la barra del LMC usant dades de *Gaia* DR3). Aquest és el primer estudi d'una sèrie que es dedicarà a una anàlisi més específica de la interacció LMC-SMC.

En conclusió, aquesta tesi proporciona a la comunitat científica un catàleg que separa les estrelles del LMC i el SMC del fons estel·lar de la MW. Amb aquestes mostres netes, hem aprofundit en el coneixement de la cinemàtica interna del disc del LMC mitjançant mapes de cinemàtica 3D i l'anàlisi de la velocitat de rotació de la barra. Finalment, hem començat a avaluar l'impacte del SMC en la subestructura del disc del LMC mitjançant l'ús de les simulacions KRATOS, les quals continuarem explotant i completant en treballs futurs.

ABSTRACT

The more clearly visible galaxies to the naked eye in the night sky are the Magellanic Clouds, the biggest galaxies in the Milky Way (MW) neighbourhood. Because they are so close, the Large and Small Magellanic Cloud (LMC and SMC, respectively) provide astronomers with a unique window into the complexities of galactic systems, which make them the ideal case for studying galactic interactions, stellar evolution, and the fundamental principles underlying the formation and dynamics of galaxies.

The LMC is so peculiar that it gives name to a type of galaxy, the Barred Magellanic Spirals. This galaxy is a dwarf bulgeless disc with a single spiral arm, and an off-centred and asymmetric stellar bar. It lies at a distance of around 50 kpc and is a gas-rich galaxy characterised by an inclined disc, with a warp. The SMC has long been thought to be a satellite of the LMC due to its proximity. It is at around 62 kpc from the MW and 20-25 kpc away from the LMC. The SMC is a gas rich dwarf irregular galaxy.

The *Gaia* satellite was launched on the 19th of December of 2013, and it is currently operational (as of January 2024). The spacecraft precisely measures the positions, movements and distances (through their parallax) of stars by repeatedly observing them over time. *Gaia* is the main scientific endeavour undertaken by the European Space Agency (ESA) to map and study the stars in our Galaxy. However, *Gaia* collects light from all sources: asteroids, unresolved binaries, quasars, and other sources that enter the focal plane. Among the light sources that cross the *Gaia* focal plane, we have the stars of the MCs. These galaxies are close enough that *Gaia* is able to individually resolve many of their stars.

This thesis is focused on the kinematic analysis of the LMC disc. To do so, we applied a selection strategy based on neural networks to distinguish the LMC stars from the MW foreground using most of the available information from *Gaia*. With the LMC clean samples, we generated 3D velocity maps and profiles of the LMC measured using *Gaia* DR3 proper motions and line-of-sight velocities. It was the first time that a homogeneous data set of a galaxy that is not the MW is generated with 3D velocity information, resulting in an ensemble containing more than 20 thousand stars. We used these kinematics maps to provide novel constraints on the corotation and pattern speed of the stellar bar of the LMC. Following the LMC/MW classifier's success, we trained and used a neural network to also separate the SMC stars from the MW foreground.

However, the study of the formation and evolution of the LMC-SMC system cannot be fully carried out only by using observational data. Observations give us only a static picture of the whole process, and that is why most researchers complement them with numerical simulations. In the last years, these studies have been focused on trying to recreate the distribution of neutral gas and the position and properties of the streams using hydrodynamical simulations, and not the internal kinematics of the MCs. In this context, in this thesis we present KRATOS, a comprehensive suite of 28 open access pure N-body simulations of isolated and interacting LMC-like and SMC-mass galaxies. With these models it is possible to study the formation of substructures in an LMC-like disc after the interaction with an SMC-mass system and to compare them with the observations (e.g. the kinematic maps and the bar pattern speed of the LMC using *Gaia* DR3 data). This is the first study of a series of papers that will be dedicated to a more specific analysis of the LMC-SMC interaction.

In conclusion, this thesis provides the scientific community with a catalogue that disentangles LMC and SMC stars from foreground MW stars. With these clean samples, we have deepened the knowledge of the internal kinematics of the LMC disc through 3D kinematic maps and the analysis of the bar pattern speed. Finally, we started assessing the impact of the SMC on the LMC disc substructure through the use of the KRATOS simulations, which we will continue updating and exploiting in future works.

Complete list of publications at the moment of thesis deposit.

Published / accepted articles in this thesis (3)

Jiménez-Arranz, Ó. et al. (2023). "The bar pattern speed of the Large Magellanic Cloud." In: *A&A* (accepted 22 December 2023); arXiv e-prints, arXiv:2312.11192, arXiv:2312.11192.

Jiménez-Arranz, Ó. et al. (2023a). "Application of a neural network classifier for the generation of clean Small Magellanic Cloud stellar samples." In: *A&A* 672, A65, A65.

Jiménez-Arranz, Ó. et al. (2023b). "Kinematic analysis of the Large Magellanic Cloud using Gaia DR3." In: *A&A* 669, A91, A91.

Articles submitted in this thesis (1)

Jiménez-Arranz, Ó. et al. (2023). "KRATOS: A large suite of N-body simulations to interpret the kinematics of the LMC disc." In: *A&A* (submitted 22 December 2023).

Other published articles (1)

Anders, F. et al. (2022). "Photo-astrometric distances, extinctions, and astrophysical parameters for Gaia EDR3 stars brighter than G = 18.5." In: *A&A* 658, A91, A91.

Collaboration articles (17)

Babusiaux, C. et al. (2023). "Gaia Data Release 3. Catalogue validation." In: *A&A* 674, A32, A32.

Gaia Collaboration et al. (2022). "Gaia Early Data Release 3. The celestial reference frame (Gaia-CRF3)." In: *A&A* 667, A148, A148.

Gaia Collaboration et al. (2023a). "Gaia Data Release 3. A golden sample of astrophysical parameters." In: *A&A* 674, A39, A39.

Gaia Collaboration et al. (2023b). "Gaia Data Release 3. Chemical cartography of the Milky Way." In: *A&A* 674, A38, A38.

Gaia Collaboration et al. (2023c). "Gaia Data Release 3. Exploring and mapping the diffuse interstellar band at 862 nm." In: *A&A* 674, A40, A40.

Gaia Collaboration et al. (2023d). "Gaia Data Release 3. Mapping the asymmetric disc of the Milky Way." In: *A&A* 674, A37, A37.

Gaia Collaboration et al. (2023e). "Gaia Data Release 3. Pulsations in main sequence OBAF-type stars." In: *A&A* 674, A36, A36.

Gaia Collaboration et al. (2023f). "Gaia Data Release 3. Reflectance spectra of Solar System small bodies." In: *A&A* 674, A35, A35.

Gaia Collaboration et al. (2023g). "Gaia Data Release 3. Stellar multiplicity, a teaser for the hidden treasure." In: *A&A* 674, A34, A34.

Gaia Collaboration et al. (2023h). "Gaia Data Release 3. Summary of the content and survey properties." In: *A&A* 674, A1, A1.

Gaia Collaboration et al. (2023i). "Gaia Data Release 3. The Galaxy in your preferred colours: Synthetic photometry from Gaia low-resolution spectra." In: *A&A* 674, A33, A33.

Gaia Collaboration et al. (2023j). "Gaia Data Release 3. The extragalactic content." In: *A&A* 674, A41, A41.

Gaia Collaboration et al. (2023k). "Gaia Focused Product Release: A catalogue of sources around quasars to search for strongly lensed quasars." In: *arXiv e-prints*, arXiv:2310.06295, arXiv:2310.06295.

Gaia Collaboration et al. (2023l). "Gaia Focused Product Release: Asteroid orbital solution. Properties and assessment." In: *A&A* 680, A37, A37.

Gaia Collaboration et al. (2023m). "Gaia Focused Product Release: Radial velocity time series of long-period variables." In: *A&A* 680, A36, A36.

Gaia Collaboration et al. (2023n). "Gaia Focused Product Release: Sources from Service Interface Function image analysis. Half a million new sources in omega Centauri." In: *A&A* 680, A35, A35.

Gaia Collaboration et al. (2023o). "Gaia Focused Product Release: Spatial distribution of two diffuse interstellar bands." In: *A&A* 680, A38, A38.

CONTENTS

INTRODUCTION

The more clearly visible galaxies to the naked eye in the night sky are the Magellanic Clouds (MCs), the biggest galaxies in the Milky Way (MW) neighbourhood. They can be observed from the southern hemisphere, in the Dorado and Tucana constellations.

The MCs (see Fig. 1.1), named after the renowned Portuguese explorer Fernão de Magalhães who observed them on his expedition in 1519–1522, offer an invaluable opportunity to study galaxies in detail due to their proximity. Located at distances of approximately 160,000 and 200,000 light-years from the MW, the Large Magellanic Cloud (LMC) and the Small Magellanic Cloud (SMC) provide astronomers with an accessible window into the complexities of galactic systems. Their close distance and the high abundance of observable features in these galaxies make them ideal cases for studying galactic interactions, stellar evolution, and the fundamental principles underlying the formation and dynamics of galaxies.

1.1 LARGE MAGELLANIC CLOUD

At a distance of around 50 kpc (Pietrzyński et al. 2019), the LMC represents the prototype Barred Magellanic Spiral, a type of galaxies with unusual structural characteristics.

The LMC (see Fig. 1.1 left panel) is a dwarf, bulgeless spiral galaxy, with an asymmetric stellar bar, many star forming regions and a prominent spiral arm (e.g. Elmegreen and Elmegreen 1980; Gallagher and Hunter 1984; Zaritsky 2004; Yozin and Bekki 2014; Gaia Collaboration et al. 2021). The LMC is a gas-rich galaxy (e.g. Luks and Rohlfs 1992; Kim et al. 1998) characterised by an inclined disc (e.g. van der Marel and Cioni 2001; van der Marel 2001) with a warp (e.g. Olsen and Salyk 2002; Nikolaev et al. 2004; Ripepi et al. 2022).

The luminosity of the LMC is one-tenth of that the MW (e.g. Sparke and Gallagher 2000), and its stars are concentrated on a flat disk tilted at an inclination of around $i \sim 30°$ with respect to the line-of-sight, though there remains a large uncertainty in the literature on what the inclination angle is (e.g. Haschke et al. 2012; van der Marel and Kallivayalil 2014; Gaia Collaboration et al. 2021; Ripepi et al. 2022).

The total mass of the LMC is currently estimated to be around $1.8 \times 10^{11} M_\odot$ (e.g. Peñarrubia et al. 2016; Erkal et al. 2019), an order of magnitude larger than in earlier estimations (e.g. Avner and King 1967; van der Marel and Kallivayalil 2014). The large mass of the
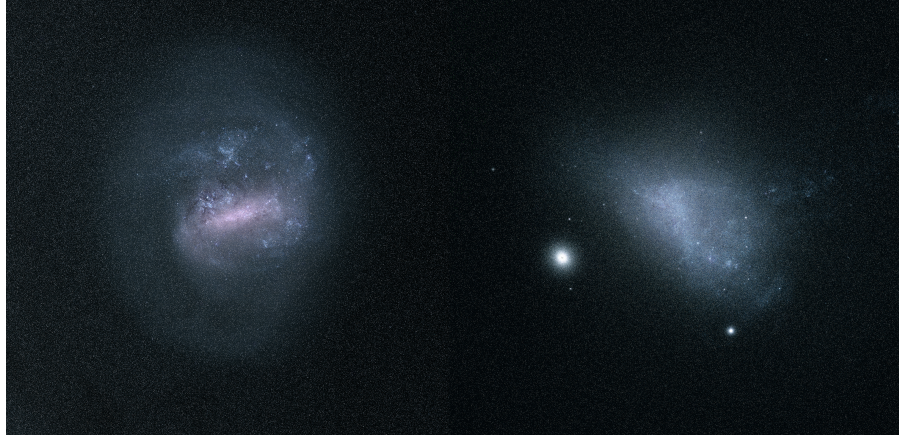
Figure 1.1: The Large (left) and Small (right) Magellanic Cloud as viewed by European Space Agency (ESA)'s *Gaia* satellite using information from the mission's Data Release 2 (DR2). Credit: ESA/Gaia/D-PAC, CC BY-SA 3.0 IGO.

LMC naturally explains a variety of newly discovered independent dynamical effects, which are discussed in Section 1.3.

The LMC line-of-sight velocity with respect to the Sun is $\sim 262.2 \pm 3.4$ km s^{-1}, moving away from it. Regarding the LMC centre, there is some ambiguity (e.g. van der Marel and Kallivayalil 2014; Gaia Collaboration et al. 2021; Vasiliev 2023b, for a review). The rotational centre of the LMC has been a matter of debate, most notably with the photometric centre and the centre of rotation for the HI gas lying at different positions. Due to perspective effects and internal motion in the LMC, different centre locations lead to different values of mean proper motions (e.g. Wan et al. 2020; Gaia Collaboration et al. 2021). The LMC moves away from the MW with a galactocentric radial velocity of about 70 km s^{-1}, and with a tangential velocity of about 310 km s^{-1}, which is significantly faster than the circular velocity at that distance (e.g. Vasiliev 2023b). These values suggest that it recently passed the pericentre of its orbit; however, the reconstruction of its orbit further in the past depends on a number of variables (more in Section 1.3).

1.2   SMALL MAGELLANIC CLOUD

The SMC (see Fig. 1.1 right panel) has long been thought to be a satellite of the LMC due to its close proximity. It is at around 62 kpc from the MW (e.g. Cioni et al. 2000b; Hilditch et al. 2005; Graczyk et al. 2014) and 20-25 kpc away from the LMC. Being only a few times less luminous than the LMC, the SMC is a dwarf irregular galaxy characterised by a gas rich (e.g. Rubio et al. 1993; Staveley-Smith et al. 1998), and low metallicity environment (e.g. Choudhury et al. 2018; Grady et al. 2021). Red clump (RC) stars and other standard candles

were used to reconstruct its 3D shape, and this revealed that it is fairly extended along the line of sight (e.g. Subramanian and Subramaniam 2012; Ripepi et al. 2017).

The galaxy is characterised by a distorted shape with an elongated bar-like structure along the North East–South West axis (e.g., de Vaucouleurs and Freeman 1972; Subramanian and Subramaniam 2012; Scowcroft et al. 2016; Jacyszyn-Dobrzeniecka et al. 2016; Ripepi et al. 2017) and an eastern Wing towards the Magellanic Bridge (e.g. Shapley 1940). The SMC has a complex morphology and dynamics as a result of its high gravitational interaction with the LMC, with the gas behaving differently from the star populations. Young stellar populations follow the irregular and asymmetric distribution typical of the HI gas (e.g. Zaritsky et al. 2000; Stanimirović et al. 2004; Di Teodoro et al. 2019) while older stellar populations depict an elliptical/spheroidal distribution (e.g. Cioni et al. 2000a; Zaritsky et al. 2000; Rubele et al. 2015; El Youssoufi et al. 2019).

Given that it has lost a significant portion of its gas and the majority of its dark matter (DM) halo (e.g., Bekki and Stanimirović 2009), it is very likely that the SMC was once much more massive than it is currently. Its estimated current mass is $1.9 \times 10^{10} M_\odot$ (e.g. Pardy et al. 2018; Lucchini et al. 2020), thus it has little impact on the MW but a noticeable effect on the LMC. As for the LMC, the current accepted value for the SMC total mass is an order of magnitude larger than previously though in the past (e.g. Stanimirović et al. 2004).

1.3 THE MAGELLANIC CLOUDS AS AN INTERACTING SYSTEM

The long-held belief that the MCs have been orbiting our Galaxy for a significant number of orbits (e.g. Tremaine 1976; Murai and Fujimoto 1980; Lin and Lynden-Bell 1982; Gardiner et al. 1994) gradually gave way to the now-accepted theory that their orbits were highly eccentric, with apocentres well beyond 200 kpc and orbital periods exceeding 5 Gyr, or even unbound (e.g. Besla et al. 2007). The current preferred scenario (proposed by Besla et al. 2007) is that the MCs are just after the first approach of the MW, with no prior pericentre passages within the previous 10 Gyr (although see Vasiliev 2023a). This conclusion is largely supported by the high measured tangential velocity component of the LMC (see Section 1.1), but it would also naturally account for the current existence of the SMC and other more recently discovered satellites of the LMC, which would have been stripped by the MW tidal field if the MCs were in a much closer orbit to the Galaxy. Another argument supporting this scenario is that up until a recent burst that began about 3–4 Gyr ago (e.g. Harris and Zaritsky 2009; Meschin et al. 2014; Hasselquist et al. 2021; Massana et al. 2022), the LMC's star formation rate had been unusually low. This burst may have been caused by gas being compressed as it underwent a bow shock

upon entering the MW's gas corona, though interaction with the SMC is another explanation. The argument against a previous pericentre passage may be seen in the absence of evidence for an earlier episode of increased star formation rate. Moreover, there is not a large-scale stellar tidal stream like the one in the Sagittarius galaxy, which has orbited the MW several times (e.g. Ibata et al. 1994; Gómez et al. 2012; Antoja et al. 2020; Ramos et al. 2022). It is worth mentioning that very recently Vasiliev (2023a) proposed an alternative scenario in which the LMC is on its second passage around the MW, where the LMC's previous pericentre passage may have happened 5–10 Gyr ago at a distance larger than 100 kpc, which would be large enough to preserve its current population of satellites. In this second-passage model, the distribution of LMC debris is much wider, but the perturbations of the MW halo caused by the LMC appear to be almost identical to those in the first-passage scenario.

We can observe in our surroundings some consequences of the recent interaction of the MCs with the MW. The most well-known manifestation of this interaction is the accumulation of stars behind the moving object (the LMC) and the associated dynamical friction force created by this density wake. The so-called Pisces plume, observed by Belokurov et al. (2019) as an overdensity in the 3D distribution of RR Lyrae stars and as a kinematical offset in the co-spatial population of blue horizontal branch (BHB) stars, is an observational evidence for such a wake created by the LMC and is qualitatively consistent with the wake signatures predicted by Garavito-Camargo et al. (2019) from N-body simulations. Again, any such wake would be blurred away if the MCs had looped around our Galaxy twice or three times; the fact that we can see it indicates that the dwarfs are making their initial pass around the MW.

More recently, Conroy et al. (2021) selected a sample of 1,301 red giant (RG) stars beyond 60 kpc using photometry of the optical and infrared satellites *Gaia* from the ESA and Wide-field Infrared Survey Explorer (WISE) from the National Aeronautics and Space Administration (NASA), respectively. The overdensity of MW halo stars stood out in two areas of the sky, one above and one below the galactic plane (see Fig. 1.2). As explained above, the latter was previously observed by Belokurov et al. (2019) and extends towards the LMC in the south. The former was interpreted by the authors as an offset of the outer halo creating an overdensity in the north, which they call it "collective response". However, even the heaviest-LMC model underestimated the amplitude of the observed asymmetries by a factor of 2. Later studies (Chandra et al. 2022) hypothesised that these asymmetries could be caused by leftovers from an early massive merger of the MW.

Regarding the interaction between the MCs, the pair has been heavily influenced by dynamical interactions of tidal and/or ram pressure
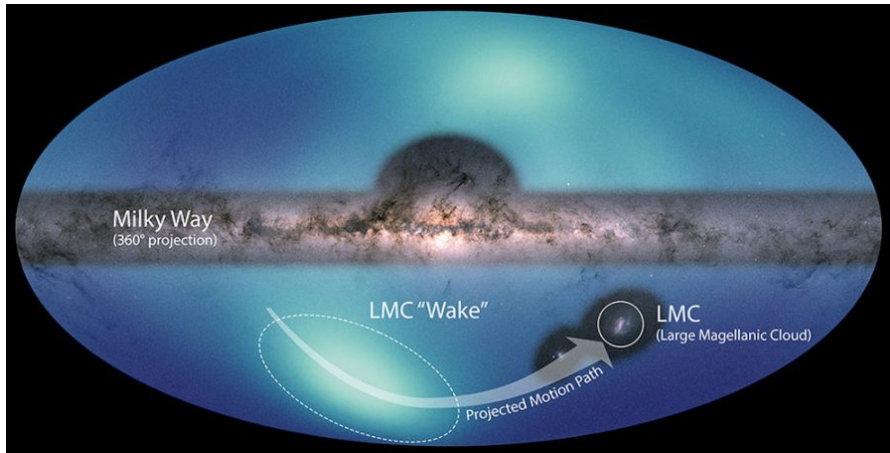
Figure 1.2: Images of the MW disk and the LMC superimposed on a blue-hued map of the MW halo. The light-blue blob below the galactic plane is a region densely populated with MW halo stars that the LMC provoked when passing through, the LMC's wake. Credit: NASA / ESA / JPL-Caltech / Conroy et. al. 2021.

nature. The requirement that the MCs form a bound pair imposes a lower limit on their total mass of the order of $10^{11} M_\odot$.

The two Clouds' most recent near encounter took place between 150 and 200 Myr ago at a distance of less than 10 kpc, leading to the formation of the Magellanic Bridge (see Fig. 1.3), a stellar structure in the region between the two MCs. First, Hindman et al. (1963) identified the Bridge of gas connecting the MCs in neutral hydrogen emission. In earlier studies, Kerr et al. (1954) observed that the HI in the MCs were shown to be more stretched than their stars, but the hazy bridge connecting the two galaxies was not discovered. More recently, Misawa et al. (2009) discovered that the metallicity of the Bridge is similar to the current-day SMC's metallicity rather than the LMC's. This discovery suggested that materials that were once in the SMC were used to create the Bridge. Moreover, there is a stellar population in the Bridge, which was first noticed by Irwin et al. (1985), and has been studied using both simulations (e.g. Besla et al. 2012; Diaz and Bekki 2012) and observations (e.g. Irwin et al. 1985, 1990; Demers and Irwin 1991; Yoshizawa and Noguchi 2003; Harris 2007; Kallivayalil et al. 2013; Bagheri et al. 2013; Noël et al. 2013; Skowron et al. 2014; Carrera et al. 2017; Zivick et al. 2019; Schmidt et al. 2020; Gaia Collaboration et al. 2021).

The second close-in-time encounter between the MCs occurred ∼2 Gyr ago leading to the formation of the Magellanic Stream (see Fig. 1.4), a massive network of gaseous filaments trailing behind the Clouds (e.g. Bajaja et al. 1985; Putman 2000; Putman et al. 2003; Nidever et al. 2008; D'Onghia and Fox 2016; Lucchini et al. 2021). The Stream was discovered by Mathewson et al. (1974) characterising the HI 21 cm emission and the length of the known Stream has grown with time
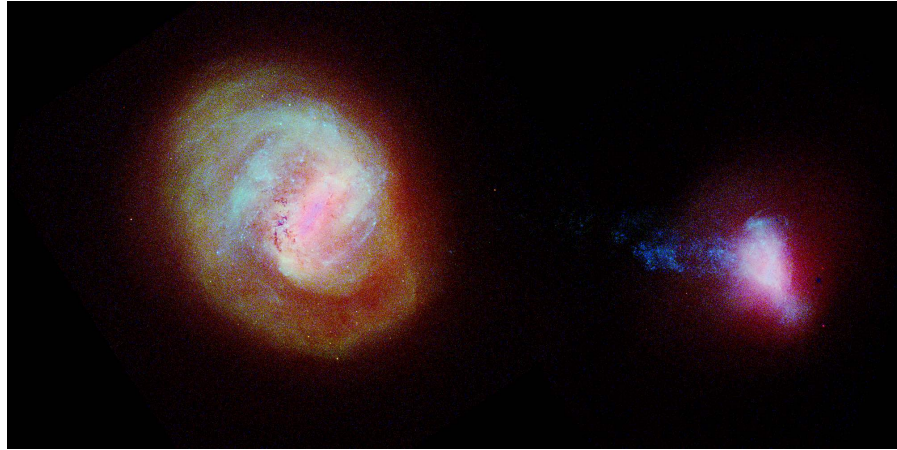
Figure 1.3: The Large (left) and Small (right) Magellanic Cloud as viewed by ESA's *Gaia* satellite. Colour coded by the different stellar populations being the bluer (redder) the younger (older) stars. On the left part of the SMC we can observe the Magellanic Bridge (in blue), a structure joining the MCs that formed as a result of tidal forces that stripped gas and stars from the SMC towards the LMC. Credit: ESA/Gaia/DPAC, CC BY-SA 3.0 IGO.

as more diffuse gas clouds have been discovered (e.g. Nidever et al. 2010). In contrast to the Magellanic Bridge, a stellar population has not been found in the Stream (e.g. Recillas-Cruz 1982; Brueck and Hawkins 1983; Guhathakurta and Reitzel 1998).

1.4 GROUND-BASED SURVEYS DEDICATED TO THE CLOUDS

As mentioned above, the observation of the MCs is exclusive to the Southern Hemisphere. Thus, most observational endeavours aimed at studying these galaxies are conducted from strategic points in South America, with Chile serving as a primary hub for these scientific explorations.

Back in the past, surveys like the Magellanic Clouds Photometric Survey (MCPS) led by Zaritsky et al. (1997) and conducted at La Silla Observatory, and spectroscopic investigations undertaken by the Magellanic Cloud Emission Line Survey (MCELS) led by Smith et al. (2005) and conducted at Cerro Tololo Inter-American Observatory, significantly contributed to our understanding of these galaxies. By the end of the 1990s, the MCPS survey performed a UBVI photometric survey of over one million stars. Years later, the MCELS survey studied the bright emission of hydrogen, sulphur and oxygen from the interstellar gas of these two galaxies to study the properties, kinematics, and dynamics of the interstellar medium.

At present, institutions such as the European Southern Observatory (ESO), perched atop the arid plateaus of the Atacama Desert, have housed telescopes and instruments pivotal in conducting comprehen-
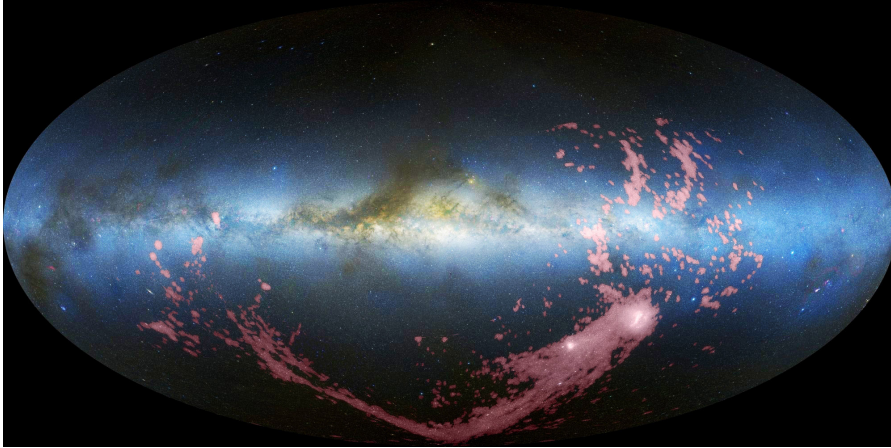
Figure 1.4: The Magellanic Stream (pink) displayed in Galactic coordinates using an all-sky Hammer-Aitoff projection centred on the Galactic Centre. Credit: Nidever et al. 2010, NRAO/AUI/NSF, Mellinger 2009, Leiden-Argentine-Bonn Survey, Parkes Observatory, Westerbork Observatory, Arecibo Observatory.

Figure 1.5: The Magellanic Clouds seen above the Auxiliary Telescopes of ESO's Very Large Telescope (VLT) in Paranal, Chile. Credit: J. C. Muñoz/ESO.

sive surveys of the MCs (see Fig. 1.5). Specifically, in the 4-m Visible and Infrared Survey Telescope for Astronomy (VISTA) telescope, the VISTA Magellanic Survey YJKs Catalogue (VMC) aimed the MCs as a benchmark for the study of stellar populations and galaxy interactions (Cioni et al. 2011). Among the notable achievements of the VMC collaboration is the determination of proper motions (e.g., Cioni et al. 2016; Niederhofer et al. 2022; Schmidt et al. 2022) using ground-based telescopes to study considerably larger samples of stars surpassing the targets specifically aimed (at that time) by space telescopes. It is also remarkable the discovery and characterisation of many variable stars within the MCs (e.g. Ripepi et al. 2012, 2014, 2015, 2016). These studies allowed to investigate the internal kinematics of galaxies as a function of stellar population age and to relate their geometry to their dynamical history (e.g. Cioni et al. 2016; Mazzi et al. 2021; Tatton et al. 2021; Schmidt et al. 2022).

The Survey of the Magellanic Stellar History (SMASH) stands as a pioneering effort aimed at unravelling the intricate stellar history and evolution of the MCs (Nidever et al. 2017). Conducted primarily using the Dark Energy Camera (DECam) mounted on the Blanco 4-meter telescope at Cerro Tololo Inter-American Observatory in Chile, the multi-band photometry of the SMASH survey provides an unprecedented panoramic view, enabling the detection and characterisation of a diverse array of stellar populations. By meticulously charting the stellar content and distribution across the MCs, the SMASH survey has significantly contributed to the understanding of their formation, interactions, and evolution, shedding light on their complex dynamical histories (e.g. Choi et al. 2018a,b; Massana et al. 2022).

Looking at the future, the 4-meter Multi-Object Spectroscopic Telescope (4MOST) represents a cutting-edge instrument poised to revolutionise our comprehension of the MCs in the upcoming era of astronomical research (de Jong et al. 2019). Equipped with a state-of-the-art spectrograph and located at the ESO's Paranal Observatory in Chile, 4MOST is set to undertake a comprehensive spectroscopic survey of millions of celestial objects, including stars within the MCs. This ambitious endeavour aims to unravel the chemical compositions, kinematics (i.e. line-of-sight velocities, V_{los}), and stellar populations across these galaxies with unprecedented precision.

Nevertheless, the limitations inherent in ground-based observations, such as atmospheric interference and observational constraints from Earth's surface, beckon us towards the next frontier: space missions dedicated to studying the MCs. With Hubble Space Telescope (HST) playing a key role in determining accurate proper motions within these galaxies (e.g. Kallivayalil et al. 2013), the launch of *Gaia* in 2013 signalled the beginning of a new chapter in the dynamics studies of these nearby galaxies.

Figure 1.6: Artist's impression of *Gaia* mapping the stars of the MW. Copyright: ESA/ATG medialab; background: ESO/S. Brunier.

1.5 GAIA MISSION

The *Gaia* mission (see Fig. 1.6) is a scientific endeavour undertaken by the ESA to map and study the stars in our Galaxy, the MW. The mission's primary goal is to create the most precise and detailed 3D map of our Galaxy ever made. It has catalogued and determined astrometric and photometric data of more than one billion stars, representing around 1% of the total stars of our own Galaxy.

The *Gaia* satellite was launched on the 19th of December of 2013, and it is currently operational (at date 12 January 2024). By repeatedly observing the stars over time, the spacecraft precisely measures their positions, movements and distances (throughout their parallax, e.g. Gaia Collaboration et al. 2016; Lindegren et al. 2016). However, *Gaia* does not only observe stars, but collects light from all sources: asteroids (e.g. Gaia Collaboration et al. 2022a; Tanga et al. 2022), unresolved binaries (e.g. Halbwachs et al. 2022), quasars (e.g. Gaia Collaboration et al. 2022b), and others point-like objects that enter the focal plane. Among the objects that cross the *Gaia* focal plane, we also have the stars that conform the MCs. These galaxies are at such close distance (50 kpc and 62 kpc for the LMC and SMC, respectively) that *Gaia* is able to individually resolve many of their stars.

With every *Gaia* Data Release, the Gaia Collaboration publishes a set of papers to give an overview of its scientific potential, the *Gaia* performance verification papers (PVPs). The purpose of these papers is to demonstrate the scientific quality of the data through examples without going into in-depth analysis, giving a short introduction to

the selected science topics that can be addressed with the new data release.

For Early Data Release 3 (eDR3), the *Gaia* Collaboration published a PVP (Gaia Collaboration et al. 2021) using the first 34 months of data of the mission to study the structure and kinematics of the MCs. The galaxies were chosen by the Collaboration as an excellent case for evaluating the characteristics and quality of the *Gaia* data. This is because the tens of millions of MCs stars in the *Gaia* catalogue are very far away when compared to the MW stars, which puts them on the very edge of the data's usability. In this work the authors demonstrated that the systematics present in the data made it challenging to determine the 3D geometry of the LMC just using the stars' position and parallax, which is the absolute limit of the utility of the *Gaia* eDR3 astrometry. Also, it was the first time that the two planar (radial and tangential) velocity components were derived for multiple stellar evolutionary phases in a galactic disc outside the MW, showing the differences between younger and older phases. Finally, by tracing the density and velocity flow of the stars from the SMC towards the LMC, the authors demonstrated that the *Gaia* eDR3 data clearly resolved the Magellanic Bridge (see Section 1.3). This was achieved not only using all MCs stars but also separating the young and evolved populations.

On the 13th June 2022, with the *Gaia* Data Release 3 (DR3), the analysis and study of the MCs made a step forward thanks to the publication of mean line-of-sight velocity (V_{los}) for 33 million stars (Katz et al. 2022), where tens of thousands of them belong to LMC and SMC stars. Forthcoming releases from the *Gaia* mission will offer improved data quality, with enhanced angular resolution, more precise proper motion measurements, and increased access to line-of-sight velocities, expecting less crowding of stars at low radius.

1.6   SIMULATING THE MAGELLANIC CLOUDS WITH THE MILKY WAY

An important goal for the study of the MW is to understand the history of our Galaxy and the interaction with its neighbours. However, for human scales, the timescales of the Universe are immense and we cannot perform experiments, making astronomy an observational science. Unfortunately, observations give us only a static picture of the whole process. It is in here were simulations play a crucial role in this endeavour by allowing us to create virtual representations of the MW and its surrounding environment. These simulations incorporate a multitude of parameters and by compare each simulation's prediction with the observables we can try to infer the MW's past history.Thus, we can try to infer the MW and MCs common history by simulating this three-body system since their complex evolutionary history is encoded in the MCs present structure and dynamics.

However, reconstructing the MCs' orbits is a difficult task. If the LMC mass was negligible in comparison to the MW, it would be easy to integrate the equations of motion backward in time for any assumed MW potential. However, the orbit parameters, even in this simplistic example, are surprisingly sensitive to small changes in the assumed present-day position and velocities (Vasiliev 2023b, Fig. 2). A variation of ~ 10 km s^{-1} in today's velocity can change the orbital periods by a factor of two, since the current velocity is quite close to the local escape velocity. Also, the orbits are drastically altered by changing in 1% the assumed distance; this alteration is caused by an increase in tangential velocity of ~ 5 km s^{-1} rather than the change in position by itself. On the other hand, the assumed MW potential has a significant impact on the LMC orbit (Vasiliev 2023b, Fig. 3). The orbital period changes to 30 Gyr or 6 Gyr with just a 10% shift in the MW mass, which lies within current uncertainties. Furthermore, although little is known about the MW halo's shape, it also has a considerable impact on the LMC's past orbit (Vasiliev 2023b, Fig. 4). The LMC past orbits also depends on its mass (e.g. Besla et al. 2007; Besla et al. 2010; Besla et al. 2012; Erkal et al. 2019). Lastly, to complicate it more, even the slightest change in the SMC can significantly alter the LMC's position and velocity with respect to their shared centre of mass.

We can find some works in the literature with modern high-resolution simulations for both the LMC and the SMC. When the focus of study is on the past orbits and the effect of the interaction of the three galaxies, pure N-body simulations are used because they are computationally less expensive. In this case, ignoring the gas does not affect the results since the orbits of the galaxies are determined by the total gravitational potential, which is primarily made up of dark matter with minor contributions from stars and gas. Some examples are Garavito-Camargo et al. (2019), Petersen and Peñarrubia (2021), and Vasiliev (2023b,a).

Until today, the main focus of simulations related to the MCs and the MW is directed towards understanding their gas components (e.g. Besla et al. 2007, 2012; Hammer et al. 2015; Pardy et al. 2018; Tepper-García et al. 2019; Lucchini et al. 2020; Lucchini et al. 2021). Hence, hydrodynamical simulations are employed for this purpose (see, for example, Fig. 1.7). However, the study of the effect of interactions on the internal structures of a LMC-like disc, such as the bar and the spiral arm, has only been carried out by a few authors. In particular, only the work by Besla et al. (2012) extensively explored these features. Understanding the formation process of these LMC morphological attributes can potentially unveil the details on the interaction occurred between these two satellite galaxies, and also with the MW.
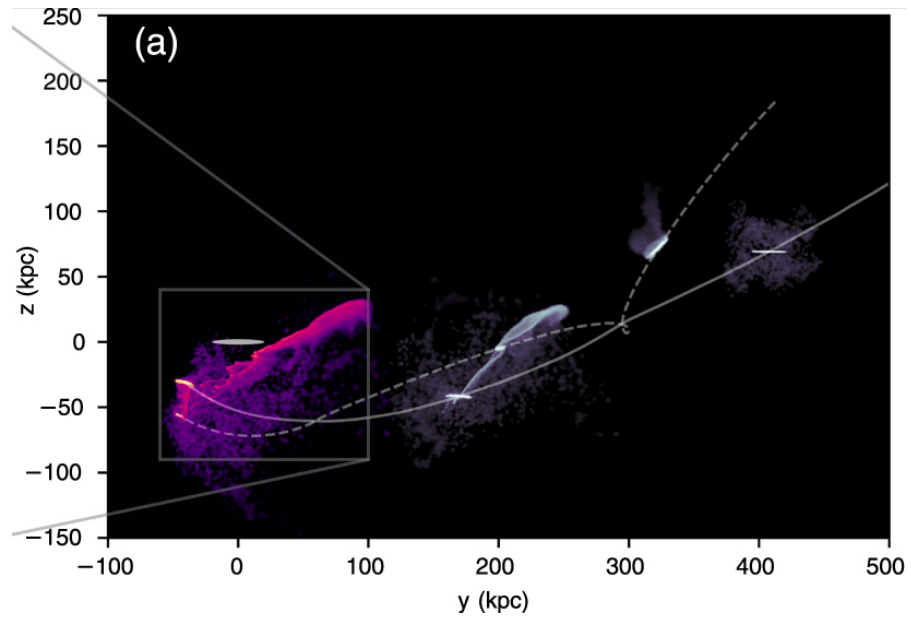
Figure 1.7: Hydrodynamical simulation of the orbital story of the Magellanic Clouds. It shows the Magellanic Stream at three different times during the MCs infall, with the present-day distribution shown in color. The solid and dashed lines represent the past orbital trajectories of the LMC and SMC, respectively. Credit: S. Lucchini.

1.7   OVERVIEW OF THIS THESIS

The main purpose of this thesis is to deepen in our understanding of the interaction of the MCs between them and with the MW using both *Gaia* data and the KRATOS simulations.

Part i focuses on the observational analysis of the MCs using *Gaia* DR3 data. In Chapter 2, we define and validate a new supervised classification strategy based on neural networks (NNs) to distinguish the LMC stars from the MW foreground and we present, for the first time, the 3D velocity maps and profiles in the plane of the LMC. In Chapter 3, similarly to what we did for the LMC, we train and validate a NN classifier to distinguish the SMC stars from the MW foreground. In Chapter 4 we make use of the LMC in-plane velocity maps to determine the LMC bar pattern speed.

Part ii of this thesis, consisting of a single chapter, is focused on the description and the preliminary analysis of KRATOS, a suite of 28 open access and pure N-body simulations of isolated and interacting LMC-like galaxies, to study the formation of substructures in their disc after the interaction with an SMC-mass galaxy.

In Part iii, a summary of all the work done is presented, together with the main conclusions and future work that can be extracted from each chapter.

Part I

THE MAGELLANIC CLOUDS IN THE GAIA DR3
ERA

KINEMATIC ANALYSIS OF THE LARGE MAGELLANIC CLOUD

This Chapter contains the published version of Jiménez-Arranz et al. (2023b, A&A, 669, A91).

We define and validate a new supervised classification method based on neural networks (NNs) to distinguish the Large Magellanic Cloud (LMC) stars from the Milky Way (MW) foreground. We use as much as of the *Gaia* DR3 data as possible (astrometry and photometry). As a result of the application of our method, we are able to define three samples, with different levels of purity and, complementarily, completeness. We validated these classification results using different test samples with known contents or independently classified (LMC RR Lyrae, LMC Cepheids and LMC-MW StarHorse (SH) samples).

By using *Gaia* DR3 proper motions and line-of-sight velocities (V_{los}), we present the first 3D velocity maps and profiles in the plane of the LMC. For the first time, an homogeneous data set of this type for a galaxy that is not the MW is presented with 3D velocity information, using more than 20 thousand stars.

We show that the contamination of MW stars in the samples only has a significant impact on the LMC's outskirts. We also demonstrate that the results for the kinematics of the inner disc, which is is mainly bar dominated, are not biased when V_{los} is not available. The spiral arm's kinematics appear to be dominated by an inward motion and a faster rotation than the disc in the portion of the arm that is attached to the bar. Finally, uncertainties regarding the LMC's systemic motions and assumed disc morphological parameters may, in some cases, significantly affect the analysis's results.

The article received recognition from *Gaia* as Image of the Week for contributing to the kinematic analysis of the LMC.

Astronomy
&
Astrophysics

Kinematic analysis of the Large Magellanic Cloud using *Gaia* DR3[⋆,⋆⋆]

Ó. Jiménez-Arranz[1,2,3], M. Romero-Gómez[1,2,3], X. Luri[1,2,3], P. J. McMillan[4], T. Antoja[1,2,3], L. Chemin[5], S. Roca-Fàbrega[6,7], E. Masana[1,2,3], and A. Muros[1,2]

1 Departament de Física Quàntica i Astrofísica (FQA), Universitat de Barcelona (UB), C Martí i Franqués, 1, 08028 Barcelona, Spain
2 Institut de Ciències del Cosmos (ICCUB), Universitat de Barcelona, Martí i Franquès 1, 08028 Barcelona, Spain
  e-mail: ojimenez@icc.ub.edu
3 Institut d'Estudis Espacials de Catalunya (IEEC), C Gran Capità, 2-4, 08034 Barcelona, Spain
4 Lund Observatory, Department of Astronomy and Theoretical Physics, Lund University, Box 43, 22100 Lund, Sweden
5 Centro de Astronomía – CITEVA, Universidad de Antofagasta, Avenida Angamos 601, Antofagasta 1270300, Chile
6 Departamento de Física de la Tierra y Astrofísica, Facultad de Ciencias Físicas, Plaza de las Ciencias, 1, 08028 Madrid, Spain
7 Instituto de Astronomía, Universidad Nacional Autónoma de México, Apartado Postal 106, 22800 Ensenada, B.C., Mexico

ABSTRACT

Context. The high quality of the *Gaia* mission data has allowed for studies of the internal kinematics of the Large Magellanic Cloud (LMC) to be undertaken in unprecedented detail, providing insights into the non-axisymmetric structure of its disc. Recent works by the *Gaia* Collaboration have already made use of the excellent proper motions of *Gaia* DR2 and *Gaia* EDR3 for a first analysis of this sort, but these were based on limited strategies aimed at distinguishing the LMC stars from the Milky Way foreground that did not use all the available information. In addition, these studies could not access the third component of the stellar motion, namely, the line-of-sight velocity – which has now become available via *Gaia* DR3 for a significant number of stars.
Aims. Our aim is twofold: 1) to define and validate an improved, more efficient and adjustable selection strategy to distinguish the LMC stars from the Milky Way foreground; 2) to check the possible biases that assumed parameters or sample contamination from the Milky Way can introduce in analyses of the internal kinematics of the LMC based on *Gaia* data.
Methods. Our selection was based on a supervised neural network classifier, using as much as of the *Gaia* DR3 data as possible. Based on this classifier, we selected three samples of candidate LMC stars with different degrees of completeness and purity. We validated these classification results using different test samples and we compared them with the results from the selection strategy used in the *Gaia* Collaboration papers, based only on the proper motions. We analysed the resulting velocity profiles and maps for the different LMC samples and we checked how these results change when we use the line-of-sight velocities that are available for a subset of stars.
Results. We show that the contamination in the samples from Milky Way stars basically affects the results for the outskirts of the LMC. We also show that the analysis formalism used in absence of line-of-sight velocities does not bias the results for the kinematics in the inner disc. Here, for the first time, we performed a kinematic analysis of the LMC using samples with the full three dimensional (3D) velocity information from *Gaia* DR3.
Conclusions. The detailed 2D and 3D kinematic analysis of the LMC internal dynamics demonstrate that: 1) the dynamics in the inner disc is mainly bar dominated; 2) the kinematics on the spiral arm overdensity seems to be dominated by an inward motion and a rotation that is faster than that of the disc in the part of the arm attached to the bar; 3) the contamination of Milky Way stars seem to dominate the outer parts of the disc and mainly affects old evolutionary phases; and 4) uncertainties on the assumed disc morphological parameters and line-of-sight velocity of the LMC can (in some cases) have significant effects on the results of the analysis.

Key words. galaxies: kinematics and dynamics – Magellanic Clouds – astrometry

1. Introduction

The Large Magellanic Cloud (LMC) is one of the Milky Way (MW) satellite galaxies and a member of the Local Group.

The LMC is the prototype of dwarf, bulgeless spiral galaxy (the so-called Magellanic type: Sm), with an asymmetric stellar bar, many star forming regions, including the Tarentula Nebula, and prominent spiral arms (e.g., Elmegreen & Elmegreen 1980; Gallagher & Hunter 1984; Yozin & Bekki 2014; Gaia

Collaboration 2021b). The LMC is a gas-rich galaxy characterised by an inclined disc (e.g., van der Marel & Cioni 2001; van der Marel 2001), with several warps (e.g., Olsen & Salyk 2002; Choi et al. 2018; Ripepi et al. 2022) and an offset bar whose origin is not well understood (e.g., Zaritsky 2004). Due to its proximity, the LMC is a perfect target for many studies and focused photometric surveys, such as VMC-VISTA Survey of the Magellanic Clouds system (Cioni et al. 2011) or SMASH-Survey of the Magellanic Stellar History (Nidever et al. 2017), as well as the astrometric mission *Gaia* (ESA). Already in Gaia Collaboration (2018; 2021b, hereafter, MC21), the authors show the capabilities of *Gaia* to characterise the structure and kinematics of this nearby galaxy. The recovery of its three-dimensional (3D) structure using *Gaia* data only has been shown to be complex due to the zero

---

point in parallax and limit in parallax uncertainties (MC21, Lindegren et al. 2021a,b). Recent attempts using specific populations for which individual distances can be anchored, such as in the populations of Cepheids (Ripepi et al. 2022) or RR Lyrae (Cusano et al. 2021), have been more effective. Three-dimensional structure analysis is not the only tool for inferring the characteristics and morphologies of the galaxy under study. Kinematic profiles and kinematic maps provide additional information on the characteristics and dynamical evolution of the galaxy (Gaia Collaboration 2018; Vasiliev 2018, MC21).

The presence of non-axisymmetric features, such as a bar or spiral arms, modifies the velocity map of a simply rotating disc. The nature of the spiral arms – whether it is a density wave (Lindblad 1960; Lin & Shu 1964), a tidally induced arm (e.g., Toomre & Toomre 1972), transient co-rotating arms (Goldreich & Lynden-Bell 1965; Julian & Toomre 1966; Toomre 1981), or bar induced (e.g., Athanassoula 1980; Romero-Gómez et al. 2007; Salo et al. 2010; Garma-Oehmichen et al. 2021) – can be disentangled from its signature in the velocity field (e.g., Roca-Fàbrega et al. 2013, 2014). The question of how the LMC became so asymmetric, particularly with regard to the ultimate origin of its spiral arm in contrast to more massive spiral galaxies, remains unclear. Thus, detailed kinematic profiles and maps are necessary to supplement its investigation.

Kinematics of stars in the outskirts of the LMC have shed some light on the characteristics of the stellar bridge generated by the tidal interaction between the Large and Small Magellanic Clouds (Zivick et al. 2019; Schmidt et al. 2020), the formation of the LMC's northern arm (Cullinane et al. 2022a), or the dynamical equilibrium of the disc (Cullinane et al. 2022b). Pre-*Gaia* proper motions and line-of-sight velocities of less than a thousand stars where used by Kallivayalil et al. (2013), van der Marel & Kallivayalil (2014) to show the detailed large-scale rotation of the LMC disc. The number of sources increased by orders of magnitude when using *Gaia* DR2 proper motions to study the internal motion of the LMC (Gaia Collaboration 2018; Vasiliev 2018). Wan et al. (2020) used Carbon Stars and *Gaia* DR2 proper motions to infer the LMC centre, systemic motion, and morphological parameters to compare them with other stellar populations. Similarly, the improved accuracy of *Gaia* EDR3 (MC21, Niederhofer et al. 2022) allowed for a detailed study of the LMC disc kinematics with the aim of separating the analysis based on different stellar evolutionary phases, in addition to extending the study to the LMC outskirts and bridge between the LMC and SMC.

In this work, we focus on the general kinematic analysis of the LMC disc and we present the first 3D velocity maps and profiles of the LMC measured using *Gaia* DR3 proper motions and line-of-sight velocities. It is the first time that a homogeneous data set of a galaxy that is not the Milky Way is presented with 3D velocity information, for more than 20 thousand stars. We compare the maps with the ones obtained from previous *Gaia* releases where only astrometric motions were considered. With the new maps, we want to assess where, and to what extent, the kinematics have benefitted from the line-of-sight velocities.

This paper is organised as follows. In Sect. 2, we describe the LMC samples used throughout this work. We use a new supervised classification strategy based on neural networks to separate the LMC stars from the MW foreground stars. In this section, we also describe the training sample, along with how we applied

the classifier to *Gaia* data and how we validated the classification. In Sect. 3, we describe the formalism adopted to transform from *Gaia* observables to the LMC reference frame and demonstrate its validation using an *N*-body simulation. In Sect. 4, we show the detailed kinematic analysis of the LMC samples, showing the velocity profiles and the velocity maps of the different LMC samples. In Sect. 5, we study possible biases on the velocity maps caused by the unknown LMC 3D geometry, as well as uncertainties in the systemic motion. Finally, in Sect. 6, we summarise the main conclusions of this work.

2. Data selection

In this section, we describe the method to select the samples of stars used in this paper. Our starting point is the base sample obtained by selecting *Gaia* DR3 (Gaia Collaboration 2021a) stars around the center of the LMC. This base sample is a mixture of MW foreground stars and LMC stars. Ideally, it is possible to distinguish both types of objects through their distances, but due to the high uncertainties on the parallax-based distances at LMC (MC21, Lindegren et al. 2021b), a selection of LMC sources exclusively based on parallaxes is not possible and would be efficient only in the process of removing bright MW stars.

Therefore, in order to build a sample of LMC stars for the kinematic analysis in this paper, we need to define a selection criteria to separate them from the MW foreground. A first option is to use a proper motion based selection (Sect. 2.2) as done in MC21; we have kept this methodology to provide a common reference with the results in that paper. We also implemented an alternative selection method based on machine learning classifiers (neural networks, see Sect. 2.3) because, firstly, a selection purely based on proper motions might have some effect on the kinematic analysis and, secondly, we wanted to use the full data available in the *Gaia* catalogue to improve the classification.

We created the following working samples:

Based on *Gaia* data
Gaia base sample: initial *Gaia* DR3 sample selected around the LMC center, before applying any further cut or classification (described in Sect. 2.1)
Gaia LMC Proper Motion (PM) sample: application of a proper motion cut to the *Gaia* base sample (described in Sect. 2.2)
LMC complete, optimal, and truncated-optimal samples: resulting from the NN classification (described in Sect. 2.3.3)
LMC complete, optimal, and truncated-optimal samples: resulting from the NN classification (described in Sect. 2.3.3)
Validation samples (described in Sect. 2.3.5):   – LMC Cepheids   – LMC RR-Lyrae   – LMC+MW StarHorse
Based on simulations
Gaia (MW+LMC) training sample: simulation based on the *Gaia* Object Generator (GOG, described in Sect. 2.3.1).

2.1. Gaia base sample

The *Gaia* base sample was obtained using a selection from the `gaia_source` table in *Gaia* DR3 with a 15° radius around the LMC centre defined as $(\alpha, \delta) = (81.28°, -69.78°)$

(van der Marel 2001) and a limiting *G* magnitude of 20.5. We only kept the stars with parallax and integrated photometry information, since they are used in the LMC/MW classification. This selection can be reproduced using the following ADQL query in the *Gaia* archive:

```
SELECT * FROM gaiadr3.gaia_source as g
WHERE 1=CONTAINS(POINT('ICRS',g.ra,g.dec),
CIRCLE('ICRS',81.28,-69.78,15))
AND g.parallax IS NOT NULL
AND g.phot_g_mean_mag IS NOT NULL
AND g.phot_bp_mean_mag IS NOT NULL
AND g.phot_rp_mean_mag IS NOT NULL
AND g.phot_g_mean_mag < 20.5.
```

The resulting base sample contains a total of 18 783 272 objects.

2.2. Proper motions-based classification

We use the same selection based on the proper motions of the stars as in MC21 to provide a baseline comparison with these previous results. In short, the median proper motions of the LMC are determined from a sample restricted to its very centre, minimising the foreground contamination by a cut in magnitude and parallax. We kept only stars those whose proper motions obey the constraint of $\chi^2 < 9.21$, that is, an estimated 99% confidence region (see details in Sect. 2.2 of MC21). The resulting sample (hereafter, PM selection) contains 10 569 260 objects[1].

2.3. Neural network classifier

In order to improve the separation of the MW foreground from the LMC stars, we used classifiers exploiting all the information available in the *Gaia* DR3 catalogue. Starting from a reference sample where both types of objects are labelled, we trained a classifier that uses the DR3 data to optimize the separation. Then, we applied the trained classifier to our base dataset and checked its performance with several validation subsets. This is an approach already used in other works; for instance, Schmidt et al. (2022) applied a support vector machine classifier trained on a sample where the MW-LMC distinction is based on StarHorse (Anders et al. 2022) distances. However, these authors applied it to data from both *Gaia* EDR3 and the Visible and Infrared Survey Telescope for Astronomy (VISTA) survey of the Magellanic Clouds system (VMC; Cioni et al. 2011), limiting the number of objects available. Here, we use only *Gaia* data which allow us to obtain larger samples.

2.3.1. Description of the *Gaia* training sample

The training sample is a crucial element for the performance of a classifier. It needs to: have the same observational data we use (*Gaia* DR3) and be as representative of the problem sample as possible, while, at the same time, the classification of its elements should be very reliable. Otherwise, the trained classifier will inherit the problems of the training sample, from biases in the selection to errors in the classification. A first possible approach for building a training sample is to use real data, that

is, to use a sub-sample of our base dataset which has an (external) accurate classification of its objects into MW and LMC. We identified two possible options for this approach; on the one hand, we can use samples of RR-Lyrae and Cepheid stars. Since distances for these objects can be accurately determined using period-luminosity relations, they can be located with precision in the LMC and thus distinguished from foreground objects. However, the samples available in this case are rather small and are composed of very specific types of stars. They are not representative of our global samples, which contains stars of all types. On the other hand, we can use the distances in StarHorse EDR3 (Anders et al. 2022) to distinguish MW from LMC objects; however, these distances are based on specific priors for MW/LMC and thus impose some preconditions on the objects, with the risk of propagating these preconditions to our classification. Furthermore, StarHorse only reaches a bright limit $G \leq 18.5$ and it therefore does not cover our faint limit of $G = 20.5$, demonstrating that it is not representative of our problem. For these reasons, we preferred not to use these samples for the training of the classifiers, but we did use them later on as validation samples to check our results, as described in Sect. 2.3.5.

A second possible approach, namely, the one we adopted in this work, is to use representative simulations. A suitable training sample for the classifier would be a simulation based on stellar populations similar to the problem ones and with simulated observations mimicking the *Gaia* data. As part of the mission preparation, the *Gaia* Object Generator (GOG; Luri et al. 2014) was developed and has been regularly updated. It produces realistic simulations of the *Gaia* data and it specifically contains separate modules for the simulation of the MW and the LMC stellar content. We used GOG to produce a training dataset that, like our base sample, corresponds to a simulation of a 15° radius area around the LMC centre, defined as $(\alpha, \delta) = (81.28°, -69.78°)$, and the LMC simulation has been tailored to make it compatible with recent estimations of the mean distance and systemic motion obtained from EDR3 data: a distance of 49.5 kpc (Pietrzyński et al. 2019) and a systemic motion of $\mu_{\alpha*} = 1.858$ mas yr^{-1}, $\mu_\delta = 0.385$ mas yr^{-1} as in MC21.

This *Gaia* training dataset is divided in two parts, one for the MW and the other for the LMC. The LMC simulation contains only 277 178 stars, a number that is too small when compared with real data. This is due to the design of the GOG simulator; to provide a realistic spatial distribution of the LMC simulation, it is based on a pre-defined catalogue of OGLE stars, providing real positions (see details in Luri et al. 2014). The MW simulation, on the contrary, is based on a realistic galactic model, and generates a number of stars that matches the observations. This difference would give a too small LMC/MW ratio of objects, and we corrected it by retaining only a random 20% fraction of the MW simulation, resulting in a total of 1 269 705 stars. Furthermore, during the trial-and-error phase of our selection of the configuration for the NN, we found that the classification results for the test samples (taken from the simulation data) were rather insensitive to changes in this ratio, with almost perfect ROC curves. The characteristics of the resulting simulations are summarised in Fig. 1.

The merging of these two simulations constitute our training sample, and in Fig. 2, we compare it with the *Gaia* base sample. These plots show that the *Gaia* training sample approximately matches the main characteristics of the *Gaia* base sample, but its limitations are also apparent; the distribution of the LMC stars in the sky forms a kind of square, owing to its origin based on an extraction of the OGLE catalogue; the colour-magnitude diagram (CMD) for the LMC simulation is not fully representative

---

[1] Note that the difference in the number of sources with the ones in MC21 comes from the different cut in radius, now being of 15° instead of 20°.
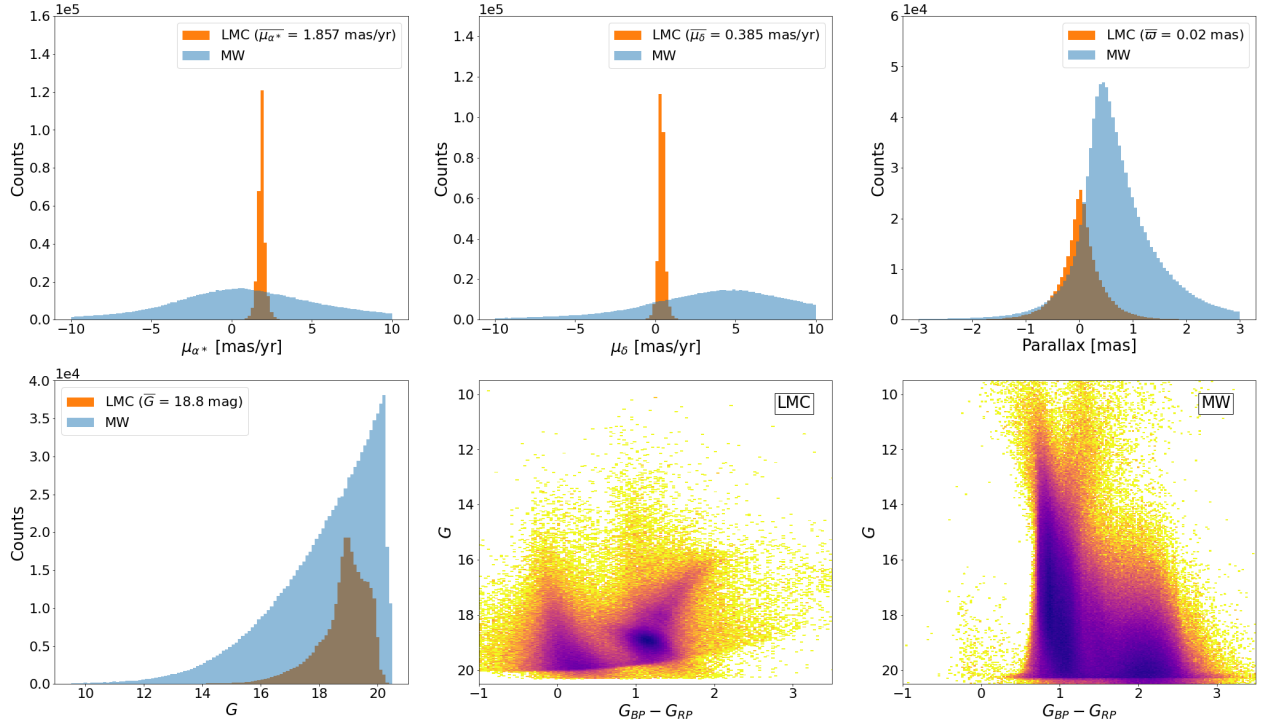
Fig. 1. Characteristics of the GOG simulated samples. Top left and middle: distribution of proper motions in right ascension and declination, respectively. In orange and blue: LMC and the MW training samples. Top right: parallax distribution. Bottom left: magnitude G distribution of the simulated samples. Bottom middle and right: colour-magnitude diagram of the LMC and MW, respectively. Colors represent relative stellar density, with darker colors meaning higher densities.

at the faintest magnitudes, with a lack of stars and an artificial cut line; and the distributions of parallaxes and proper motions do not completely match. In spite of these drawbacks, we consider these samples to be sufficiently representative and we go on to check its performance with several validation samples to confirm its suitability.

2.3.2. Training the classifier

To implement a classifier, we used the sklearn Python module (Pedregosa et al. 2011). This module contains a variety of classifiers that can be applied to our problem, given the available *Gaia* data: position (α, δ), parallax and its uncertainty (ϖ, σ_ϖ), along with the proper motions and their uncertainties $(\mu_{\alpha*}, \mu_\delta, \sigma_{\mu_{\alpha*}}, \sigma_{\mu_\delta})$, and *Gaia* photometry (G, G_{BP}, G_{RP}). Using the training sample described in the previous section, we trained a classifier to distinguish the MW foreground objects from the LMC objects in our base sample.

In the first stage, we tried a variety of algorithms and evaluated them internally using our simulated dataset: we split it into two parts: 60% for training the algorithm and 40% to test its results. We evaluated its performance by generating the corresponding receiver operating characteristic (ROC) curve and calculating the area under the curve (AUC). The ROC curve is one of the most important evaluation metrics for checking the performance of any classification model. It summarizes the trade-off between the true positive rate and false positive rate using different probability thresholds. The AUC of the ROC curve is another good classifier evaluator. The larger the AUC, the better the classifier works. An excellent model has AUC near to 1 which means

it has a good measure of separability. When AUC = 0.5, it means the model has no class separation capacity. From these results, we selected three algorithms that were providing the best results: random forest (RF), K nearest-neighbors (KNN), and a neural network (NN). In all three cases, the ROC curve was almost perfect, similar to that of Fig. 3 corresponding to the NN case.

After testing these three algorithms with the validation datasets described above (RR-Lyrae, Cepheids, and StarHorse) and checking that they retained most of the RR-Lyrae and Cepheids when completeness was prioritised (low probability threshold) we finally selected the NN algorithm. We discarded the KNN because this type of algorithm may be too sensitive to the particularities and representativeness of the training sample (which, as we have seen, is limited). This was indeed the case with our samples, where for instance the square-like shape of the training sample was clearly showing in the classification results for the base sample. We also discarded the RF algorithm because it produced a less sharp MW/LMC distinction. Thus, we ultimately retained the NN classifier.

Focusing on the NN classifier, we tested a few configurations and settled on a NN with 11 input neurons, corresponding to the 11 *Gaia* parameters listed above; three-hidden-layers with six, three, and two nodes, respectively; and a single output which gives for each object the probability P of being a LMC star (or, conversely, the probability of not being a MW star). A P value close to 1 (0) means that the object is highly likely to be of the LMC (MW). We notice that a wider exploration of NN configurations is possible and we could test selection priorities other than "purity" or "completeness" (see below) in the classification, but we leave this exploration to a future work. We used
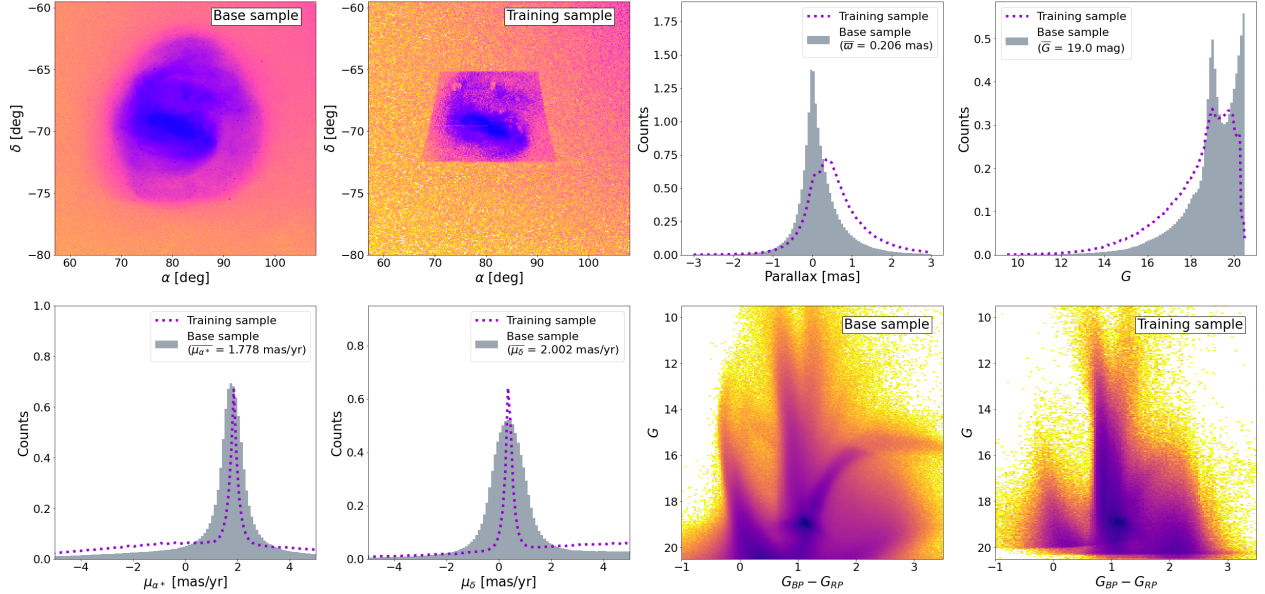
Fig. 2. Comparison between the *Gaia* base and training samples. Top from left to right: density distribution in equatorial coordinates of the *Gaia* base and *Gaia* training samples in logarithmic scale, parallax, and *G* magnitude distributions. Bottom from left to right: proper motion distributions in right ascension and declination and colour-magnitude diagrams for the *Gaia* base and training samples. In the histograms, in gray we show the *Gaia* base sample, while in dotted purple we show the *Gaia* training sample. In the color-magnitude diagrams, colors represent relative stellar density with darker colors meaning higher densities.

the rectified linear unit (ReLU) as the activation function. Our model optimizes the log-loss function using stochastic gradient descent with a constant learning rate. The L2 regularization term strength is 1e-5[2].

In the left panel of Fig. 3, we show the ROC curve of our NN classifier. We obtained an AUC equal to 0.999, which means that our classifier separates with high-precision the LMC and MW stars in the (simulated) test sample. In the right panel of Fig. 3, we show the precision-recall curve. It is another metric that is useful for evaluating the classifier output quality when the classes are very imbalanced. The precision (ratio of true positive vs. total of stars classified as LMC) is a measure of result relevancy, while recall (ratio of true positives vs. total LMC stars) is a measure of how many truly relevant results are returned. As for the ROC curve, it shows the trade-off between precision and recall for different probability thresholds.

A final warning regarding the performance of our NN: both the ROC (AUC) and the precision-recall curve show an almost perfect classifier, but these results correspond to its application to the fraction of our simulated sample used for testing. In the next section, and with the aim to evaluate the performance with real data, we go on to check the NN results when applied to real samples with independent classifications.

2.3.3. Applying the classifier to the *Gaia* base data

Once the NN is trained, we apply it to the *Gaia* base sample and obtain probabilities for each of its objects. The resulting probability distribution is shown in Fig. 4. We can notice two clear peaks, one with a probability value near 0 and another with probability value near 1. These peaks correspond to stars that the
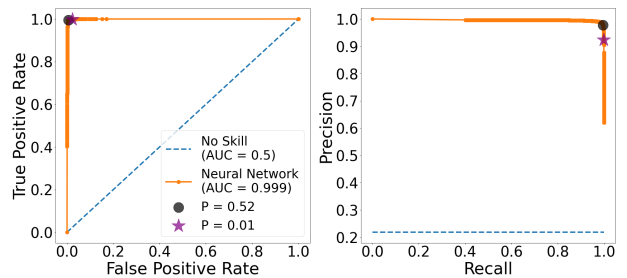

Fig. 3. Evaluation metrics for the Neural Network classifier performance. Left: ROC curve. Black dot is in the "elbow" of the ROC curve and it shows the best balance between completeness and purity. The purple star shows the completeness threshold. Right: precision-recall curve. In both cases, we compare our model (orange solid curve) with a classifier that has no class separation capacity (blue dashed curve).

classifier has clearly identified as MW and LMC, respectively; in between, there is a flat tail of intermediate probabilities.

To obtain a classification using the probabilities generated by the classifier for each star, we need to fix a probability threshold P_{cut}. If $P > P_{cut}$, the star is considered to belong to the LMC; if $P < P_{cut}$, the star is considered to belong to the MW (alternatively, we could leave stars with intermediate probabilities as unclassified). By fixing a low probability threshold we seek not to miss any LMC object, and the resulting LMC-classified sample to be more complete at the price of including more "mistaken" MW stars. On the contrary, by fixing a high probability threshold, we can make the resulting LMC-classified sample to be purer (less mistakes), at the price of missing some LMC stars and thus obtaining a less complete sample.

---

[2] Readers interested in using the Neural Network developed in the paper can contact the corresponding author.
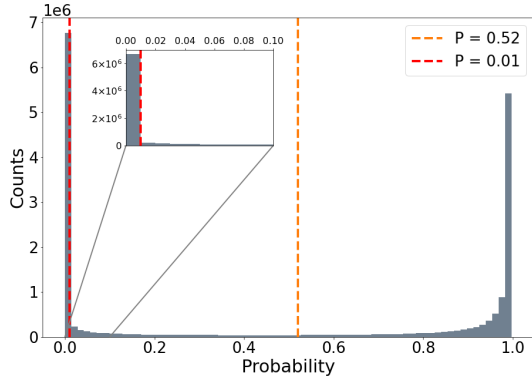
Fig. 4. Probability distribution of the *Gaia* base sample for the NN classifier. A probability value close to 1 (0) means a high probability of being a LMC (MW) star.

The purity-completeness trade-off is a decision that will define the properties of the resulting sample and therefore can have an effect on the results obtained from it. In this work , we define three different samples to explore the effects of this trade-off:

1. Complete sample ($P_{cut} = 0.01$). In this case a cut at small probabilities prioritizes completeness, making sure that no LMC objects are missed at the prize of an increased MW contamination. The cut value was chosen by inspecting the probability histogram of the classification (Fig. 4) and selecting the limit of the main peak of small probability values.

2. Optimal sample ($P_{cut} = 0.52$). In this case the probability cut was chosen to be optimal in a classification sense; the value corresponds to the "elbow" of the ROC curve (Fig. 3), which is in principle the best balance between completeness and purity.

3. Truncated-optimal sample ($P_{cut} = 0.52$), plus an additional cut for $G > 19.5$ mag.

We introduced the third case because, after examining the results for the optimal sample, we noticed that the faint tail of its magnitude distribution most likely corresponds to MW stars; MW stars exponentially increase at fainter magnitudes, while LMC stars quickly decrease after $G \simeq 19.5$ (see discussion in the next section). Furthermore, with this cut we manage to avoid a region in the faint end where the LMC training sample is not representative, as discussed above; removing these stars can reduce the MW contamination (see Sect. 2.3.5) and also discards the stars with larger uncertainties and, therefore, less useful for our kinematic analysis. A further selection could be made by excluding regions of the CMD diagram where contamination is more likely, but given the cleanliness of the LMC diagrams in Fig. 6 we deemed this not necessary.

Finally, for each of the four samples we consider two datasets. First, the full sample where we assume that all the stars have no line-of-sight velocity information. Second, a sub-sample of the first one where we only keep stars with *Gaia* DR3 line-of-sight velocities. We refer to these sub-samples as the corresponding V_{los} sub-samples. The number of stars per dataset is in the second and third column of Table 1, respectively, together with the mean astrometric information.

2.3.4. Comparison of classifications

The sky density distributions for the classified LMC/MW members in our different samples are shown in Fig. 5. In the left

column, we show the LMC selection in each of the samples, while in the right column, we show the sources classified as MW. Each row corresponds to one selection strategy: proper motion selection (first row) followed by the three NN based ones. As expected, the results of the proper motion based selection are very similar to that described in MC21.

We note here that the limited spatial distribution of the LMC training sample (square region in top-left panel of Fig. 2) does not pose a problem for extrapolating the membership beyond this region, since an anomalous classification in the LMC outskirts is not observed in these figures. In order to evaluate the extrapolation performance, we also tested the NN classifier when not taking into account the positional information; the results show that even in this extreme case the classifier does not have problems with the spatial distribution of the resulting samples.

We also note that sources classified as belonging to the MW by all four samples show an overdensity in the most crowded region of the LMC, that is, the bar, indicating misclassifications of LMC stars. We also see that, as expected by the definition of the probability cut, the more complete the LMC sample, the less stars are classified as belonging to the MW. In this respect, a cross-matching of the proper motion selection sample and the complete sample shows that the second almost completely contains the former: of the 10 569 260 stars of the Proper motion sample, 10 432 704 of them are included in the complete sample and the complete sample contains almost two million additional stars.

In Table 1 we also see that the dispersion of the astrometric parameters diminish from the NN complete to the NN truncated-optimal samples. This is expected, since the stricter sequence of selection criteria lead to a higher similarity in distance and velocity inside the samples.

In Fig. 6, we compare the astrometry and photometry distribution of the different LMC samples. In the proper motion selection sample, we see that the sharp cut in proper motion imposed makes the distribution of proper motion to be narrow around the bulk motion of the LMC, while in the MW classification, two small peaks are present, following a continuation of the LMC peak. Clearly, some LMC stars are misclassified as MW using the sharp cut in proper motion. This misclassification is not visible in the NN complete sample and is present again in the more restrictive optimal and truncated-optimal samples. The parallax distribution in the four LMC samples are very similar, with the truncated optimal sample being the most narrow. The G magnitude distributions are quite different in the four LMC selections. Both the PM and the NN samples show a peak in G magnitude around $G \sim 19$ mag, which corresponds to the LMC sample, and a secondary peak at the limiting magnitude of $G = 20.5$, corresponding to MW contamination. For this reason, as described above, we define the truncated-optimal sample by removing the secondary peak in the optimal sample. Conversely, the MW selection in all cases should show an exponential distribution in G, though the PM, the complete and the optimal samples show a secondary peak of varying significance amongst them around $G \sim 19$ mag. The CMD of all LMC samples is very similar. Small differences only appear in the MW selection of the optimal and truncated optimal sample which contain, as expected, sources of the red giant branch of the LMC, which the NN classifier misclassifies as MW.

2.3.5. External validation of the classification

As indicated in previous sections, to validate the results of our selection criteria we compare them with external independent

Table 1. Comparison of the LMC samples number of sources and mean astrometry between the proper motion selection (MC21) and the neural networks.

LMC sample	N	N_{vlos}	$\overline{\varpi}$	σ_ϖ	$\overline{\mu_{\alpha*}}$	$\sigma_{\mu_{\alpha*}}$	$\overline{\mu_\delta}$	σ_{μ_δ}
Proper motion selection	10 569 260	29 678	−0.006	0.333	1.800	0.408	0.369	0.541
NN complete	12 116 762	30 749	−0.008	0.382	1.808	0.563	0.348	0.653
NN optimal	9 810 031	22 686	−0.016	0.346	1.819	0.446	0.364	0.488
NN truncated-optimal	6 110 232	22 686	−0.008	0.211	1.820	0.353	0.357	0.423

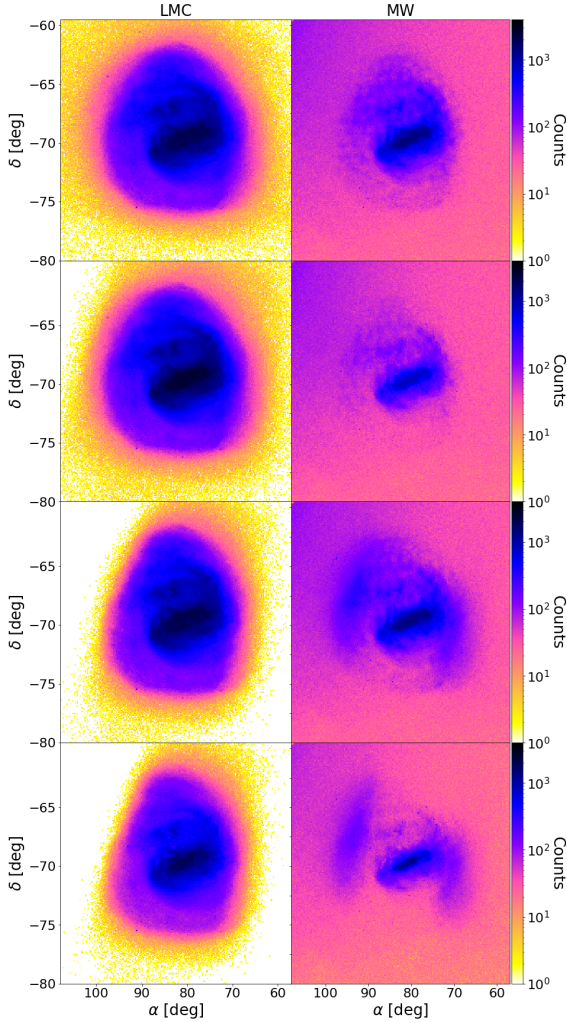**Notes.** Parallax is in mas and proper motions in mas yr^{-1}.

Fig. 5. Sky density distribution in equatorial coordinates of both the LMC (left) and MW (right) sample obtained from the different classifiers. First row: proper motion selection classification. Second row: Complete NN classification. Third row: optimal NN classification. Fourth row: truncated-optimal NN classification. Note: in the fourth row, we display a cut in magnitude $G > 19.5$ for both the LMC and MW samples and, therefore, the total number of stars is reduced.

classifications. To do so, we cross-matched our base sample with three external samples:

– LMC Cepheids (Ripepi et al. 2022): we used the paper's sample of 4500 Cepheids as a set of high-reliability LMC objects. To obtain the *Gaia* DR3 data we cross-matched the positions given in the paper with the *Gaia* DR3 catalogue, using a 0.3″ search radius to obtain high confidence matches, thus retaining 4485 stars. Finally, we introduced a cut of 15° radius around the LMC center (mimicking our base sample), leading to a final selection of 4467 LMC Cepheids.

– LMC RR-Lyrae (Cusano et al. 2021): similarly to the process above, we used the paper's sample of 22 088 RR-Lyrae as high-reliability LMC objects. After the cross-match with the *Gaia* DR3 catalogue, the sample is reduced down to 22 006 stars and after the in 15° radius cut around the LMC center we obtain a final sample of 21 271 LMC RR-Lyrae.

– StarHorse (Anders et al. 2022): we cross-matched this catalogue with the *Gaia* DR3 data using a cut of 15° radius around the LMC center and obtained a sample of 3 925 455 stars. Following a similar criteria to the one proposed in Schmidt et al. (2020, 2022), we separated MW and LMC stars through the StarHorse distances, but making a cut at $d = 40$ kpc. This decision is motivated by the distance distribution of the StarHorse sample, which is shown in Fig. 7. A cut in $d = 40$ kpc gives a very restrictive classification, minimizing the contamination of MW stars (see discussion below). We thus obtain a StarHorse LMC sample with 985 173 stars and a StarHorse MW sample with 2 940 282 stars. Notice that being based on StarHorse, this sample contains stars only up to $G = 18.5$.

The Cepheids and RR-Lyrae samples contain objects classified with high reliability as LMC stars, so they serve as a check of the completeness of our classification for LMC objects ("how many we lose"). On the other hand, the StarHorse sample is helpful to estimate the contamination caused by wrongly classified MW stars, although this can only be taken as an indication, since the StarHorse classification itself is not perfect. Furthermore, given the very stringent criteria used for the separation in StarHorse (the cut in $d = 40$ kpc), the resulting estimation of MW contamination in the classification will be a "worst case".

In Table 2, we summarize the comparison of the results of our four classification criteria applied to stars contained in the three validation samples. It can be seen that the completeness of the resulting LMC classifications is quite good, usually above 85%, as shown for the results with the Cepheids, RR-Lyrae and StarHorse LMC validation samples. The exception is the truncated-optimal sample, where the completeness is reduced for the RR-Lyrae, due to the cut in faint stars.

On the other hand, the relative contamination by MW stars in the samples is more difficult to assess. We have to rely on the StarHorse distance-based classification as an external comparison, with the caveat that this classification contains its own classification errors. To do so, we re-calculate the precision-recall curve, but this time taking the StarHorse classification as a reference; the result is shown in Fig. 8. We can see that the precision remains quite flat for almost all the range of the plot, that is, for all the range of probability threshold values. This
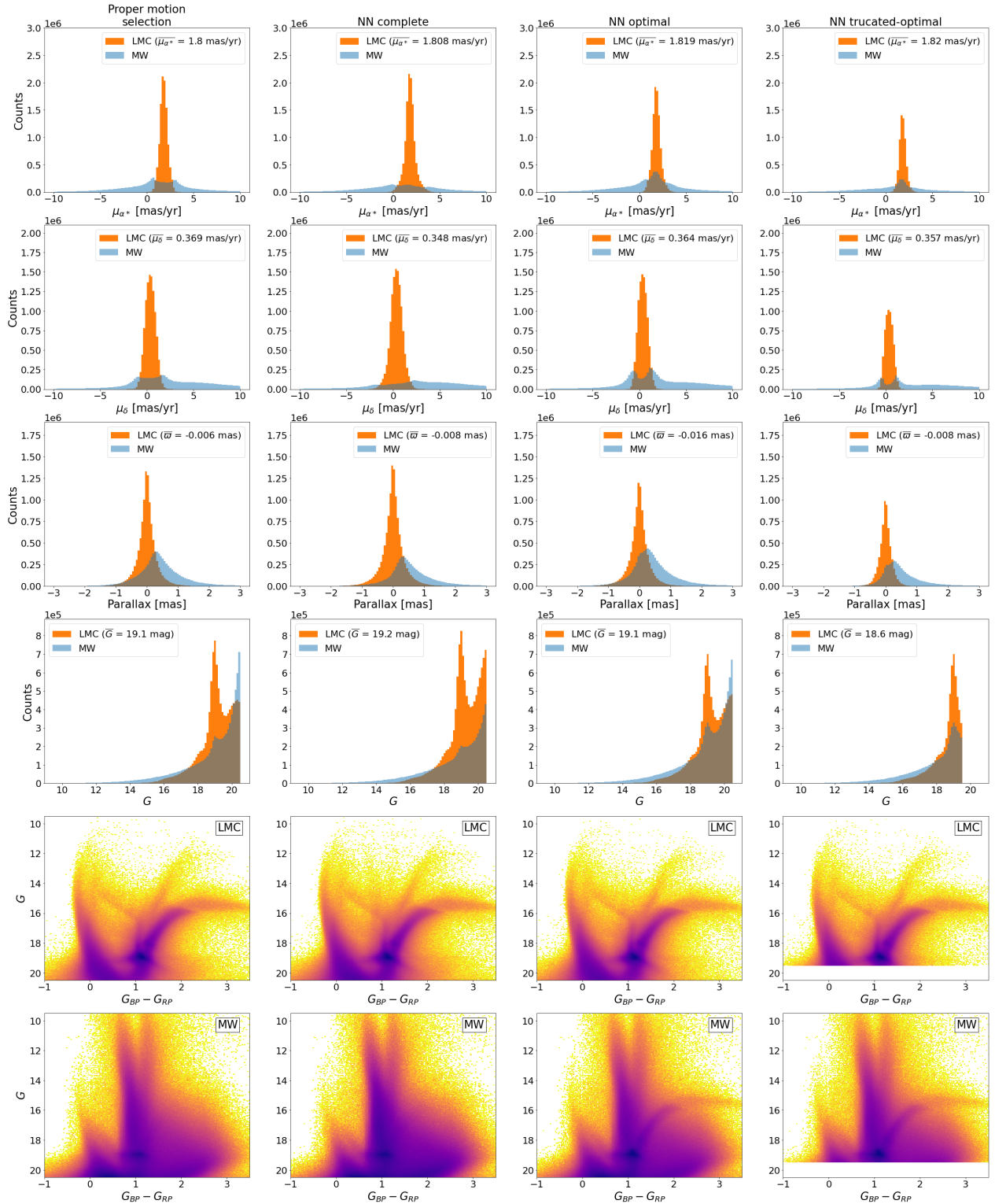
Fig. 6. Astrometric and photometric characteristics of the LMC and MW samples. From left to right: PM sample, NN complete, NN optimal and NN trucated-optimal samples. In the first four rows, we show distributions of proper motion in right ascension and declination, parallax, and *G* magnitude, respectively, of the LMC (orange) and MW (blue) samples. In the last two rows, we show the colour-magnitude diagram of the samples classified as LMC and MW, respectively. Color represents the relative stellar density, with darker colors meaning higher densities.
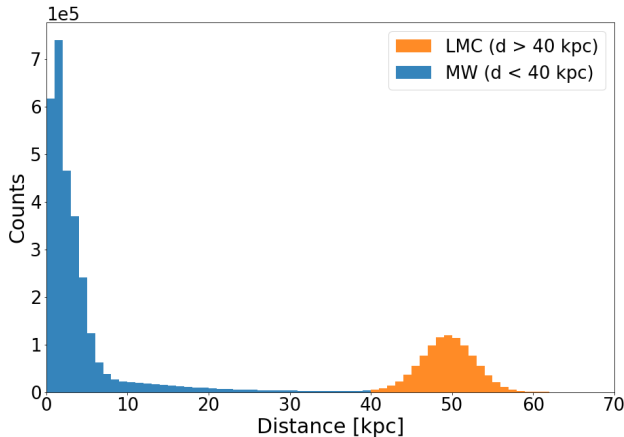
Fig. 7. Distance distribution of the StarHorse validation sample. In blue (orange), the StarHorse stars classified as MW (LMC) according to the $d = 40$ kpc criteria.

indicates that the relative contamination (percentage of stars in the samples that are MW stars wrongly classified as LMC stars) is similar in the complete and optimal samples (the more restrictive we are, the more MW stars we remove, but also we lose more LMC stars). Taking the precision values in Fig. 8 indicates that in using the classification based on SH distances as a reference, the relative contamination of our samples could be around 40%; this is a worst case, since we used a very restrictive distance cut (40 kpc) and when using less restrictive cuts (down to 10 kpc), the estimation of the contamination can be lowered to ~30%. These numbers have to be taken with care, since the MW-LMC separation based on the SH distances is not perfect, just another possible classification criteria that in fact is using less information than our criteria. As pointed in the SH paper (Anders et al. 2022), these populations are clearly visible as overdensities in the maps, although a considerable amount of stars still has median distances that fall in between the Magellanic Clouds and the MW – a result of the multimodal posterior distance distributions.

These results point out to a possible contamination by MW stars in our samples around some tens of percentage but we can do an additional check using the line-of-sight velocities in *Gaia* DR3, which are available only for a (small) subset of the total sample. These line-of-sight velocities are not used by any of our classification criteria and have different mean values for the MW and LMC (therefore providing an independent check). In Fig. 9, we plot the histograms of line-of-sight velocities separately for stars classified as MW and LMC, and it is clear from these that the contamination of the LMC sample is reduced, likely to be significantly below the levels suggested above. For instance, if we consider the LMC NN complete sample and (roughly) separate the MW stars with a cut at $V_{los} < 125$ km s^{-1}, we estimate the MW contamination to be around 5%. However, since the subset of *Gaia* DR3 stars with measured line-of-sight velocities contains only stars at the bright end of the sample ($G \lesssim 16$), this check is not fully representative either.

Finally, we made a new query to the *Gaia* archive that was similar to that defined in Sect. 2.1. This time, we made a selection from the *gaia_source* table in *Gaia* DR3 with a 15° radius in a nearby region with homogeneous sky density. This way we can make an estimation of the MW stars expected in a regions similar to that covered by our *Gaia* base sample. From this new

query, we obtained 4 240 771 stars, so we would expect a similar number of MW stars in the region we selected around the LMC. Given that the *Gaia* base sample contains 18 783 272 objects and the number of objects classified as LMC (Table 1) is around 6−12 million, the number of stars classified as MW is around 12−6 million; therefore, we can conclude that our NN LMC samples prioritise purity over completeness since there are too many stars classified as MW (an excess of 2–8 million). This is also evident from the right panels of Fig. 5, where the distribution of stars classified as MW shows the pattern of LMC contamination.

3. Coordinate transformations and validation

3.1. Coordinate transformations

Since the main goal of this work is to look at the internal kinematics of the LMC, we review the coordinate transformations used to compute the LMC-centric velocities. To do so, we revisit the formalism introduced in van der Marel & Cioni (2001) and van der Marel et al. (2002) and describe the two-step process used to transform the *Gaia* heliocentric measurements to the LMC reference frame (full details are given in Appendix A).

First, we introduce a Cartesian coordinate system (x, y, z), whose origin, O, is placed at $(\alpha_0, \delta_0, D_0)$, the LMC centre. The orientation of the x-axis is anti-parallel to the right ascension axis, the y-axis parallel to the declination axis, and the z-axis towards the observer. This is somehow similar to considering the orthographic projection – a method of representing 3D objects where the object is viewed along parallel lines that are perpendicular to the plane of the drawing – of the usual celestial coordinates and proper motions (see Fig. 10 for a schematic view of the observer-galaxy system). We refer to this reference frame as the orthographic projection centred at the LMC.

Second, we transform from the (x, y, z) frame to the final Cartesian coordinate system whose reference plane is the LMC plane, (x', y', z'). It consists of the superposition of a counterclockwise rotation around the z-axis by an angle θ, followed by a clockwise rotation around the new x'-axis by an angle i. With this definition, the (x', y') plane is inclined with respect to the sky tangent plane by an angle i. Face-on (face-off) viewing corresponds to $i = 0°$ ($i = 90°$). The angle θ is the position angle of the line-of-nodes or, in other words, the intersection of the (x', y')-plane and the (x, y)-plane of the sky. By definition, it is measured counterclockwise from the x-axis. In practice, i and θ will be chosen such that the (x', y')-plane coincides with the plane of the LMC disk. Therefore, we refer to this final reference frame as the LMC in-plane reference system.

Since we do not have reliable information for individual distances because the parallaxes are very small and close to the noise (MC21, Lindegren et al. 2021b), we assume that all the stars lie on the LMC disc plane, as an approximation. Thus, we impose z' to be zero, which leads to a distance of $D_{z'=0}$ (different to the real one) for each star. In Fig. 11, we show a schematic representation of what this assumption implies. We represent the position of a real star in dark gray, while the white star in red solid line is the projection of the real star on the LMC plane. With this strategy all LMC stars are assumed to lie on its plane.

When these two rotations are applied and the stars are made to lie in the LMC plane; for each star, we have LMC-centric positions $(x', y', 0)$ and velocities $(v_{x'}, v_{y'}, v_{z'})$. The last step is to make these velocities internal by removing the LMC systemic motion (see details in Appendix A.2.1). In this work (as in MC21), we consider the following LMC parameters: $i = 34°$,

Table 2. Matches of the classified LMC members in our four considered samples against the validation samples.

Stars classified as LMC	LMC Cepheids (4467)	LMC RR-Lyrae (21 271)	LMC StarHorse (985 173)	MW StarHorse (2 940 282)
Proper motion selection	4 366 (97.7%)	18 673 (87.8%)	970 173 (98.5%)	704 932 (24.0%)
NN complete	4 407 (98.7%)	20 223 (95.1%)	970 719 (98.5%)	722 750 (24.6%)
NN optimal	4 160 (93.1%)	17 860 (84.0%)	832 733 (84.5%)	627 619 (21.3%)
NN truncated-optimal	4 160 (93.1%)	14 750 (69.3%)	832 733 (84.5%)	627 619 (21.3%)

Notes. Percentages are calculated with respect to the total number of stars given below the sample name.
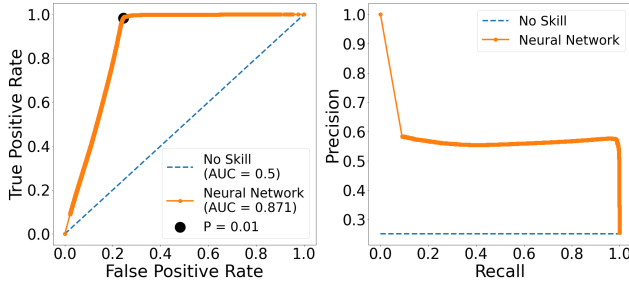

Fig. 8. Evaluation metrics for the Neural Network classifier performance using the StarHorse sample. Left: ROC curve. Black dot is in the "elbow" of the ROC curve and it shows the best balance between completeness and purity. Right: precision-recall curve. In both cases, we compare our model (orange solid curve) with a classifier that has no class separation capacity (blue dashed curve).

$\theta = 220°$, $(\alpha_0, \delta_0) = (81.28°, -69.78°)$, and $(\mu_{x,0}, \mu_{y,0}, \mu_{z,0}) = (-1.858, 0.385, -1.115)$ mas yr^{-1}, where we take into account that our x and z-axes have the opposite sense from the one considered in MC21. These values are derived assuming a specific centre, the same one as we use in this work. The distance to the LMC centre is assumed to be $D_0 = 49.5$ kpc (Pietrzyński et al. 2019).

As shown in Eq. (A.8), the formalism presented in van der Marel & Cioni (2001) and van der Marel et al. (2002) allows taking into account line-of-sight velocities, which is something that could not be done when using MC21 transformations. As detailed in Sect. 2.3.3, in this work we deal with two different datasets: the full samples, without line-of-sight velocity information and the sub-samples of stars with individual line-of-sight velocities. For the former, we estimate each star line-of-sight velocity by taking into account its position and proper motion and the global parameters of the LMC plane (full details in Appendix A.3).

In the top panel of Fig. 12, we show the LMC density map for the NN complete sample in the LMC cartesian coordinate system. The density maps for the rest of the three samples are analogous and show the same morphological features as in the corresponding sample of the left column of Fig. 5. Here, we want to point out that the coordinate transformation from the heliocentric equatorial system to the LMC cartesian system inverts the vertical axis, so now the spiral arm starts at negative x' and y', and the deprojection of the inclination angle in the sky makes the galaxy elongated along the vertical axis.

3.2. Validation of the formalism with a N-body simulation

In this section, we use N-body simulations to test the new formalism introduced above. We use the "B5" isolated barred galaxy simulation of Roca-Fàbrega et al. (2013), which consists of a live disc of 5 million particles and a Toomre parameter of $Q = 1.2$, and a live NFW halo. The disc to halo mass ratio is the appropriate so that the simulation develops a strong bar and two spiral arms which are transient in time. The snapshot used in this analysis corresponds to an evolution time of $T \simeq 500$ Myr, and the density distribution is shown in the top left panel of Fig. 13. Using the 6D information of positions and velocities at this given time, we carry out the following exercise. First, we convert the galactocentric cartesian coordinates to heliocentric equatorial $(\alpha, \delta, d, \mu_{\alpha^*}, \mu_\delta, V_{los})$ at the line of sight, spatial orientation, distance, and systemic motion of the LMC. Then, we consider these particles as a data set and we apply the same formalism described in Sect. 3 to compute the coordinates in the LMC frame and the velocities in cylindrical coordinates. The radial component (left panels) indicates the motion towards as well as away from the galactic centre, while the residual tangential velocity (middle panels) is obtained by subtracting the tangential velocity curve to the tangential velocity component, indicating the motion with respect to the tangential curve. The vertical component (right panels) indicates the motion across the galactic plane.

We applied the coordinate transformations twice. In the first case, we imposed, as in the LMC full samples, that V_{los} is not available and use the internally derived from Eq. (A.15). Secondly, we used the available V_{los}, as in the sub-samples, from the 3D velocity data. We computed the velocity profiles and velocity maps with the simulation data as follows. The same procedure is performed when applying it to the LMC samples in Sect. 4. Each curve is obtained by computing the median value of all stars located in radial bins of 0.5 kpc-width in the (x', y')-plane. The error in each bin is computed as the division between the median absolute deviation and the square root of the number of stars. The resulting velocity profiles are shown in the top right panel of Fig. 13. The velocity maps are obtained by plotting the median in 100×100 bins in the (x', y')-plane from -8 kpc to 8 kpc. The resulting velocity maps are shown in the second to fourth row panels of Fig. 13. In the second row, we show the radial, residual tangential, and vertical velocity maps obtained directly from the N-body simulation. In the third and fourth rows, we show the velocity maps when V_{los} is not available and when it is, respectively.

From the velocity profiles and maps, we note that the approximation used, when V_{los} is not available, does not modify the velocity profiles as seen in the top right panel of Fig. 13, nor the radial and residual tangential velocity maps (see left and middle panels of Fig. 13). The only effect is in the vertical component in the case where V_{los} is not available; so, in this case, we obtain $V_z' = 0$ km s^{-1}, which is a consequence of the fact that the internal line-of-sight velocity is estimated by computing the derivative of the distance as function of time (see Eq. (A.15)), which makes V_z' become null when substituting into the
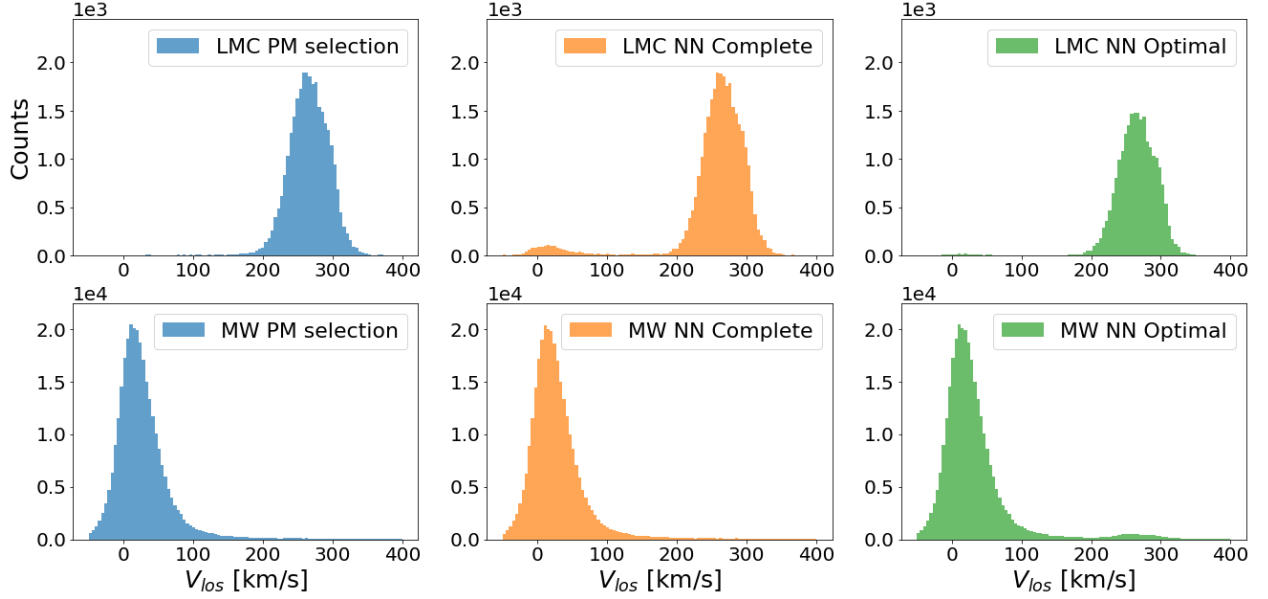
Fig. 9. Line-of-sight velocity distribution for the stars classified as LMC (top) and MW (bottom). We show the three $V_{\rm los}$ sub-samples of the PM selection (left), NN complete (middle) and NN optimal (right) samples.

analogous Eq. (A.8) for the internal motion. In the other two cases, namely, when we use the input data or the derived V'_z from the $V_{\rm los}$, we obtain a median profile and median velocity map centered at zero within the Poisson noise. In the radial and residual tangential velocity component (left and middle panels), we clearly see the quadrupole effect due to the presence of a rotating bar. As expected, the change in sign in V_R occurs along the major and minor axes of the bar and the residual tangential velocity is minimum along the bar major axis. Also, we successfully validated the coordinate transformation formalism by artificially inflating the vertical component ten times larger than that of the original B5 simulation to make the radial, tangential, and vertical velocity components comparable in range.

In conclusion, the formalism used to derive the velocities in the LMC frame, when the line-of-sight velocity is not available, does not introduce any bias in the velocity profiles or maps. The most important assumption in the formalism is that all stars lie on a plane.

4. Analysis of the velocity profile and maps

In this section, we analyse the velocity profiles (Sect. 4.1) and velocity maps (Sect. 4.3) for the four samples, and their corresponding $V_{\rm los}$ sub-samples (described in Sect. 2). To allow for a comparison between density and kinematics, we overplot the overdensity contour in the velocity maps, as described in Sect. 4.2.

4.1. LMC velocity profiles

Here, we analyse the velocity profiles in the LMC coordinate system. We computed the LMC velocity profiles by using a similar methodology to that used in MC21 (as specified in Sect. 3.2).

In the left panels of Fig. 14, we show the velocity profiles (radial, tangential, and vertical – from top to bottom) for each of the four full LMC samples. In all samples, the radial velocity profile slightly decreases with radius up to 2.5 kpc, where it

increases again. The tangential velocity profile shows the rotation curve of the galaxy, having a linear growth until $R \sim 4$ kpc in all samples and becoming flat in the outer disc. The maximum tangential velocity varies between LMC samples, with a maximum difference of ~15 km s^{-1} at $R = 4.7$ kpc between the NN complete and NN optimal samples. We use these rotation curves to derive residual tangential velocity maps in Sect. 4.3. The vertical velocity profile for the four samples is completely flat and centered at 0 km s^{-1}, which is a consequence of not using the observational $V_{\rm los}$ in these samples, as mentioned in Sect. 3.2. As noted above, the internal line-of-sight velocity is estimated by computing the derivative of the distance as function of time (see Eq. (A.15)), which makes V'_z become null when substituting into the analogous Eq. (A.8) for the internal motion, so we will not use it in the following analysis.

We can summarise the comparison between the samples in the following points:

– The PM sample profiles are almost the same as the MC21 for the radial and tangential velocity curves.

– The NN complete sample profiles are very similar to the ones of the PM selection, as also seen in the density maps (see Sect. 2.3.4), with a maximum difference of ~2 km s^{-1} at $R \gtrsim 4.5$ kpc in the radial component.

– The NN optimal and NN truncated-optimal samples, while they are indeed purer, also have larger inward-streaming motion and rotate about ~10−15 km s^{-1} more slowly than the more complete samples in the outer disc.

In the right panels of Fig. 14, we show the same velocity profiles, this time with the sub-samples that have full 3D velocity components, this is, with $V_{\rm los}$. The trends observed in the left panels for the radial and tangential profiles are reproduced in the right panels. We note that the radial velocity profile of the $V_{\rm los}$ sub-samples has a larger negative amplitude at $R = 2 - 3$ kpc, of around $\overline{V_R} = -10$ km s^{-1}, compared to the $\overline{V_R} = -5$ km s^{-1} of the full samples. Also, the tangential velocity for the NN sub-samples is now a bit larger and they are all centered around $\overline{V_\phi} \sim 80$ km s^{-1}. The largest difference between the main samples and
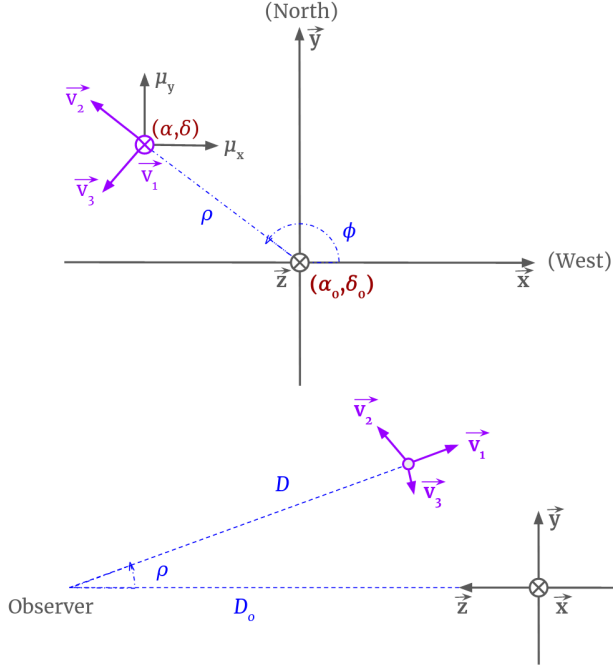
Fig. 10. Schematic view of the observer-galaxy system. The LMC center $O(\alpha_0, \delta_0, D_0)$ is chosen to be the origin O of the (x, y, z) coordinate system. Top: projected view of the sky. All vectors and angles lie in the plane of the paper. The angles ρ and ϕ define the projected position on the sky of a given point with coordinates (α, δ). Bottom: side view of the observer-galaxy system. The distance from the observer to the LMC center is D_0 and the distance from the observer to an object is D. The component v_1 lies along the line-of-sight and points away from the observer.

the V_{los} sub-samples arises in the vertical velocity component, where we observe different trends between sub-samples:

– The NN truncated optimal sample provides the same profile as the NN optimal sample. This is expected since, in this case, both sub-samples are the same because line-of-sight velocities are available up to G magnitude < 16, and the truncation is performed at $G = 19.5$.

– All sub-samples have a slightly negative vertical velocity profile. The PM sample is the one that has a flatter profile, centered around $-3\,\mathrm{km\,s^{-1}}$ up to $\sim 5\,\mathrm{kpc}$. The NN complete sample has an increasing trend from $-4\,\mathrm{km\,s^{-1}}$ to positive values at $R = 6\,\mathrm{kpc}$ and NN optimal presents a wave-like pattern having a change of sign at $R \sim 4\,\mathrm{kpc}$. These trends are very sensitive to the imposed $\mu_{z,0}$. A small shift to the vertical component of the systemic motion will translate into a shift in the V'_z profile, while differences between sub-samples arise from contamination from the MW, mostly present in the outer disc (see discussion in Sect. 5).

4.2. Determination of the LMC overdensity maps

In this section, we introduce and describe the mask used to highlight the LMC overdensities, such as the bar and the spiral arm.

To analyse the data, we considered 100×100 bins in the (x', y')-plane of range $-8\,\mathrm{kpc}$ to $8\,\mathrm{kpc}$, as when constructing the velocity maps. Then, a Gaussian kernel density estimation (KDE) of $0.4\,\mathrm{kpc}$-bandwidth is applied. To highlight the star overdensities, we compute for each bin $N/N_{KDE} - 1$, where N
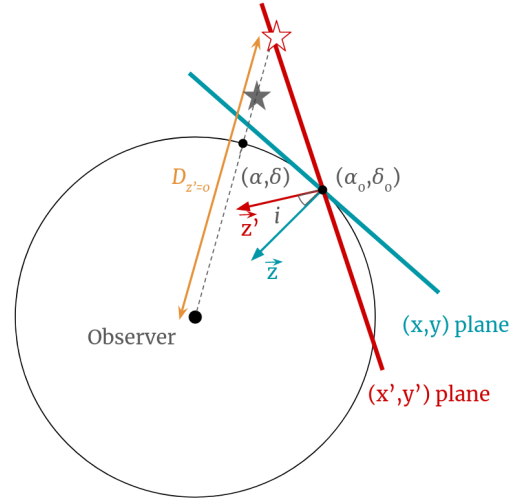

Fig. 11. Schematic representation of the reference frames used, all of them centred on the LMC centre (α_0, δ_0). In blue, we show the orthographic reference frame, (x, y, z), whereas in red, we show the Cartesian LMC frame, (x', y', z'). We also show the position of a real star (solid dark gray), its projection in the LMC cartesian frame under the imposition of $z' = 0$ (red frame).

and N_{KDE} are the number of stars corresponding to the data histogram and the KDE, respectively. The mask $N/N_{KDE} - 1$ has positive (negative) values for overdensities (underdensities). The value of N_{KDE} is computed by integrating the KDE for the bin area. The choice of the KDE bandwidth was empirical. We built overdensity maps for bandwidths ranging from $0.2-1\,\mathrm{kpc}$ and we considered that a $0.4\,\mathrm{kpc}$-bandwidth fulfills our objective of highlighting both the LMC bar and arm.

In the bottom panel of Fig. 12, we show the LMC overdensity map in the (x', y') Cartesian coordinate system. We can clearly see how both the LMC bar and spiral arm stand out as overdensities, as shown by the black contour of overdensity equal to zero. We first observe how the LMC spiral arm starts at the end of the bar around $(-3, 0)\,\mathrm{kpc}$. Then, if we analyse the spiral arm following a counter-clockwise direction, the spiral arm breaks into two parts: an inner and an outer arm. Finally, both parts join further on and continue together until the spiral arm ends, performing close to a full rotation around the LMC centre.

4.3. LMC velocity maps

In this section, we analyse the velocity maps in the LMC coordinate system for the four LMC samples. The results are shown in Figs. 15–17 for the radial, tangential, and vertical components, respectively. Results are shown from top to bottom for PM selection, NN complete, NN optimal and NN truncated optimal samples, respectively, while left (right) panels show the velocity maps for the full (V_{los} sub-) samples. The black line shows the overdensity contour corresponding the overdensity equals to zero (as in the bottom panel of Fig. 12), which helps in making the comparison between density and kinematics.

Regarding the radial velocity maps (Fig. 15), the quadrupole pattern already reported in MC21 related to the motion of stars in the bar is present for all samples; however, for V_{los} sub-samples, an asymmetry clearly becomes apparent along the semi-major axis of the bar, shown by the change in sign of the radial velocity. We estimate the bar major axis is inclined with respect to the
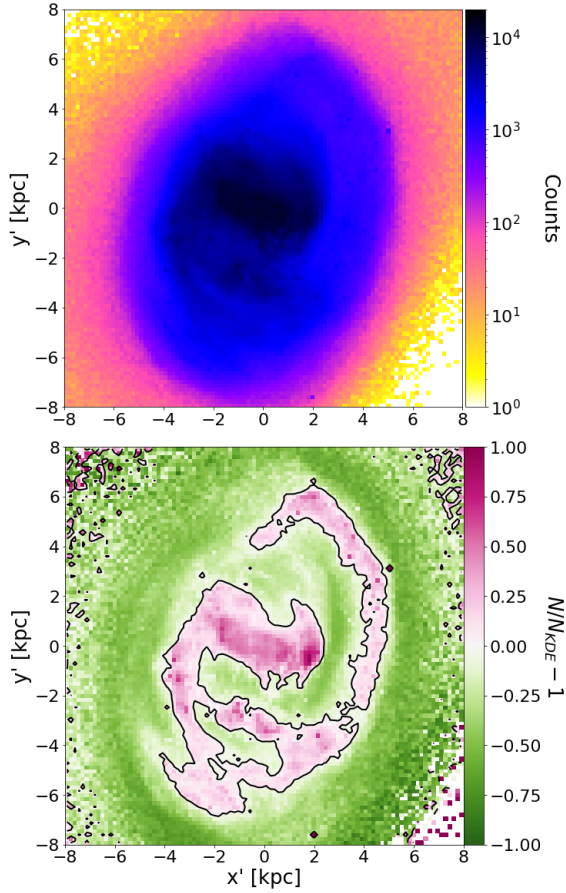
Fig. 12. Comparison between density and overdensity maps. Top: LMC density map for the NN complete sample. Bottom: LMC overdensity map for a 0.4 kpc-bandwidth KDE. A black line splitting the overdensities from the underdensities is plotted. Both maps are shown in the (x', y') Cartesian coordinate system.

x'-axis about $\sim -10°$. The radial velocities in the upper half of the semi-major axis have larger values (in absolute value) than those on the bottom half. Further research is required to analyse whether this asymmetry is an effect of the inclination of the bar with respect to the galactic plane or whether it is an artifact of the assumption that all stars lie in the plane; although this latter assumption is also present in the full sample, where the asymmetry is also present but less clear. The trend in the outer disc is similar in all full samples, though a strong inward or outward motion in the outskirts of the sample is present in the NN optimal and NN truncated-optimal samples. In particular, the strong inward motion detected in the upper periphery of the NN optimal and NN truncated samples is coherent with the region where the Magellanic Bridge connects to the LMC, and this could represent in-falling stellar content from the SMC. Along the LMC spiral arm, there is a negative (inward) motion along the spiral arm overdensity when this is still attached to the bar, regardless of the sample and the number of velocity components used (left panels of Fig. 15). After the break, there is no clear trend. In the right panels, the V_{los} sub-samples do not have enough number of stars on the spiral arms to provide a clear conclusion.

Regarding the residual tangential velocity maps (Fig. 16), the conclusions with regard to the bar region are analogous to those

related to the radial velocity maps, namely, the quadrupole pattern expected for the motion of the stars in elliptical bar orbits is present. The asymmetry in terms of larger velocity in absolute value above the bar major axis is clear in both the full samples and the V_{los} sub-samples. This asymmetry in the velocity seems slightly larger in the NN optimal and NN truncated-optimal samples, with a maximum difference of $10\,km\,s^{-1}$. Along the spiral arm the residual tangential velocity is in general positive in all samples, that is, stars on the spiral arm move faster than the mean motion at the same radius, except for the part of the arm with a density break. When making comparisons among samples, this aspect represents the effect of the contamination of MW stars in the velocity maps and we can see the decrease of the residual tangential velocity in the edges of the sample in the NN optimal and truncated-optimal samples, which could be a bias of the sample. Regarding the V_{los} sub-samples (right panels of Fig. 16), there is no clear sign of the residual tangential velocity along the part of the spiral arm attached to the bar.

Finally, we show in Fig. 17 the vertical velocity component for the V_{los} sub-samples. We see, as in the vertical velocity profile, that the vertical velocity map has second order differences between the different samples. More complete samples, such as PM and NN complete samples show a bimodal trend, where half of the galaxy ($x' < 0$) is moving upwards, while the other half ($x' > 0$) is moving downwards. There also seems to be a positive gradient (in absolute value) of increasing vertical velocities from the inner to the outer disc. This could be associated with an overestimation of the disc inclination angle or to the presence of a galactic warp (e.g., Choi et al. 2018), or to the contamination of MW stars. Purer samples, such as the NN optimal or NN truncated-optimal still show a similar wave-like motion that can be associated to the warp or to the fact that the LMC is still not in dynamical equilibrium (e.g., Choi et al. 2022). Also, there seems to be a clear negative motion of stars located at the end of the bar with $x' > 0$, which could be an evidence of the inclination of the bar with respect to the galactic plane.

5. Biases and different evolutionary phases

Velocity maps may be affected by the choice of the galaxy parameters, namely, the inclination, i, and position angle, θ, or the systemic motion, $(\mu_{x,0}, \mu_{y,0}, \mu_{z,0})$. There remains a large uncertainty in the literature on what the inclination angle of the galactic plane with respect to the line-of-sight and the line-of-nodes of the position angle are, with differences as large as 10° (e.g., van der Marel & Kallivayalil 2014; Haschke et al. 2012; Ripepi et al. 2022). In this work, we use $i = 34°$ and $\theta = 220°$, as nominal values, as in MC21 work. In order to study the possible systematic that a different inclination angle or position angle can induce in the velocity maps, we reproduce the velocity maps for the NN complete sample and corresponding V_{los} sub-sample, by varying the nominal values by ±10°, only one at a time. In general, the effect of having a larger (smaller) inclination angle, elongates (stretches) the velocity map, in either of the velocity components, and a different position angle, rotates the velocity maps. In detail, they also introduce the following trends:

Regarding the inclination angle: *i)* The variation of the inclination angle from $i - 10°$ to $i + 10°$, can reverse the radial motion in the outer disc from being positive to negative along the y'-axis. *ii)* The median vertical component can even change sign and become negative if using a smaller inclination angle; whereas when this is 10° larger, a clear bi-symmetry is introduced. *iii)* The inner disc is not affected, nor the residual tangential component. Regarding the position angle, systematics are of second
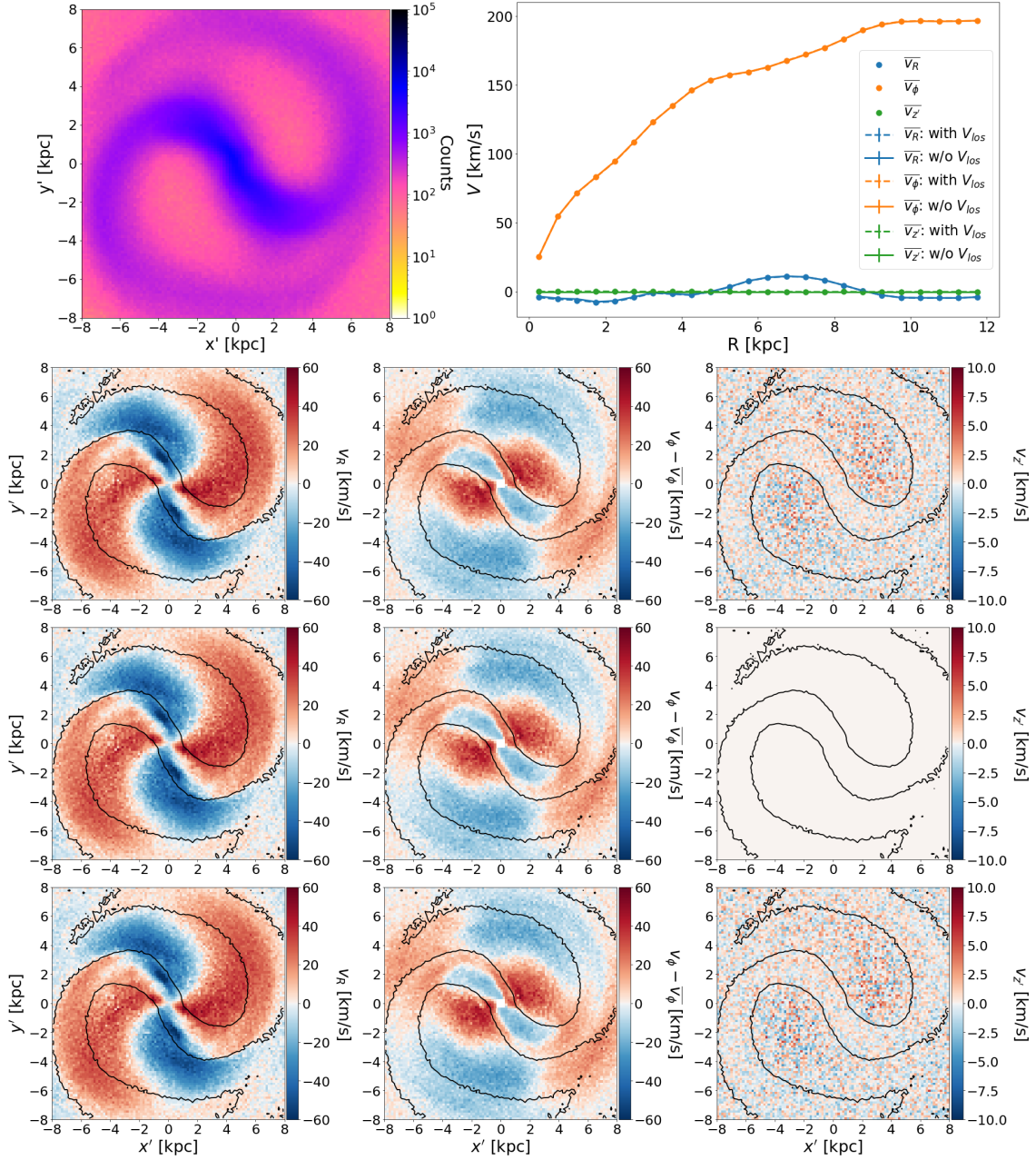
Fig. 13. Simulation B5. First row left panel: density distribution in logarithmic scale. First row, right panel: velocity profiles of the B5 simulation. In blue, orange and green, for the radial, tangential, and vertical components, respectively, when taking into account the full velocity information (dashed lines), or when $V_{\rm los}$ is not available (solid lines). Differences are negligible and both curves overlap. Scatter points show the real velocity profiles. Second row: N-body simulation maps (left, radial; middle, residual tangential; right, vertical), without applying any coordinate transformation. Third row: same as above computed applying the (Sect. 3) coordinate transformations without line-of-sight information. Fourth row: same as above computed applying the (Sect. 3) coordinate transformations with line-of-sight information. The black line shows the contour corresponding to overdensity equal to zero for a 0.4 kpc-bandwidth KDE (see details in Sect. 4.2).

order and mainly affect the azimuthal angle in the disc where the motion is inwards or outwards and upwards or downwards.

The choice of the systemic motion $(\mu_{x,0}, \mu_{y,0}, \mu_{z,0})$ used to compute the internal velocities in the LMC reference frame may also introduce systematics in the velocity profile and maps. In this work, we adopted the same systemic motion as in MC21

to allow a direct comparison. The availability of line-of-sight velocities in *Gaia* DR3 allows a better estimation of $\mu_{z,0}$. For each $V_{\rm los}$ sub-sample, we fit a Kernel density estimation of $2\,{\rm km\,s^{-1}}$ bandwidth to the distribution of line-of-sight velocities (see top panels of Fig. 9) and obtain at which line-of-sight velocity this distribution is maximum $V_{\rm los,0}$. We assume, then, that the
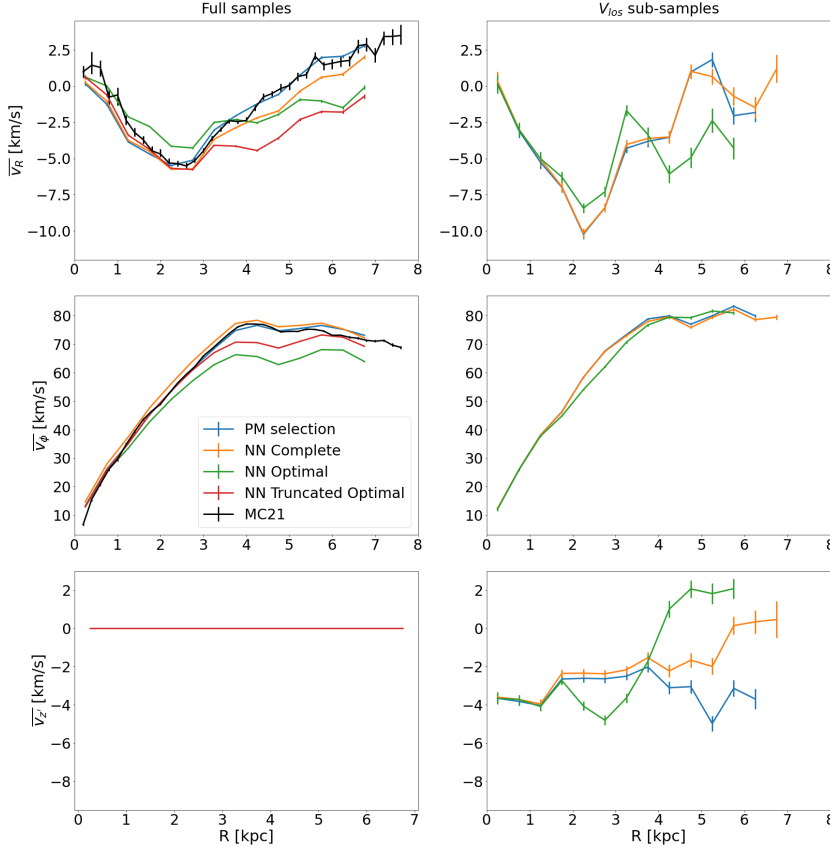
Fig. 14. Velocity profiles for the four LMC samples in the case $V_{\rm los}$ is not available (left) and when it is available (right). From top to bottom: radial, tangential, and vertical velocity profiles. Each curve corresponds to one LMC sample: PM selection (blue), NN complete (orange), NN optimal (green) and NN truncated-optimal (red). In black, the radial and rotation curve published in MC21 (their Fig. 14) is shown. For most of the bins, the error bar is small and cannot be seen. Only bins with more than 300 sources are plotted.

line-of-sight systemic motion, $\mu_{z,0}$ of the LMC is given by $\mu_{z,0} = V_{{\rm los},0}/D_0$. Results are shown in Table 3, where we show for each sub-sample $V_{{\rm los},0}$ and the corresponding $\mu_{z,0}$. We note that for the PM and NN complete samples $\mu_{z,0} = -1.112\,{\rm mas\,yr}^{-1}$ and similar to the value adopted in this work, which is $-1.115\,{\rm mas\,yr}^{-1}$. As discussed previously, NN complete sample and PM sample have a very similar LMC classification and thus provide similar density and kinematic distributions. On the other hand, the line-of-sight systemic motion for the NN optimal sample gives $\mu_{z,0} = -1.132\,{\rm mas\,yr}^{-1}$, which can provide a different velocity profile in the vertical in-plane component, while it barely has no effect on the planar components. In Fig. 18, we show the vertical velocity profile for each of the three sub-samples when we use either the MC21 adopted value for $\mu_{z,0}$ (dashed lines) or the derived using the *Gaia* DR3 line-of-sight velocities (solid lines). We note that a bias in the $\mu_{z,0}$ translates in a shift in the V'_z profile. The small difference between the PM and NN complete samples with respect to the MC21 value falls within the error bars. For the NN optimal sample, the currently derived value shifts the median vertical velocity to be centered at zero in the inner 3 kpc, while it is slightly oscillating towards positive values in the outer disc.

Regarding the tangential systemic motion, $(\mu_{x,0},\mu_{y,0})$, van der Marel et al. (2002) determined $(\mu_{x,0},\mu_{y,0}) = (-1.68, 0.34)\,{\rm mas\,yr}^{-1}$ using Carbon stars, while Schmidt et al. (2022) found $(\mu_{x,0},\mu_{y,0}) = (-1.95, 0.43)\,{\rm mas\,yr}^{-1}$. In this work, we use the values derived in MC21, namely $(\mu_{x,0},\mu_{y,0}) = (-1.858, 0.385)\,{\rm mas\,yr}^{-1}$. The choice of values for $(\mu_{x,0},\mu_{y,0})$ affects the three components of the internal velocities (see Eqs. (A.15) and (A.13)). We test how a possible change of the systemic motion

within values given by different models in MC21 (their Table 5) and in the literature affects the velocity profile and maps. Regarding the MC21 values, the velocity maps do not change qualitatively, and the largest change is in the vertical velocity profile with a shift of the order of $2\,{\rm km\,s}^{-1}$ within the uncertainty range of $0.02\,{\rm mas\,yr}^{-1}$ in either of the tangential systemic components, similar to what we see for the vertical component of the systemic motion (see Fig. 18)[3]. When considering literature values, and due to the strong correlation between the systemic motion and the position of the kinematic centre, we had to build the velocity maps fixing the kinematic centre to the coordinates given in the respectively works. Regarding the radial and residual tangential components, we observe strong systematic effects such as gradients across the LMC plane. The vertical velocity is systematically negative (using van der Marel et al. 2002 values), or positive (using Schmidt et al. 2022 values), indicating that the values of centre coordinates and systemic transverse motions from the literature cannot apply to our samples. We conclude that the systematic gradients are very sensitive to small variations in the kinematic parameters. Only a narrow range of values can match the data, namely, they do not create such systematic effects and these values are the best-fit solutions given in MC21.

Finally, in Fig. 19, we show the radial and tangential velocity profiles for the NN complete (left) and NN optimal (right) full samples separated by the same evolutionary phases selection as in MC21. We impose an additional constraint on the minimum

---

[3] Animations of the variation of the morphological parameters and systemic motion in the velocity profile and maps are made available online.
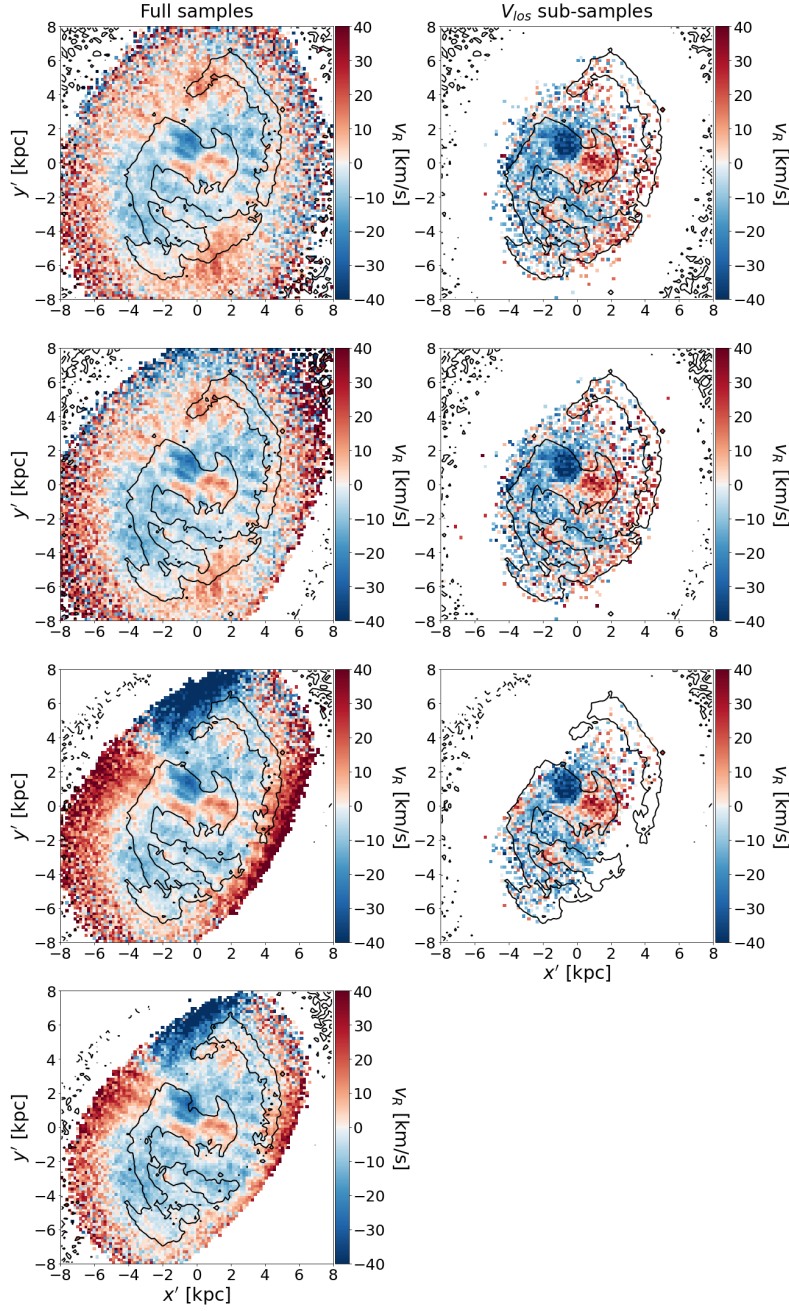
Fig. 15. LMC median radial velocity maps. All maps are shown in the (x', y') Cartesian coordinate system. From top to bottom: PM sample, NN complete, NN optimal, and NN truncated-optimal sample. Left: line-of-sight velocity not included. Right: line of sight velocity included. NN truncated-optimal V_{los} sub-sample map is not shown because it is the same as the NN optimal V_{los} sub-sample (see text for details). For each colormap, a black line splitting the overdensities from the underdensities for a 0.4 kpc-bandwidth KDE is plotted and a minimum number of 3 (20) stars per bin is imposed when the line-of-sight is (not) considered.

number of 500 sources per bin. The radial velocity profiles for the young (Young1, Young2, and Young3) samples are almost identical among the NN complete and NN optimal samples, so they are mostly unaffected by MW contamination. We can see how for older samples, for example, in the case of RR Lyrae samples, the sharp minimum of velocity at $R = 3$ kpc smooths out in the outer disc and becomes more planar and even centered at zero. Differences arise in the AGB sample between the NN complete and NN optimal samples, oscillating as the Young1 population in the NN complete sample, while remaining negative as the Young2 and Blue Loop evolutionary phases in the NN optimal sample. The Young1 population highly oscillates from negative

values in the inner disc to positive values at the ends of the bar. This trend might be due to a limitation in the training sample, which due to its characteristics, lacks AGB and Young1 stars. Despite this limitation, the NN classifier does an excellent job in these areas of the colour-magnitude diagram (see the two bottom rows of Fig. 6, where both the AGB and Young1 areas for all LMC samples are well defined). The gradient in age observed in the tangential velocity profile in the MC21 sample is conserved in both the NN complete and NN optimal samples. There seems to appear a bimodality in the NN optimal sample separating the young and old evolutionary phases, which is not present in the NN complete sample, indicating that it might be an artifact of the
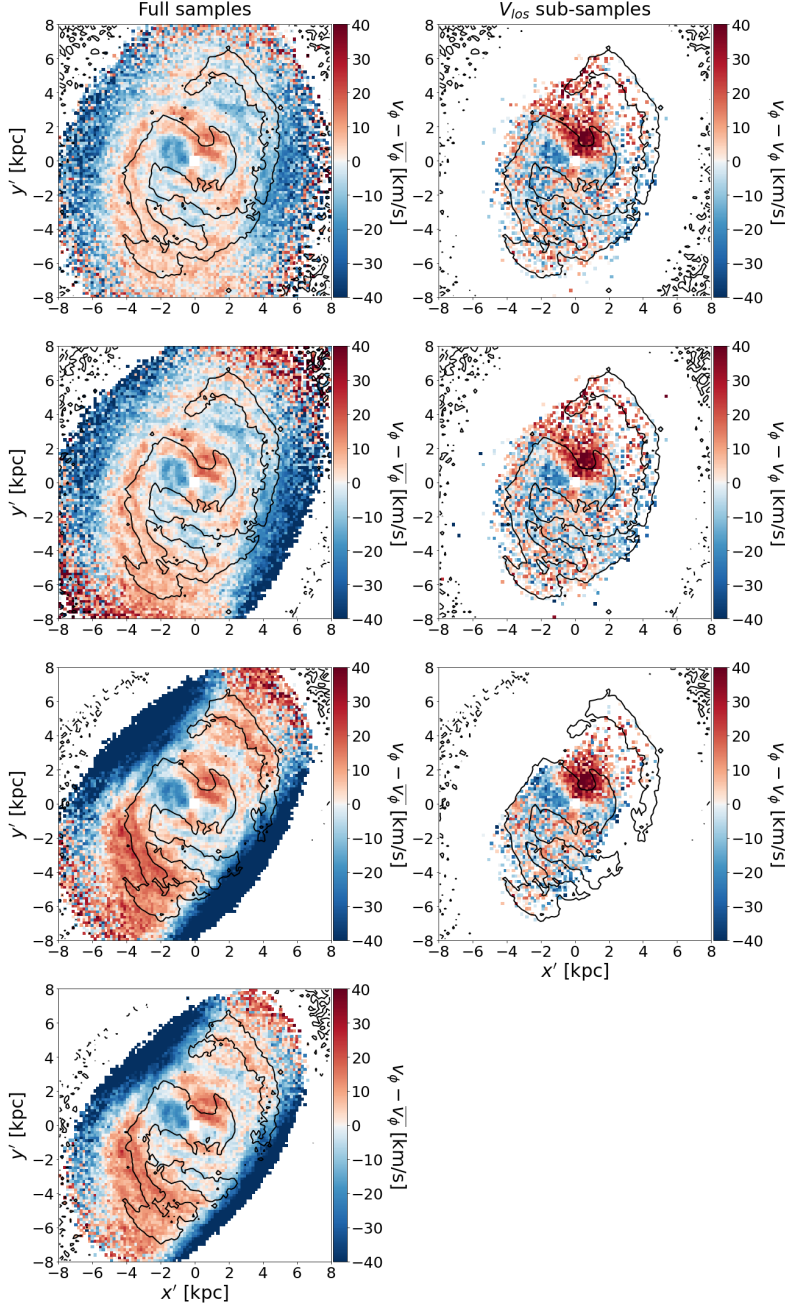
Fig. 16. LMC median residual tangential velocity maps. All maps are shown in the (x', y') Cartesian coordinate system. From top to bottom: PM sample, NN complete, NN optimal, and NN truncated-optimal sample. Left: line-of-sight velocity not included. Right: line-of-sight velocity included. NN truncated-optimal V_{los} sub-sample map is not shown because it is the same as the NN optimal V_{los} sub-sample (see text for details). For each colormap, a black line splitting the overdensities from the underdensities for a 0.4kpc-bandwidth KDE is plotted and a minimum number of 3 (20) stars per bin is imposed when the line-of-sight is (not) considered.

imbalance between completeness and purity. Therefore, further investigation is required in the analysis of stellar populations of the different samples.

6. Conclusions

In this work, we analyse the velocity maps of four LMC samples, defined using different selection strategies, namely, the proper motion selection, as in MC21, and three samples based on a neural network classification, trained using a MW+LMC simulation created by GOG. Using different probability cuts, P_{cut}, we defined two LMC samples: NN complete, with $P_{cut} = 0.01$, and NN opti-

mal, with $P_{cut} = 0.52$, corresponding to the optimal value based on the receiver operating characteristics (ROC) curve. We applied to this last sample an extra cut on the apparent G magnitude of $G < 19.5$ mag, in order to remove further contamination of mis-classified faint stars. Taking advantage of the recently released spectroscopic line-of-sight velocities published in *Gaia* DR3, we generated sub-samples that include both proper motions and line-of-sight velocities. We also adopt a new formalism in order to transform from the observable space $(\alpha, \delta, \mu_{\alpha*}, \mu_\delta, V_{los})$ to the LMC frame $(x', y', z', v_{x'}, v_{y'}, v_{z'})$. The advantage of this formalism based on that of van der Marel & Cioni (2001) and van der Marel et al. (2002) is the possibility to
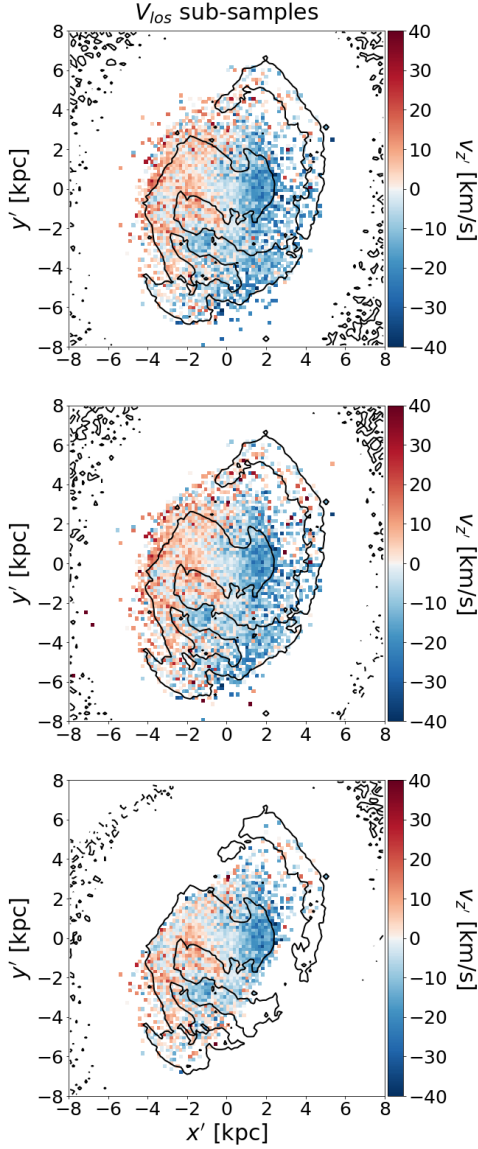
Fig. 17. Same as Fig. 15 for the median vertical velocity of the V_{los} sub-samples.

include the V_{los} component when deriving internal LMC velocities.

We analysed the velocity profile and maps in the LMC coordinate system for the full samples and the V_{los} sub-samples. The velocity maps corresponding to the radial and tangential component of the velocity for the PM sample are analogous to those presented in the MC21 paper, while in Sect. 4.3, we analysed the differences between the samples based on a NN classification. As shown, differences are of second order and mainly located in the outer disc, where differences in density also arise. As a novelty, we also include the V_{los} sub-samples with line-of-sight velocities from *Gaia* DR3 (Katz et al. 2022), which allows for the analysis of the vertical velocity component.

The main conclusions of this work are as follow:

- In all samples and sub-samples, the dynamics in the inner disc are mainly dominated by the bar, and this is a confirma-

Table 3. Determination of the line-of-sight systemic motion.

V_{los} sub-sample	$V_{los,0}$ [km s^{-1}]	$\mu_{z,0}$ [mas yr^{-1}]
PM	260.86	−1.112
NN complete	260.86	−1.112
NN optimal	265.66	−1.132

Notes. Second column gives the V_{los} for which the KDE (see text for details) is maximum. Third column provides the corresponding value of $\mu_{z,0}$.
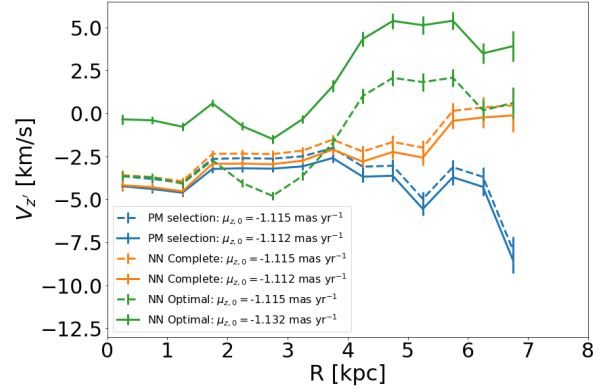

Fig. 18. Stellar vertical velocity profiles of the LMC V_{los} sub-samples (blue, orange and green for the PM, NN complete, and NN optimal samples, respectively) for different input values of $\mu_{z,0}$: the *Gaia* DR3 derived in solid lines and the MC21 adopted value in dashed lines (values given in the legend).

tion of what was first found in MC21. An asymmetry along the bar-major axis is emphasised , especially when mapping the kinematics with the V_{los} sub-samples.
- The kinematics on the spiral arm overdensity seem to be dominated by an inward ($V_R < 0$) motion and a rotation faster than that of the disc ($V_\phi - \bar{V}_\phi > 0$) in the part of the arm attached to the bar, although V_{los} sub-samples are not conclusive in this region.
- The dynamics seems to change in the part of the arm with lower density or even detached from the main arm after the density break, in the sense that the radial velocity and residual tangential velocity can reverse signs.
- The contamination of MW stars seems to dominate the outer parts of the disc, mainly affecting older and later evolutionary phases (e.g.,, RRL or AGB stars).
- Uncertainties in the LMC systemic motion largely affect the vertical component of the velocity, even causing a change in sign. Uncertainties in the morphological parameters of the LMC (inclination and position angle) can modify the radial and vertical velocity maps, apart from inducing a stretch or rotation of them.
- The lack of a V_{los} value for all stars does not substantially impact the kinematic profiles or maps. The approximation used to derive the internal kinematics is accurate.

The available *Gaia* DR3 dataset and the new strategy to select LMC clean samples have proven to be suitable to performing kinematic studies and allowing for a deep analysis of the nature of the LMC morphology. Comparisons with realistic LMC mock catalogues are crucial and this will be the focus of further work.
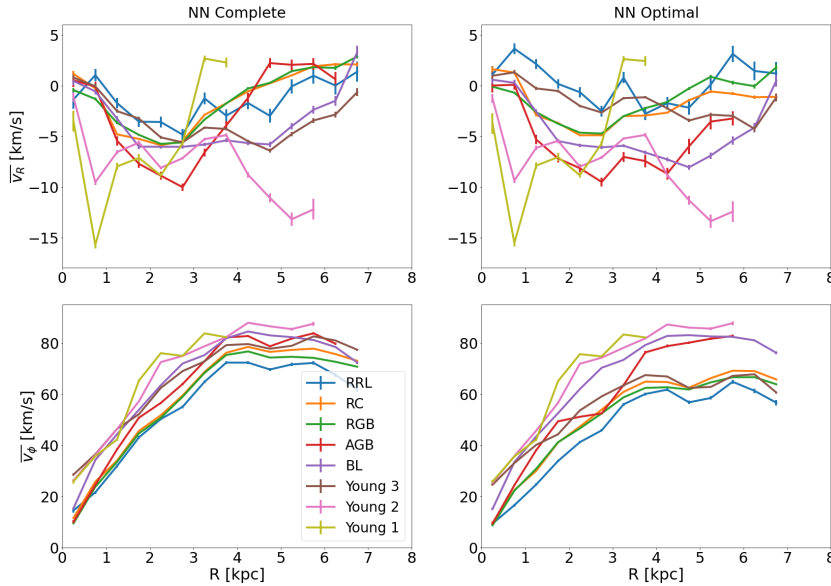
Fig. 19. Stellar velocity curves of the LMC evolutionary phases. Top and bottom panels show the radial motions and rotation curves, respectively, for both NN complete (left) and NN optimal samples (right). Coloured lines are for the eight evolutionary phases. Only bins with more than 500 sources are plotted.

References

Anders, F., Khalatyan, A., Queiroz, A. B. A., et al. 2022, A&A, 658, A91

Athanassoula, E. 1980, A&A, 88, 184

Choi, Y., Nidever, D. L., Olsen, K., et al. 2018, ApJ, 866, 90

Choi, Y., Olsen, K. A. G., Besla, G., et al. 2022, ApJ, 927, 153

Cioni, M. R. L., Clementini, G., Girardi, L., et al. 2011, A&A, 527, A116

Cullinane, L. R., Mackey, A. D., Da Costa, G. S., et al. 2022a, MNRAS, 510, 445

Cullinane, L. R., Mackey, A. D., Da Costa, G. S., et al. 2022b, MNRAS, 512, 4798

Cusano, F., Moretti, M. I., Clementini, G., et al. 2021, MNRAS, 504, 1

Elmegreen, D. M., & Elmegreen, B. G. 1980, AJ, 85, 1325

Gaia Collaboration (Helmi, A., et al.) 2018, A&A, 616, A12

Gaia Collaboration (Luri, X., et al.) 2021a, A&A, 649, A7

Gaia Collaboration (Brown, A. G. A., et al.) 2021b, A&A, 649, A1

Gallagher, J. S. I., & Hunter, D. A. 1984, ARA&A, 22, 37

Garma-Oehmichen, L., Martinez-Medina, L., Hernández-Toledo, H., & Puerari, I. 2021, MNRAS, 502, 4708

Goldreich, P., & Lynden-Bell, D. 1965, MNRAS, 130, 125

Haschke, R., Grebel, E. K., & Duffau, S. 2012, AJ, 144, 106

Julian, W. H., & Toomre, A. 1966, ApJ, 146, 810

Kallivayalil, N., van der Marel, R. P., Besla, G., Anderson, J., & Alcock, C. 2013, ApJ, 764, 161

Katz, D., Sartoretti, P., Guerrier, A., et al. 2022, A&A, submited, ArXiv e-prints [arXiv:2206.05902]

Lin, C. C., & Shu, F. H. 1964, ApJ, 140, 646

Lindblad, P. O. 1960, Stockholms Observatoriums Annaler, 4, 4

Lindegren, L., Bastian, U., Biermann, M., et al. 2021a, A&A, 649, A4

Lindegren, L., Klioner, S. A., Hernández, J., et al. 2021b, A&A, 649, A2

Luri, X., Palmer, M., Arenou, F., et al. 2014, A&A, 566, A119

Nidever, D. L., Olsen, K., Walker, A. R., et al. 2017, AJ, 154, 199

Niederhofer, F., Cioni, M.-R. L., Schmidt, T., et al. 2022, MNRAS, 512, 5423

Olsen, K. A. G., & Salyk, C. 2002, AJ, 124, 2045

Pedregosa, F., Varoquaux, G., Gramfort, A., et al. 2011, J. Mach. Learn. Res., 12, 2825

Pietrzyński, G., Graczyk, D., Gallenne, A., et al. 2019, Nature, 567, 200

Ripepi, V., Chemin, L., Molinaro, R., et al. 2022, MNRAS, 512, 563

Roca-Fàbrega, S., Valenzuela, O., Figueras, F., et al. 2013, MNRAS, 432, 2878

Roca-Fàbrega, S., Antoja, T., Figueras, F., et al. 2014, MNRAS, 440, 1950

Romero-Gómez, M., Athanassoula, E., Masdemont, J. J., & García-Gómez, C. 2007, A&A, 472, 63

Salo, H., Laurikainen, E., Buta, R., & Knapen, J. H. 2010, ApJ, 715, L56

Schmidt, T., Cioni, M.-R. L., Niederhofer, F., et al. 2020, A&A, 641, A134

Schmidt, T., Cioni, M.-R. L., Niederhofer, F., et al. 2022, A&A, 663, A107

Toomre, A. 1981, in Structure and Evolution of Normal Galaxies, eds. S. M. Fall, & D. Lynden-Bell, 111

Toomre, A., & Toomre, J. 1972, ApJ, 178, 623

van der Marel, R. P. 2001, AJ, 122, 1827

van der Marel, R. P., & Cioni, M.-R. L. 2001, AJ, 122, 1807

van der Marel, R. P., & Kallivayalil, N. 2014, ApJ, 781, 121

van der Marel, R. P., Alves, D. R., Hardy, E., & Suntzeff, N. B. 2002, AJ, 124, 2639

Vasiliev, E. 2018, MNRAS, 481, L100

Wan, Z., Guglielmo, M., Lewis, G. F., Mackey, D., & Ibata, R. A. 2020, MNRAS, 492, 782

Yozin, C., & Bekki, K. 2014, MNRAS, 439, 1948

Zaritsky, D. 2004, ApJ, 614, L37

Zivick, P., Kallivayalil, N., Besla, G., et al. 2019, ApJ, 874, 78

Appendix A: Coordinate changes

In this appendix, we detail the steps performed to transform from heliocentric equatorial coordinates to LMC internal coordinates. This formalism is based on van der Marel & Cioni (2001) and van der Marel et al. (2002).

A.1. Positions

The position of any point in space is uniquely determined by its right ascension and declination on the sky, (α, δ), and its distance, D, which can be referenced to a particular point, O, with coordinates $(\alpha_0, \delta_0, D_0)$. We chose the LMC centre to be the reference centre.

We introduce the angular coordinates (ϕ, ρ) (Figure 10) which are defined in the celestial sphere:
- ρ is the angular distance between the points (α, δ) and (α_0, δ_0).
- ϕ is the position angle of the point (α, δ) with respect to (α_0, δ_0). In particular, ϕ is the angle at (α_0, δ_0) between the tangent to the great circle on the celestial sphere through (α, δ) and (α_0, δ_0), and the circle of constant declination δ_0. By convention, ϕ is measured counterclockwise starting from the axis that runs in the direction of decreasing right ascension at constant declination δ_0.

We can uniquely define (ρ, ϕ) as function of (α, δ), for a choice of the origin O, by using:

$$\rho = \arccos\left[\cos\delta\cos\delta_0\cos(\alpha - \alpha_0) + \sin\delta\sin\delta_0\right],$$
$$\phi = \arctan\left[\frac{\sin\delta\cos\delta_0 - \cos\delta\sin\delta_0\cos(\alpha - \alpha_0)}{-\cos\delta\sin(\alpha - \alpha_0)}\right]. \tag{A.1}$$

These previous equations have been obtained by using the cosine, sine rule of spherical trigonometry and the so-called analogue formula:

$$\cos\rho = \cos\delta\cos\delta_0\cos(\alpha - \alpha_0) + \sin\delta\sin\delta_0,$$
$$\sin\rho\cos\phi = -\cos\delta\sin(\alpha - \alpha_0),$$
$$\sin\rho\sin\phi = \sin\delta\cos\delta_0 - \cos\delta\sin\delta_0\cos(\alpha - \alpha_0) \tag{A.2}$$

Then, we can introduce a Cartesian coordinate system (x, y, z) that has its origin at O, with the x-axis anti-parallel to the right ascension axis, the y-axis parallel to the declination axis, and the z-axis towards the observer. This is somehow similar to considering the orthographic projection -a method of representing 3D objects where the object is viewed along parallel lines that are perpendicular to the plane of the drawing of the usual celestial coordinates and proper motions. This yields the following transformations:

$$x = D\sin\rho\cos\phi,$$
$$y = D\sin\rho\sin\phi, \tag{A.3}$$
$$z = D_0 - D\cos\rho.$$

A second Cartesian coordinate system (x', y', z') is then introduced. It is obtained from the system (x, y, z) by counterclockwise rotation around the z-axis by an angle θ, followed by a clockwise rotation around the new x'-axis by an angle i. With this definition, the (x', y') plane is inclined with respect to the sky by an angle, i, (with face-on viewing corresponding to $i = 0°$). The angle, θ, is the position angle of the line-of-nodes - the intersection of the (x', y')-plane, and the (x, y)-plane of the sky, measured counterclockwise from the x-axis. In practice, i and θ ought to be chosen such that the (x', y')-plane coincides

with the plane of the LMC disk. The transformations between the (x', y', z') and the (x, y, z) coordinates are represented by:

$$\begin{pmatrix} x' \\ y' \\ z' \end{pmatrix} = \begin{pmatrix} \cos\theta & \sin\theta & 0 \\ -\sin\theta\cos i & \cos\theta\cos i & -\sin i \\ -\sin\theta\sin i & \cos\theta\sin i & \cos i \end{pmatrix} \begin{pmatrix} x \\ y \\ z \end{pmatrix}, \tag{A.4}$$

The distance, D, of points in the (x', y') plane is of interest here, as a function of the position (ρ, ϕ) on the sky. The points in this plane fulfil $z' = 0$, which yields:

$$D = D_{z'=0} \equiv \frac{D_0\cos i}{\cos i\cos\rho - \sin i\sin\rho\sin(\phi - \theta)}. \tag{A.5}$$

A.2. Velocities

At any given position (D, ρ, ϕ) a velocity vector can be decomposed into a sum of three orthogonal components:

$$v_1 \equiv \frac{dD}{dt}, \qquad v_2 \equiv D\frac{d\rho}{dt}, \qquad v_3 \equiv D\sin\rho\frac{d\phi}{dt}. \tag{A.6}$$

Here, v_1 is the line-of-sight velocity and v_2 and v_3 are the velocity components in the plane of the sky. Computing the time derivative of Eq. (A.3) yields:

$$\begin{pmatrix} v_x \\ v_y \\ v_z \end{pmatrix} = \begin{pmatrix} \sin\rho\cos\phi & \cos\rho\cos\phi & -\sin\phi \\ \sin\rho\sin\phi & \cos\rho\sin\phi & \cos\phi \\ -\cos\rho & \sin\rho & 0 \end{pmatrix} \begin{pmatrix} v_1 \\ v_2 \\ v_3 \end{pmatrix}, \tag{A.7}$$

where (v_x, v_y, v_z) is the three-dimensional velocity in the (x, y, z) coordinate system. Again, to describe the internal kinematic of the galaxy it is useful to adopt the second Cartesian coordinate system (x', y', z'). We recall that the (x', y')-plane coincides with the plane of the LMC disk. Upon taking the time derivative on both sides on Eq. (A.4) yields the transformation equations from (v_x, v_y, v_z) to (v'_x, v'_y, v'_z). This result can be used with Eq. (A.7) to obtain:

$$\begin{pmatrix} v'_x \\ v'_y \\ v'_z \end{pmatrix} = \begin{pmatrix} \cos\theta & \sin\theta & 0 \\ -\sin\theta\cos i & \cos\theta\cos i & -\sin i \\ -\sin\theta\sin i & \cos\theta\sin i & \cos i \end{pmatrix} \times$$
$$\times \begin{pmatrix} \sin\rho\cos\phi & \cos\rho\cos\phi & -\sin\phi \\ \sin\rho\sin\phi & \cos\rho\sin\phi & \cos\phi \\ -\cos\rho & \sin\rho & 0 \end{pmatrix} \begin{pmatrix} v_1 \\ v_2 \\ v_3 \end{pmatrix}. \tag{A.8}$$

We know that v_1 is the line-of-sight velocity. Now, we need to relate the velocities v_2 and v_3 with the proper motions $\mu_{\alpha*}$ and μ_δ. In these directions, the proper motions are defined as:

$$\mu_{\alpha*} \equiv \cos\delta\frac{d\alpha}{dt}, \qquad \mu_\delta \equiv \frac{d\delta}{dt}. \tag{A.9}$$

Upon taking time derivative of Eq. (A.2) we obtain relations between $d\rho/dt$ and $d\phi/dt$ on the one hand, and $d\alpha/dt$ and $d\delta/dt$ on the other. This system can be solved to obtain:

$$\begin{pmatrix} v_2 \\ v_3 \end{pmatrix} = D \begin{pmatrix} \sin\Gamma & \cos\Gamma \\ \cos\Gamma & -\sin\Gamma \end{pmatrix} \begin{pmatrix} \mu_{\alpha*} \\ \mu_\delta \end{pmatrix}, \tag{A.10}$$

where the angle Γ determines the rotation angle of the (v_2, v_3) frame on the sky. It is given by:

$$\cos \Gamma = [\sin \delta \cos \delta_0 \cos(\alpha - \alpha_0) - \cos \delta \sin \delta_0]/ \sin \rho,$$
$$\sin \Gamma = [\cos \delta_0 \sin(\alpha - \alpha_0)]/ \sin \rho. \tag{A.11}$$

A.2.1. Correcting from the systemic motion

For a planar system, the velocity of a tracer can be written as a sum of three components: the velocity corresponding to the systemic motion, the velocity corresponding to precession and nutation of the disk plane, and the velocity corresponding to the internal motion of the tracer:

$$\begin{pmatrix} v_1 \\ v_2 \\ v_3 \end{pmatrix} = \begin{pmatrix} v_1 \\ v_2 \\ v_3 \end{pmatrix}_{sys} + \begin{pmatrix} v_1 \\ v_2 \\ v_3 \end{pmatrix}_{pn} + \begin{pmatrix} v_1 \\ v_2 \\ v_3 \end{pmatrix}_{int}. \tag{A.12}$$

Then, if we neglect the effect of precession and nutation, we can determine the internal motion by using:

$$\begin{pmatrix} v_1 \\ v_2 \\ v_3 \end{pmatrix}_{int} = \begin{pmatrix} v_1 \\ v_2 \\ v_3 \end{pmatrix} - \begin{pmatrix} v_1 \\ v_2 \\ v_3 \end{pmatrix}_{sys}, \tag{A.13}$$

where we explain how to compute the first term in Section A.2. On the other hand, we can determine the systemic motion using the inverse relation of Eq. (A.7):

$$\begin{pmatrix} v_1 \\ v_2 \\ v_3 \end{pmatrix}_{sys} = \begin{pmatrix} \sin \rho \cos \phi & \sin \rho \sin \phi & -\cos \rho \\ \cos \rho \cos \phi & \cos \rho \sin \phi & \sin \rho \\ -\sin \phi & \cos \phi & 0 \end{pmatrix} \begin{pmatrix} v_x \\ v_y \\ v_z \end{pmatrix}_{sys} =$$
$$= D_0 \begin{pmatrix} \sin \rho \cos \phi & \sin \rho \sin \phi & -\cos \rho \\ \cos \rho \cos \phi & \cos \rho \sin \phi & \sin \rho \\ -\sin \phi & \cos \phi & 0 \end{pmatrix} \begin{pmatrix} \mu_{x,0} \\ \mu_{y,0} \\ \mu_{z,0} \end{pmatrix}, \tag{A.14}$$

where $\mu_{x,0}$ and $\mu_{y,0}$ are the associated proper motions in the x and y directions at the centre of the disc, and $\mu_{z,0} = v_{z,0}/D_0$, the associated line-of-sight velocity, expressed on the same scale as the proper motions by dividing by D_0.

A.3. Estimating the observational line-of-sight velocity

In a case where we do not have observational information on the line-of-sight velocity, we can estimate $v_{1,int}$ by computing the derivative of the distance as function of time:

$$v_{1,int} \equiv \frac{dD}{dt} = \frac{d}{dt}\left[\frac{D_0 \cos i}{\cos i \cos \rho - \sin i \sin \rho \sin(\phi - \theta)} \right]$$
$$= \frac{v_{2,int}[\cos i \sin \rho + \sin i \cos \rho \sin(\phi - \theta)] + v_{3,int} \sin i \cos(\phi - \theta)}{\cos i \cos \rho - \sin i \sin \rho \sin(\phi - \theta)}. \tag{A.15}$$

To compute $v_{2,int}$ and $v_{3,int}$ when observational information on the line-of-sight velocity is lacking, we proceed the way that is described in Section A.2, since $v_{2,int}$ and $v_{3,int}$ only depend on the proper motions.

A SMALL MAGELLANIC CLOUD STELLAR CLASSIFIER

This Chapter contains the published version of Jiménez-Arranz et al. (2023a, A&A, 672, A65).

Based on Jiménez-Arranz et al. 2023b, we define and validate a new supervised classification strategy based on neural networks (NNs) to distinguish the Small Magellanic Cloud (SMC) stars from the Milky Way (MW) foreground stars. We use as much as of the *Gaia* DR3 data as possible (astrometry and photometry). As a result of the application of our method, we are able to define three samples, with different levels of purity and, complementarily, completeness. We validated these classification results using different test samples (SMC RR Lyrae, SMC Cepheids and SMC-MW StarHorse (SH) samples).

The estimated MW contamination in each of the three SMC samples is in the 10-40% range; the "best case" is obtained for bright stars ($G < 16$), which are part of the line-of-sight velocity (V_{los}) sub-samples, and the "worst case" corresponds to the entire SMC sample determined by applying a strict criteria based on SH distances. A further check based on the comparison with a nearby area with uniform sky density indicates that the global contamination in our samples is probably close to the low end of the range, around 10%.

**Astronomy
&
Astrophysics**

Application of a neural network classifier for the generation of clean Small Magellanic Cloud stellar samples⋆

Ó. Jiménez-Arranz[1,2,3], M. Romero-Gómez[1,2,3], X. Luri[1,2,3], and E. Masana[1,2,3]

[1] Departament de Física Quàntica i Astrofísica (FQA), Universitat de Barcelona (UB), C Martí i Franquès, 1, 08028 Barcelona, Spain
e-mail: ojimenez@icc.ub.edu
[2] Institut de Ciències del Cosmos (ICCUB), Universitat de Barcelona, Martí i Franquès 1, 08028 Barcelona, Spain
[3] Institut d'Estudis Espacials de Catalunya (IEEC), C Gran Capità 2–4, 08034 Barcelona, Spain

ABSTRACT

Context. Previous attempts to separate Small Magellanic Cloud (SMC) stars from the Milky Way (MW) foreground stars are based only on the proper motions of the stars.
Aims. In this paper, we aim to develop a statistical classification technique to effectively separate the SMC stars from the MW stars using a wider set of *Gaia* data. We aim to reduce the possible contamination from MW stars compared to previous strategies.
Methods. The new strategy is based on a neural network classifier, applied to the bulk of the *Gaia* DR3 data. We produce three samples of stars flagged as SMC members, with varying levels of completeness and purity, obtained by application of this classifier. Using different test samples, we validated these classification results and compared them with the results of the selection technique employed in the *Gaia* Collaboration papers, which was based solely on the proper motions.
Results. The contamination of the MW in each of the three SMC samples is estimated to be in the 10–40% range; the "best case" in this range is obtained for bright stars ($G < 16$), which belong to the $V_{\rm los}$ sub-samples, and the "worst case" for the full SMC sample determined by using very stringent criteria based on StarHorse distances. A further check based on the comparison with a nearby area with uniform sky density indicates that the global contamination in our samples is probably close to the low end of the range, around 10%.
Conclusions. We provide three selections of SMC star samples with different degrees of purity and completeness, for which we estimate a low contamination level and which we have successfully validated using SMC RR Lyrae, SMC Cepheids, and SMC-MW StarHorse samples.

Key words. Magellanic Clouds – astrometry – methods: data analysis

1. Introduction

This paper is a follow-up of (Jiménez-Arranz et al. 2023, hereafter J23). In that paper, the authors analyzed the kinematics of the Large Magellanic Cloud (LMC) using the *Gaia* DR3 data; the analysis required a reliable separation of LMC and foreground (Milky Way) stars in the dataset; for this purpose, a classification method based on a neural network (NN) was developed, tested, and applied. The result was a series of datasets providing a reliable selection of LMC objects, published through the Centre de Données de Strasbourg for public use.

In this work, we extended the application of this methodology to the Small Magellanic Cloud (SMC) in order to obtain similarly reliable datasets for the study of this object. We made them public for general use.

The paper is organized as follows. In Sect. 2, we describe the *Gaia* base sample and the training sample. In Sect. 3, we explain how we trained the classifier and applied it to the *Gaia* base sample. We also compared the different datasets obtained. In Sect. 4, we validate the datasets with external data such as Cepheids (Ripepi et al. 2017), RRLyrae (Muraveva et al. 2018), and StarHorse (Anders et al. 2022). Finally, we give our conclusions in Sect. 5.

2. Data selection

In this section, we introduce the samples used in this paper. First, we characterize the *Gaia* DR3 base sample (Gaia Collaboration 2021a) with stars selected around the SMC center. The contamination of foreground MW stars in this sample is nonnegligible. One may consider distinguishing the SMC and MW through their distances; however, due to the large uncertainties in the parallax-based distances at the SMC (Lindegren et al. 2021) it is not possible and would only be effective when subtracting bright MW stars. Second, we characterize the *Gaia* training sample we used to train the machine learning classifier (NN) to distinguish SMC stars from MW foreground stars. This training sample intends to mimic the full dataset available in the *Gaia* catalog.

2.1. Gaia base sample

The *Gaia* base sample was obtained using a selection from the `gaia_source` table in *Gaia* DR3 with a 10° radius around the SMC center defined as $(\alpha, \delta) = (12.80°, -73.15°)$ (Cioni et al. 2000a) and a limiting G-magnitude of 20.5. We only kept the
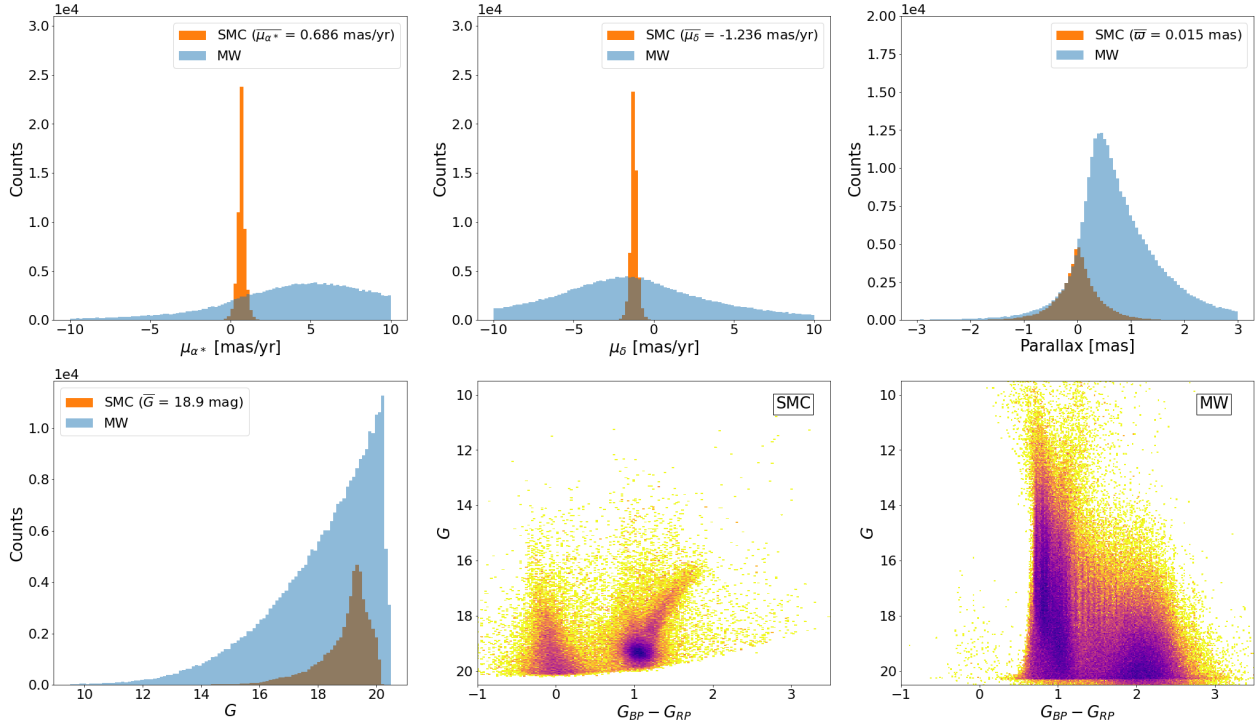
Fig. 1. Characteristics of GOG simulated samples in orange and blue: SMC and the MW training samples, respectively. Top left and middle: distribution of proper motions in right ascension and declination, respectively. Top right: parallax distribution. Bottom left: magnitude G distribution of the simulated samples. Bottom middle and right: color-magnitude diagram of the SMC and MW, respectively. Colors represent relative stellar density, with darker colors meaning higher densities.

stars with parallax and integrated photometry information, since they are used in the SMC/MW classification. This selection can be reproduced using the following ADQL query in the *Gaia* archive:

```
SELECT * FROM gaiadr3.gaia_source as g
WHERE 1=CONTAINS(POINT('ICRS',g.ra,g.dec),
CIRCLE('ICRS',12.80,-73.15,10))
AND g.parallax IS NOT NULL
AND g.phot_g_mean_mag IS NOT NULL
AND g.phot_bp_mean_mag IS NOT NULL
AND g.phot_rp_mean_mag IS NOT NULL
AND g.phot_g_mean_mag < 20.5
```

The resulting base sample contains a total of 4 047 225 objects.

2.2. Gaia training sample

As in J23, we used GOG (Luri et al. 2014) to produce a training dataset with similar characteristics to the base sample. We selected particles within 10° of the SMC center. We made it compatible with recent estimations of the mean distance and systemic motion obtained from EDR3 data: a distance of 62.8 kpc (Cioni et al. 2000b) and a systemic motion of $\mu_{\alpha*} = 1.858$ mas yr^{-1}, $\mu_\delta = 0.385$ mas yr^{-1} as inferred in the linear fit (Table 4) to the proper motions in Gaia Collaboration (2021b, hereafter MC21).

The *Gaia* training sample is split into two labelled subsets, one containing SMC stars and the other MW stars. The SMC simulation includes 54 109 sources, a smaller number of stars in comparison to what was expected for the data. That is because

the GOG simulator is based on a pre-defined catalog of OGLE stars to provide real positions for the SMC stars (see details in Luri et al. 2014). On the other hand, the MW simulation is based on a realistic Galactic model that generates a number of stars that matches the observations. Similarly to the strategy used in J23, we compensated this unbalanced and unrealistic ratio between SMC and MW stars by retaining a random 20% fraction of the MW simulation, obtaining 285 258 sources. In Fig. 1, both SMC and MW training subsets are characterised.

Our training sample is the result of combining these two simulations, which we contrast with the *Gaia* base sample in Fig. 2. These plots demonstrate that the *Gaia* training sample roughly matches the major characteristics of the *Gaia* base sample, but they also highlight some of its limitations. For example, the color–magnitude diagram (CMD) for the SMC simulation is not fully representative at the faintest magnitudes – with a lack of stars and an artificial cut line- and the distribution of the SMC stars in the sky forms a kind of square due to its origin based on an extraction from the OGLE catalog. We tested their effectiveness using a number of validation samples to ensure that they are appropriate.

2.3. Proper motions-based classification

To establish a baseline comparison with previous methods, we used the same selection based on the proper motions as in MC21. In short, the MW foreground contamination is minimized by computing the median proper motions of the SMC from a sample constrained to its very center and cutting the magnitude and parallax. We only kept stars whose proper motions obey the
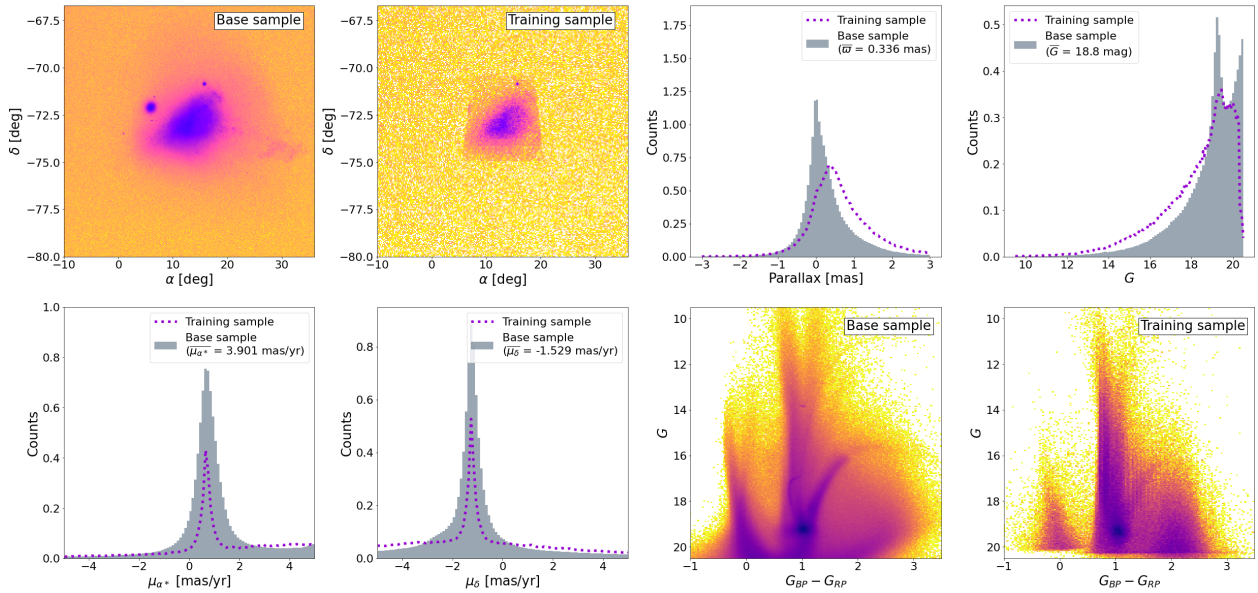
Fig. 2. *Gaia* base and training samples comparison. Top from left to right: density distribution in equatorial coordinates of the *Gaia* base and *Gaia* training samples in logarithmic scale, parallax, and *G*-magnitude distributions. Bottom from left to right: proper motion distributions in right ascension and declination and color–magnitude diagrams for the *Gaia* base and training samples. In the histograms, we show the *Gaia* base sample, while in dotted purple we show the *Gaia* training sample. In the color–magnitude diagrams, colors represent relative stellar density with darker colors meaning higher densities.

constraint of $\chi^2 < 9.21$, that is, an estimated 99% confidence region (see details in Sect. 2.2 of MC21). The resulting sample (hereafter PM selection) contains 1 720 856 objects[1].

3. SMC/MW classification

In this section, we define an improved, more efficient, and adjustable selection strategy to distinguish the SMC stars from the MW foreground. Based on this classifier, we selected three samples of candidate SMC stars with different degrees of completeness and purity.

3.1. Training the classifier

The sklearn Python package (Pedregosa et al. 2011) was used to create a classifier. Using the *Gaia* data, this module includes a number of classifiers that can be used to differentiate the MW foreground objects from the SMC objects in our base sample using the training sample mentioned in the preceding section. We used the position (α, δ), parallax, and its uncertainty (ϖ, σ_ϖ), along with the proper motions and their uncertainties $(\mu_{\alpha*}, \mu_\delta, \sigma_{\mu_{\alpha*}}, \sigma_{\mu_\delta})$, and *Gaia* photometry (G, G_{BP}, G_{RP}).

As in J23, we select as classifier the NN. The NN has 11 input neurons, corresponding to the 11 *Gaia* parameters listed above; three-hidden-layers with six, three, and two nodes, respectively; and a single output that gives the probability P of being a SMC star for each object (or, conversely, the probability of not being a MW star). The object is very likely to belong to the SMC (MW) if the P value is close to 1 (0). The activation function that we employed was the rectified linear unit (ReLU). With a

constant learning rate, stochastic gradient descent is used in our model to optimize the log-loss function. The strength of the L2 regularization term is 1e-5[2].

To train the algorithm, we used 60% of the training sample, and the remaining 40% was used for testing purposes. By creating the receiver operating characteristic (ROC) curve and computing the area under the curve (AUC), we assessed the classifier performance. One of the most crucial evaluation criteria for determining the effectiveness of any classification model is the ROC curve. Using various probability thresholds, it summarizes the trade-off between the true positive rate and false positive rate. Another useful tool for classifier evaluation is the AUC of the ROC curve. The larger the AUC, the better the classifier works. An excellent model has an AUC that is close to 1, indicating that it has a high level of separability. Having an AUC equal to 0.5 indicates that the model is incapable of classifying the data.

We provide the ROC curve of our NN classifier in the left panel of Fig. 3. We achieve an AUC of 0.998, indicating that our classifier accurately distinguishes between SMC and MW stars in the test sample. We show the precision-recall curve in the right panel of Fig. 3. When the classes are severely unbalanced, it is another helpful indicator to assess the output quality of the classifier. Both evaluation criteria display a nearly flawless classifier when applied to the training (simulated) data; however, the same warnings regarding the classifier described in J23 apply here.

3.2. Applying the classifier to the Gaia base data

After the NN has been trained, we use it to extract probabilities for each object in the *Gaia* base sample. Figure 4 displays

---

[1] We note that the difference in the number of sources with the ones in MC21 comes from the different cut in radius, now being of 10° instead of 11°.

[2] The corresponding author can be contacted if readers are interested in using the NN developed in the paper.
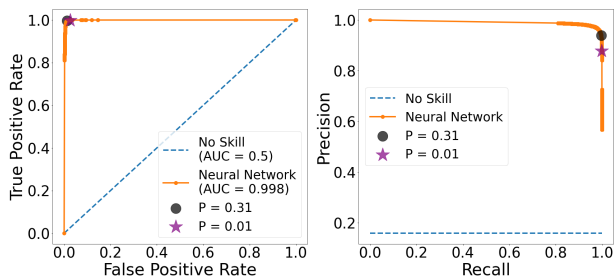
Fig. 3. Evaluation metrics for NN classifier performance. Left: ROC curve. Black dot is in the "elbow" of the ROC curve and shows the best balance between completeness and purity. The purple star shows the completeness threshold. Right: precision–recall curve. In both cases, we compare our model (orange solid curve) with a classifier that has no class separation capacity (blue dashed curve).
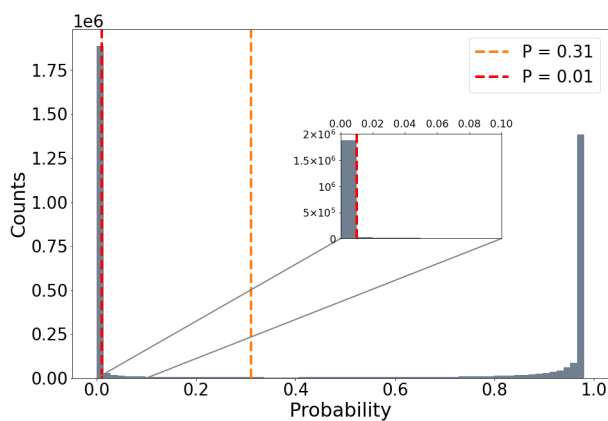

Fig. 4. *Gaia* base sample's probability distribution for the NN classifier. A high likelihood of being an SMC (MW) star is indicated by a probability value close to 1 (0).

the resulting probability distribution. Two distinct peaks can be seen, one with probability near 0 and the other with probability near 1. These peaks match stars that the classifier can definitely identify as being MW and SMC sources, respectively. There is a flat tail with intermediate probability in between, which represents sources for which the NN has more difficulties classifying. Only 537 137 stars have a probability P between 0.01 and 0.9, corresponding to 13% of the SMC base sample.

We must establish a probability threshold P_{cut} in order to acquire a classification using the probabilities that the classifier generated for each star. The star is thought to belong to the SMC if $P > P_{cut}$ and the MW if $P < P_{cut}$ (alternatively, we could deem stars with intermediate probabilities as unclassified). Fixing a low probability threshold allows us to ensure that no SMC objects are missed, but at the cost of having more "mistaken" MW stars in the SMC-classified sample. Conversely, by setting a high probability threshold, we can reduce contamination in the resultant SMC-classified sample, but at the cost of omitting some SMC stars and producing a less complete sample.

As seen in J23, a choice regarding the purity-completeness trade-off will determine the characteristics of the final sample and may, therefore, have an impact on the results. To examine

the impact of this trade-off, we defined two different samples in this work:

1. Complete sample ($P_{cut} = 0.01$). In this case, a cut at low probability prioritizes completeness at the cost of larger MW contamination. We determined the cut value by looking at the classification's probability histogram (Fig. 4) and selecting the upper limit of the peak of small probability values.
2. Optimal sample ($P_{cut} = 0.31$). The probability cut in this instance was determined to be the best possible in terms of classification; the value corresponds to the "elbow" of the ROC curve (Fig. 3), which is in principle the ideal compromise between completeness and purity.

Additionally, and because MW stars exponentially rise at fainter magnitudes whereas SMC stars rapidly decrease beyond $G \simeq 19.5$ (see discussion in the next section), we introduced the third case after carefully studying the results for the optimal sample. We refer to it as the truncated-optimal sample ($P_{cut} = 0.31$) with $G < 19.5$ mag. As mentioned above, this cut avoids a region in the faint end, where the SMC training sample is not representative; by removing these stars, the MW contamination can be reduced and the stars with larger uncertainties are also discarded. Given the purity of the SMC diagrams in Fig. 5, we decided against making a second selection by excluding areas of the CMD diagram where contamination is more likely.

Finally, we take into account two datasets for each of the four samples: firstly, the full sample, where we assume that there is no information on the line-of-sight velocities for any of the stars; secondly, a subset of the first sample that only contains stars with *Gaia* DR3 line-of-sight velocities is kept. These samples are referred to as the corresponding V_{los} samples. In Table 1, the second and third columns show the number of stars for each data set together with the mean astrometric information.

3.3. Comparison of classifications

Figure 6 displays the sky density distributions for the classified SMC/MW members in our various samples. We provide the SMC selection for each sample in the left column, and the sources designated as MW are displayed in the right column. Proper-motion selection is the first row, followed by the three NN-based selection strategies, and each row corresponds to one selection technique. As may be expected, the outcomes of the proper-motion-based selection closely resemble those of MC21.

Since an anomalous classification in the SMC outskirts is not seen in these figures, we notice that the restricted spatial distribution of the SMC training sample (square region in top left panel of Fig. 2) does not pose an issue for extrapolating the membership outside this region. Additionally, we observe that sources identified as MW by all four samples exhibit an overdensity in the SMC central part, the most populated region, indicating that SMC stars were misidentified. Two globular clusters, Tuc 47 and NGC362, were successfully removed from the SMC samples (see the concentration of stars around $(\alpha, \delta) \simeq (5°, -72°)$ and $(16°, -71°)$, respectively). Moreover, we observe that, in accordance with the concept of the probability cut, fewer stars are categorized as belonging to the MW the more complete the SMC sample is. In this regard, a cross-match between the complete sample and the proper motion selection sample reveals that the latter almost entirely contains the former: of the 1 720 856 stars in the proper motion sample, 1 697 614 of them are included in the complete sample, and the complete sample also contains nearly 400 000 additional stars. Regarding the MW samples, we can estimate their SMC contamination by comparing its density
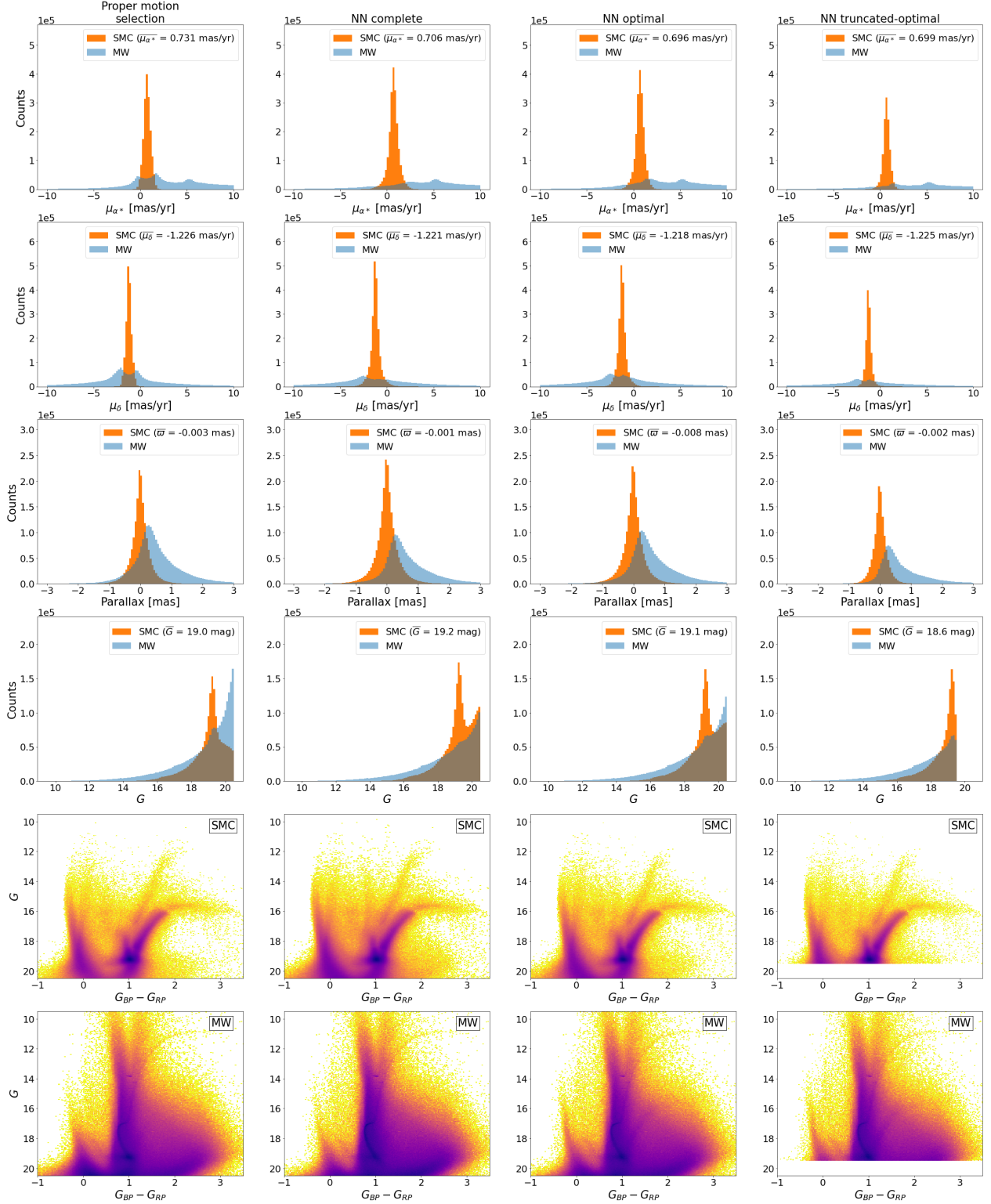
Fig. 5. Astrometric and photometric characteristics of the SMC and MW samples. From left to right: PM sample, NN complete, NN optimal, and NN truncated-optimal samples. In the first four rows, we show distributions of proper motion in right ascension and declination, parallax, and *G*-magnitude, respectively, of the SMC (orange) and MW (blue) samples. In the last two rows, we show the color–magnitude diagram of the samples classified as SMC and MW, respectively. Color represents the relative stellar density, with darker colors meaning higher densities.

Table 1. Comparison of the SMC samples' number of sources and mean astrometry between the proper motion selection (MC21) and the NNs.

SMC sample	N	$N_{\rm vlos}$	$\overline{\varpi}$	σ_ϖ	$\overline{\mu_{\alpha*}}$	$\sigma_{\mu_{\alpha*}}$	$\overline{\mu_\delta}$	σ_{μ_δ}
Proper motion selection	1 720 856	4014	−0.0029	0.323	0.731	0.370	−1.226	0.297
NN complete	2 172 427	4195	−0.0013	0.417	0.706	0.580	−1.221	0.558
NN optimal	1 979 603	3335	−0.0083	0.381	0.696	0.485	−1.218	0.463
NN truncated-optimal	1 265 824	3335	−0.0018	0.254	0.700	0.383	−1.225	0.349

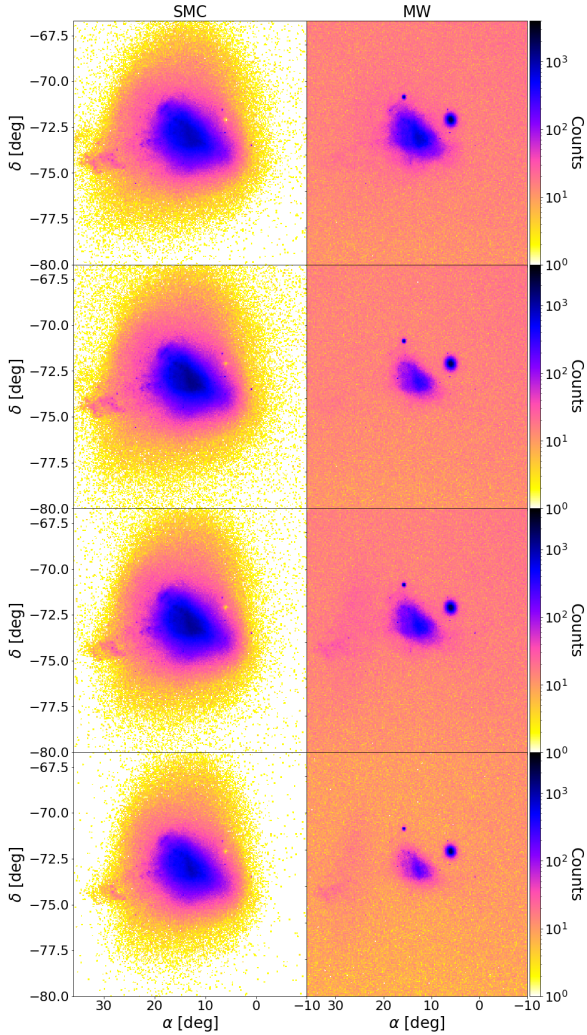**Notes.** Parallax is in mas and proper motions in mas yr^{-1}.

Fig. 6. Sky density distribution in equatorial coordinates of both the SMC (left) and MW (right) sample obtained from the different classifiers. First row: proper motion selection classification. Second row: complete NN classification. Third row: optimal NN classification. Fourth row: truncated-optimal NN classification. We note that in the fourth row, we display a cut in magnitude $G > 19.5$ for both the SMC and MW samples and, therefore, the total number of stars is reduced.

with the one of a uniform sky field observed nearby, but away from the SMC center; the observed overdensity gives an estimation of the "excess" of SMC stars. From this comparison, the percentage of SMC stars in the MW sample is estimated

to be around 5–10%, the MW optimal sample being the less contaminated one.

We also notice that the astrometric parameter dispersion decreases from the NN complete to the NN truncated-optimal samples. This is to be expected given that the samples' distance and velocities are more similar due to the stricter sequence of selection criteria.

In Fig. 5, we compare the astrometry and photometry distribution of the different SMC samples. In the proper motion selection sample, the distribution of proper motion is observed to be narrow around the bulk motion of the SMC due to the severe cut in proper motion enforced; however, in the MW classification, two minor peaks are evident after the SMC. The NN samples do not reveal this misclassification. We observe a secondary peak in the right ascension proper motion around 5.2 mas yr^{-1}, which corresponds to the systemic motion of Tuc 47 (Gaia Collaboration 2018). The truncated-optimal sample has the narrowest parallax distribution among the four LMC samples, which are all quite similar to one another. The G-magnitude distributions in the four SMC selections vary significantly from one another. Both the PM and the NN samples have a G-magnitude peak at $G \sim 19$ mag, which is related to the SMC stars, and a secondary peak at the limiting magnitude $G = 20.5$ mag, which corresponds to the MW contamination. Due to this, we define the truncated-optimal sample by subtracting the secondary peak from the optimal sample, as mentioned above. This secondary peak is caused by the exponential distribution in G of the MW stars, arising from the logarithmic relation between the stellar flux and the apparent magnitude combined with the magnitude cut and the spatial distribution of the stars in the disk. The SMC stars, on the other hand, exhibit a significant peak at $G \simeq 19$ mag, slightly differing between samples depending on the amount of MW misclassified sources.

All SMC samples have a fairly similar CMD. Only minor variations are visible in the MW selection of the optimal and truncated-optimal samples, which comprise, as expected, sources of the red giant branch of the SMC that the NN classifier misidentifies as MW.

4. External validation of the classification

In order to validate the results of our selection criteria we compare each of the generated samples with external independent classifications. To do so, we cross-matched our samples with dedicated catalogues of the SMC chosen to have a high degree of purity in the visible band. For this reason, we exclude from this exercise the VMC survey (Cioni et al. 2011) for being in the near-infrared and the SMASH survey (Nidever et al. 2017) for not performing any contamination study, and we use the following:

– SMC Cepheids (Ripepi et al. 2017): we used the 4793 Cepheids from the paper's sample as a set of highly reliable SMC objects. Using a 0.3″ search radius to find high

Table 2. Matches of the classified SMC members in our four considered samples against the validation samples.

Stars classified as SMC	SMC Cepheids (4765)	SMC RR-Lyrae (2922)	SMC StarHorse (193 402)	MW StarHorse (806 664)
Proper motion selection	4578 (96.1%)	2447 (83.7%)	190 166 (98.3%)	114 354 (14.2%)
NN complete	4688 (98.4%)	2814 (96.3%)	191 692 (99.1%)	125 200 (15.5%)
NN optimal	4599 (96.5%)	2694 (92.2%)	186 063 (96.2%)	110 704 (13.7%)
NN truncated-optimal	4598 (96.5%)	821 (28.1%)	186 063 (96.2%)	110 704 (13.7%)

Notes. The total number of stars, which is listed beneath the sample name, is used to determine percentages.
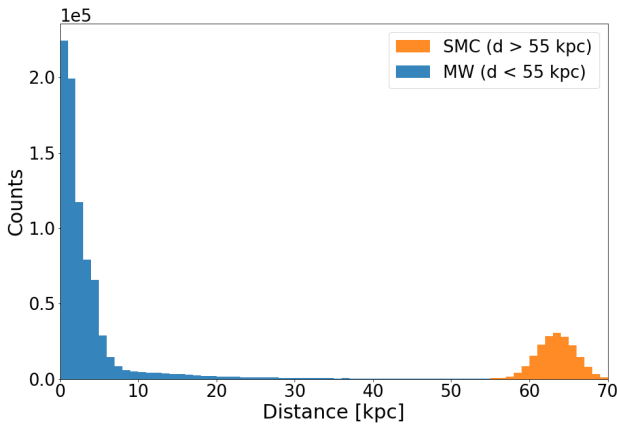

Fig. 7. StarHorse validation sample distance distribution. In blue (orange), the StarHorse stars classified as MW (SMC) according to the $d = 55$ kpc criteria.

Fig. 8. Evaluation metrics for NN classifier performance using the StarHorse sample. Left: ROC curve. Black dot is in the "elbow" of the ROC curve and it shows the best balance between completeness and purity. Right: precision–recall curve. In both cases, we compare our model (orange solid curve) with a classifier that has no class separation capacity (blue dashed curve).

confidence matches and keeping 4788 stars, we cross-matched the positions supplied in the study with the *Gaia* DR3 catalogue to obtain the *Gaia* DR3 data. To make a final selection of 4765 SMC Cepheids, we introduced a cut with a 10° radius around the SMC center (replicating our base sample).

– SMC RR-Lyrae (Muraveva et al. 2018): we employed the 2997 RR-Lyrae sample from the paper as high-reliability SMC objects in a manner similar to the foregoing. After the sample is cross-matched with the *Gaia* DR3 catalog, it is downsized to 2982 stars, and then we cut a final sample of 2922 SMC RR-Lyrae in a 10° radius around the SMC center.

– StarHorse (Anders et al. 2022): using a cut of 10° around the SMC center, we cross-matched this catalog with the *Gaia* DR3 data and obtained a sample of 1 000 066 stars. We distinguished MW and SMC stars using the StarHorse distances, but with a cutoff of $d = 55$ kpc, using criteria similar to those put forward in Schmidt et al. (2020, 2022) for the LMC. This choice is supported by the StarHorse sample's distance distribution, which is depicted in Fig. 7. A very stringent categorization is produced by a cut in $d = 55$ kpc, reducing the pollution of MW stars (see discussion below). As a result, we are left with a StarHorse SMC sample of 193 402 stars and a StarHorse MW sample of 806 660 stars. We note that this sample only has stars up to $G = 18.5$.

The Cepheids and RR-Lyrae datasets contain objects that are highly reliably identified as SMC stars; therefore, they are used to assess how complete our classification of SMC objects is (i.e., how many we lose). On the other hand, because the StarHorse classification is imperfect, this sample can be used to estimate
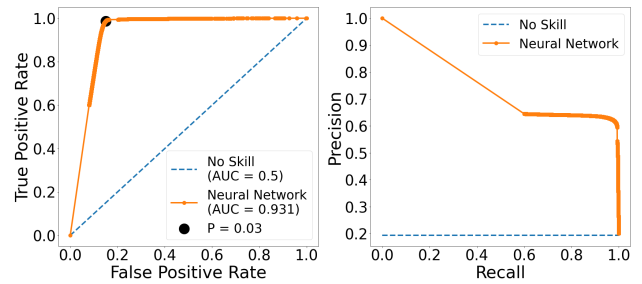
the contamination brought on by incorrectly identified MW stars. Furthermore, the estimated amount of MW contamination in the classification will be a "worst case" scenario because of the extremely strict criteria utilized in StarHorse for the separation (cut in $d = 55$ kpc).

Table 2 compares the outcomes of our four classification criteria as they were applied to the stars in the three validation samples. The results using the Cepheids, RR-Lyrae, and StarHorse SMC validation samples reveal that the completeness of the resulting SMC classifications is excellent, typically exceeding 95%. The truncated-optimal sample is the exception, where the cut in faint stars reduces the RR-Lyrae's completeness.

On the other hand, the relative contamination by MW stars is more challenging to evaluate in the samples. We rely on an external comparison, the StarHorse distance-based classification, with the caveat that this classification also includes its own classification errors. In order to do this, we recalculate the precision-recall curve using the StarHorse classification as a reference this time; the outcome is depicted in Fig. 8. We can observe that the precision essentially stays flat across the plot's entire range, or across the entire range of probability threshold values. This suggests that the complete and optimal samples both have identical relative contamination since the more restrictive we are, the more MW stars we remove, but we also lose more SMC stars. According to the precision values in Fig. 8, using the classification based on StarHorse distances as a reference, the relative contamination of our samples could be around 40%; this is a worst-case scenario, because we used a very restrictive distance cut. These statistics need to be interpreted carefully because the MW-SMC separation based on StarHorse distances is not a perfect classification criterion and actually uses less data than our criterion. Although many stars still have intermediate
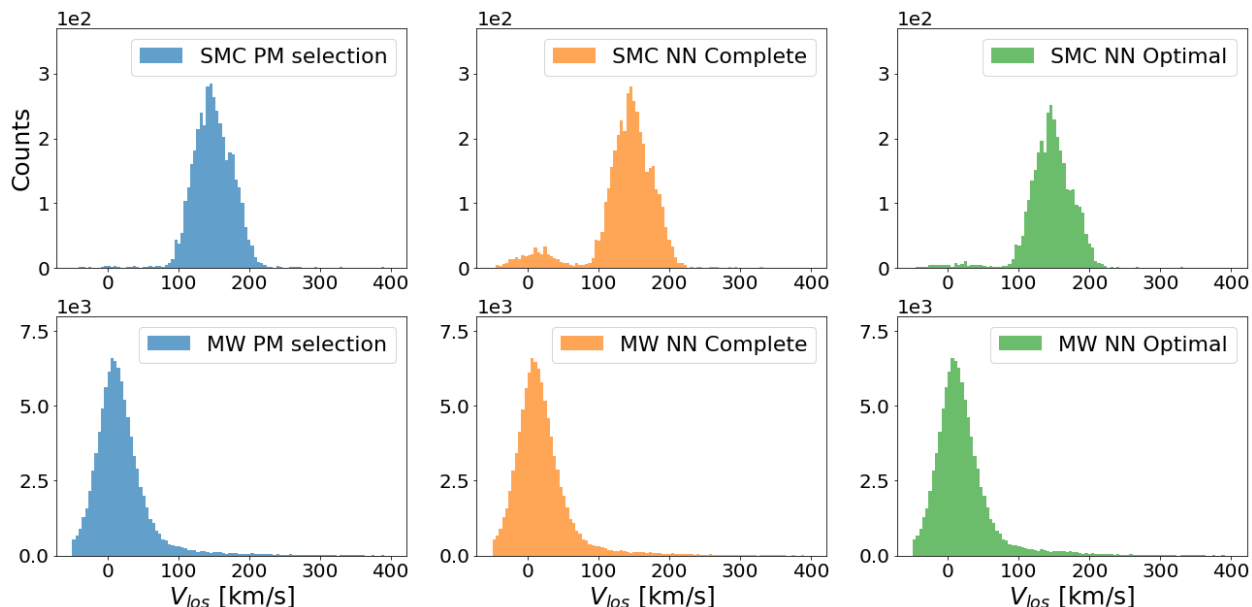
Fig. 9. Line-of-sight velocity distribution for stars classified as SMC (top) and MW (bottom). We show the three V_{los} subsamples of the PM selection (left), NN complete (middle), and NN optimal (right) samples.

distances that fall between the Magellanic Clouds and the MW as a result of the multimodal posterior distance distributions, these populations are plainly evident as overdensities in the maps as mentioned in the StarHorse publication (Anders et al. 2022).

These findings indicate that there may be a few tens of percent of MW stars in our samples, but we can further investigate using the line-of-sight velocities in *Gaia* DR3, which are only available for a (small) subset of the full sample. These line-of-sight velocities have distinct mean values for the MW and SMC, are not used by any of our classification criteria, and, therefore, provide an independent check. The contamination of the SMC sample is evident from the histograms of line-of-sight velocities plotted separately for MW and SMC stars in Fig. 9. This contamination is most likely far lower than the values mentioned above. For instance, we estimate the MW contamination to be around 10% if we take into account the SMC NN complete sample and (roughly) separate the MW stars with a cut at $V_{los} < 75\,\mathrm{km\,s^{-1}}$. Also, this check is not entirely representative since only stars at the bright end of the sample ($G \lesssim 16$) are included in the subset of *Gaia* DR3 stars with observed line-of-sight velocities.

Finally, we made a new query to the *Gaia* archive similar to the one described in Sect. 2.1. This time, we select all the sources within a $10°$ radius in a nearby area with uniform sky density from the *Gaia* DR3 database. By doing so, we may estimate the number of MW stars that should be present in locations that our *Gaia* base sample covers. We found 932 332 stars from this new query, so we may anticipate a comparable number of MW stars in the area we chose to surround the SMC. Given that the *Gaia* base sample contains 4 047 225 objects and the number of objects classified as SMC (Table 1) is around 1–2 million, the number of stars classified as MW is around 3–2 million; therefore, we can conclude that our NN SMC samples prioritise purity over completeness since there are too many stars classified as MW (an excess of 1–2 million). This is also clear from the right panels of Fig. 6, where the pattern of SMC contamination is displayed in the distribution of stars classified as MW.

5. Conclusions

In this work, we present a new SMC/MW classification method that is compared with previous selection strategies based on the proper motion. It is based on NNs and trained using a MW+SMC simulation created by GOG. We created two SMC samples using various probability cuts, P_{cut}, the NN complete, with $P_{cut} = 0.01$, and the NN optimal sample, with $P_{cut} = 0.31$, which corresponds to the best value according to the ROC curve. In order to remove any remaining contamination from incorrectly categorised faint stars, we added an additional cut to this final sample at the apparent G-magnitude of $G < 19.5$ mag, creating the NN truncated-optimal sample. Moreover, we created sub-samples that contain both proper motions and line-of-sight velocities by using the recently released spectroscopic line-of-sight velocities provided in *Gaia* DR3. Finally, we successfully validated our classifier using external and independent classifications: SMC Cepheids, SMC RR Lyrae, and SMC/MW StarHorse stars. In general, the estimated contamination of MW stars in each of the SMC samples is about 10–40%, the "best case" being for the bright stars ($G < 16$), which belong to the V_{los} subsamples, and the "worst case" being for the full SMC sample determined by the very stringent criteria used for the separation in the StarHorse validation sample. A further check based on the comparison with a nearby area with uniform sky density indicates that the global contamination in our samples is probably close to the low end of the range, around 10%.

References

Anders, F., Khalatyan, A., Queiroz, A. B. A., et al. 2022, A&A, 658, A91
Cioni, M. R. L., Habing, H. J., & Israel, F. P. 2000a, A&A, 358, A9
Cioni, M. R. L., van der Marel, R. P., Loup, C., & Habing, H. J. 2000b, A&A, 359, 601
Cioni, M. R. L., Clementini, G., Girardi, L., et al. 2011, A&A, 527, A116
Gaia Collaboration (Helmi, A., et al.) 2018, A&A, 616, A12
Gaia Collaboration (Brown, A. G. A., et al.) 2021a, A&A, 649, A1
Gaia Collaboration (Luri, X., et al.) 2021b, A&A, 649, A7
Jiménez-Arranz, Ó., Romero-Gómez, M., Luri, X., et al. 2023, A&A, 669, A91
Lindegren, L., Klioner, S. A., Hernández, J., et al. 2021, A&A, 649, A2
Luri, X., Palmer, M., Arenou, F., et al. 2014, A&A, 566, A119
Muraveva, T., Subramanian, S., Clementini, G., et al. 2018, MNRAS, 473, 3131
Nidever, D. L., Olsen, K., Walker, A. R., et al. 2017, AJ, 154, 199
Pedregosa, F., Varoquaux, G., Gramfort, A., et al. 2011, J. Mach. Learn. Res., 12, 2825
Ripepi, V., Cioni, M.-R. L., Moretti, M. I., et al. 2017, MNRAS, 472, 808
Schmidt, T., Cioni, M.-R. L., Niederhofer, F., et al. 2020, A&A, 641, A134
Schmidt, T., Cioni, M.-R. L., Niederhofer, F., et al. 2022, A&A, 663, A107

4

THE BAR PATTERN SPEED OF THE LARGE MAGELLANIC CLOUD

This Chapter contains the accepted version (on 22 December 2023) of Jiménez-Arranz et al. (2023c). DOI: 10.1051/0004-6361/202347266.

The work presented here makes use of the Large Magellanic Cloud (LMC) in-plane velocity maps obtained in Chapter 2. We aim to determine the LMC bar pattern speed using the astrometric and spectroscopic data from the *Gaia* mission.

The LMC bar pattern speed is determined using three different methods: *i)* the Tremaine-Weinberg (TW) method, which is applied to both line-of-sight and in-plane velocities, *ii)* the Dehnen method, which is applied to in-plane velocities, and *iii)* the bisymmetric velocity (BV) model of the tangential velocity that determines the bar pattern speed by inferring the corotation radius.

Due to a significant dependence on the orientation of the galaxy frame and the viewing angle of the bar perturbation, the TW method infers a wide diversity of pattern speed values in both the line-of-sight and planar versions. The Dehnen method works well with numerical simulations and is invariant to the frame orientation. It is able to recover pattern speeds from isolated and interacting galaxy simulations with little uncertainty. When applied to the LMC data, it results in a bar pattern speed of $\Omega_p = -1.0 \pm 0.5$ km s^{-1} kpc^{-1}, which translates to a bar that barely rotates, possibly slightly counter-rotating with respect to the LMC disc. The LMC bar corotation radius is recovered by the BV method to be $R_c = 4.20 \pm 0.25$ kpc, which corresponds to a pattern speed of $\Omega_p = 18.5^{+1.2}_{-1.1}$ km s^{-1} kpc^{-1}.

We discard the pattern speeds found with the TW method, because no obvious privileged value is obtained, owing to strong variations with the frame orientation. The pattern speed obtained using the Dehnen method has implications that are difficult to reconcile with the kinematics and structure of the LMC disc because it corresponds to a non-rotating bar. The BV method result is consistent with previous estimates and gives a bar corotation-to-length ratio of 1.8 ± 0.1, suggesting that the LMC is hosting a slow bar.

The bar pattern speed of the Large Magellanic Cloud

Ó. Jiménez-Arranz[1, 2, 3], L. Chemin[4], M. Romero-Gómez[1, 2, 3], X. Luri[1, 2, 3],

P. Adamczyk[5], A. Castro-Ginard[6], S. Roca-Fàbrega[7, 8], P. J. McMillan[7], and M.-R. L. Cioni[9]

[1] Departament de Física Quàntica i Astrofísica (FQA), Universitat de Barcelona (UB), C Martí i Franquès, 1, 08028 Barcelona, Spain
[2] Institut de Ciències del Cosmos (ICCUB), Universitat de Barcelona, Martí i Franquès 1, 08028 Barcelona, Spain
[3] Institut d'Estudis Espacials de Catalunya (IEEC), C Gran Capità, 2-4, 08034 Barcelona, Spain
[4] Instituto de Astrofísica, Universidad Andres Bello, Fernandez Concha 700, Las Condes, Santiago RM, Chile
[5] Centro de Astronomía - CITEVA, Universidad de Antofagasta, Avenida Angamos 601, Antofagasta 1270300, Chile
[6] Leiden Observatory, Leiden University, Niels Bohrweg 2, 2333 CA Leiden, The Netherlands
[7] Lund Observatory, Division of Astrophysics, Department of Physics, Lund University, Box 43, SE-221 00 Lund, Sweden
[8] Departamento de Física de la Tierra y Astrofísica, UCM, and IPARCOS, Facultad de Ciencias Físicas, Plaza Ciencias, 1, Madrid, E-28040, Spain
[9] Leibniz-Institut für Astrophysik Potsdam, An der Sternwarte 16, D-14482 Potsdam, Germany

ABSTRACT

Context. The Large Magellanic Cloud (LMC) internal kinematics have been studied in unprecedented depth thanks to the excellent quality of the *Gaia* mission data, revealing the disc's non-axisymmetric structure.
Aims. We want to constrain the LMC bar pattern speed using the astrometric and spectroscopic data from the *Gaia* mission.
Methods. We apply three methods to evaluate the bar pattern speed: it is measured through the Tremaine-Weinberg (TW) method, the Dehnen method and a bisymmetric velocity (BV) model. The methods provide additional information on the bar properties such as the corotation radius and the bar length and strength. The validity of the methods is tested with numerical simulations.
Results. A wide range of pattern speeds are inferred by the TW method, owing to a strong dependency on the orientation of the galaxy frame and the viewing angle of the bar perturbation. The simulated bar pattern speeds (corotation radii, respectively) are well recovered by the Dehnen method (BV model). Applied to the LMC data, the Dehnen method finds a pattern speed $\Omega_p = -1.0 \pm 0.5$ km s^{-1} kpc^{-1}, thus corresponding to a bar which barely rotates, slightly counter-rotating with respect to the LMC disc. The BV method finds a LMC bar corotation radius of $R_c = 4.20 \pm 0.25$ kpc, corresponding to a pattern speed $\Omega_p = 18.5^{+1.2}_{-1.1}$ km s^{-1} kpc^{-1}.
Conclusions. It is not possible to decide which global value best represents an LMC bar pattern speed with the TW method, due to the strong variation with the orientation of the reference frame. The non-rotating bar from the Dehnen method would be at odds with the structure and kinematics of the LMC disc. The BV method result is consistent with previous estimates and gives a bar corotation-to-length ratio of 1.8 ± 0.1, which makes the LMC hosting a slow bar.

Key words. Galaxies: kinematics and dynamics - Magellanic Clouds - Astrometry

1. Introduction

The angular speed of stellar bars is a fundamental parameter in dynamics of galaxies from which the principal bar-disc resonances can be identified, and the structure of stellar orbits can be studied in a given gravitational potential (e.g. Contopoulos & Grosbol 1989; Binney & Tremaine 2008). Furthermore, the bar pattern speed is thought to reflect certain properties of the halo density at low radius because bars and haloes of stars and/or dark matter are believed to continuously interact during galaxy evolution through dynamical friction. Numerical models and observations suggest that the bar speed is slower when the inner halo is denser (Debattista & Sellwood 2000; Buttitta et al. 2023). The pattern speed of simulated bars is also seen to slow down with the secular evolution, as opposed to its growing length and strength (Sellwood 2014).

The importance of measuring bar pattern speeds in the dynamics and evolution of galaxies has thus grown significantly with the emergence of large-scale long-slit and 3D spectroscopic surveys, which have enabled the estimations of a few hundreds

of pattern speeds (Cuomo et al. 2019; Guo et al. 2019; Géron et al. 2023, and references therein). These works found that most stellar bars are fast, i.e. bars show a ratio of corotation-to-bar radius smaller than 1.4 (following Athanassoula 1992), and that high angular speeds are for small and weak bars, and within faint galaxies (Cuomo et al. 2020). However, the large occurrence of fast bars is a critical issue for the simulations made in a cosmological context, as the inner density of simulated dark matter halos is so cuspy that the parent discs should host mostly slow bars. This discrepancy suggests a failure in cosmological simulations (Roshan et al. 2021), or, perhaps, a bias in estimating pattern speeds of bars from observations (Fragkoudi et al. 2021). This highlights the difficult part of measuring pattern speeds from observation since it represents a single time instant in the entire evolution of galaxies.

Bar pattern speeds from these studies have been inferred exclusively by means of the Tremaine-Weinberg method (Tremaine & Weinberg 1984, hereafter TW). Its direct application makes use of integrals of kinematics and positions of a tracer that should obey the continuity equation, like stars. Alternatively, Dehnen

et al. (2023) proposed a new method for determining bar pattern speeds in numerical simulations using a single time snapshot. This involves measuring the Fourier amplitudes of particle positions and velocities within the bar region. In another work, Gaia Collaboration et al. (2023) proposed an indirect measurement of the bar angular speed by fitting a bisymmetric model to the tangential velocities to get the bar phase angle and corotation radius. Unfortunately, these last two methods have limited applicability due to their reliance on the availability of objects with individually measured planar (tangential and radial) velocities, which are rare. Only the Milky Way (MW) and the Large Magellanic Cloud (LMC) offer this possibility. To our knowledge, the Dehnen et al. (2023) formalism has never been applied to observations, while the method in Gaia Collaboration et al. (2023) estimated the bar corotation, orientation and pattern speed for the MW, using data from the *Gaia* mission (Gaia Collaboration et al. 2016, 2021a). Interestingly, they found a Galactic bar speed consistent with the value inferred with the TW method (Bovy et al. 2019).

Our objective in this study is to determine the pattern speed and corotation region of the stellar bar in the LMC. The LMC is a dwarf spiral (or irregular) galaxy and one of the closest and brightest satellites of the MW, in interaction with the Small Magellanic Cloud (SMC) and the MW. It could thus be a challenge to study the properties of a system like the LMC, because of its structure and velocity field impacted by the interaction, at least in the outermost regions (e.g. Belokurov & Erkal 2019; Gaia Collaboration et al. 2021b). It is however a unique object of its kind for testing the three aforementioned methods due to the availability of different kinds of kinematic data for the entire disc. To achieve the objective, we are taking advantage of the opportunity to use both astrometric and spectroscopic data from the *Gaia* mission. First, the TW method can be applied to line-of-sight (l.-o.-s.) velocities of thousands of LMC stars, as measured by the *Gaia* Radial Velocity Spectrometer (Katz et al. 2022; Jiménez-Arranz et al. 2023), yielding *a single value* of the LMC bar pattern speed, similarly to other galaxies. Second, the *Gaia* astrometric data allow us to estimate the two components of the velocity tensor for millions of stars in the LMC plane (Gaia Collaboration et al. 2021b). Unlike the l.-o.-s. velocities given in the sky frame, these two components make it possible to apply the Dehnen method, the bisymmetric model, as well as a modified version of the TW method, adapted to the disc plane. In this latter case, *multiple values* of the LMC bar pattern speeds can be inferred, corresponding to multiple orientations of the Cartesian frame of the LMC plane, thus multiple viewing angles of the bar in the disc reference frame. This allows us to compare various estimates of the bar pattern speed, and assess the validity of the methods.

The paper is organised as follows. In Section 2, we describe the methods used to measure the bar pattern speed. In Section 3, we validate the methods using two N-body simulations, one representing an isolated disc and the other an interacting disc. In Section 4, we apply the three methods to the LMC sample (Jiménez-Arranz et al. 2023), to try to determine the pattern speed of the LMC bar. In Section 5, we discuss the implications of our findings for our understanding of the LMC and barred spiral galaxies in general. Finally, in Section 6, we summarise the main conclusions of this work.

2. Methods

In this section, we describe the three methods applied to the *Gaia* data to infer the bar pattern speed of the LMC. The first is the Dehnen method (Sect. 2.1), which can be applied to astrometric

data. Secondly, we describe the Tremaine-Weinberg method (TW, Sect. 2.2), which can be applied to astrometric or spectroscopic data. Finally, we describe the bisymmetric velocity method (BV, Sect. 2.3), which can only be applied to astrometric data.

In the Cartesian frame of the galaxy, the methods assume that the disc is in equilibrium (which may not be fully the case for the LMC), rotation is done around the *z*-axis, the kinematic center is located at the origin of the Cartesian coordinate frame, and the density is stationary in the frame rotating at Ω_p. Furthermore, it is also assumed that the region where Ω_p is constrained should only contain the bar, that is well distinguishable from other structures in the galaxy, such as spiral arms. It is worth mentioning that other density perturbations may exist in the region where the bar influences the stellar dynamics, and thus could impact the estimation of the bar Ω_p.

2.1. The Dehnen method

The first method we use in this work is that of Dehnen et al. (2023). We use the version of the code made publicly available with the paper. Here we summarise some of the main aspects of the method.

Dehnen et al. (2023) developed an unbiased, precise, and consistent method that simultaneously measures Ω_p and the orientation angle ϕ_b of the bar from single snapshots of simulated barred galaxies. These parameters are found assuming that the continuity equation applies:

$$\frac{\partial \Sigma v_x}{\partial x} + \frac{\partial \Sigma v_y}{\partial y} + \frac{\partial \Sigma}{\partial t} = 0 \tag{1}$$

where v_x and v_y are the disc's velocity components in Cartesian coordinates (x, y), where $\Sigma = \Sigma(x, y, t) = \Sigma(R, \phi - \Omega_p t)$ is the disc surface density, (R, ϕ) the corresponding cylindrical coordinates, and Ω_p is the angular speed of the rotating frame of the bar perturbation, considered invariant with time. The method assumes that the centre of rotation is known, that the rotation is around the z-axis and that the density is stationary in the rotating frame. With these assumptions, $\partial \Sigma / \partial t = -\Omega_p \partial \Sigma / \partial \phi$ and Eq. 1 becomes :

$$\Omega_p \frac{\partial \Sigma}{\partial \phi} = \frac{\partial \Sigma v_x}{\partial x} + \frac{\partial \Sigma v_y}{\partial y} . \tag{2}$$

This expression is the traditionally used in the TW method (see Section 2.2 below). Here we use the Fourier method, as implemented in the public code, which consists of multiplying Eq. 2 by the weight function $w(x) = W(R)e^{-im\phi}$, where m is the azimuthal wave number and $W(R)$ a smooth window function (see their Eq. 25), and integrating over all space. The smooth window function is necessary to avoid issues at the edges of radial bins. The resulting expression for the pattern speed of an N-body model is the real value form (see details in their Appendix A) of the following equation:

$$\Omega_p + \frac{i}{m} \frac{\dot{\Sigma}_m}{\Sigma_m} = \frac{\Sigma_i \mu_i \left[\dot{\phi}_i W_i + \frac{i}{m} \dot{R}_i (\partial W / \partial R)_i \right] e^{-im\phi_i}}{\Sigma_i \mu_i W_i e^{-im\phi_i}}, \tag{3}$$

where μ_i are the individual particle masses.

In fact, the method is divided in two steps. First, it defines which particles belong to the bar region, $[R_0, R_1]$, defined as a continuous range of radial bins with large amplitude of the bisymmetric density perturbation of second order, and having a roughly constant phase angle (see their Appendix B for details). Hereafter we will refer to R_1 as the bar radius or length, as it

agrees well with the definition of best estimates for bar lengths in numerical simulations (Ghosh & Di Matteo 2023). And second, once the bar region is determined, it computes the bar pattern speed and the bar phase angle together with their uncertainties using the covariance matrix of the real part of Eq. 3 with $m = 2$, this is their Eq. A4.

Dehnen et al. (2023) applied their method to a suite of N-body models of isolated barred spiral galaxies. By comparing the results to Ω_p calculated using time-centred finite-differences from three consecutive snapshots, they found that their method is reliable and accurate, provided that the bar region is well-determined and a smooth window function is utilised.

2.2. The Tremaine-Weinberg method

The second method we use is the Tremaine-Weinberg (TW) method (Tremaine & Weinberg 1984). As mentioned above, the main assumption of the method developed is that the density and kinematics of the tracer obey the continuity equation (Eq. 1). The method is designed for galactic systems in equilibrium and with a single pattern (see its application to a simulated disc with a bar perturbation in App. A). The best kinematic tracer satisfying this condition is the old stellar population of galaxies. Estimates of Ω_p of galaxies using the TW method were thus mostly obtained from absorption lines of stellar populations, as observed by means of optical long-slit or integral field spectroscopy (e.g. Merrifield & Kuijken 1995; Gerssen et al. 1999; Aguerri et al. 2003; Debattista & Williams 2004; Aguerri et al. 2015; Cuomo et al. 2019), although emission lines of interstellar gas for a few galaxies were used as well (e.g. Bureau et al. 1999; Hernandez et al. 2005; Rand & Wallin 2004; Meidt et al. 2008; Chemin & Hernandez 2009; Williams et al. 2021).

As shown in Gaia Collaboration et al. (2021b) and Jiménez-Arranz et al. (2023), we can select millions of stars in the LMC disc with proper motions, from which the in-plane components v_x and v_y can be measured. Therefore, Eq. 2 can be solved directly for the LMC, unlike any other galaxies. Integrating it with respect to x yields:

$$\Omega_p = \frac{\langle v_y \rangle}{\langle x \rangle}, \quad \text{where } \langle v_y \rangle = \frac{\int_{-\infty}^{+\infty} v_y(x,y)\Sigma(x,y)dx}{\int_{-\infty}^{+\infty} \Sigma(x,y)dx},$$
$$\langle x \rangle = \frac{\int_{-\infty}^{+\infty} x\Sigma(x,y)dx}{\int_{-\infty}^{+\infty} \Sigma(x,y)dx}. \quad (4)$$

These integrals can be numerically solved by discretising the space, i.e., by summing the surface density and kinematics along x−wedges at different y positions (hereafter, pseudo-slit). Then, the pattern speed Ω_p can be determined by doing a linear fit of $\langle v_y \rangle$ vs $\langle x \rangle$. Interestingly, a permutation of x and y can be done in Eq. 4, so that Ω_p can also be estimated from $\langle v_x \rangle$ vs $\langle y \rangle$. To keep the analysis simple, we defer to another study the test of this alternative derivation.

The continuity assumption is independent on the choice of the Cartesian frame. This implies that we can choose arbitrarily the orientation of the reference $x - y$ plane by rotating it around the z−axis, and measure the TW integrals of Eq. 4 at various orientations. Only astrometric data can make such analysis possible, unlike spectroscopic data. This is thus a good opportunity for us to assess for the first time the effect of the viewing angle of the bar in the disc plane on the TW integrals of Eq. 4 (Sect. 3), and on the LMC bar pattern speed (Sect. 4).

To get an unbiased value of the bar angular speed, we must restrict the linear regression by selecting exclusively the integrals

from the bar region. This is defined as the points located out to the radius R_1 obtained with the Dehnen method (Sect. 2.1), and the best fit of the pattern speed Ω_p arises from selecting the integrals with $(\langle x \rangle^2 + y^2)^{1/2} < R_1$, thus avoiding the outer disc that mostly traces the spiral structure, which is expected to show a lower angular speed from the bar (see e.g. Merrifield et al. 2006, with the example of the grand design spiral NGC 1068).

Additionally, the LMC is the only galaxy for which both transverse and l.-o.-s. kinematics are available. Because of such a lack of galaxies having observed planar kinematics, Tremaine & Weinberg (1984) have historically adapted Eq. 4 to work with sky plane coordinates $(X, Y) = (x, y\cos i)$ and the l.-o.-s. velocity $V_{\text{los}} = v_y \sin i + v_z \cos i$, where i is the galaxy inclination, leading to:

$$\Omega_p \sin i = \frac{\langle V_{\text{los}} \rangle}{\langle X \rangle}, \quad \text{where } \langle V_{\text{los}} \rangle = \frac{\int_{-\infty}^{+\infty} V_{\text{los}}(X,Y)\Sigma(X,Y)dX}{\int_{-\infty}^{+\infty} \Sigma(X,Y)dX},$$
$$\langle X \rangle = \frac{\int_{-\infty}^{+\infty} X\Sigma(X,Y)dX}{\int_{-\infty}^{+\infty} \Sigma(X,Y)dX}. \quad (5)$$

with $\langle V_{\text{los}} \rangle$ and $\langle X \rangle$ being the intensity-weighted means of the l.-o.-s. velocity and position of the tracer, respectively. These integrals can numerically be solved by discretising the space, selecting the disc areas parallel to the disc major axis, yielding a value of $\langle X \rangle$ and $\langle V_{\text{los}} \rangle$ for each Y. Unlike the previous case, we cannot vary the orientation of the reference frame here because the l.-o.-s. kinematics is firmly attached to the unique position angle of line of nodes (disc major axis). Then, $\Omega_p \sin i$ is the result of the linear fit of $\langle V_{\text{los}} \rangle$ vs $\langle X \rangle$. Similarly to the planar velocities, only $\langle X \rangle$ and $\langle V_{\text{los}} \rangle$ from the bar region must be considered, thus by selecting the TW points inside the sky region where R_1 is projected.

For clarity, we hereafter refer to the version of the TW method involving the planar velocities as the In-Plane TW method (IPTW, Eq. 4), and the one using V_{los} data as the l.-o.-s. TW method (LTW, Eq. 5).

2.3. Bisymmetric model of the tangential velocity

In Gaia Collaboration et al. (2023), indirect measurements of the pattern speed Ω_p were performed by searching for the corotation radius R_c within a simulated barred galaxy. Here, a second order asymmetry of the tangential velocity field V_ϕ was fitted. Variations at low radius of the phase angle $\phi_{2,\text{kin}}$ of the bisymmetry were then studied to locate R_c. Ignoring the first order perturbation (lopsidedness), the Fourier decomposition $V_{\phi,\text{mod}}$ is given by:

$$V_{\phi,\text{mod}}(R,\phi) = V_0(R) + V_2(R)\cos(2(\phi - \phi_{2,\text{kin}}(R))), \quad (6)$$

where V_0 and V_2, which only depend on the galactocentric radius R, are the rotation curve of the disc and the amplitude of the bisymmetric perturbation, respectively. Despite its empirical nature, this method is based on the principle that the bar pattern heavily influences, if not entirely governs, the structure of stellar orbits and the velocity field within R_c. In the ideal case of only a barred perturbation, with no spiral arms, the periodic orbits inside corotation, called the x_1 family, are elongated with the bisymmetric perturbation (they are the back-bone of bars), while beyond corotation, the orbits are elongated perpendicularly to the bar major axis (Contopoulos & Papayannopoulos 1980; Contopoulos & Grosbol 1989). Inside corotation, the tangential velocity is

maximum (minimum) perpendicularly to (along) the direction of elongation of the orbits, and the opposite outside corotation. We thus expect $\phi_{2,\text{kin}}$ roughly constant within the bar, then changing significantly its orientation near corotation, by an angle of $\sim 90°$. This variation can be even larger in presence of a winding spiral structure beyond corotation which perturbs the orbits and kinematics as well. Furthermore, the possible existence of other resonances before corotation, like the ultra-harmonic one (Buta & Combes 1996), and the development of spiral arms before or near the bar ends complicate the shapes, orientations and kinematics of periodic orbits inside corotation. In these cases, we can also expect a variation of $\phi_{2,\text{kin}}$ between the bar ends and the corotation radius. Once R_c is determined near the location where $\phi_{2,\text{kin}}$ changes significantly, we can infer Ω_p with the angular velocity curve, $\Omega(R) = V_0/R$, since stars move at the same speed as the bar at R_c, thus $\Omega_p = \Omega(R_c)$. One should note that the harmonic decomposition is reminiscent of the bisymmetric flow model applied to l.-o.-s. kinematics of barred spirals (Spekkens & Sellwood 2007).

Gaia Collaboration et al. (2023) applied their recipe to data from the Third Data Release of *Gaia* (DR3, Gaia Collaboration et al. 2021a, 2022). They evidenced a region of steep change of phase angle of the kinematic bisymmetry of $\sim 70°$ over a range of 2 kpc. A comparison with a test-particle simulation in which the *Gaia* errors model was propagated made them find the MW corotation at the radius where $\phi_{2,\text{kin}}$ is minimum, just after the location of the sharp transition of phase angle mentioned above. Gaia Collaboration et al. (2023) estimated a Galactic bar orientation with respect to the Galactic Center-Sun direction of $\sim 20°$, the Galactic bar corotation at $R \sim 5.4$ kpc, and a pattern speed of ~ 38 km s^{-1} kpc^{-1}, in good agreement with previous measurements involving a modified version of the TW method (Bovy et al. 2019).

3. Testing the methods with simulations

In this section we use a snapshot of a simulation of a MW-mass galaxy, with no external perturbations, and a snapshot of a simulation of a LMC-like system interacting with a SMC-mass and MW-like systems to apply and validate the Dehnen method, the two variations of the TW method, and the BV model.

First, we use the B5 N-body simulation of an isolated barred galaxy from Roca-Fàbrega et al. (2013), which consists of a live disc of 5 million particles and a Toomre parameter of $Q = 1.2$, and a live NFW halo. The disc to halo mass ratio is the appropriate so that the simulation develops a strong bar and two spiral arms which are transient in time. The snapshot we use has a counter-clockwise rotating bar with a pattern speed of $\Omega_p = 21.5 \pm 0.1$ km s^{-1} kpc^{-1} determined as the average of finite-differences on the rate of change of the phase angle of the bar major axis in three consecutive snapshots over the radial range of the bar. The quoted uncertainty on the bar pattern speed refers to the standard deviation of the pattern speeds derived from the three successive snapshots. The simulation time step is 16 Myr, representing 6% of the bar period, which is appropriate to infer a robust bar pattern speed. The pattern speed places the bar corotation resonance at $R_c = 8.3 \pm 0.05$ kpc, computed as the radius at which the angular frequency curve, $\Omega(R) = V_0/R$, of the particles is equal to the bar pattern speed, with V_0 given by the bisymmetric model (see Eq. 6). It corresponds to a fast bar with a rotation rate of $R_c/R_1 = 1.1^{+0.01}_{-0.01}$.

Second, we use one simulation of the KRATOS (Kinematic Reconstruction of the mAgellanic sysTem within the OCRE Scenario) suite, a comprehensive suite of 12 sets of pure N-body

simulations of isolated or single-interacting galaxies, for a total of 30 models (Jiménez-Arranz et al., in preparation). The simulation we use in this paper models both an LMC-like and an SMC-mass system in the presence of a MW-mass system. We model the LMC-like system as a stellar exponential disc of 1.2M stars embedded in a live dark matter NFW halo. We consider a disc and DM halo with a mass of $5 \times 10^9 M_\odot$ and $1.8 \times 10^{11} M_\odot$, respectively, in agreement with observations as discussed in Lucchini et al. (2022, and references therein). The disc's Toomre Q parameter is 1.0, i.e. slightly gravitationally unstable. The SMC-mass system is modelled as a simple NFW halo. Both dark matter and stellar particles in the SMC-mass system are generated at once following the NFW profile with a total mass of $1.9 \times 10^{10} M_\odot$ (Lucchini et al. 2022, and references therein). For the MW-mass system, we only model its DM content since we are not interested in its stellar component but only in its gravitational effects on the LMC-SMC-like system. The DM mass of the MW-mass system is considered to be $10^{12} M_\odot$ (Bobylev & Bajkova 2023, and references therein). In this work, we analyse a snapshot of the simulation taken just after the LMC-like system suffered a second close encounter with the SMC-mass system that generated an off-centred and out-of-equilibrium bar in the LMC-like system. The bar has a counter-clockwise rotation with a pattern speed of $\Omega_p = 17.2 \pm 1.6$ km s^{-1} kpc^{-1} measured as the difference of the rate of change of the phase angle of the bar perturbation, using three consecutive snapshots with a time interval of 2 Myr. The pattern speed places the bar corotation resonance at $R_c = 3.6^{+0.8}_{-0.5}$ kpc. It corresponds to a bar rotation rate of $R_c/R_1 = 1.3^{+0.3}_{-0.2}$.

Figure 1 shows the surface density (left column), the radial velocity (middle column) and the residual tangential velocity maps for the B5 and KRATOS simulations (top and bottom rows, respectively). The map of the residuals has been obtained by subtracting the rotation curve to the V_ϕ map. In the surface density plot, the B5 simulation shows a strong bar accompanied by two strong spiral arms. In the KRATOS simulation, we observe a strong bar accompanied by a broken interacting arm. The radial and residual tangential velocity maps show the characteristic kinematic imprint of the bar, namely a quadrupole pattern. Larger velocities are observed in the B5 simulation than in the KRATOS simulation (see also Sect. 3.3).

We show first the results when applying the Dehnen method (Sect. 3.1), because it defines the bar region in the simulations, which are used by the TW method (Sect. 3.2). Finally, the results corresponding to the BV method are presented in Sect. 3.3.

3.1. Results of the Dehnen method

Dehnen et al. (2023) made their numerical tool to infer some bar properties from a single simulation snapshot available to the community. We thus used the Python code they provide, and, for both simulations we have set various parameters. We fixed a minimum and maximum number of particles in the radial bins to 10^4 and 5×10^4 (respectively) for the B5 and KRATOS simulations. We adopted a maximum size of the sampling of the radial bins of 1.25 kpc, a minimum ratio of the strength of the surface density in the bar region of $\Sigma_2/\Sigma_0 = 0.1$ (Σ_0 and Σ_2 being the amplitudes of the axisymmetric and bisymmetric surface density components), a maximum angular width of the bar of $10°$, a minimum size of the bar of 1.25 kpc, respectively, with a minimum required number of particles in bar region of 1000. Following Dehnen et al. (2023) recommendations, we assumed a top-hat weighting function to constrain Σ_2/Σ_0 and ϕ_b in each bin from the surface density, and a smooth window to estimate

Ω_p and the bar orientation in the entire bar region. We refer the reader to Dehnen et al. (2023) for more complete information of the code. The application of the Dehnen method to a simulated disc with a barred perturbation and no spiral structure is given in App. A.

Figure 1 shows the performance of the Dehnen method with both simulations. Left, centre and right panels show the surface density, the median radial velocity map and median residual tangential velocity map, respectively. In every panel, we highlight the bar region identified by the method by green dashed circles, with inner and outer circles corresponding to R_0 and R_1, respectively. The grey dashed lines trace the bar minor and the major axes found by the method. For both simulations ϕ_b is in agreement with the orientation observed in the surface density, and separates remarkably the quadrupole patterns in two parts. For the B5 simulation (top panels), the method infers a value of $\Omega_p = 21.2 \pm 0.1 \,\mathrm{km\,s^{-1}\,kpc^{-1}}$, in good agreement with the value found using finite-differences. For the KRATOS simulation (bottom panels), the method infers a value of $\Omega_p = 16.5 \pm 0.1 \,\mathrm{km\,s^{-1}\,kpc^{-1}}$, also in agreement with the value obtained using finite-differences. Values are summarised in Table 1. These tests are thus another way to validate the method, in agreement to those performed in Dehnen et al. (2023). It can be concluded that, under ideal conditions in which data are devoid of observational and numerical noise, the Dehnen method successfully recovers the imposed values of Ω_p.

This method yields a corotation radius of 8.3 kpc for the B5 simulation, corresponding to the ground-truth value. It gives a corotation radius of 4.0 kpc for KRATOS, which is very close to the ground-truth value.

3.2. Results of the TW method

As mentioned above, the applicability of the TW method in either of the two versions is designed for galaxies in equilibrium and, moreover, with a single pattern speed. We can nevertheless evaluate their performance by applying them to the simulations of isolated and interacting spiral discs. Application of the methods to a simulated disc with a barred perturbation and no spiral structure is given in App. A.

Hereafter, the domain $[-\infty/+\infty]$ of the numerical integration of Eqs. 4 and 5 is the maximum extent of the disc allowed inside each pseudo-slit parallel to the $x-$axis at a given y coordinate, or the line-of-nodes for the LTW method. Within this maximum range, the integrals have converged to stable values. Furthermore, we investigated the impact of the width of the pseudo-slits. Within a range of 50-500 pc, we found that the width has no effect on the results described below. Only the uncertainties on Ω_p are seen to increase for wider pseudo-slits, by a factor of 3.5 from 50 pc to 500 pc width. In this Section, we show the results obtained for a width of 200 pc.

3.2.1. Results of the LTW method

We simulate a galaxy observation by projecting the particles from each simulation onto a galactic plane with arbitrary inclination (i) and position angle (PA) of the semi-major axis of the receding half. For the result described here, we adopted a disc projected with PA = 60°, and inclinations of $i = 25°$, $45°$ and $75°$. Assuming a mock disc distance of 10 Mpc, which is well suited to mock galaxies on which the LTW method can been applied, the maps of the projected density and l.-o.-s. velocity have 512×512 pixels sampled at $1''$ (~ 50 pc/pixel). We do not investigate the impact

of varying the distance of the mock disc on the results. We chose the $x-$axis aligned with the line of nodes, so that the reference of the azimuthal angle $\phi = 0$ is along the semi-major axis of receding disc half. The small angle approximation can be applied, and the l.-o.-s. kinematics of each particle simply resumes to $V_{\mathrm{los}} = V_z \cos i + V_y \sin i = V_z \cos i + (V_R \sin \phi + V_\phi \cos \phi) \sin i$. The adopted velocity in each pixel of the map is the mean of the V_{los} of the particles. The LTW integrals of Eq. 5 are performed at each $Y-$coordinate, selecting all pixels from the maps within pseudo-slits parallel to the disc major axis. The derivation of the slope $\Omega_p \sin i$ is performed using the $\langle X \rangle$-$\langle V_{\mathrm{los}} \rangle$ points located inside the region encompassing the projected value of the bar radius R_1 from in Table 1.

We investigate the impact of the variation of the orientation of the Cartesian frame on the results, by rotating the reference x and y axes around the $z-$axis in the simulation. The rotation of the Cartesian frame before projection on the sky plane allows the TW integrals to view the bar and spiral perturbations through various angles. In practice, this is achieved by adding a $\Delta\phi$ to the angular position ϕ of each particle in the disc plane, from which new x and y positions are derived. Then, new density maps and l.-o.-s. kinematics and Ω_p can be inferred. A range of $\Delta\phi$ spanning 180° has been probed, with a step of 3°. Figure 2 (upper panel) shows the resulting bar pattern speed as a function of the frame orientation $\Delta\phi$ for the case $i = 45°$ only (red open symbols) and the B5 simulation. The quoted uncertainties correspond to the 1σ error of the covariance matrix of the fitting. We highlight the frame orientations parallel and perpendicular to the bar major axis as orange and navy vertical lines, respectively. Results for the KRATOS simulation are shown in the lower panel of Fig. 2 for the three assumed inclinations.

The variation of the pattern speed with $\Delta\phi$ is very important in both simulations, and makes it rarely consistent with the ground-truth values (shown as horizontal green dashed lines), whatever the adopted disc inclination. The strongest disagreement occurs at frame orientations very close to the major axis of the bar, and $\sim 15°$ before its minor axis. For the B5 simulation, the LTW results are consistent with the real value only at frame orientations $\Delta\phi \sim 70 - 75°$, thus when the $x-$axis in the galaxy plane makes an angle of $\sim 55 - 60°$ with respect to the bar major axis. The LTW pattern speeds agree with the ground-truth value only occasionally for the KRATOS simulation, within the quoted uncertainties (shown as shaded areas). A strong dependency with the inclination of the disc is observed. The best agreement with ground-truth is for a mock disc at $i = 45°$, for $7° < \Delta\phi < 38°$, thus when the $x-$axis in the galaxy plane makes an angle of $\sim 30 - 60°$ with respect to the bar major axis. Another interesting result is that no symmetry around the bar minor axis is observed, indicating that having a wide range of agreement with ground-truth is unlikely (see Sect. 3.2.2 for more details).

3.2.2. Results of the IPTW method

As in the LTW method, we varied $\Delta\phi$ between 0° and 180° to study the dependency of the in-plane TW integrals of Eq. 4 with the frame orientation. Figure 3 shows results for the B5 simulation for two examples of frame orientations[1]. The upper row corresponds to the original frame orientation, with $\Delta\phi = 0°$, while in the bottom row, the x-axis is chosen aligned with the bar major axis, corresponding to a frame orientation of 16.5°,

---

[1] Animations of the variation of the pattern speed Ω_p inferred by the IPTW with different frame orientations $\Delta\phi$ are available online, for both simulations and data.
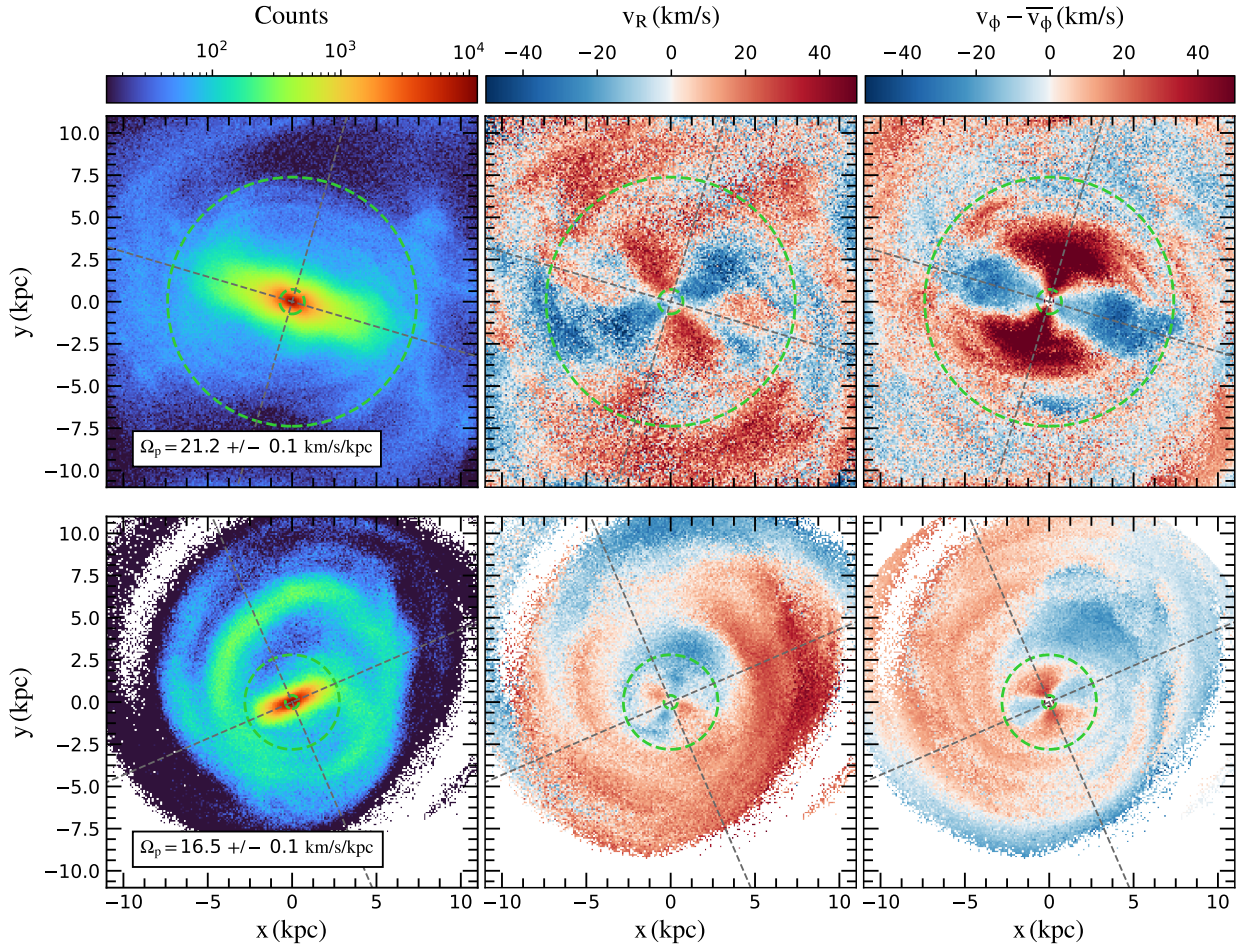
Fig. 1: Application of the Dehnen method to B5 (top) and KRATOS (bottom) simulations. Surface density (left), median radial velocity map (centre) and median residual tangential velocity map (right). The bar region identified by Dehnen method (see values in Table 1) is indicated by green dashed circles. The grey dashed lines trace the bar minor and the major axes.

| Simulation | Reference | Dehnen method | | | | BV method | |
	Ω_p	R_0	R_1	Ω_p	ϕ_b	R_c	Ω_p
B5	21.5 ± 0.1	0.73	7.38	21.2 ± 0.1	163.5 ± 0.1	8.0 ± 0.5	$22.2^{+0.7}_{-1.2}$
KRATOS	17.2 ± 1.6	0.40	2.80	16.5 ± 0.1	23.4 ± 0.1	3.3 ± 0.5	$18.2^{+2.9}_{-1.3}$

Table 1: Results of the Dehnen and the BV methods applied to B5 and KRATOS simulations, compared to the reference value (obtained using finite-differences). The inner, outer and corotation radii R_0, R_1 and R_c are in kpc. The bar pattern speed Ω_p and phase angle ϕ_b are in km s^{-1} kpc^{-1} and degrees, respectively.

which corresponds to $\Delta\phi = 16°$. The left panels show the surface density maps, with the bar region outer radius R_1 identified with the Dehnen method highlighted by a green dashed circle. The coloured dots represent the $\langle x \rangle$ integrals for each slice in y, with greener (redder) colours for larger (smaller) values of $|y|$. In the case where the bar major axis is parallel to the x-axis, $\langle x \rangle$ is observed close to the $x = 0$ axis in the bar region, thus rather aligned with the bar minor axis. In the case where the bar major axis is 30° rotated counter-clockwise with respect to the x-axis,

$\langle x \rangle$ varies significantly in the bar region, almost tracing the bar major axis.

The right panels show the TW integrals, $\langle x \rangle$ versus $\langle v_y \rangle$, with the same colour code for the various y as those in the left panels. The points with a black circle are those located inside R_1, while the rest of the points are the ones outside the bar region, therefore, not considered for fitting Ω_p. In the case with $\Delta\phi = 0$, thus the original frame orientation, there is a clear linear trend with small dispersion for points inside the bar region, as shown
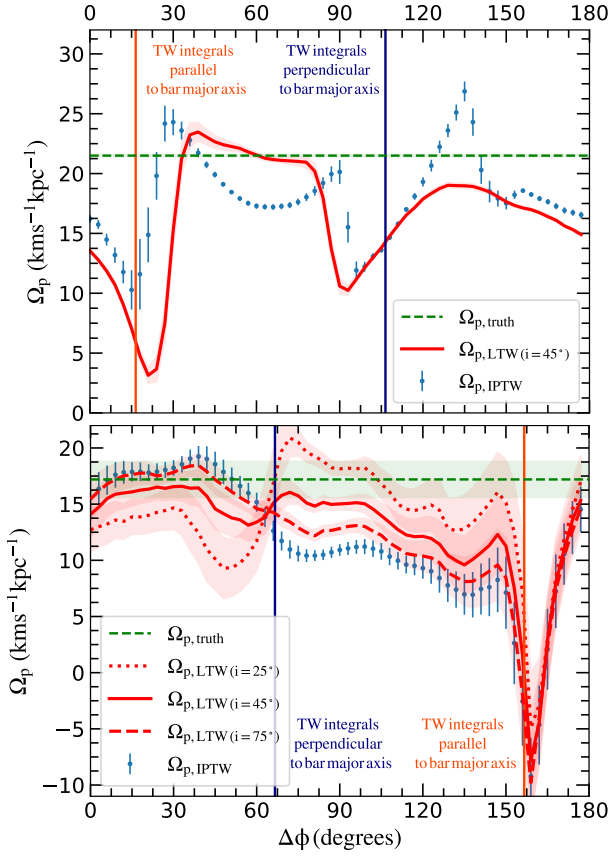
Fig. 2: Variation of Ω_p as as function of the reference frame orientation $\Delta\phi$. Results for the B5 and KRATOS simulations are shown in the upper and lower panels, respectively. Results of the IPTW method are shown as open symbols, while those of the LTW method are drawn as a solid line (for the $i = 45°$ case, upper panel), and as dotted, solid and dashed lines (for the $i = 25, 45$ and $75°$ cases, lower panel). Horizontal dashed green lines are the ground-truth bar pattern speeds. The vertical orange (navy) vertical line corresponds to the frame orientation where the x-axis of the disc lies along the major axis of the bar (y-axis, respectively).

by the dashed straight line fit. In the case where the bar major axis is parallel to the x-axis, several linear trends are observed, hence a significantly larger dispersion. The fitted slope of the TW integrals is 10.3 ± 2.1 km s^{-1} kpc^{-1}, as shown by a dashed straight line. However, none of these values are consistent with the real pattern speed of 21.5 ± 0.1 km s^{-1} kpc^{-1}, or the value of 21.2 ± 0.1 km s^{-1} kpc^{-1} from the Dehnen method.

Figure 4 presents results of the IPTW method for the KRATOS simulation. Again, we show here two different reference frame orientations: the original one, with $\Delta\phi = 0°$ (top row) and the one with the bar major axis parallel to the x-axis, $\Delta\phi = 156°$ (bottom row). In the first case, there is a linear trend and the IPTW recovers a bar pattern speed $\Omega_p = 15.5 \pm 1.7$ km s^{-1} kpc^{-1}, compatible with the real pattern speed. In the second case, the TW x−integrals are perfectly aligned with the bar major axis, as expected in the presence of only a bar potential. The $\langle x \rangle$ values are then very close to zero, so there is not a clear trend in

this case (it would give similar results when the TW integrals are evaluated at another viewing angle along the bar minor axis). We recover here a clockwise pattern speed of $\Omega_p = -4.2 \pm 4.0$ km s^{-1} kpc^{-1} which differs from the real value. Note also that in this configuration, the linear trend is more scattered, not as clear as the configuration from the upper panel, in agreement with what was seen with for the B5 simulation.

We then assess whether there is (or not) a favoured frame orientation where the IPTW method works better, by plotting the fitted Ω_p as a function of $\Delta\phi$ (filled blue symbols in Fig. 2). Qualitatively, the IPTW and LTW methods show similar trends: the agreement with the ground-truth bar pattern speed is rarely observed, no symmetry with respect to the bar major axis is found, and stronger discrepancies are near the positions of the major and minor axes of the bar. The B5 simulation (upper panel) shows that $\Delta\phi \sim 135°$ is also a location of stronger disagreement, which was not observed for the LTW method. Since the IPTW method works directly with coordinates and velocities in the Cartesian frame of the disc, no variation with inclination needs to be evaluated here. It is interesting to note that the LTW pattern speeds with better agreement with the IPTW method are for the intermediate inclination of $45°$ (lower panel for the KRATOS simulation). It is important to remind that the Dehnen method does not show such systematic variation with $\Delta\phi$, as its results are invariant with the frame orientation.

The median and mean absolute deviation of all the IPTW values are 17.9 ± 1.9 km s^{-1} kpc^{-1} and 11.0 ± 3.7 km s^{-1} kpc^{-1} for the B5 and KRATOS simulations, respectively. We note that the difference is larger in the KRATOS simulation. While the B5 simulation presents a strong spiral pattern in the outer disc, the KRATOS simulation additionally is not in equilibrium.

Finally, we can estimate the incidence of finding a bar pattern speed consistent with the ground-truth value for both the LTW and IPTW methods, with the two simulations. We define this likelihood as the number of frame orientations where the measured and real Ω_p agree within the quoted (1σ) uncertainties on measured and ground truth values. For the B5 simulation, the IPTW and LTW methods give a correct Ω_p in 5% and 8% of the cases only. For the KRATOS simulation, the incidence is 37% (IPTW case), 57% (LTW case at $i = 25°$), 48% (LTW case at $i = 45°$) and 42% (LTW case at $i = 75°$). Larger inclinations are thus less prone to the LTW method. More generally, our two sets of simulations show it is highly unlikely to find a consistent Ω_p by means of the TW method. It is also hard to reconcile the strong variations with $\Delta\phi$ seen here, i.e the bar orientation with respect to the disc x−axis, with the wide range of "allowed" orientations quoted in other studies (e.g. Zou et al. 2019, see also Sect. 5 for the LMC).

3.3. Results of the bisymmetric velocity model

Bayesian inferences of Fourier coefficients to the tangential velocities were performed in radial bins through Markov Chain Monte Carlo fits, using the Python library Emcee (Foreman-Mackey et al. 2013). The model is fitted to a map of V_ϕ (pixel size of 50 pc), where the velocity at each pixel of the map is the median of the velocity distribution from all particles/stars inside the given pixel. Defining the residual velocity as $V_{\phi,\text{res}} = V_\phi - V_{\phi,\text{mod}}$, the conditional likelihood function at each radial bin is expressed by:

$$\mathcal{L}(V_0, V_2, \phi_{2,\text{kin}}, V_s) = -\frac{1}{2}\left(n_{\text{pix}}\ln(2\pi)\sum^{n_{\text{pix}}}\left(V_{\phi,\text{res}}^2/\xi^2 + \ln(\xi^2)\right)\right),$$
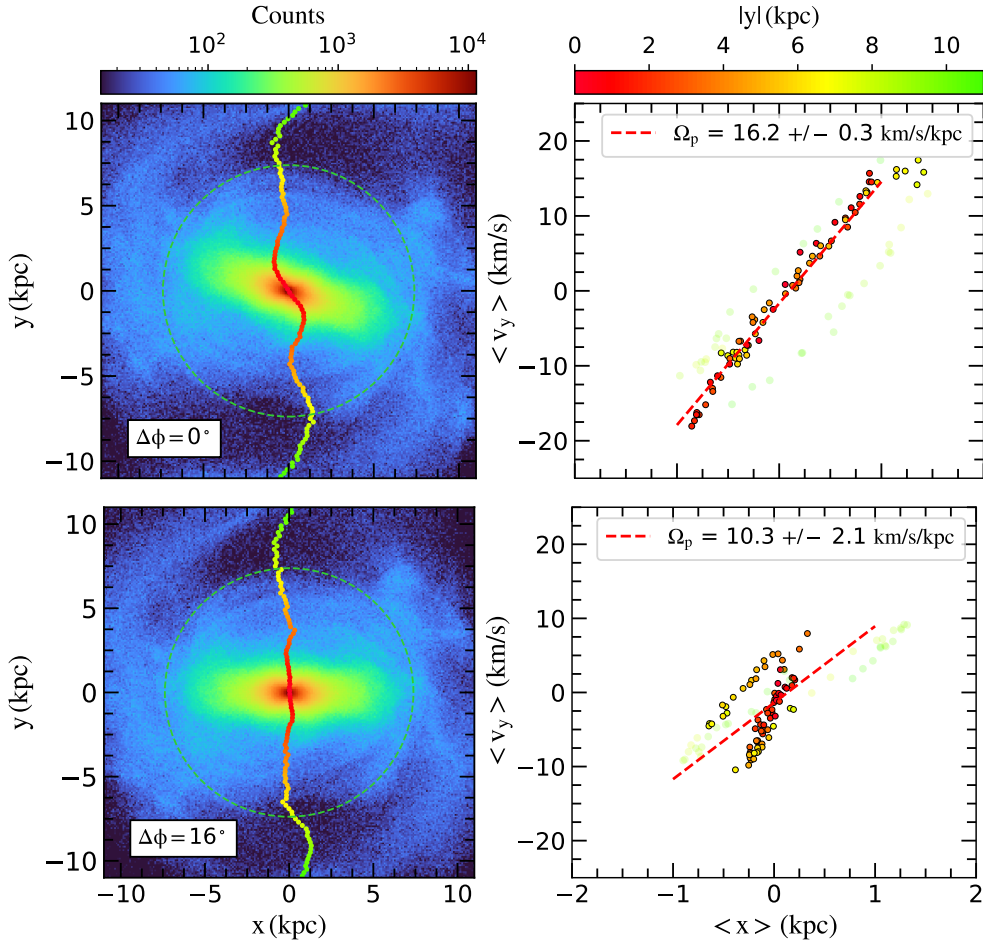
Fig. 3: Application of the IPTW method to B5 simulation. Top: The bar major axis at $\phi_b = 163.5°$, as in the original snapshot and shown in Fig. 1. Bottom: After applying a rotation of $\Delta\phi = 16.5°$ to put the bar major axis along the x-axis. Left: Surface density where the bar region (obtained using Dehnen method) is indicated by the green dashed circle. A scatter plot representing the value of $\langle x \rangle$ for each slice in y is overlapped. The scatter plot varies its colour as function of the distance to the centre in the y-axis, being the red points close to the centre and the green close to the external parts of the galaxy. Right: Scatter plot of the Tremaine-Weinberg integrals $\langle x \rangle$ and $\langle v_y \rangle$ for the different slices in the y-axis. The colour of the scatter plot is the same in both left and right panels. In the right panel, the points with a black circle are inside of the bar region and, therefore, the only considered for fitting Ω_p.

where V_0, V_2 and ϕ_2 are as in Eq. 6, $\xi^2 = \sigma^2_{V_\phi} + V_s^2$, σ_{V_ϕ} are the V_ϕ uncertainties, V_s is the scatter of the modelling, and n_{pix} the number of pixels of the map inside the corresponding radial bin at which parameters are fitted. No uncertainties are measured while making the velocity map, thus $\sigma_{V_\phi} = 0$. Therefore, measuring V_s is an indirect way to take into account the lack of uncertainties (Hogg et al. 2010).

The left column of Fig. 5 shows the results of the model to the B5 simulation. In the top panel, we show the rotation curve of the simulated disc (gray solid line, measured as the median velocity in the map a each R), the fitted axisymmetric velocity component (black solid line, V_0), the amplitude of the bisymmetry V_2 (blue dashed line), and the scatter in $V_{\phi,\text{res}}$ (orange dotted line, V_s). The bar strength is maximum at $R \sim 2$ kpc, reaching more than 50% of V_0. Within $R = 5$ kpc, V_0 and the median rotation curve can differ by up to ~ 20 km s^{-1}, which indicates the

significant impact of the bisymmetry on the rotation curve. In the middle panel, we show the phase angle $\phi_{2,\text{kin}}$ of the bar recovered from the modelling of the tangential velocity map. The phase angle of the bar is well recovered by the bisymmetric model at low radius, then smoothly varies. At $R \sim 7.5$ kpc, an abrupt change in $\phi_{2,\text{kin}}$ is observed. Following prescriptions given in Sect. 2, we can identify the corotation radius just after the steep change of phase angle, $R_c = 8.0 \pm 0.5$ kpc, which corresponds to a bar pattern speed is $\Omega_p = 22.2^{+0.7}_{-1.2}$ km s^{-1} kpc^{-1} (bottom panel, the Ω curve being derived from the solid curve of the upper panel, i.e. the 0th order Fourier coefficient). This agrees with the value computed using finite-differences. By construction, the bisymmetric velocity model is invariant with the frame orientation, as $\phi_{2,\text{kin}}$ are shifted by $\Delta\phi$ when a rotation of $\Delta\phi$ is applied to the $x - y$ plane.

Similarly, in the right panels of Fig. 5, we show the results of applying this method to the KRATOS simulation, the value for
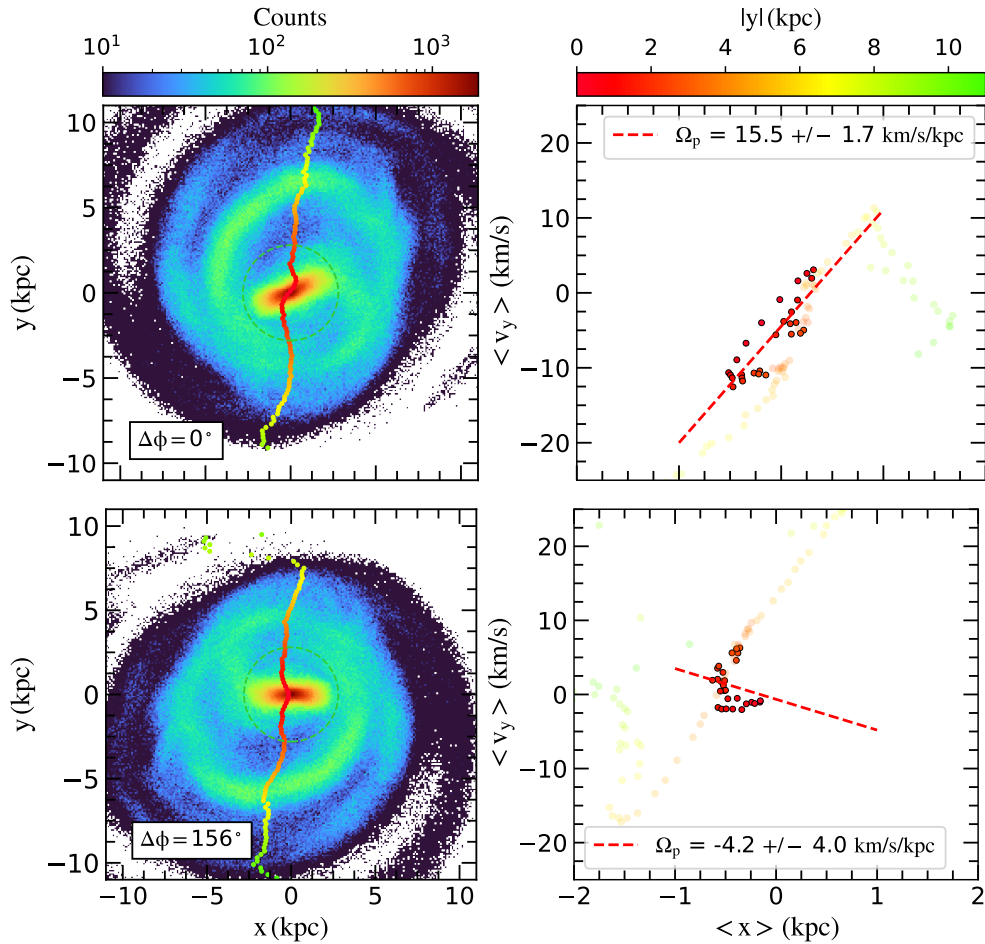
Fig. 4: As in Fig. 3 for the KRATOS simulation.

corotation we derive is $R_c = 3.3 \pm 0.5$ kpc, and the bar pattern speed is $\Omega_p = 18.2^{+2.9}_{-1.3}$ km s^{-1} kpc^{-1}, which is consistent with the true value of 17.2 ± 1.6 km s^{-1} kpc^{-1}, within the quoted uncertainties. Values are summarised in Table 1.

This method yields a bar rotation rate of $R_c/R_1 = 1.1$ and 1.2 for the B5 and KRATOS simulations, respectively, in agreement with the ground-truth values.

4. Measuring the LMC bar pattern speed

In the previous section, we have assessed the performance, robustness and limitations of the methods when applied to simulated data. The TW method, in both versions using either line-of-sight or in-plane velocities, shows a clear dependence of the measured pattern speed on the frame orientation, and significant differences with the ground-truth values. The recovered value can be lower or higher than the simulated speed when both bar and spiral arms intervene in the simulation. These results already warn us to take the value of the LMC pattern speed inferred from the TW method with caution.

The LMC stars we use in this study are those in the NN complete sample of Jiménez-Arranz et al. (2023). The selection of LMC stars was based on a supervised neural network classi-

fier, using full astrometric and photometric data from *Gaia* DR3. Based on this classifier, the authors select three samples of candidate LMC stars with different degrees of completeness and purity. The NN complete sample corresponds to the sample that prioritises not missing LMC stars at the price of a possible increased MW contamination. It contains 12 116 762 stars. The sample is dominated by older stellar populations (see, e.g., Fig.3 from Gaia Collaboration et al. 2021b), thus fulfils the continuity equation necessary to the TW and Dehnen methods. Combining the selection function of the *Gaia* parent catalogue (Cantat-Gaudin et al. 2023) and the selection effects from the generation of the LMC NN complete sample (estimated as in Castro-Ginard et al. 2023), the completeness estimates of our sample are above 50% in the bar region for $G = 19 - 19.5$ mag. As seen in Fig. 6 of Jiménez-Arranz et al. (2023), 60% of stars in the LMC NN complete sample have magnitude below $G < 19.5$. To better estimate the completeness and purity of the LMC NN complete sample, and their effect on the inner kinematics, a more detailed study of the selection function is required, which is out of the scope of this paper.

For each star, we apply the coordinate transformation detailed in Jiménez-Arranz et al. (2023) to express the deprojected positions and velocities in the in-plane coordinate system of the
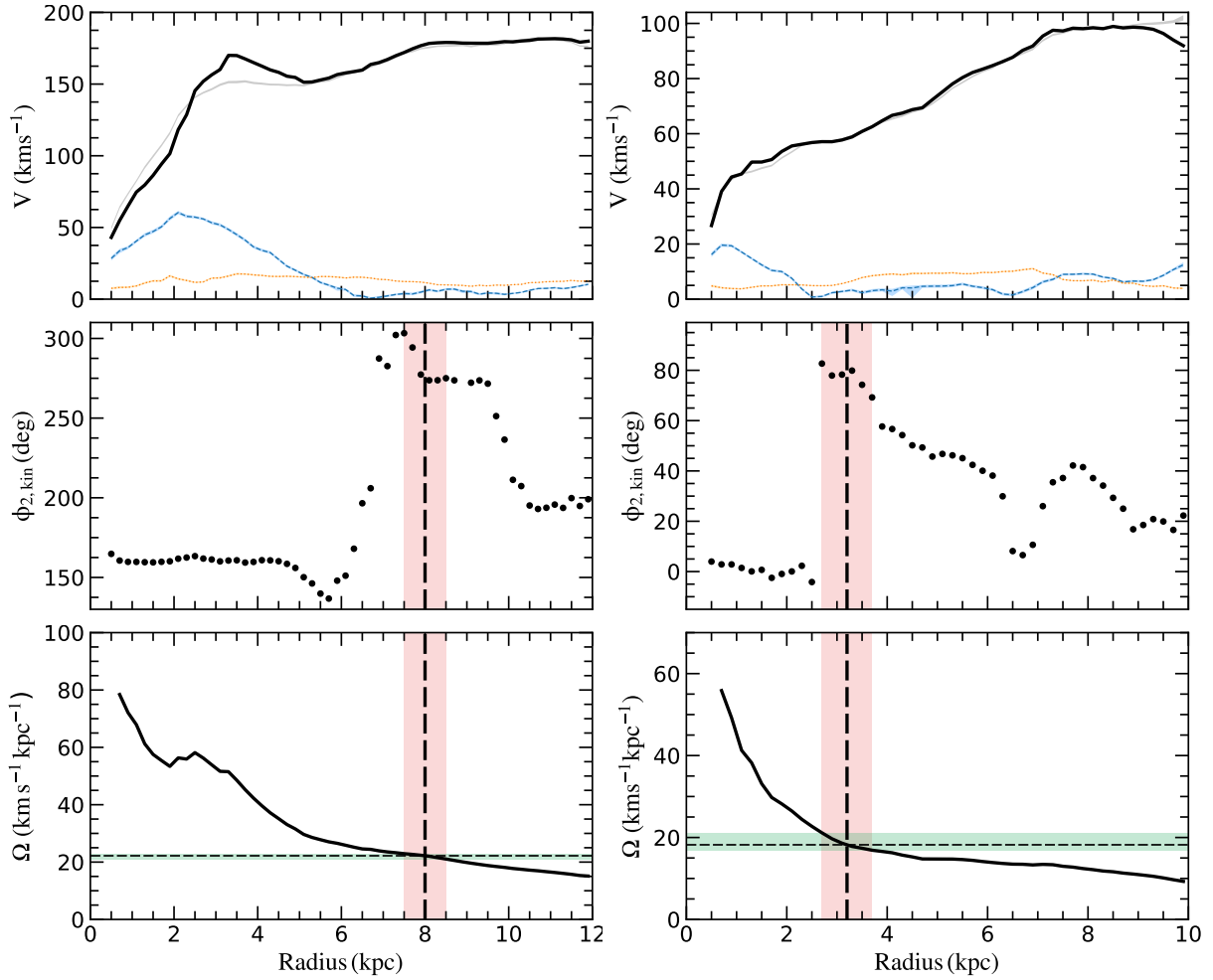
Fig. 5: Results of the BV model of the stellar tangential velocity map of the B5 (left panels) and KRATOS (right panels) simulations: amplitude (upper panels), phase angle, $\phi_{2,\mathrm{kin}}$ of the Fourier modes (middle panels), and angular frequency Ω (bottom panels). In the top panels, the black solid line is the fitted axisymmetric velocity component V_0 (the rotation curve), the grey line is the median velocity (initial value for the model), the blue dashed curve is the amplitude of the tangential bisymmetry V_2, and the orange dotted line is the scatter of the model V_s. In the middle and bottom panels, the vertical light coral area and dashed line shows the adopted bar corotation radius, $R_c = 8.0 \pm 0.5$ kpc for B5 and $R_c = 3.3 \pm 0.5$ kpc for KRATOS simulations. In the bottom panel, the black solid line is the angular velocity derived from V_0, while the horizontal green area and dotted line shows the corresponding bar pattern speed $\Omega_p = 22.2^{+0.7}_{-1.2}$ km s^{-1} kpc^{-1} and $\Omega_p = 18.2^{+2.9}_{-1.3}$ km s^{-1} kpc^{-1}, for the B5 and KRATOS simulations, respectively. Values are summarised, and compared with the reference values, in Table 1.

LMC, using the inclination, position angle, systemic velocity, and position of the LMC centre given in Jiménez-Arranz et al. (2023), assuming all stars lying in the $z = 0$ plane. The LMC centre used is the same as in Gaia Collaboration et al. (2018, 2021b), which corresponds to the LMC photometric center (van der Marel 2001). The infinitely thin disc approximation is inherent to any studies of the kinematics of disc galaxies because the 3D position space of stars in galaxies is never available, unlike stars in the MW (e.g. Gaia Collaboration et al. 2023), or a few variable young stars in the LMC (Ripepi et al. 2022a).

Figure 6 shows the results of the application of the Dehnen method to the LMC. The left, middle and right panels show the surface density, the median Galactocentric radial velocity, and residual of the median tangential velocity, respectively. Both the radial and residual tangential velocity maps show the imprint of a

rigidly rotating bar in the galactic centre, as clear hints of x_1 stellar orbits (see also Gaia Collaboration et al. 2021b; Niederhofer et al. 2022; Jiménez-Arranz et al. 2023). The quadrupole pattern is the natural reflex of the motion of stars in elliptical orbits present in the bar potential. In contrast to the simulations, the method was not able to find the bar region $[R_0, R_1]$ on its own, probably due to the fact that the quadrupole is not perfectly symmetric, or that the contrast of the bar region with respect to the disc is not as clear as in simulations because of the presence of dust lanes and spiral arms at low radius. We solved this issue by analyzing the outputs of the numerical code of Dehnen et al. (2023) which, in addition to the bar parameters and pattern speed, provide results of a second order Fourier model of the stellar density. Figure 7 shows the amplitude Σ_2 of the $m = 2$ Fourier coefficient, relatively to the axisymmetric density Σ_0, and the

phase angle ϕ_2 of the bisymmetric density perturbation. In the upper panel, a peak of the relative strength ~ 0.2 is observed at $R \sim 2$ kpc. This amplitude is comparable to that at larger radius, meaning a small contrast between the LMC bar and the spiral arm(s) within the selected sample of stars. This probably explains why the Dehnen method cannot establish properly the bar region in its automated way. The phase angle (bottom panel of Fig. 7) has a constant value of $\phi_2 \simeq 15 - 20^{\circ}$ from $R = 0.75$ kpc to $R \sim 2.3$ kpc. We can establish that the bar region is theferore $[R_0, R_1] = [0.75, 2.3]$ kpc. Within this region, the Dehnen method gives a value of $\Omega_p = -1.0 \pm 0.5$ km s^{-1} kpc^{-1}, thus corresponding to an almost non-rotating stellar bar, seemingly in counter-rotation.

Now for the TW method, we adopted an pseudo-slit length and width of $[-\infty, +\infty]$ and 50 pc, respectively. For both versions of the method, the slopes of the integrals are fitted using only points located inside the bar radius (for the IPTW case) and projected radius (for the LTW case), as defined by $R_1 = 2.3$ kpc.

In Fig. 8, we show the stellar l.-o.-s. velocity field corrected for the systemic motion of the LMC NN complete V_{los} sub-sample, which contains 30 749 stars. These are predominantly the AGB stars from Gaia Collaboration et al. (2021b). This is in good agreement with the l.-o.-s. velocity field traced by carbon stars (van der Marel et al. 2002). We apply the LTW method to this l.-o.-s. velocity map, as described in Sect. 2.2, with pseudo-slits parallel to the line-of-nodes. Figure 9 shows the linear fit to the LTW integrals, yielding a bar pattern speed of $\Omega_p = 30.4 \pm 1.3$ km s^{-1} kpc^{-1}, using an inclination of $i = 34^{\circ}$.

Figure 10 shows the results of the IPTW method applied to the LMC Cartesian velocity fields (not shown here, but obtained from the cylindrical velocities shown in Fig. 6). We recover as many values as adopted orientations $\Delta\phi$ of the Cartesian frame in the LMC plane. Interestingly, a good agreement is seen between the LTW Ω_p (open red dot at $\Delta\phi = 0^{\circ}$) and the IPTW Ω_p inferred at this orientation. However, and unsurprisingly, the estimated values of the IPTW method display a strong variation with the frame orientation. A wide range of possibilities is found for the LMC Ω_p, from 0 to 55 km s^{-1} kpc^{-1}. Note also the clear correlation between the bar major and minor axis with the orientations where the shape of the Ω_p curve vary significantly. The median of all IPTW values seen in this graph is 23 ± 12 km s^{-1} kpc^{-1}, adopting here the mean absolute deviation as the uncertainty.

Finally, in Fig. 11 we show the results of the BV method applied to the LMC tangential velocity map of Fig. 6. The LMC rotation curve from the NN complete sample (upper panel, light grey) is very similar to the 0th order Fourier component of the BV model (black solid line). The amplitude of the LMC bar perturbation is stronger at $R = 0.75$ kpc (blue line). The orange dotted line showing the scatter in the residual tangential velocity is often larger than the bisymmetric mode. It thus shows that the bar is not the only perturber in the LMC disc, but this does not prevent the bisymmetry from being detected efficiently by the method. Note that seeing the scatter in the model stronger with radius is reminiscent to the finding of the KRATOS simulation (top right panel of Fig. 5). This is consistent with the observed complex stellar morphology in this region. A roughly constant value of $\phi_{2,kin} \simeq 15 - 20^{\circ}$ is seen out to $R = 2$ kpc, in good agreement with the phase angle of the bisymmetry of the density (Fig. 7, bottom panel), followed with a smooth decrease out to $R = 3.95$ kpc, as evidence of the impact of arms in the kinematics even in the bar region. This radius is the location from where the amplitude V_2 starts to increase. At this radius, $\phi_{2,kin}$ changes by $\sim 100^{\circ}$ to recover a constant value comparable to the bar phase

Method	R_1	R_c	Ω_p
LTW			30.3 ± 1.3
IPTW			23.1 ± 12
Dehnen	2.3		-1.0 ± 0.5
BV		4.20 ± 0.25	$18.5^{+1.2}_{-1.1}$

Table 2: Results of applying the method used in this work to the LMC complete sample. Bar radius and bar corotation are in kpc and the bar pattern speed is in km s^{-1} kpc^{-1}.

angle at low radius. Following prescriptions from the numerical modelling, we adopt the radius just after the sharp transition of phase angle as the bar corotation radius, placing the LMC bar corotation at $R_c = 4.20 \pm 0.25$ kpc. Relative to the angular velocity curve Ω (solid line in the bottom panel of Fig. 11), it corresponds to a LMC bar pattern speed of $\Omega_p = 18.5^{+1.2}_{-1.1}$ km s^{-1} kpc^{-1}.

5. Discussion

Table 2 is a summary of the LMC bar properties obtained with the different methods in the previous section. At first glance, it is difficult to conclude the pattern speed of the stellar bar of the LMC given the large range of values. Only a few studies have provided estimates of the LMC bar pattern speed. Shimizu & Yoshii (2012) derived a value for the bar pattern speed based on the idea that the Shapley Constellation III star forming region (Shapley 1951) is located at the L_4 Lagrangian point of the non-axisymmetric bar potential rotating frame. The authors found $\Omega_p = 21 \pm 3$ km s^{-1} kpc^{-1}. Unfortunately, they did not report on the distance to the LMC they have assumed, which makes the comparison with our results not trivial. Nevertheless, the value they quote is in good agreement with the one inferred from the BV method. In another work, Wan et al. (2020) used SkyMapper (Wolf et al. 2018) data to study the internal kinematics of the LMC populations, following coordinate transformations described in van der Marel (2001) and van der Marel et al. (2002), thus, the same transformations we applied here. For their Carbon Stars, Wan et al. (2020) fit a rotation curve built on a constant angular speed of stars as a function of radius. This may seem a simplistic assumption because Ω must vary with radius (see e.g. Fig. 11). Therefore, they did not constrain the pattern speed of the bar, but their result gives an estimate of what the rough angular frequency of stars should be within $R \sim 8$ kpc, thus on Ω_p since at corotation Ω equals the desired pattern speed. They found $\Omega = 24.6 \pm 0.6$ km s^{-1} kpc^{-1}, which is not far from the BV value derived in our work.

A second important result is that the TW method is extremely sensitive to the orientation of the x-y frame, and therefore to the way the integrals view the bar perturbation in the disc. Finding a dependency of the TW integrals with viewing angles in galaxies is not a new result. Using a numerical simulation, Zou et al. (2019) found that the accuracy on bar pattern speeds could be kept under $\sim 10\%$ for a bar orientated by 10°-75° and 105°-170° with respect to the reference axis of the disc, while configurations where the integrals are measured perpendicularly to the bar major axis were shown to imply values systematically different from reality. This led for instance Cuomo et al. (2019) to define their sample of barred galaxies with bar position angles by 10° or more apart from the disc major and minor axes. With our simulations,
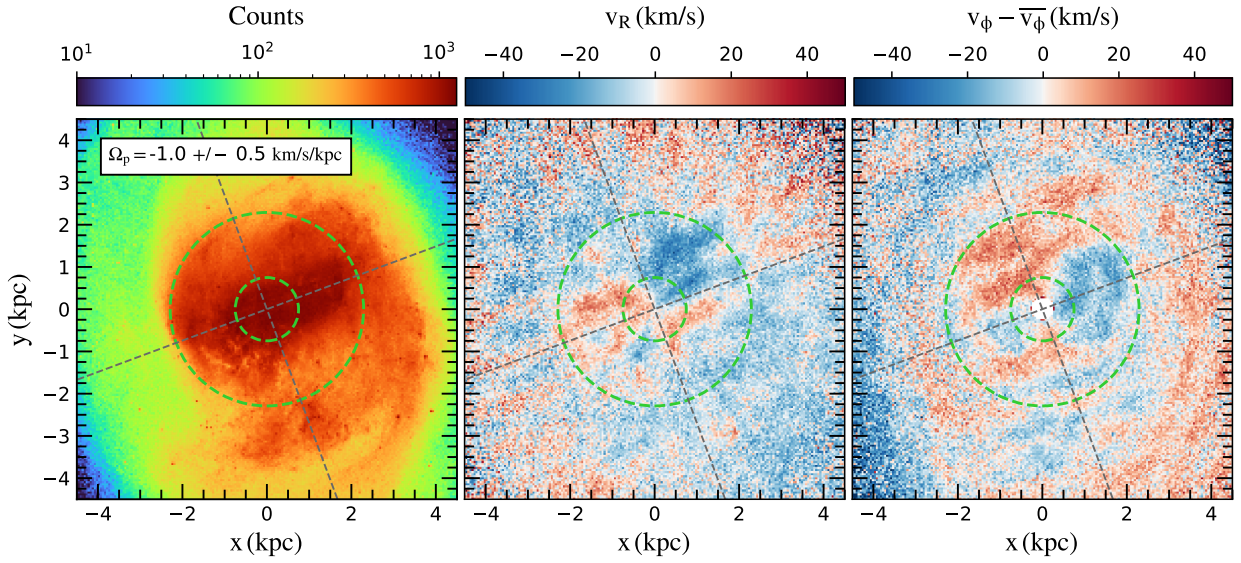
Fig. 6: Application of the Dehnen method to the LMC NN complete sample. Surface density (left), median radial velocity map (center) and median residual tangential velocity map (right). The bar region identified by Dehnen method is indicated by green dashed circles, $[R_0, R_1] = [0.75, 2.3]$ kpc. The grey dashed lines trace the bar minor and the major axes.
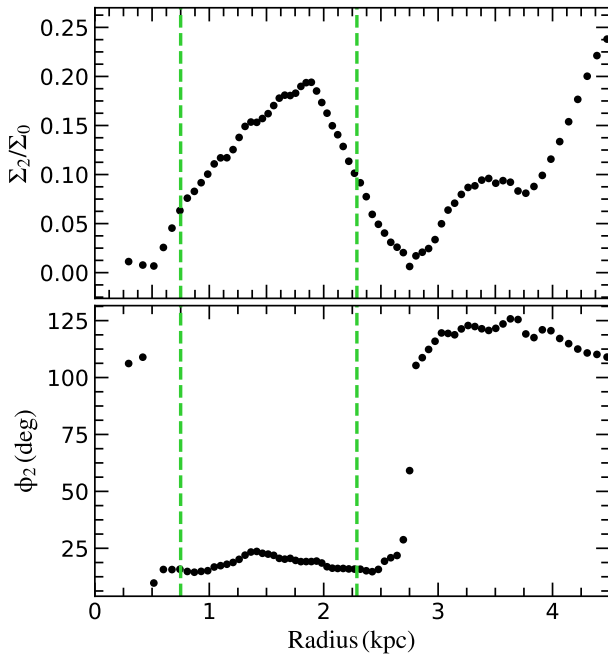

Fig. 7: Application of the Dehnen method to the LMC NN complete sample. The relative $m = 2$ Fourier amplitude (top) and orientation (bottom). The bar region identified by the method is indicated by green dashed vertical lines, $[R_0, R_1] = [0.75, 2.3]$ kpc.

Fig. 8: Stellar line-of-sight velocity field of the LMC NN complete V_{los} sub-sample, corrected from the systemic motions. Data are from *Gaia* RVS (Katz et al. 2022; Jiménez-Arranz et al. 2023).

speed estimates are reliable, and that the probability of agreement is low. It is worth mentioning here that bar pattern speeds of galaxies, as measured with the LTW method, are also known to be sensitive to the orientation of the pseudo-slits with respect to the disc line-of-nodes (Debattista 2003). Still with the help of numerical simulations, these authors showed that assuming an incorrect position angle for the disc major axis can lead to large errors on Ω_p when performing the numerical LTW integrals. Of course, this is not directly linked to the viewing angle of the bar itself in the considered disc plane, as shown above in the IPTW case, but it illustrates nicely how sensitive to orientations the TW method can be.

The origin of the strong variations with the bar angle, and of the large discrepancy with true values, may be the impact of

although frame orientations near the principal axes of the bar should be avoided, which agrees with the findings of Zou et al. (2019), the results of Sect. 3 and 4 did not allow us to identify any particular wide range of orientations where the bar pattern
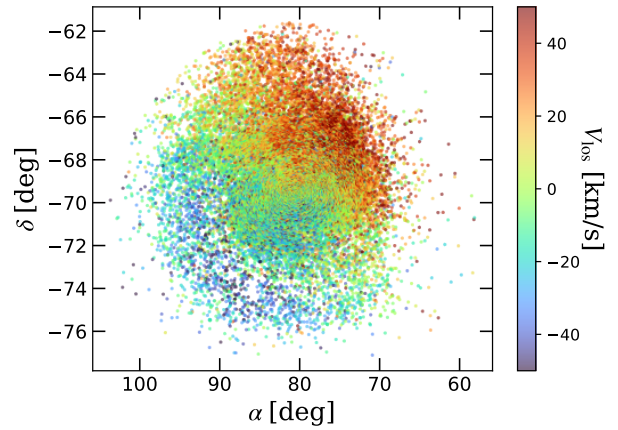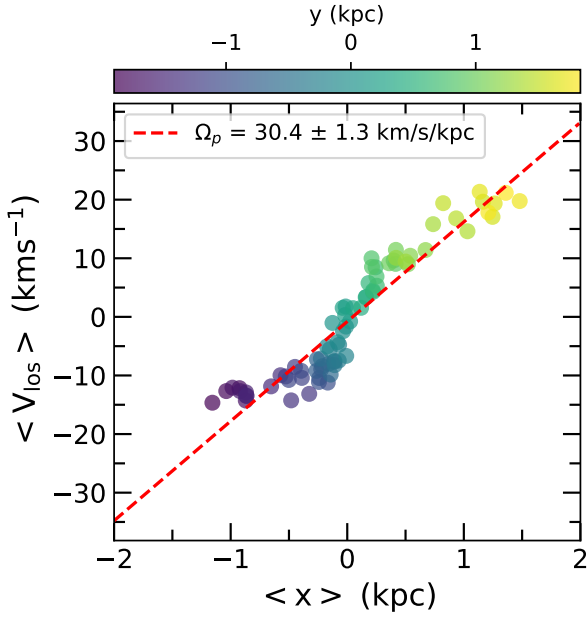
Fig. 9: Result of the TW method applied to the l.-o.-s. velocity field of the LMC from Fig. 8. Only points within the radius R_1 defined by the Dehnen method are shown. The red dashed line shows the result of the linear fit to the points, $\Omega_p \sin i$, with $\Omega_p = 30.4 \pm 1.3$ km s^{-1} kpc^{-1}.
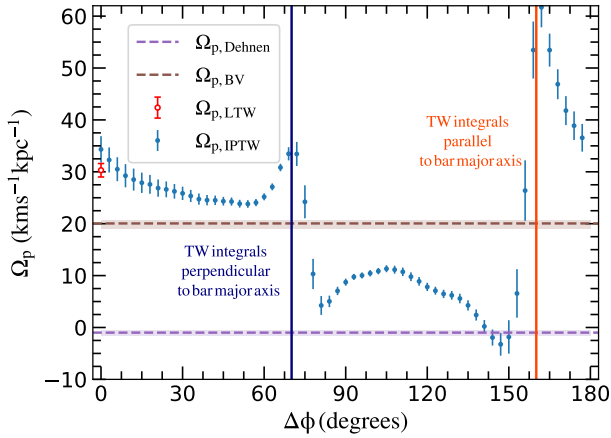

Fig. 10: Results of applying the LTW and IPTW to the LMC NN complete sample. The open red dot shows the bar pattern speed recovered with the LTW method. The blue dotted curve shows the bar pattern speed obtained using the IPTW with different frame orientations $\Delta\phi$. The dashed purple (brown) line shows the bar pattern speed obtained using the Dehnen (BV) method.

patterns other than the bar in the TW integrals, like spiral arms in the N-body simulation and the LMC. A possible solution to overcome this issue could be to measure Ω_p as a function of radius, as done in Merrifield et al. (2006) or Meidt et al. (2008) for other galaxies. However, such analysis is beyond the scope of this article.
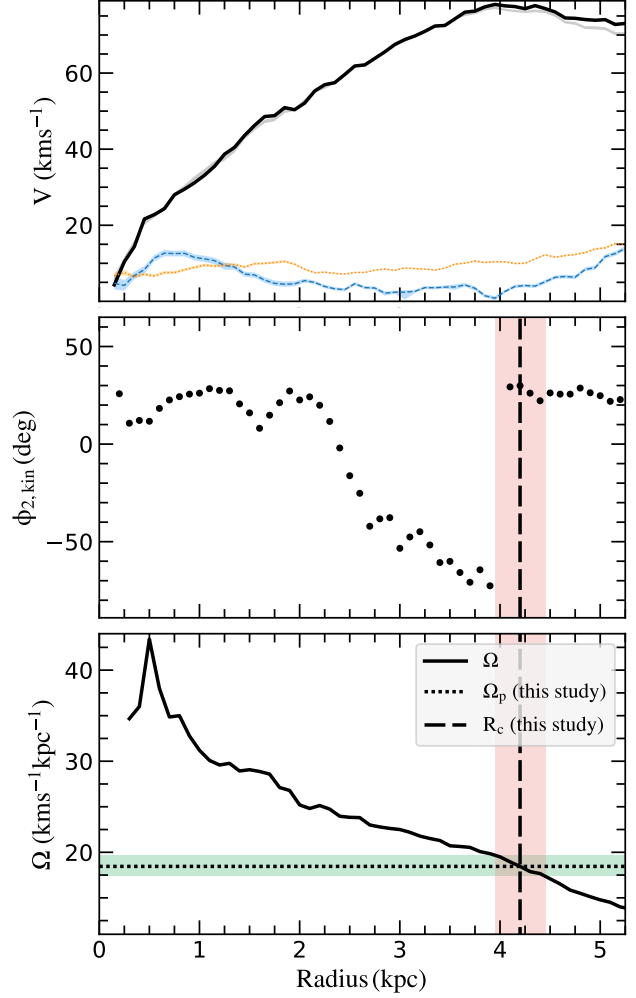

Fig. 11: Results of the BV model of the stellar tangential velocity map of the LMC NN complete sample: strength (upper row) and phase angle (lower row, $\phi_{2,\text{kin}}$) of the bisymmetric Fourier mode. The black solid line is the fitted axisymmetric velocity component (the rotation curve), the grey line is the median velocity (initial value for the model), the blue dashed curve is the strength of the tangential bisymmetry, and the orange dotted line is the scatter of the model. The vertical light coral area and dashed line shows the adopted bar corotation radius of the LMC, $R_c = 4.20 \pm 0.25$ kpc. In the bottom panel, we show the angular velocity of the LMC as a function of radius. The vertical light coral area and dashed line show the corotation radius of the bar. The horizontal green area and dotted line shows the corresponding bar pattern speed $\Omega_p = 18.5^{+1.2}_{-1.1}$ km s^{-1} kpc^{-1}.

Nevertheless, the impact of other patterns than the bar on Ω_p can be tested by studying the convergence of the TW integrals as a function of the aperture $|\Delta x|$ in which the integrals are measured. This is achieved by progressively increasing $|\Delta x|$ (see e.g. Chemin & Hernandez 2009; Zou et al. 2019). In particular, if the outer LMC spiral arms contaminate the TW integrals when the maximum range of $|\Delta x|$ allowed by the extent of the observation is adopted (as we did in previous sections), then the derived pattern speed is mixing both the bar and spiral patterns, and the bar
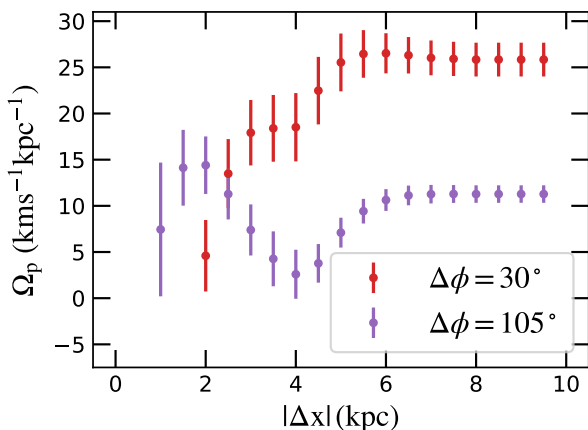
Fig. 12: Convergence tests of the LMC pattern speed from the IPTW method. $|\Delta x|$ is the domain of the numerical integrations of the TW equations (Eq. 4). The convergence has been measured at two orientations of the frame $\Delta\phi = 30°$ and $105°$.

speed may be underestimated. Indeed, pattern speeds of spiral arms are expected to be lower than those of bars (Merrifield et al. 2006; Zou et al. 2019). But with a smaller domain of integration, chosen wisely, the pattern speed could converge to another Ω_p, that of the bar only. We thus varied $|\Delta x|$ within 1 to 9 kpc in the LMC, for two examples of frame orientations, $\Delta\phi = 30°$ and $\Delta\phi = 105°$ (directions outside the LMC principal bar axes, see Fig. 10). Figure 12 presents results of this test for the IPTW method. We find that the integrals have converged at $|\Delta x| = 6$ kpc at the constant values reported in Fig. 10 at the selected $\Delta\phi$ (~ 25 and ~ 10 km s^{-1} kpc^{-1}, respectively). But, for $|\Delta x| < 6$ kpc, Ω_p varies significantly, either increasing and/or decreasing. In other words, we do not find hints of secondary convergence regions of the integrals that would correspond to the LMC bar Ω_p only. To the benefits of the TW method, we can nonetheless see that a rough LMC pattern speed Ω_p found by averaging the TW values over all $\Delta\phi$ orientations is 23.1 km s^{-1} kpc^{-1}, but with a large scatter of 12 km s^{-1} kpc^{-1}. This compares with the value found with the BV model, but not with the one from the Dehnen method.

As consequence, without agreement among the trends found with the various simulations used in the previous works and our present study, and without an identifiable region of bar orientation where ground-truth and measured pattern speeds agree within simulations, the individual pattern speeds found by the TW method in Fig. 10 cannot be representative of the real LMC bar Ω_p. The agreement of Ω_p found by the LTW method with the value found by the IPTW method for the LMC also indicates that the pattern speed of bars measured by means of the LTW method may likely be only representative of any value stemming from random frame orientations fixed by the position angle of the major axis of discs on the sky plane, but not of a global bar angular frequency. The reason of the failure of the TW method in giving a coherent LMC bar pattern speed is unclear. It could be that the tidal interaction with the SMC has broken the conditions of applicability of the method, the disc being no more in full equilibrium. However, both isolated and interacting discs in the simulations show similarities with the observations. It could also indicate that the impact of the spiral arms on the TW integrals is not as negligible as initially thought. More work will be necessary to investigate the origin of this issue with the TW method applied to the simulations and the LMC data.

The pattern speed obtained with the Dehnen method is significantly different from the one of the BV model. Unlike the TW method, we have shown that the Dehnen method performs nicely with an idealised simulation with a well defined rotationally supported stellar disc and no external perturbations and a simulation of an interacting and out-of-equilibrium disc, as it is insensitive to the bar orientation and the outer spiral perturbation, by construction. Applied to the LMC NN complete sample, it surprisingly results in a bar with null rotation, perhaps slightly counter-rotating with respect to the LMC disc. Is this finding realistic? Peculiar bars with such property exist in numerical simulations. In a recent work, it was shown how a bar embedded in a counter-rotating dark matter halo can decelerate, then flip its pattern speed, and finally decoupling its rotation from the disc (Collier & Madigan 2023). After the sign flip, the bar suffers from a large inclination and develops a warped disc. This scenario is difficult to test in real data because we need an observable to check the dark matter halo rotation. Evidence exists that LMC disc is warped (e.g. Choi et al. 2018; Ripepi et al. 2022b), however we do not observe in the kinematic maps a decoupling of the bar motion from that of the disc. Another possible origin of the bar deceleration and counter-rotation could be external and due to the interaction with the SMC and/or the MW. This scenario could be tested with appropriate numerical simulations such as the KRATOS suite of simulations of LMC-SMC-MW-like tidal encounters (Jiménez-Arranz et al., in preparation).

This result does not come without issues, however. An almost non-rotating LMC bar would indeed not show any corotation within the disc since such Ω_p should never cross the Ω curve. It is not an easy task to imagine how the orbits and the disc structure would respond to this peculiar circumstance. An absence of corotation could allow the bar to increase its length and strength out to the disc outskirts, that is, make the orbits of stars and the LMC stellar gravitational potential very elongated throughout the whole LMC disc. Indeed, nothing could prevent it here from growing significantly owing to the absence of corotation and the expected destructive orbits perpendicular to the bar beyond corotation. The LMC stellar density map shows that the outer LMC disc is elliptical (see Fig. 6, and also e.g. Gaia Collaboration et al. 2021b), but the elongation occurs along a direction that is not aligned with the LMC bar. The elongated potential of the LMC likely comes from the tidal interaction with the MW and the SMC. Furthermore, the absence of bar resonances in the inner disc in this framework would make it difficult to interpret the strong variation of the orientation of the velocity bisymmetry evidenced in Fig. 11, which is expected to occur naturally around corotation. We think that the method may be sensitive to dust extinction and completeness effects in the inner LMC region, perhaps more strongly than the other methods. Also, the inner disc is not fully traced by a bar pattern, and the density map clearly shows pieces of spiral arms inside the circle encompassing the bar region. The inner kinematics is not fully dominated by the bar either, due to the smoothly varying phase angle of the velocity bisymmetry within $R = 2 - 4$ kpc (see Fig. 11), likely caused by a winding spiral structure near the tips of the bar. All of these effects may hamper the method from yielding a Ω_p representative of the bar.

Assuming that the corotation radius $R_c = 4.20 \pm 0.25$ kpc measured by the BV model is more representative of the bar properties, it corresponds to a pattern speed of $18.5^{+1.2}_{-1.1}$ km s^{-1} kpc^{-1}. The LTW pattern speed of 30.4 ± 1.3 km s^{-1} kpc^{-1}

would thus be discrepant by 64% from the one inferred here. When compared to its radius of 2.3 kpc, the LMC stellar bar has $R_c/R_1 = 1.8 \pm 0.1$, thus corresponding to a slow bar, according to numerical methods (Athanassoula 1992). Finally, if we assume that the pattern speed has to be estimated using a velocity curve tracing more closely the circular velocity (the rotation curve of the younger stellar populations in Jiménez-Arranz et al. 2023) than the tangential velocity of the whole sample dominated by older stars (upper panel of Fig. 11), then $R_c = 4.2$ kpc would translate into $\Omega_p = 20.9 \pm 1.1$ km s^{-1} kpc^{-1}, which still compares well with the value found for the whole sample.

6. Conclusions

In this work we use three different methods to determine the LMC bar pattern speed, namely the TW method in its original form, when only line-of-sight velocities are available (LTW), and a variation of it that also makes use of astrometric data and in-plane velocity fields (IPTW); the Dehnen method, which is recently published and tested using single snapshots of N-body simulations; and the bisymmetric velocity (BV) method, which is based on the Fourier decomposition of the tangential velocity of a bisymmetric model to constrain the corotation radius of the bar. In order to characterise the strengths and limitations of each of the methods, we applied them to two different simulated barred galaxies. One snapshot of an N-body simulation of an isolated disc galaxy (B5, Roca-Fàbrega et al. 2013) and one snapshot of a N-body simulation of an interacting disc galaxy (KRATOS, Jiménez-Arranz et al., in preparation). The results show that:

- The TW method shows a large dependency on the frame orientation when applied to both B5 and KRATOS simulations.
- The Dehnen method recovers with good accuracy and precision the true pattern speed when applied to both: an idealised simulation with a well defined rotationally supported stellar disc and no external perturbations and a simulation of an interacting and out-of-equilibrium disc.
- The BV method determines the corotation radius and pattern speed of both simulations. The accurate constraint of the strong variation of the kinematic phase angle is crucial for the determination of the corotation radius and thus the bar pattern speed.

From these points, and when applying the methods to the LMC sample, we are inclined to:

- Discard the pattern speeds found with the TW method, because no obvious privileged value is found with the IPTW method, owing to the strong variation of the integrals with the orientation of the $x - y$ plane, thus with the bar viewing angle inside the LMC disc. Also, the unique pattern speed found by the LTW method cannot be representative of a global bar frequency either.
- Evaluate the validity of the bar pattern speed obtained with the Dehnen method. It corresponds to a non-rotating bar, with implications hard to reconcile with the structure and kinematics of the LMC disc.
- Provide a first tentative value of the LMC bar corotation radius at $R = 4.20 \pm 0.25$ kpc with the BV method, as the sharp change of the kinematic phase angle measured through a Fourier modelling is very reminiscent to the signature of corotation seen in numerical simulations. It gives a bar corotation-to-size ratio of $R_c/R_1 = 1.8 \pm 0.1$, which places the LMC bar in the slow rotation regime. The corresponding LMC bar pattern speed is $\Omega_p = 18.5^{+1.2}_{-1.1}$ km s^{-1} kpc^{-1}, reasonably consistent with other estimates found in the literature.

This research has presented novel constraints on the corotation and pattern speed of the stellar bar of the LMC. Our intention is to continue this investigation, taking advantage of forthcoming releases from the *Gaia* mission that will offer improved data quality. With enhanced angular resolution, more precise proper motion measurements, and increased access to line-of-sight velocities, we anticipate it will become easier to establish an LMC sample with reduced limitations, such as the crowding of stars at low radius, or contamination from foreground MW stars. Moreover, working with the 3D velocities of LMC stars will offer new opportunities. These approaches have already been initiated by Jiménez-Arranz et al. (2023). By doing so, we will obtain more reliable estimates of the LMC pattern speed and potentially alleviate tensions that exist among the Dehnen and bisymmetric velocity methodologies tested in this study, which may arise because of the perturbed equilibrium of the LMC. This could be tested with various numerical simulations of the LMC, SMC and MW encounters. We will also study possible variations of the bar pattern speed among various stellar evolutionary phases of the LMC.

References

Aguerri, J. A. L., Debattista, V. P., & Corsini, E. M. 2003, MNRAS, 338, 465
Aguerri, J. A. L., Méndez-Abreu, J., Falcón-Barroso, J., et al. 2015, A&A, 576, A102
Allen, C. & Santillan, A. 1991, Rev. Mexicana Astron. Astrofis., 22, 255

Athanassoula, E. 1992, MNRAS, 259, 345

Belokurov, V. A. & Erkal, D. 2019, MNRAS, 482, L9

Binney, J. & Tremaine, S. 2008, Galactic Dynamics: Second Edition

Bobylev, V. V. & Bajkova, A. T. 2023, arXiv e-prints, arXiv:2305.18408

Bovy, J., Leung, H. W., Hunt, J. A. S., et al. 2019, MNRAS, 490, 4740

Bureau, M., Freeman, K. C., Pfitzner, D. W., & Meurer, G. R. 1999, AJ, 118, 2158

Buta, R. & Combes, F. 1996, Fund. Cosmic Phys., 17, 95

Buttitta, C., Corsini, E. M., Aguerri, J. A. L., et al. 2023, MNRAS, 521, 2227

Cantat-Gaudin, T., Fouesneau, M., Rix, H.-W., et al. 2023, A&A, 669, A55

Castro-Ginard, A., Brown, A. G. A., Kostrzewa-Rutkowska, Z., et al. 2023, arXiv e-prints, arXiv:2303.17738

Chemin, L. & Hernandez, O. 2009, A&A, 499, L25

Choi, Y., Nidever, D. L., Olsen, K., et al. 2018, ApJ, 866, 90

Collier, A. & Madigan, A.-M. 2023, arXiv e-prints, arXiv:2305.06383

Contopoulos, G. & Grosbol, P. 1989, A&A Rev., 1, 261

Contopoulos, G. & Papayannopoulos, T. 1980, A&A, 92, 33

Cuomo, V., Aguerri, J. A. L., Corsini, E. M., & Debattista, V. P. 2020, A&A, 641, A111

Cuomo, V., Lopez Aguerri, J. A., Corsini, E. M., et al. 2019, A&A, 632, A51

Debattista, V. P. 2003, MNRAS, 342, 1194

Debattista, V. P. & Sellwood, J. A. 2000, ApJ, 543, 704

Debattista, V. P. & Williams, T. B. 2004, ApJ, 605, 714

Dehnen, W., Semczuk, M., & Schönrich, R. 2023, MNRAS, 518, 2712

Ferrers, N. 1877, Q.J. Pure Appl. Math, 14, 1

Foreman-Mackey, D., Hogg, D. W., Lang, D., & Goodman, J. 2013, PASP, 125, 306

Fragkoudi, F., Grand, R. J. J., Pakmor, R., et al. 2021, A&A, 650, L16

Gaia Collaboration, Brown, A. G. A., Vallenari, A., et al. 2018, A&A, 616, A1

Gaia Collaboration, Brown, A. G. A., Vallenari, A., et al. 2021a, A&A, 649, A1

Gaia Collaboration, Drimmel, R., Romero-Gómez, M., et al. 2023, A&A, 674, A37

Gaia Collaboration, Luri, X., Chemin, L., et al. 2021b, A&A, 649, A7

Gaia Collaboration, Prusti, T., de Bruijne, J. H. J., et al. 2016, A&A, 595, A1

Gaia Collaboration, Vallenari, A., Brown, A. G. A., et al. 2022, arXiv e-prints, arXiv:2208.00211

Géron, T., Smethurst, R. J., Lintott, C., et al. 2023, MNRAS, 521, 1775

Gerssen, J., Kuijken, K., & Merrifield, M. R. 1999, MNRAS, 306, 926

Ghosh, S. & Di Matteo, P. 2023, arXiv e-prints, arXiv:2308.10948

Guo, R., Mao, S., Athanassoula, E., et al. 2019, MNRAS, 482, 1733

Hernandez, O., Wozniak, H., Carignan, C., et al. 2005, ApJ, 632, 253

Hogg, D. W., Bovy, J., & Lang, D. 2010, arXiv e-prints, arXiv:1008.4686

Jiménez-Arranz, Ó., Romero-Gómez, M., Luri, X., et al. 2023, A&A, 669, A91

Katz, D., Sartoretti, P., Guerrier, A., et al. 2022, arXiv e-prints, arXiv:2206.05902

Lucchini, S., D'Onghia, E., & Fox, A. 2022, in AAS/Division of Dynamical Astronomy Meeting, Vol. 54, AAS/Division of Dynamical Astronomy Meeting, 201.01

Meidt, S. E., Rand, R. J., Merrifield, M. R., Shetty, R., & Vogel, S. N. 2008, ApJ, 688, 224

Merrifield, M. R. & Kuijken, K. 1995, MNRAS, 274, 933

Merrifield, M. R., Rand, R. J., & Meidt, S. E. 2006, MNRAS, 366, L17

Miyamoto, M. & Nagai, R. 1975, PASJ, 27, 533

Niederhofer, F., Cioni, M.-R. L., Schmidt, T., et al. 2022, MNRAS, 512, 5423

Rand, R. J. & Wallin, J. F. 2004, ApJ, 614, 142

Ripepi, V., Chemin, L., Molinaro, R., et al. 2022a, MNRAS, 512, 563

Ripepi, V., Chemin, L., Molinaro, R., et al. 2022b, MNRAS, 512, 563

Roca-Fàbrega, S., Valenzuela, O., Figueras, F., et al. 2013, MNRAS, 432, 2878

Romero-Gómez, M., Figueras, F., Antoja, T., Abedi, H., & Aguilar, L. 2015, MNRAS, 447, 218

Roshan, M., Ghafourian, N., Kashfi, T., et al. 2021, MNRAS, 508, 926

Sellwood, J. A. 2014, Reviews of Modern Physics, 86, 1

Shapley, H. 1951, Publications of Michigan Observatory, 10, 79

Shimizu, T. & Yoshii, Y. 2012, in Astronomical Society of the Pacific Conference Series, Vol. 458, Galactic Archaeology: Near-Field Cosmology and the Formation of the Milky Way, ed. W. Aoki, M. Ishigaki, T. Suda, T. Tsujimoto, & N. Arimoto, 341

Spekkens, K. & Sellwood, J. A. 2007, ApJ, 664, 204

Tremaine, S. & Weinberg, M. D. 1984, ApJ, 282, L5

van der Marel, R. P. 2001, AJ, 122, 1827

van der Marel, R. P., Alves, D. R., Hardy, E., & Suntzeff, N. B. 2002, AJ, 124, 2639

Wan, Z., Guglielmo, M., Lewis, G. F., Mackey, D., & Ibata, R. A. 2020, MNRAS, 492, 782

Williams, T. G., Schinnerer, E., Emsellem, E., et al. 2021, AJ, 161, 185

Wolf, C., Onken, C. A., Luvaul, L. C., et al. 2018, PASA, 35, e010

Zou, Y., Shen, J., Bureau, M., & Li, Z.-Y. 2019, ApJ, 884, 23

Appendix A: Test-particle simulation

In this section, we apply the methods described in Section 2 to an idealised simulation of a barred disc galaxy in statistical equilibrium with the imposed potential. We briefly describe the characteristics of the simulation and the results of the methods applied to it.

We use a 5 million test particle simulation with initial conditions, galactic potential, and steps performed in the integration process as described in Romero-Gómez et al. (2015). We refer to this simulation as the TP simulation. The initial conditions for positions and velocities were drawn for a disc density distribution following a Miyamoto-Nagai disc potential (Miyamoto & Nagai 1975) with a typical scale-height ($h_z = 300$ pc) and radial velocity dispersion ($\sigma_U = 30.3$ km s^{-1}) of a red clump star. Then we integrate the initial conditions in the axisymmetric potential of Allen & Santillan (1991) for 10 Gyr, after that we introduce the Galactic bar potential adiabatically during four bar rotations, and we integrated another 16 bar rotations so that the particles achieve a statistical equilibrium with the final bar potential. The galactic bar consists of the superposition of two aligned Ferrers ellipsoids (Ferrers 1877), one modelling a triaxial bulge with a semi-major axis of 3.13 kpc, and the second modelling a long thin bar with a semi-major axis of 4.5 kpc, with an angular orientation of 20°. In the TP simulation, we impose that the bar rotates counter-clockwise as a rigid body with a constant pattern speed of 42 km s^{-1} kpc^{-1}, placing the corotation resonance at $R_c = 4.9$ kpc, measured as in the B5 simulation. The TP simulation represents the ideal configuration to estimate a bar pattern speed with the different methods due to the only barred perturbation and being in statistical equilibrium with the imposed potential.

Figure A.1 shows the surface density (left panel), the radial velocity (middle panel) and the residual tangential velocity (right panel) maps for the TP simulation. The map of the residuals has been obtained by subtracting the rotation curve to the V_ϕ map. We observe the bar and no obvious spiral arms, which is expected because only a bar potential is modelled. In both radial and residual tangential velocity maps, we also observe a kinematic quadrupole caused by the stellar orbits shaping the bar. In every panel, we highlight the bar region identified by the Dehnen method by green dashed circles, with inner and outer circles corresponding to R_0 and R_1, respectively. The grey dashed lines trace the bar minor and the major axes found by the method. The bar orientation ϕ_b is in agreement with the orientation observed in the surface density, and separates remarkably the quadrupole patterns in two parts. The Dehnen method infers a value of $\Omega_p = 42.0 \pm 0.2$ km s^{-1} kpc^{-1}, in agreement with the imposed value. Values are summarised in Table A.1.

Figure A.2 shows the impact of the variation of the orientation of the Cartesian frame on the derived pattern speed using the LTW and IPTW methods, by rotating the reference x and y axes around the $z-$axis in the simulation. The rotation of the Cartesian frame before sky projection allows the TW integrals (measured parallel to the major axis) to view the bar and spiral perturbations through various angles. Note that in this case, where no other non-axisymmetric component but the bar, and being in statistical equilibrium, the recovered pattern speed using both versions of the TW method show comparable trends. As a known issue of the TW, the integrals do not converge when the slit is aligned with the bar axes (Tremaine & Weinberg 1984). The IPTW shows a pattern speed systematically lower by $\sim 10\%$ from the true value, about twice as large as the systematic shown by the LTW method.

Figure A.3 presents results of the IPTW method for the TP simulation. Again, we show here two different reference frame orientations: the original one, with $\Delta\phi = 0°$(top row) and the one with the bar major axis parallel to the x-axis, $\Delta\phi = 159°$(bottom row), for illustrative purposes. In the first case, there is a clear linear trend and the IPTW recovers a bar pattern speed $\Omega_p = 39.9 \pm 0.4$ km s^{-1} kpc^{-1}, with a relative difference smaller than 5% from the imposed value. In the second case, the TW $x-$integrals are perfectly aligned with the bar major axis, as expected in the presence of only a bar potential. The $\langle x \rangle$ values are then very close to zero, so there is not a clear trend in this case (it would give similar results when the TW integrals are evaluated at another viewing angle along the bar minor axis). We recover here a counter-clockwise pattern speed of $\Omega_p = 23.4 \pm 2.8$ km s^{-1} kpc^{-1} which differs by almost 50% from the imposed value. The TW method thus performs better when no prominent sub-structures exist in the disc, as a well-known issue, integrals should not be made along the major or minor axes of the bar.

Finally, in Fig. A.4, we show the results of applying the BV method to the TP simulation, the value for corotation we derive is $R_c = 4.8 \pm 0.5$ kpc, and the bar pattern speed is $\Omega_p = 43.3^{+5.0}_{-4.2}$ km s^{-1} kpc^{-1}, which exceeds the true value of 42 km s^{-1} kpc^{-1}, although remaining comparable with it given the lower quoted uncertainties. Values are summarised in Table A.1.
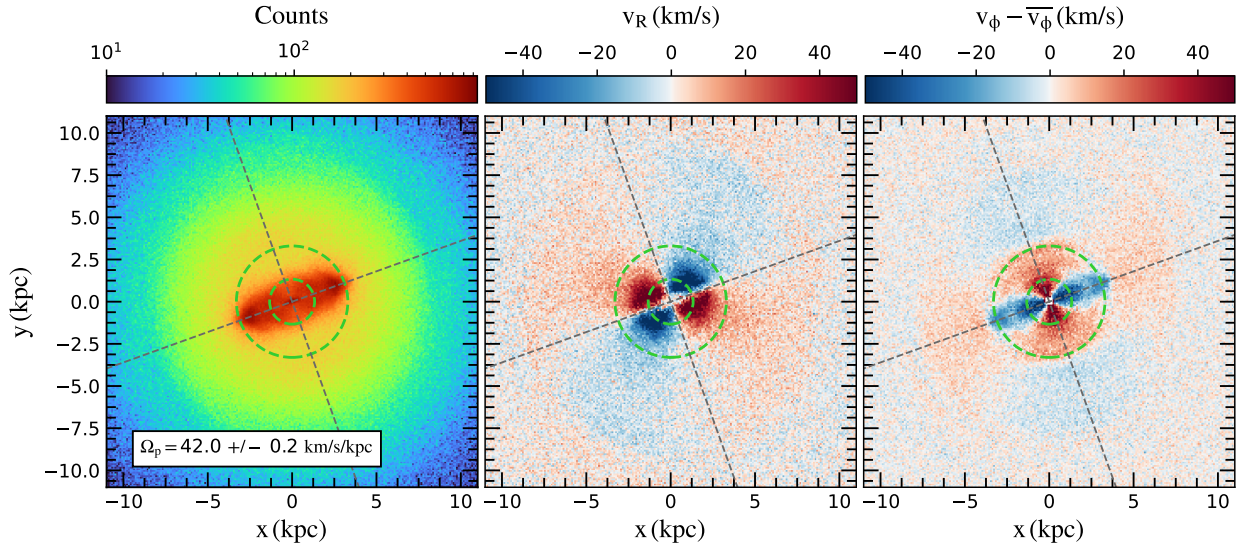
Fig. A.1: Application of the Dehnen method to the TP simulation. Surface density (left), median radial velocity map (center) and median residual tangential velocity map (right). The bar region identified by Dehnen method (see values in Table A.1) is indicated by green dashed circles. The grey dashed lines trace the bar minor and the major axes.

Simulation	Reference	Dehnen method				BV method	
	Ω_p	R_0	R_1	Ω_p	ϕ_b	R_c	Ω_p
TP	42.0	1.33	3.30	42.0 ± 0.2	19.8 ± 0.1	4.8 ± 0.5	$43.3^{5.0}_{-4.2}$

Table A.1: Results of the Dehnen and the BV methods applied to TP simulation, compared to the reference value (obtained using finite-differences). The inner, outer and corotation radii R_0, R_1 and R_c are in kpc. The bar pattern speed Ω_p and phase angle ϕ_b are in km s^{-1} kpc^{-1} and degrees, respectively.

Fig. A.2: Same as in Fig. 2 but for the TP simulation.

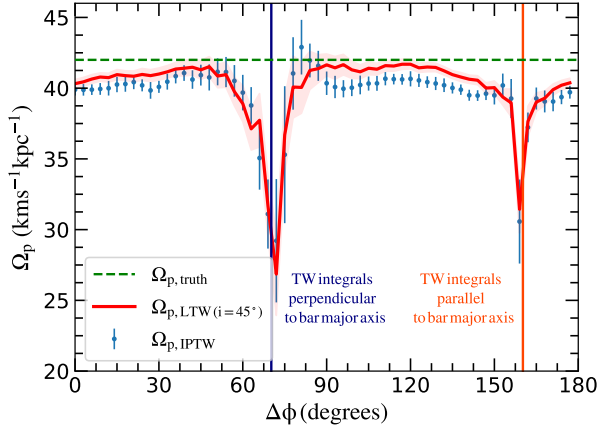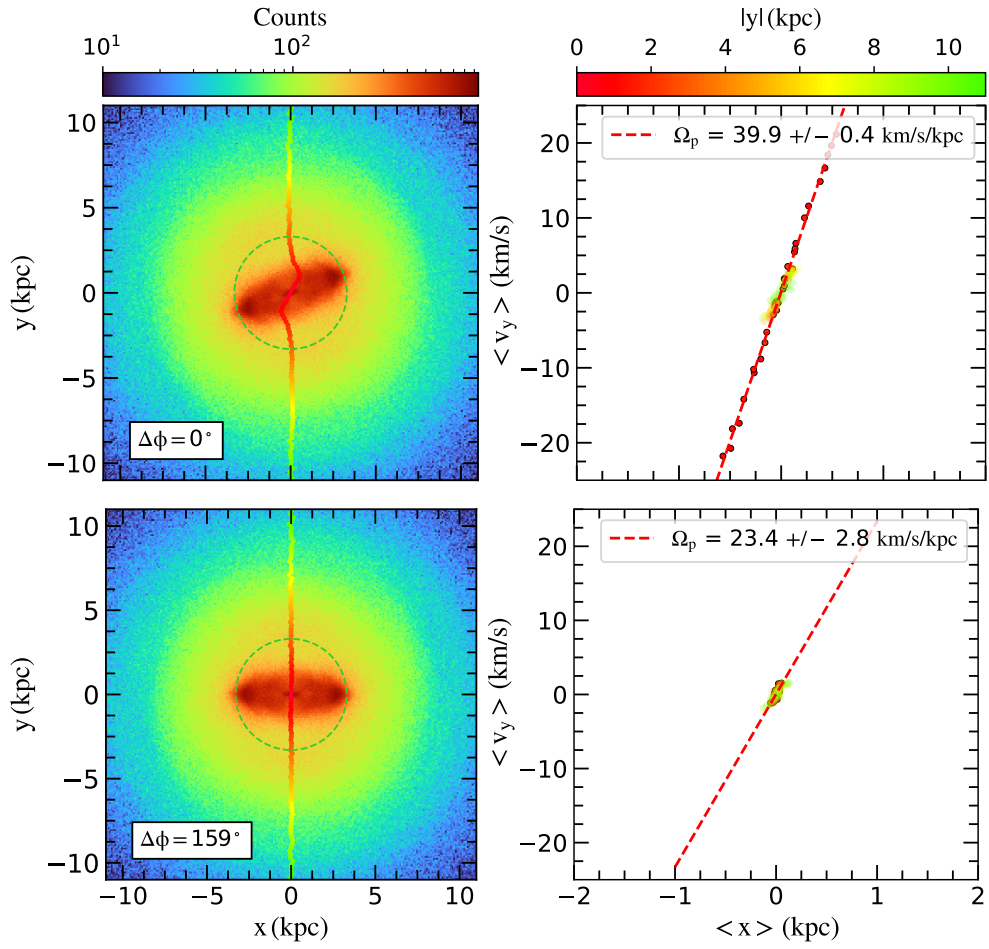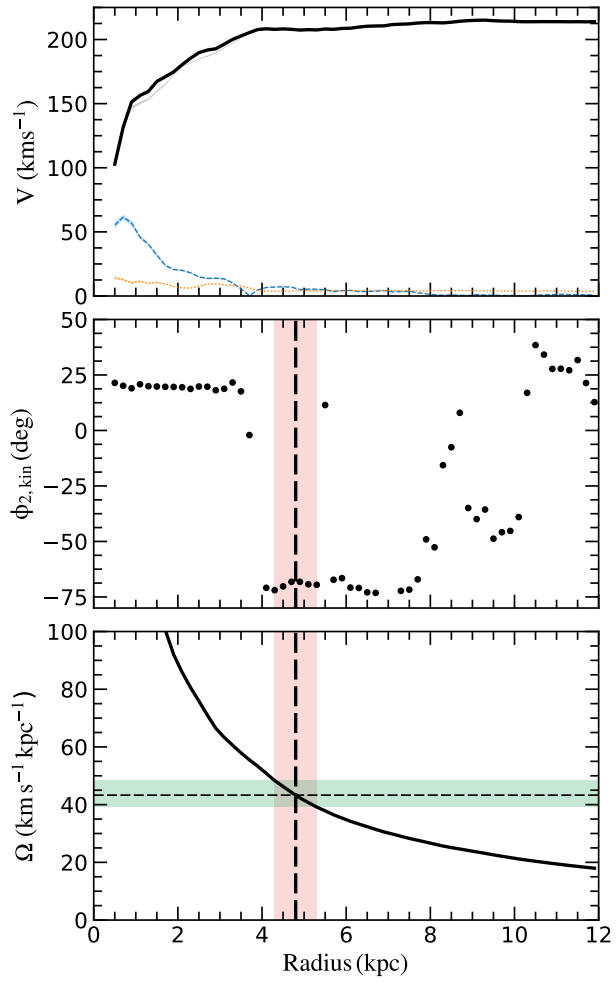Fig. A.3: Same as in Fig. 3 for the TP simulation.

Fig. A.4: Same as in Fig. 5 but for the TP simulation.

Part II

SIMULATIONS OF THE MAGELLANIC CLOUDS

KRATOS: N-BODY SIMULATIONS FOR THE LMC DISC KINEMATICS

This Chapter contains a paper submitted (on 22 December 2023) to the Astronomy and Astrophysics journal.

For the last thousands of million years, the Large Magellanic Cloud (LMC) and Small Magellanic Cloud (SMC) have been interacting with one another, while falling towards the Milky Way (MW). Since observations only offer a static picture of the entire process, numerical simulations are used to study these kinds of systems. In the last years, most of the efforts have been centred around attempting to recreate the neutral gas characteristics and distribution of those galaxies through hydrodynamical simulations.

In this work, we present KRATOS, a comprehensive suite of 28 open access and pure N-body simulations of isolated and interacting LMC-like galaxies, to study the formation of substructures in their disc after the interaction with an SMC-mass galaxy. This is the first paper of a series that will be dedicated to the analysis of this complex interaction.

The 11 sets of simulations, each with a maximum of three configurations, contain: 1) a control model of an isolated LMC-like galaxy; 2) a model including the interaction with an SMC-mass galaxy; and 3) the most realistic configuration in which the LMC-like galaxy may interact with both an SMC-mass and MW-mass galaxy.

First, the infall history between the three galaxies is studied in each simulation. Second, the morphological and kinematic characteristics of the LMC-like disc galaxy are analysed during the interaction, which include investigating the disc scale height and kinematic maps. Finally, our analysis involves describing the strength, length, off-centeredness, and pattern speed of the bar when it is developed.

The wide range of results obtained in the KRATOS simulations, such as the formation of bars, warped discs, or different spiral arm configurations, show that these simulations are capable of investigating a large variety of galaxy morphologies that are similar to the LMC. Those directly correspond to distinct disc kinematic maps, making them well-suited for an initial interpretation of the data (see Chapters 2 and 4). We observe from the simulations that tidal interactions can: increase the height of the disc scale; generate and destroy bars; and provide a natural explanation for the off-centered stellar bars. Interaction has no significant effect on the pattern speed or bar length of long-lived bars.

The first scientific results presented in this work demonstrate that the high spatial, temporal, and mass resolution employed in the KRATOS simulations is suitable for the goal of investigating the internal kinematics of LMC-like discs.

KRATOS: A large suite of N-body simulations to interpret the kinematics of the LMC disc

Ó. Jiménez-Arranz[1,2,3], S. Roca-Fàbrega[4,5], M. Romero-Gómez[1,2,3], X. Luri[1,2,3],
M. Bernet[1,2,3], P. J. McMillan[6,4], and L. Chemin[7]

[1] Departament de Física Quàntica i Astrofísica (FQA), Universitat de Barcelona (UB), C Martí i Franquès, 1, 08028 Barcelona, Spain
[2] Institut de Ciències del Cosmos (ICCUB), Universitat de Barcelona, Martí i Franquès 1, 08028 Barcelona, Spain
[3] Institut d'Estudis Espacials de Catalunya (IEEC), C Gran Capità, 2-4, 08034 Barcelona, Spain
[4] Lund Observatory, Division of Astrophysics, Lund University, Box 43, SE-221 00 Lund, Sweden
[5] Departamento de Física de la Tierra y Astrofísica, UCM, and IPARCOS, Facultad de Ciencias Físicas, Plaza Ciencias, 1, Madrid, E-28040, Spain
[6] School of Physics Astronomy, University of Leicester, University Road, Leicester, LE1 7RH, UK
[7] Instituto de Astrofísica, Universidad Andres Bello, Fernandez Concha 700, Las Condes, Santiago RM, Chile

ABSTRACT

Context. The Large and Small Magellanic Cloud (LMC and SMC, respectively) are the closest and brightest satellites of the Milky Way (MW) and, for the previous thousands of million years, they have been interacting with one another. Since observations only provide a static picture of the entire process, numerical simulations are used to study these kinds of systems, and most of them have been focused on attempting to recreate the neutral gas distribution and characteristics through hydrodynamical simulations.
Aims. We present KRATOS, a comprehensive suite of 28 open access pure N-body simulations of isolated and interacting LMC-like galaxies, to study the formation of substructures in their disc after the interaction with an SMC-mass galaxy. This is the first paper of a series that will be dedicated to the analysis of this complex interaction.
Methods. Simulations are grouped in 11 sets of at most three configurations each containing: 1) a control model of an isolated LMC-like galaxy; 2) a model that contains the interaction with an SMC-mass galaxy, and; 3) the most realistic configuration where both an SMC-mass and MW-mass galaxies may interact with the LMC-like galaxy. In each simulation, we analyse the infall history between the three galaxies and examine the morphological and kinematic features of the LMC-like disc galaxy throughout the interaction. This includes investigating the disc scale height and velocity maps. When a bar develops, our analysis involves characterising its strength, length, off-centeredness and pattern speed.
Results. The diverse outcomes found in the KRATOS simulations, including the presence of bars, warped discs, or various spiral arm shapes, demonstrate their capability to explore a range of LMC-like galaxy morphologies. Those directly correspond to distinct disc kinematic maps, making them well-suited for an initial interpretation of the LMC's kinematic maps. From the simulations we note that tidal interactions can: boost the disc scale height; both destroy and create bars, and; naturally explain the off-center stellar bars. The bar length and pattern speed of long-lived bars are not appreciably altered by the interaction.
Conclusions. The high spatial, temporal, and mass resolution used in the KRATOS simulations has been shown to be appropriate for the purpose of studying the internal kinematics of LMC-like disks, as evidenced by the first scientific results presented in this work.

Key words. Galaxies: kinematics and dynamics - Magellanic Clouds - interactions

1. Introduction

Only a few extragalactic stellar structures are visible to the naked eye from Earth. The closest and brightest of those are the Magellanic Clouds (MCs), which are the most massive of the Milky Way (MW) satellite galaxies. Because they are so close, the Large and Small Magellanic Cloud (LMC and SMC, respectively) provide astronomers with a unique window into the complexities of galactic systems. Furthermore, the evident large scale structures they contain, in particular the disc-like structure, the spiral arm and the bar in the LMC, and the stellar bridge that connects both (e.g. Harris 2007; Kallivayalil et al. 2013; Zivick et al. 2019; Gaia Collaboration et al. 2021), makes the LMC-SMC system an ideal laboratory to study the effects of galactic interactions on the evolution of galaxies and their structures with the current amount of data.

The LMC is so peculiar that gives name to a type of galaxies, the Barred Magellanic Spirals (de Vaucouleurs & Freeman 1972). This galaxy is a dwarf bulgeless spiral with a single spiral arm, an off-centred and asymmetric stellar bar, and many star forming regions (e.g. Elmegreen & Elmegreen 1980; Gallagher & Hunter 1984; Zaritsky 2004; Yozin & Bekki 2014; Gaia Collaboration et al. 2021). It is a gas-rich galaxy (e.g. Luks & Rohlfs 1992; Kim et al. 1998) characterised by an inclined disc (e.g. van der Marel & Cioni 2001; van der Marel 2001), with a warp (e.g. Olsen & Salyk 2002; Nikolaev et al. 2004; Ripepi et al. 2022), that lies at a distance of around 50 kpc (Pietrzyński et al. 2019). The SMC has long been thought to be a satellite of the LMC due to its proximity. It is at around 62 kpc from the MW (e.g. Cioni et al. 2000; Hilditch et al. 2005; Graczyk et al. 2014) and 20-25 kpc away from the LMC. The SMC is a gas rich dwarf irregular galaxy (e.g. Rubio et al. 1993; Staveley-Smith et al. 1998), and features a

low metallicity environment (e.g. Choudhury et al. 2018; Grady et al. 2021). An attempt to reconstruct its 3D shape has been carried out using red clump stars and other standard candles and revealed that it is elongated about 15-30 kpc approximately in the east/north-east towards south-west direction (e.g. Subramanian & Subramaniam 2012; Ripepi et al. 2017).

Because of the lack of high-precision data it has been difficult to study the complex interaction between these two satellite galaxies and the MW. With the available data at the time, and by using theoretical models, many authors suggested that the MCs were in fact orbiting the MW, and that they had multiple experienced pericentric passages (e.g. Tremaine 1976; Murai & Fujimoto 1980; Lin & Lynden-Bell 1982; Gardiner et al. 1994). This conclusion was accepted for many years, till new data revealed a different history. This scenario proposed by Besla et al. (2007) using data from HST (Kallivayalil et al. 2006b,a) and theoretical models showed that the MCs are most probably just after their first approach to the MW, with no prior pericentre passages within the last 10 Gyr. Moreover, the authors showed that the orbits of these two galactic systems around the MW are highly eccentric, with apocentres well beyond 200 kpc, and with orbital periods exceeding 5 Gyr. The debate on the date of the first pericenter is however not closed, for instance, Vasiliev (2023a) claims that a scenario in which the LMC is on its second passage around the MW (that would have occurred 5-10 Gyr ago at a distance ≳ 100 kpc) is consistent with current observational constraints on the mass distribution and relative velocity of both galaxies.

Focusing now on the LMC-SMC system, there is also controversy on when the interaction between the two satellites started. Gardiner & Noguchi (1996) stated that the two MCs most recent near encounter took place in between 150 and 200 Myr ago and that it was with a distance of less than 10 kpc. They also showed that this interaction would have led to the formation of the tidal structure known as Magellanic Bridge, which is a structure found in the region between the two galaxies (e.g. Kerr et al. 1954; Misawa et al. 2009). First, Hindman et al. (1963) found that this tidal structure contains neutral hydrogen suggesting that it should have been formed recently and could host active star formation. Decades later, a stellar population of blue main-sequence stars in the Bridge was discovered by Irwin et al. (1985) confirming that star formation is ongoing within this structure. In the last years the Magellanic Bridge has been studied using both simulations (e.g. Besla et al. 2012; Diaz & Bekki 2012) and observations (e.g. Harris 2007; Kallivayalil et al. 2013; Bagheri et al. 2013; Noël et al. 2013; Skowron et al. 2014; Carrera et al. 2017; Zivick et al. 2019; Schmidt et al. 2020; Gaia Collaboration et al. 2021) trying to learn about its formation mechanism and also using it to better understand the complex interaction between the two satellite galaxies.

The study of the formation and evolution of the LMC-SMC system cannot be done only by using observational data. Observations give us only a static picture of the whole process, and that is why most researchers studying these kinds of systems use numerical simulations. These studies have naturally been focused on trying to recreate the distribution of neutral gas and the position and properties of the streams using N-body simulations that include hydrodynamics, with the goal of reproducing the whole past interaction process.

For instance, Pardy et al. (2018) presented hydrodynamic simulations to reproduce the observations by Hammer et al. (2015) that showed that the Magellanic Stream is structured into two filaments. In this study, the authors suggested that to reproduce the observations, the MCs should have been more gas-rich in the past, and that the gas stripping efficiency of the LMC

should have been much higher. Later, Wang et al. (2019) show, for the first time, that a physical modelling is capable to explain and reproduce the enormous quantities of gas stripped from the MCs, namely more than 50 per cent of their initial content. More recently, Tepper-García et al. (2019) include for the first time a weakly magnetised and spinning Magellanic Corona, a halo of warm gas surrounding the LMC and SMC, in their simulations to reproduce the location and the extension of the Magellanic Stream on the sky. Lucchini et al. (2020) also included a Magellanic Corona to show that its presence can explain the ionised gas component of the Magellanic Stream. Finally, Lucchini et al. (2021) present new simulations of the formation of the Magellanic Stream with a new first-passage interaction history of the MCs where the orientation of the SMC's orbit around the LMC is qualitatively different and leads to a different 3D spatial positioning of the Stream from previous models. Their simulated Stream is only at ∼20 kpc away from the Sun at its closest point, whereas previous first-infall models predicted a distance of 100-200 kpc.

Similarly, the study of the interaction between the MCs and the MW can not only rely on observations but requires again the use of numerical simulations. As mentioned before, several N-body simulations have been run and used to analyse the effect of the MCs (or, more specifically, the LMC) on the MW (e.g. Garavito-Camargo et al. 2019; Petersen & Peñarrubia 2021) and to determine the MCs past orbits (e.g. Vasiliev 2023b,a). However, the study of the effect of these interactions on the internal structures of the LMC-like the disc, the bar and the spiral arm has only been carried out by a few authors. In particular, only the work by Besla et al. (2012) extensively explored these features. Understanding the formation process of these LMC morphological attributes can potentially unveil the details on the interaction occurred between these two satellite galaxies, and also of them with the MW.

In this context, here we present KRATOS, a comprehensive suite of 28 open access pure N-body simulations of isolated and interacting LMC-like and SMC-mass galaxies. With these models we study the formation of substructures in an LMC-like disc after the interaction with an SMC-mass system and we compare them with the observations (see, for example, the kinematic maps of the LMC using *Gaia* data on Gaia Collaboration et al. 2021; Jiménez-Arranz et al. 2023b). This is the first paper of a series that will be dedicated to the analysis of this complex interaction. In this work, we show the high degree of detail of the simulations and, as a first scientific case, we study the infall history between the three galaxies and the evolution of the LMC-like morphological and kinematic features, such as the kinematic maps, the disc scale height and the properties of the bar, when this is formed. A more specific analysis on the LMC-SMC interaction is left for successive papers of the series.

The paper is organised as follows. In Sect. 2, we describe the code, initial conditions and tools used to run and analyse the KRATOS suite. In Sect. 3, we characterise the infall history between the three galaxies. In Sect. 4, we study the morphological and kinematic features of the LMC-like galaxy at present time. In Sect. 5, we discuss how the scale height of the LMC-like disc changes with the different pericentres of the SMC-mass system. In Sect. 6, we study the properties' evolution of the LMC-like galaxy bar. In Sect. 7, we contextualise our results with the LMC observations and other works in the literature. Finally, in Sect. 8, we summarise the main conclusions of this work.

2. KRATOS simulations

KRATOS (Kinematic Reconstruction of the mAgellanic sysTem within the OCRE Scenario) consists of 28 pure N-body simulations of isolated and interacting LMC-like and SMC-mass galaxies[1]. In these models, we do not include hydrodynamics or cosmological environment. The 28 models are grouped in 11 sets of at most three models each containing: 1) a control model with an isolated LMC-like galactic system; 2) a model with both an LMC-like and a SMC-mass system; 3) a model that additionally includes a MW-mass system. Hereafter we refer to the LMC-like, SMC-mass, and MW-mass galactic systems as $G_{\rm LMC}$, $G_{\rm SMC}$, and $G_{\rm MW}$, respectively. By implementing these three scenarios, we aim to distinguish the local instabilities in the $G_{\rm LMC}$ disc from the products of the interactions between these galaxies. For each of the three scenarios, we vary a set of free parameters, namely, the $G_{\rm LMC}$ disc instability (given by the Toomre Q parameter), the $G_{\rm LMC}$ disc mass, the $G_{\rm LMC}$ halo mass, the $G_{\rm SMC}$ mass, the $G_{\rm MW}$ mass and the $G_{\rm MW}$ halo mass distribution. In order to better understand the effect of each of the free parameters on the $G_{\rm LMC}$-$G_{\rm SMC}$ interaction and on the formation of $G_{\rm LMC}$'s disc structures, we vary one parameter at a time.

Each model in the KRATOS suite has been run within a 2.85^3 Mpc^3 box with periodic boundary conditions. The simulations have a spatial and temporal resolution of 10 pc and 5000 yr, respectively. The minimum mass per particle is $4 \times 10^3 M_\odot$. All simulations have been run for 4.68 Gyr, starting at the apocenter between the MCs after their second interaction. According to Lucchini et al. (2021), this happened 3.5 Gyr ago. Thus, we have run the simulations for more than one gigayear after the MCs match the most recent observations (see Sec. 2.2).

2.1. The code

The numerical simulations have been computed using the Eulerian pure N-body code ART (Kravtsov et al. 1997). The code is based on the adaptive mesh refinement technique, which allows to selectively boost resolution in a designated region of interest surrounding a chosen dark matter (DM) halo.

Most of the KRATOS suite was run in virtual machines in the Google cloud provided by the Open Clouds for Research Environments (OCRE) project funded by the European Union's Horizon 2020 research and innovation program. We used 24 virtual machines, each with 16 cores, 128GB RAM, and 250GB SSD to run each simulation independently (and simultaneously) for three weeks. Four additional simulations have been run in the Brigit supercomputer of the Universidad Complutense de Madrid, using 16 cores each. The full set of simulations amount to a total of 285 000 hours of computational time.

2.2. Initial conditions

As mentioned earlier, our approach involves systematically varying the parameters individually, one per simulation. The initial conditions for the construction of the fiducial $G_{\rm LMC}$, $G_{\rm SMC}$, and $G_{\rm MW}$ galaxies are outlined in Table 1, whereas the initial conditions for the other simulations of the suite are outlined in Table 2. The colour code used for each set is kept all throughout the paper. The initials conditions were produced using the RODIN code as in Roca-Fàbrega et al. (2012, 2013).

---

[1] The simulations are open access. Readers interested in using the simulations developed in the paper can access them at [include link (TBD)]

In all simulations, we model the $G_{\rm LMC}$ system as a stellar exponential disc embedded in a live dark matter Navarro-Frenk-White (NFW, Navarro et al. 1996) halo. Its stellar disc has a scale length and scale height of 2.85 and 0.20 kpc, respectively. We consider a $G_{\rm LMC}$ disc truncation radius of 11.5 kpc. The $G_{\rm LMC}$ NFW DM halo has a concentration of $C = 9$. Its DM halo is composed of 7 species of DM particles, each with twice the mass of the previous one, with the most massive ones being the farthest from the disc. It has been shown that the contamination by massive dark matter particles in the region of the disc is low, as discussed in Valenzuela & Klypin (2003). The $G_{\rm SMC}$ system is modelled as a simple NFW halo with a concentration of $C = 15$. Both $G_{\rm SMC}$ dark matter and stellar particles are generated at once following the NFW profile. For visualisation and analysis purposes we later define the stellar component of the $G_{\rm SMC}$ as the particles that have the strongest gravitational binding. This selection was carried out until the cumulative mass of the chosen particles equaled the baryonic matter mass observed in the SMC. To ensure that the inner region is not depleted of DM particles, we select one out of every two particles as a star particle. This selection process does not have any impact on the models as all particles, both DM and stellar, are treated as collisionless point-like sources of gravity. By employing this particle selection strategy, we just aimed to capture the evolution of the stellar component and its interaction with the surrounding environment. Finally, since we are mostly interested in the effects that the interaction between the three galaxies produces in the $G_{\rm LMC}$ disc, we only model the MW DM content in $G_{\rm MW}$, thus neglecting the contribution of the MW disc to the total mass of $G_{\rm MW}$. We employ an NFW profile whose concentration parameter chosen was set to $C = 12$.

The fiducial simulation has the same initial conditions as the simulations performed in Lucchini et al. (2021) for the density, kinematics and orbital parameters. The main differences between their work and our simulations are: 1) all models in the KRATOS suite are pure N-body whereas their simulation considers hydrodynamics, and; 2) the KRATOS suite has a higher spatial, temporal, and mass resolution. We consider a $G_{\rm LMC}$ disc with a mass of $5 \times 10^9 M_\odot$, a high-mass disc if we compare it with observations (e.g. van der Marel et al. 2002). The $G_{\rm LMC}$ disc Toomre Q parameter is 1.2. The $G_{\rm LMC}$ system has a total DM mass of $1.8 \times 10^{11} M_\odot$. We consider a $G_{\rm SMC}$ system with DM mass of $1.9 \times 10^{10} M_\odot$, and baryonic mass of $2.6 \times 10^8 M_\odot$. The DM mass of the $G_{\rm MW}$ system DM is considered to be $10^{12} M_\odot$. Finally, regarding the orbital parameters, we chose as the starting point the $G_{\rm SMC}$ being at the second apocenter of the LMC-SMC interaction, which occurred 3.5 Gyr ago. We choose this approximation because in the present time most morphological and kinematic footprints of this very past interaction would have been already erased by other internal and external processes within each one of the systems. For our fiducial model we also set the orbit of the $G_{\rm SMC}$ around the $G_{\rm LMC}$ as being prograde. Table 1 summarises the initial conditions of the fiducial model.

The variations of the different parameters with respect to the fiducial simulation that we consider are: 1) a lighter $G_{\rm LMC}$ disc with a baryonic mass of $3 \times 10^9 M_\odot$; 2) a lighter and a heavier $G_{\rm LMC}$ DM halo with a mass of $0.8 \times 10^{11} M_\odot$ and $2.5 \times 10^{11} M_\odot$, respectively; 3) a lighter $G_{\rm SMC}$ with DM mass of $0.5 \times 10^{10} M_\odot$; 4) a $G_{\rm MW}$ system almost an order of magnitude lighter, with mass equal to $0.15 \times 10^{12} M_\odot$, to also cover the lowest $G_{\rm MW}$ estimations; 5) a $G_{\rm MW}$ system modelled as a single particle of $10^{12} M_\odot$ (point-like mass approximation), to test the effect on the $G_{\rm LMC}$-$G_{\rm SMC}$ interaction of changing the DM distribution. Table 2 summarises the differences between the 11 sets of simulations.

	$G_{\rm LMC}$	$G_{\rm SMC}$	$G_{\rm MW}$
DM Concentration	9	15	12
DM Mass ($M_\odot$)	1.8×10^{11}	1.9×10^{10}	10^{12}
Stellar Mass ($M_\odot$)	5.0×10^{9}	2.6×10^{8}	-
Toomre parameter Q	1.2	-	-
Stellar Scale Height (kpc)	0.20	-	-
Stellar Scale Length (kpc)	2.85	-	-
Stellar Disc Truncation Radius (kpc)	11.5	-	-
Number of Stellar Particles	1 200 002	62 402	-
Number of DM Particles	24 281 795	4 497 354	1 999 733
DM Species	7	1	1
Mass Resolution ($M_\odot$)	4×10^{3}	4×10^{3}	5×10^{5}
Initial Position (kpc)	(0, 0, 0)	(-67.15, -134.09, 33.23)	(-47.36, -546.38, -150.52)
Initial Velocity (km/s)	(0, 0, 0)	(11.72, 21.81, -16.60)	(-1.71, 99.02, 63.73)

Table 1: Initial conditions of the fiducial model presented in this work.

2.3. Centering, alignment and bar's pattern speed

To study the general features of the $G_{\rm LMC}$ disc we take the center-of-mass of the $G_{\rm LMC}$ system as the center of the reference frame (see Sect. 4). On the other hand, in Sect. 6, we are interested in studying the $G_{\rm LMC}$'s bar, which is not located in the center-of-mass of the system when tidally perturbed, thus, we redefine the reference frame center to the one defined by the bar's density center. To find its density center, we first sample each particle's coordinate (x, y, z) in the range -6.2 kpc to 6.2 kpc with 301 equidistributed bins. Later, we apply a Gaussian kernel density estimation (KDE) of 3.0 kpc-bandwidth and we take the point with the highest KDE density as the reference center. This approach involved testing different bandwidth values to identify and select the most suitable value for determining the bar center.

Defining the galactic disc plane is also a difficult task, especially when the $G_{\rm SMC}$ and $G_{\rm MW}$ interact with the $G_{\rm LMC}$. In these interactions, the $G_{\rm LMC}$ disc suffers strong perturbations sometimes almost destroying the disc. In this situation, the strategy to define the $G_{\rm LMC}$ galactic disc plane is to compute the angular velocity vector $\vec{L}$ of all the disc's stars and take the perpendicular plane.

Finally, in Sect. 6, we use the Dehnen method (Dehnen et al. 2023), which was also used to determine the LMC bar pattern using *Gaia* DR3 data in Jiménez-Arranz et al. (2023a), to find the pattern speed of $G_{\rm LMC}$ bars generated in our simulations. This method measures the bar pattern speed Ω_p and the orientation angle ϕ_b of the bar from single snapshots of simulated barred galaxies. For more details about the method see Sect 2 and Appendix B of Dehnen et al. (2023).

3. Infall history

In this section, we study the infall history of the three galaxies. We notice that our results differ from the one by Lucchini et al. (2021) in the time of the closest approach to the $G_{\rm MW}$ system. Whereas Lucchini et al. (2021) needed to run the simulation for 3.46 Gyr to obtain two pericenter passages between the $G_{\rm LMC}$ and $G_{\rm SMC}$ galaxies (see their Figure 1 right panel), we needed almost half

a gigayear more for the fiducial simulation (K3). The origin of this discrepancy is still unclear but, as mentioned above, the main differences between our models and the ones in Lucchini et al. (2021) are their lower spatial and mass resolution, and the lack of the hydrodynamical content in ours. The almost one order of magnitude on the spatial resolution can drive big differences on the interaction times due to how accurately the individual orbits of stars and dark matter are calculated (see e.g. Roca-Fàbrega et al. 2023, submitted to ApJ). Also, baryonic processes like SNe feedback can modify the density distribution of the central halo which would lead to a change on the acceleration suffered by the $G_{\rm SMC}$ system and, thus, on the interaction times (e.g. Duffy et al. 2010). The Lucchini model has a hot gas corona of $10^{11} M_\odot$, which has roughly the same effect on the gravitational forces on the MCs as giving the dark-matter halo an extra $10^{11} M_\odot$ in mass. Finally, they use a Hernquist halo for the dark matter, not a NFW, which means the mass is more centrally concentrated, i.e., having something like the effect of having a point-like MW (though less extreme).

In this scenario, as the interaction history of our fiducial simulated galactic system (K3) do not match with the ones obtained in Lucchini et al. (2021), we need to determine at which time our simulated system most resembles the real situation of the $G_{\rm LMC}+G_{\rm SMC}+G_{\rm MW}$ model, i.e. to set what we call the "present time" ($t = 0$) for further analysis. We decide to set as the $t = 0$ the snapshot after 4.0 Gyr from the initial conditions for the following reasons: 1) if we assume that the $G_{\rm LMC}+G_{\rm SMC}$ system already went through two pericenters, our fiducial simulation needs to evolve, at least, for this amount of time (see Sect. 3.1); 2) the real observed LMC disc morphology has very characteristic features such as a single spiral arm and an off-center bar, and these features are observed in the $G_{\rm LMC}$ disc of the $G_{\rm LMC}+G_{\rm SMC}+G_{\rm MW}$ fiducial simulation just at this time (see Sect. 4).

3.1. G_{SMC} to G_{LMC} distance

In Fig. 1 we show the distance between the centre-of-mass of the $G_{\rm LMC}$ and the $G_{\rm SMC}$ galaxies as a function of time. In solid lines we show the $G_{\rm LMC}+G_{\rm SMC}+G_{\rm MW}$ models whereas in dashed lines

	Model label	Configuration	Changes of each set with respect to the fiducial model
K1	Fiducial	G_{LMC}	-
K2	(blue)	$G_{LMC}+G_{SMC}$	
K3		$G_{LMC}+G_{SMC}+G_{MW}$	
K4	$Q = 1.0$	G_{LMC}	$[G_{LMC}]$ Toomre parameter $Q = 1.0$
K5	(light brown)	$G_{LMC}+G_{SMC}$	
K6		$G_{LMC}+G_{SMC}+G_{MW}$	
K7	$Q = 1.5$	G_{LMC}	$[G_{LMC}]$ Toomre parameter $Q = 1.5$
K8	(light red)	$G_{LMC}+G_{SMC}$	
K9		$G_{LMC}+G_{SMC}+G_{MW}$	
K10	$0.45M_{LMC}^{halo}$	G_{LMC}	$[G_{LMC}]$ DM Mass = $0.8 \times 10^{11} M_{\odot}$
K11	(orange)	$G_{LMC}+G_{SMC}$	Number of DM Particles = 11 992 066
K12		$G_{LMC}+G_{SMC}+G_{MW}$	
K13	$1.40M_{LMC}^{halo}$	G_{LMC}	$[G_{LMC}]$ DM Mass = $2.5 \times 10^{11} M_{\odot}$
K14	(green)	$G_{LMC}+G_{SMC}$	Number of DM Particles = 34 924 737
K15		$G_{LMC}+G_{SMC}+G_{MW}$	
K16	$0.60M_{LMC}^{disc}$	G_{LMC}	$[G_{LMC}]$ Stellar Mass = $3.0 \times 10^9 M_{\odot}$
K17	(grey)	$G_{LMC}+G_{SMC}$	Number of Stellar Particles = 720 005
K18		$G_{LMC}+G_{SMC}+G_{MW}$	
K19	$0.60M_{LMC}^{disc}$; $0.45M_{LMC}^{halo}$	G_{LMC}	$[G_{LMC}]$ Stellar Mass = $3.0 \times 10^9 M_{\odot}$
K20	(yellow)	$G_{LMC}+G_{SMC}$	Number of Stellar Particles = 720 005
K21		$G_{LMC}+G_{SMC}+G_{MW}$	$[G_{LMC}]$ DM Mass = $0.8 \times 10^{11} M_{\odot}$
			Number of DM Particles = 11 992 066
K22	$0.60M_{LMC}^{disc}$; $1.40M_{LMC}^{halo}$	G_{LMC}	$[G_{LMC}]$ Stellar Mass = $3.0 \times 10^9 M_{\odot}$
K23	(cyan)	$G_{LMC}+G_{SMC}$	Number of Stellar Particles = 720 005
K24		$G_{LMC}+G_{SMC}+G_{MW}$	$[G_{LMC}]$ DM Mass = $2.5 \times 10^{11} M_{\odot}$
			Number of DM Particles = 34 924 737
K25	$0.25M_{SMC}$	$G_{LMC}+G_{SMC}$	$[G_{SMC}]$ DM Mass = $0.5 \times 10^{10} M_{\odot}$
K26	(red)	$G_{LMC}+G_{SMC}+G_{MW}$	Number of DM Particles = 1 199 900
K27	$0.15M_{MW}$	$G_{LMC}+G_{SMC}+G_{MW}$	$[G_{MW}]$ DM Mass = $0.15 \times 10^{12} M_{\odot}$
	(dark brown)		
K28	Point-like MW	$G_{LMC}+G_{SMC}+G_{MW}$	$[G_{MW}]$ Point-like
	(pink)		

Table 2: Initial conditions of all the simulations presented in this work with respect to the fiducial model. The color code used for each set is kept all throughout the paper.

we show the $G_{LMC}+G_{SMC}$. Purple vertical solid and dashed lines indicate the times of the pericenters, for each one of the models.

In the top panel, we show results from the fiducial simulations (blue lines), which are then used as guiding lines in all other panels (thin shadowed blue lines). The fiducial model shows that the time of the pericenters changes when including the gravitational pull of a G_{MW} system. In particular, when the G_{MW} system is present (solid lines), the pericenter is delayed for about 200 Myr. This result is a consequence of that the G_{SMC} is initially located in between the G_{MW} and the G_{LMC} galaxies, so the gravitational pull partially cancels-out, thus, the G_{SMC} infall towards the G_{LMC} galaxy is slower and delayed. This same effect can also be observed in all other models (see solid vs. dashed lines in all other panels). The presence of a G_{MW} system also has an impact on the orbit of the G_{SMC} around the G_{LMC} galaxy. We can see that the minimum distance at pericenter is also different between the two models (with and without the G_{MW} system). While at the first pericenter the distance is smaller when the G_{MW} system
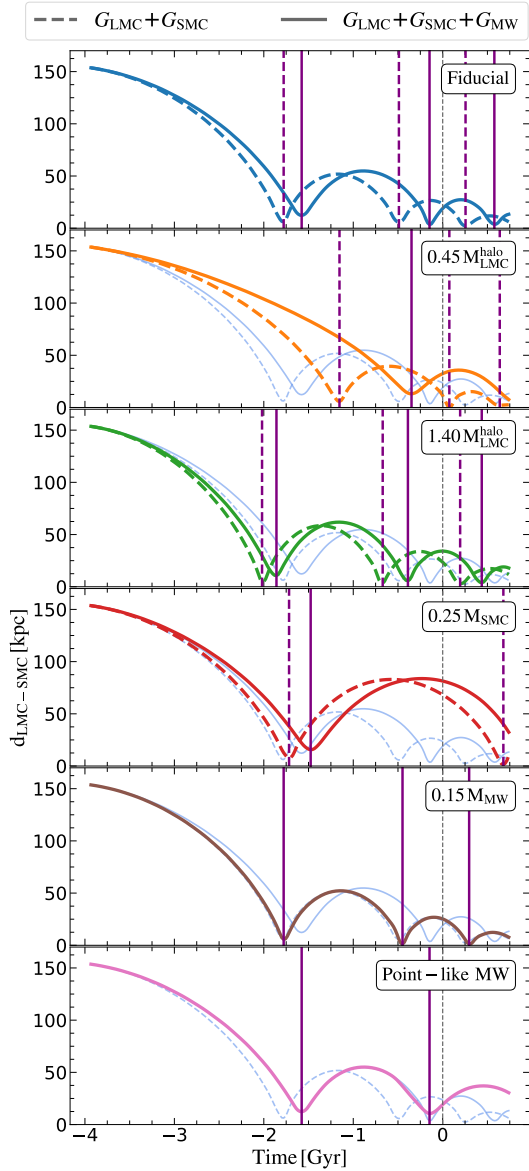
Fig. 1: Distance between the centre-of-masses of the G_{LMC} and G_{SMC} galaxies. The solid (dashed) lines corresponds to the $G_{LMC}+G_{SMC}+G_{MW}$ ($G_{LMC}+G_{SMC}$) models. The different panels represent a different set of simulations (see labels within each panel). The vertical purple solid (dashed) lines correspond to the G_{LMC}-G_{SMC} pericenters of the $G_{LMC}+G_{SMC}+G_{MW}$ ($G_{LMC}+G_{SMC}$) models. The vertical grey dashed line corresponds to the time we choose as the present time $t = 0$ (see Sec. 2.2). For the sake of comparison, in shadowed blue lines it is plotted the orbital history of the MCs for the models of the fiducial set. The set corresponding to a different G_{LMC} disc mass and Toomre parameter are not shown since they show no difference in comparison to the fiducial set.

is not present (6.2 kpc vs. 12.3 kpc), in the second the situation is reversed. This is a clear sign that the orbit has been slightly modified, i.e., that the G_{SMC} system has a different energy and

angular momentum due to the gravitational pull of the G_{MW} system. Although not analysed in this figure, this difference of the minimum distance also has a strong impact on the morphology of the G_{LMC} galaxy disc (see Fig. 3 and Sect. 4), with the disc of the $G_{LMC}+G_{SMC}$ models initially more perturbed than the one in the $G_{LMC}+G_{SMC}+G_{MW}$.

In the second and third panels, we show the effect of changing the mass of the G_{LMC} galaxy DM halo. First, we show that a lighter DM halo (orange lines) produces a delay on the pericenters, while a heavier DM halo (green lines) has the opposite effect. These differences have the same origin as the ones between the $G_{LMC}+G_{SMC}+G_{MW}$ and the $G_{LMC}+G_{SMC}$ models (solid vs. dashed lines, respectively), that is a change on the resulting acceleration over the G_{SMC} galaxy by the G_{MW} and the G_{LMC} galaxies. Like in the first panel, the variation on the pericenter time produces a change on the orbit of the G_{SMC} system bringing it closer to the G_{LMC} galaxy in the first pericenter when it happens earlier, i.e. the G_{SMC} system is in a more radial orbit when the gravity of the G_{LMC} galaxy dominates the interaction.

In the fourth panel, we show the effect of reducing the G_{SMC} system mass (red line). We see that while the first pericenter does not change significantly from the one of the fiducial model (blue solid and dashed shadowed lines), there is a strong divergence afterwards. In particular, we see that the orbit of the G_{SMC} system decays slower when it is lighter. This is not surprising as it is well known that the dynamical friction is more efficient for high-mass than for low-mass systems (e.g. Sect. 8.1 of Binney & Tremaine 2008; Chandrasekhar 1943).

The effect of changing the total mass and the mass distribution of the G_{MW} system is shown in the fifth and sixth panels (dark brown and pink lines), respectively, and is similar, but with the opposite sign, to changing the mass of the G_{LMC} galaxy DM halo. A lighter G_{MW} system makes the gravity of the G_{LMC} galaxy dominate the G_{SMC} system's infall, i.e. the first pericenter occurs earlier and the orbit is more radial (smaller G_{LMC}-G_{SMC} distance at pericenter), similar to the $G_{LMC}+G_{SMC}$ fiducial model where G_{MW} is not present. On the other hand, keeping the G_{MW} system's mass but changing its distribution to a much less realistic point-mass approximation has two effects. First, the G_{MW} system has the same effect as if it was more massive, i.e. the pericenter is delayed with respect to the models with a lighter G_{MW} system. This is because in the model with a G_{MW} system with a mass distributed in a NFW profile the G_{LMC}-G_{SMC} system is embedded into the G_{MW} DM halo much before the interaction starts, thus, a non-negligible fraction of the G_{MW} system's mass do not contribute to the total acceleration applied to the G_{SMC} system (i.e. Gauss theorem). This can also be deduced by the fact that the pink solid line perfectly overlaps the blue shadowed line (fiducial $G_{LMC}+G_{SMC}+G_{MW}$ model) almost down to the second pericenter when the G_{MW} system has a close encounter with the $G_{LMC}+G_{SMC}$ system, then the model significantly diverges from the fiducial. We note that considering a point-like MW also changes the dynamical friction of the interaction. Secondly, the model with a point-like G_{MW} system all mass is pulling the G_{SMC} in a single direction, all the time, this is the origin of the second effect we observe that is a big difference on the G_{SMC} system's orbit. The G_{SMC} system experiences a strong and well directed tide by the G_{MW} system, specially strong when it gets closer. As a consequence, the G_{SMC} total energy-angular momentum and, thus, its orbit, highly differs from the one in other models. This can be seen by comparing the behaviour of the pink solid line just before the second pericenter and later, when the G_{SMC} system follows a more circular orbit (larger radii and longer period between pericenters).
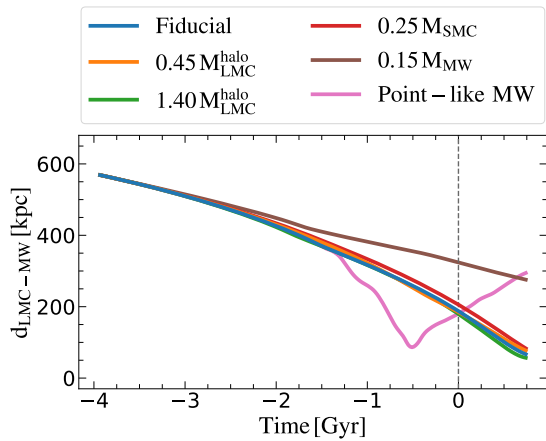
Fig. 2: Distance between the centre-of-masses of the G_{LMC} and G_{MW} galaxies. Each color represents the G_{LMC}+G_{SMC}+G_{MW} model of a different set. The vertical grey dashed line corresponds to the present time $t = 0$.

Finally, notice that in this figure we do not show the results from the set of models with a smaller G_{LMC} disc mass and different Toomre parameter since the total mass of the system is the same and, thus, they show no difference in the G_{LMC}-G_{SMC} orbital analysis with respect to the fiducial set.

3.2. G_{LMC}-G_{SMC} system to G_{MW} distance

Figure 2 shows the distance between the centre-of-mass of the G_{LMC} and G_{MW} galaxies. We show that, overall, there is no big difference between models except for two, the model with a smaller G_{MW} galaxy mass (dark brown line) and the point-like G_{MW} model (pink line). In the former, the mutual acceleration between the G_{LMC} galaxy and the G_{MW} system is smaller, so they approach each other slower (dark brown line). In the latter, although initially similar (an extended object interacts as a single-point mass when far enough), the interaction becomes stronger when the G_{MW} system approaches the G_{LMC} galaxy and reaches pericenter earlier (∼-0.5 Gyr), that is also when we observe big differences with the fiducial G_{LMC}-G_{SMC} distance (see Sect. 3.1). The variations on the G_{LMC}-G_{SMC} distance when changing the G_{LMC} and G_{SMC} masses are negligible as it is the G_{MW} system's mass that dominates the dynamics of the G_{LMC} -G_{MW} interaction. Notice that, as in the previous section, we do not analyse the set of models where we changed the G_{LMC} disc mass and Toomre parameter as these are almost identical, in total mass, to the fiducial set.

We also see that for the fiducial model (and most of the other models) the G_{MW} is at a ∼200 kpc distance from the G_{LMC} at the present time $t = 0$. This distance is much larger than the one obtained from observations (∼50 kpc, Pietrzyński et al. 2019). This is a result that differs from the results presented by Lucchini et al. (2021), and its origin can be in the difference in spatial and mass resolution between our models, as discussed above. For completeness, we also ran the G_{LMC}+G_{SMC}+G_{MW} fiducial model for one extra Gyr to find when the G_{MW} system gets as close to the G_{LMC} galaxy as in the observations (i.e. 50 kpc). The result is that this happens only after the G_{LMC}-G_{SMC} went through three pericenters instead of the two predicted by Lucchini

et al. (2021). Thus, we keep $t = 0$ as the snapshot after 4.0 Gyr from the initial conditions for the reasons given above.

4. The G_{LMC} galaxy properties

4.1. $t=0$ morphologies

In Fig. 3 we show the face-on (left columns) and edge-on (right columns) of the G_{LMC} disc stellar density at $t = 0$ for all models[2]. Each row shows a different set of models (see legend in the rightmost panels of each row). All G_{LMC} galactic discs have been centred in the centre-of-mass and aligned following the procedure described in Sect. 2.3. We warn the reader that, even though it is the same instant in time for all simulations, we may not be looking at the same stage of the G_{LMC}-G_{SMC} interaction (see Figs. 1 and 2). In this section, we qualitatively analyse some of the features present in the stellar density map, but it is not in the scope of this paper to analyse all of them in detail. In the next sections we focus only on the bar structure.

First, we qualitatively analyse the presence of galactic bars in our models. We see that only three models with the G_{LMC} galaxy isolated (leftmost panels) show the presence of a bar: the fiducial model (blue panel), the model with a G_{LMC} unstable disc (light brown panel) and the model with the G_{LMC} with lighter DM halo (orange panel). Otherwise, we observe that the G_{LMC}-G_{SMC} interaction triggers the formation of bars in most models (central columns). This is specially evident in the model with the lighter G_{LMC} disc and halo (yellow panel), the model with a G_{LMC} stable disc (light red panel). This interaction does not only trigger the formation of a galactic bar but also can perturb the entire disc in a way that the bar ends up being off-centred (see the fiducial G_{LMC}+G_{SMC}+G_{MW} simulation in the face-on top blue right panel), an observable feature of the LMC bar (e.g. Zaritsky 2004).

A second non-axisymmetric feature that is present in all our models is the spiral arms. Most of the isolated simulations (leftmost panels) show flocculent spiral structures if they do not develop a strong bar. When a strong bar is present, the spiral arms are stronger and bisymmetric (see discussion in Roca-Fàbrega et al. 2013). In most of the simulations where the interaction with the G_{SMC} or G_{MW} systems occurs, we see the coexistence of grand design and flocculent spiral arms regardless a bar is present or not, with a variety of pitch-angles. Nonetheless, in some models we see the formation of a single grand design bisymmetric spiral arm structure also in both cases, when a bar is present and when not. For instance, in the model with lighter G_{LMC} halo (orange right panel) and in the model with lighter G_{LMC} disc and halo (yellow right panel) we see the formation of a high pitch-angle bisymmetric structure. Ring-like structures are also present in some models, for example in the three-galaxy simulation of the model with a light G_{LMC} disc but heavy G_{LMC} halo (cyan right panel).

Regarding the G_{LMC} galaxy vertical structure, for the isolated simulations (leftmost panels) we have no noticeable asymmetries in the vertical profile far from a small enhancement in the cases with a bar that underwent or is experiencing a buckling event (left orange panel, e.g. Pfenniger & Friedli 1991; Łokas et al. 2014). For the interacting simulations, we observe a variety of vertical asymmetries mostly related to tidal interactions with the G_{SMC} and G_{MW} systems, and we see also that the disc is heated up at different degrees depending on the type of interaction.

---

[2] The animation showcasing the evolutionary changes in the face-on and edge-on distributions throughout the entire simulation is available online.
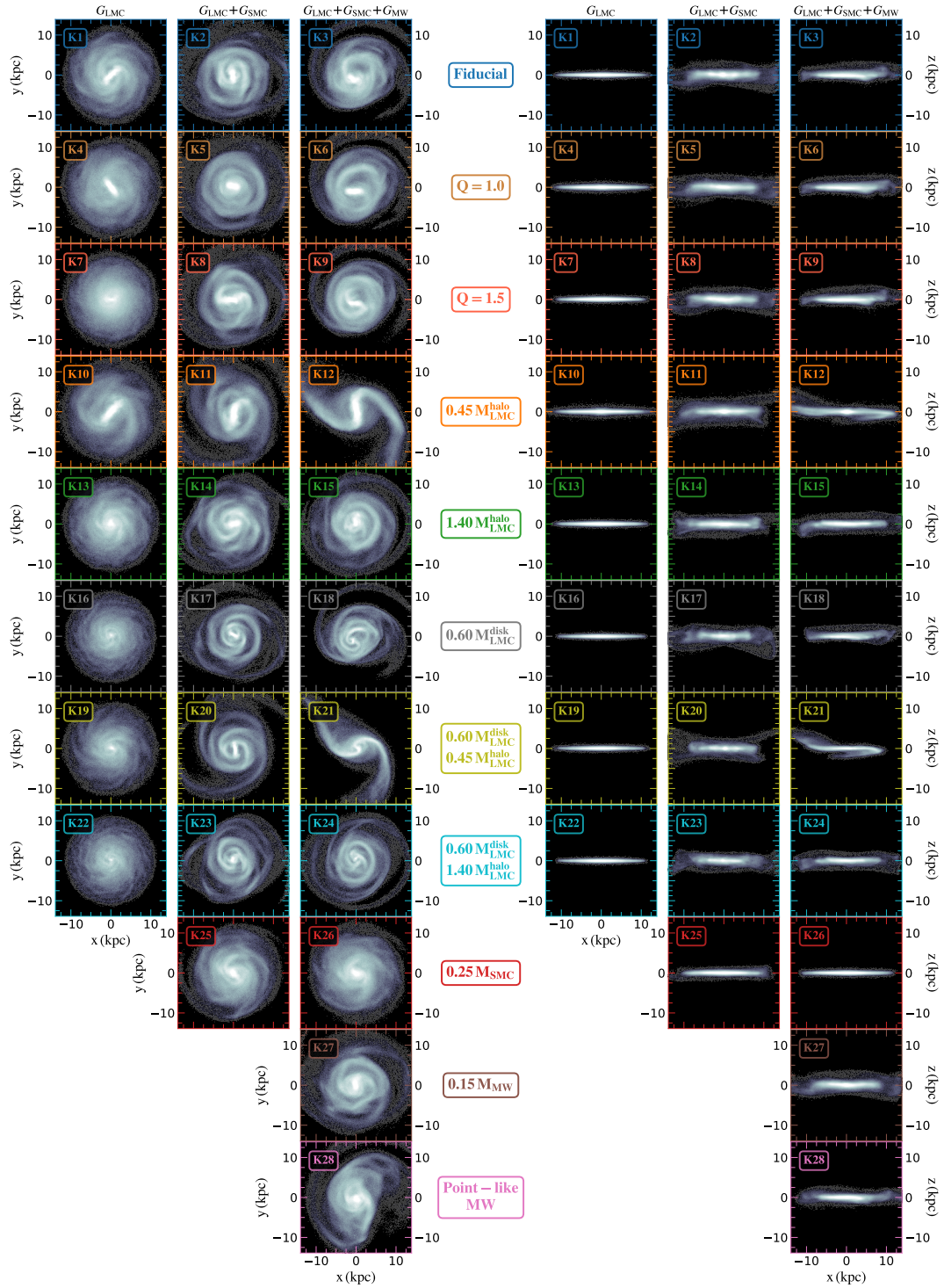
Fig. 3: Density map of the G_{LMC} disc as seen face-on (left part) and edge-on (right part) at $t = 0$. Each row corresponds to a different set of simulations and the labels are displayed in the rightmost panels. For both face-on and edge-on representations, we have the G_{LMC}, $G_{\mathrm{LMC}}+G_{\mathrm{SMC}}$ and $G_{\mathrm{LMC}}+G_{\mathrm{SMC}}+G_{\mathrm{MW}}$ models on the left, centre and right panels, respectively.

4.2. t=0 kinematics

Given that we possess full information on the position and velocity of each particle, we can show the radial, residual tangential,

and vertical velocity maps for the simulated G_{LMC} galaxy disc in the same way that was done for the LMC using *Gaia* DR3 data

(see Jiménez-Arranz et al. 2023a). The G_{LMC} centre-of-mass systemic motion is subtracted in order to obtain the internal velocities. Figure 4 shows the G_{LMC}'s disc radial and residual tangential velocity maps as seen face-on (left and right set of columns, respectively) at $t = 0$ for all models[3]. When a system is severely perturbed like in the models with G_{LMC}-G_{SMC} and G_{LMC}-G_{SMC}-G_{MW} interactions, a more detailed inspection is required, albeit we can find systematic changes. The G_{LMC}+G_{SMC}+G_{MW} simulation of the fiducial model (top blue right panels), for instance, clearly exhibits bimodality in both radial and tangential velocity. In general, the bimodality becomes more obvious when the G_{MW} system is present (rightmost panels), which is a reflex of the effect of its tides on the G_{LMC} disc.

The kinematic imprint of the bar can also be seen clearly in all models where a bar develops. In the radial and residual tangential velocity maps, the bar produces a quadrupole due to the elliptical orbits of the stars that form it. This is evident in the fiducial and light G_{LMC} halo models where the G_{LMC} is in isolation (blue and orange leftmost panels, respectively). The spiral arms also have a clear signature in the dynamics. For example, the grand design spiral arms seen in the model with lighter G_{LMC} halo (orange right panel) and in the model with lighter G_{LMC} disc and halo (yellow right panel) show clear signs of inwards radial migration (have a negative radial velocity).

In Fig. 5 we show the G_{LMC} disc vertical velocity maps as seen face-on at $t = 0$ for all models[3]. For the isolated simulations (leftmost panels) we observe no significant vertical velocities, as expected. However, for the interacting simulations (center and rightmost panels), bending modes can be observed. That may reflect the vertical structure seen in Fig. 3. This will be better analysed in a forthcoming paper.

5. The G_{LMC} disc scale height

Taking advantage that in simulations we have information of the whole temporal evolution, we can analyse how the individual G_{LMC}-G_{SMC} pericenters affect the G_{LMC} disc kinematics. In particular, we show the effect of the pericentric passages on the evolution of the G_{LMC} disc's scale height. In Fig. 6 we show the G_{LMC} disc scale height h_{LMC} as function of time for the different models. In each panel, the dotted, dashed and solid lines represent the G_{LMC}, G_{LMC}+G_{SMC} and G_{LMC}+G_{SMC}+G_{MW} models, respectively. In each panel, we include the isolated models as a reference point for comparison (dotted lines), and the results from the fiducial models (thin blue shadowed lines). In several models we see that the G_{LMC} disc heating is nearly identical to the fiducial. On the other hand, we see that in models where a strong bar is present, e.g. the low G_{LMC} halo mass model (orange dotted line), or were the G_{SMC} system is lighter (red dotted line), the disc heating changes. In particular, for the models where a strong bar is created (low G_{LMC} halo mass and low G_{LMC} disc mass models, orange and light grey lines, respectively) the disc heating jumps up fast after the creation of the bar, while otherwise it remains almost negligible when interacting with a very light G_{SMC} system (red lines).

The G_{LMC}-G_{SMC} pericenters also correlate well with a sudden increase in disc thickness, and the strength of this change correlates with the pericenter distance, the disc instability, and the merger (G_{SMC} system) mass (e.g. Quinn et al. 1993; Moetazedian & Just 2016). The change in scale height has a peak. After

the disc has heated, the thickness slightly decreases. The G_{LMC} disc relaxes to a higher scale height than the original after the G_{SMC} initial kick. This occurs following each G_{SMC} system pericenter. It is clear that the change in scale height is more impulsive when the G_{SMC} system pericenter is closer to the G_{LMC} disc than when it occurs at greater distances, as in the case of the G_{LMC}+G_{SMC}+G_{MW} simulation of the fiducial model (blue solid line) vs. the point-like MW (pink solid line) in the second pericenter (notice the pericenter distance in Fig. 1). Similar to the previous point, the simulations without G_{MW} have a thicker G_{LMC} galaxy disc than the simulations with a G_{MW} system, for all models. This might result from the first passages being closer together than they would be in the absence of the G_{MW} system.

If the mass of the G_{LMC} disc is smaller (right panels) the results do not change so much for the fiducial and heavy LMC halo (grey and cyan lines, respectively) but it does for the light G_{LMC} halo (yellow lines).

6. The G_{LMC} bar

In this section we aim to study the evolution of the G_{LMC} galaxy bar properties in a quantitative way, including the bar strength, length and pattern speed when in isolation and when interacting with the G_{SMC} and G_{MW} systems.

To do so, we apply the Dehnen method to the G_{LMC} disc for all available snapshots, for all simulations. The Dehnen method (Dehnen et al. 2023) measures the bar pattern speed Ω_p and the orientation angle ϕ_b of the bar from single snapshots of simulated barred galaxies. The method also determines the bar region, defined by the inner and outer radius $[R_0, R_1]$. Hereafter we will refer to R_1 as the bar radius or length, as it agrees well with the definition of best estimates for bar lengths in numerical simulations (Ghosh & Di Matteo 2023). For more details about the method see Sect. 2 and Appendix B of Dehnen et al. (2023).

6.1. The G_{LMC} bar strength

In Fig. 7, we show the median relative $m = 2$ Fourier amplitude Σ_2/Σ_0 in the bar region given by the inner and outer radius $[R_0, R_1]$ as function of time. Since the G_{LMC} galaxy disc is relaxing at the beginning of the simulation, we choose not to display the evolution of the disc in the first 1.25 Gyr, which corresponds to two times the disc rotation. Again, in each panel, the dotted, dashed and solid lines represent the G_{LMC}, G_{LMC}+G_{SMC} and G_{LMC}+G_{SMC}+G_{MW} configurations, respectively. To consider that the disc shows a bar, we impose a threshold of $\Sigma_2/\Sigma_0 > 0.2$ (as in Fujii et al. 2019; Bland-Hawthorn et al. 2023). As qualitatively seen in Fig. 3, when the G_{LMC} galaxy is in isolation only three models make the disc unstable enough to form a bar; the fiducial model, the G_{LMC} unstable disc model and the G_{LMC} with lighter DM halo model, corresponding to the blue, light brown and orange dotted lines, respectively.

In the fiducial model, if the G_{SMC} is present (blue dashed line), we observe how the bar strength is increased ~ 0.5 Gyr after the first pericenter and from then, it oscillates. If both G_{SMC} and G_{MW} are present (blue solid line), the amplitude of the bar formed is very near the threshold value showing a weak bar.

Analysing the consequences of having a light or heavy G_{LMC} halo mass on the G_{LMC} bar strength, we observe how reducing the G_{LMC} halo mass (orange lines) makes the disc less stable, allowing it to form a stronger bar in comparison to the fiducial model, for all configurations. The G_{LMC}+G_{SMC}+G_{MW} configuration can produce a bar up to $\Sigma_2/\Sigma_0 = 0.4$ for the present time

---

[3] The animation showcasing the evolutionary changes in the radial, residual tangential and vertical distribution throughout the entire simulation is available online.
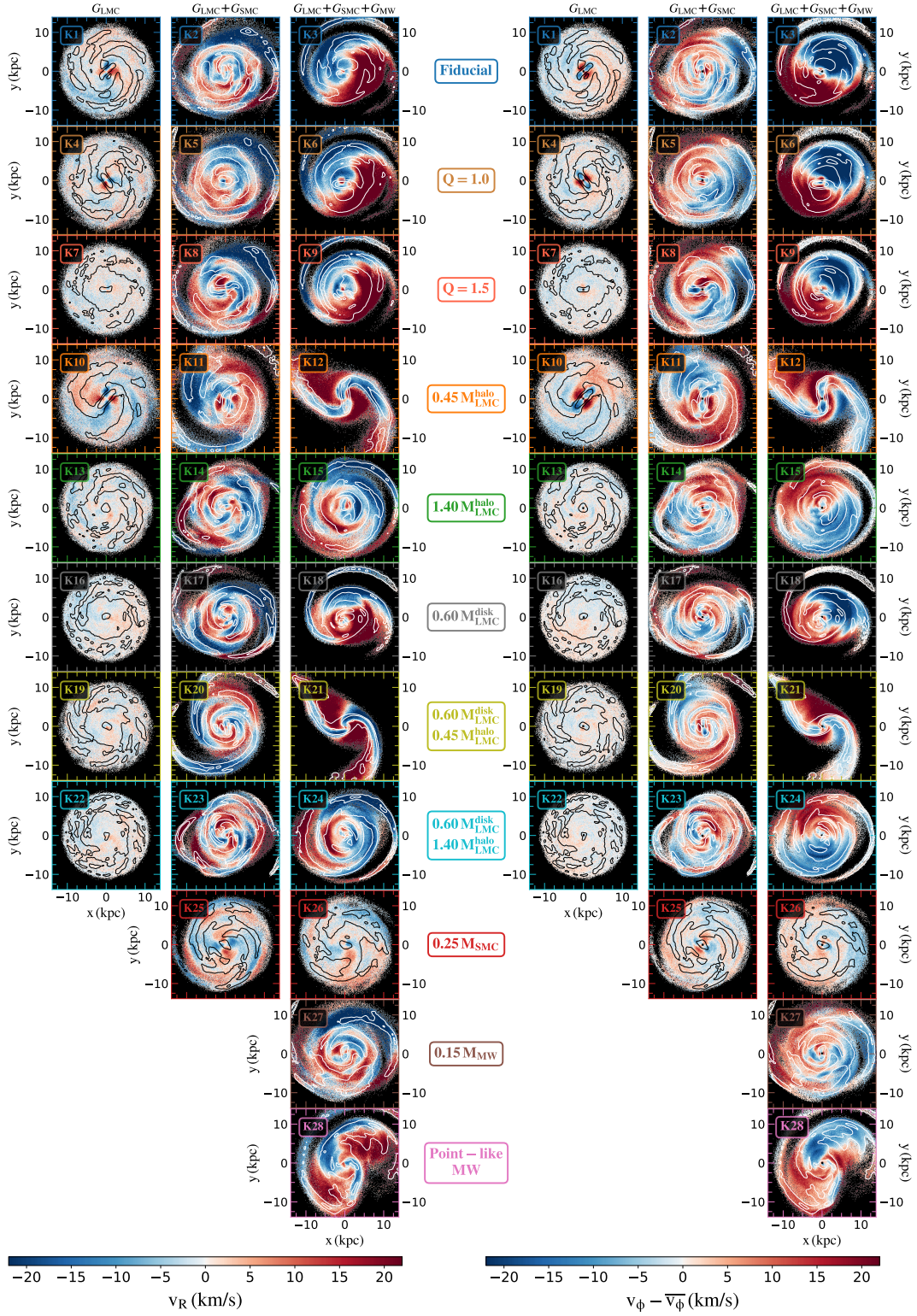
Fig. 4: Radial (left part) and residual tangential (right part) velocity maps of the G_{LMC} disc as seen face-on at $t = 0$. Each row corresponds to a different set of simulations. For both velocity maps, we have the G_{LMC}, $G_{LMC}+G_{SMC}$ and $G_{LMC}+G_{SMC}+G_{MW}$ models on the left, centre and right panels, respectively. Black and white contour lines highlight the G_{LMC} overdensities.
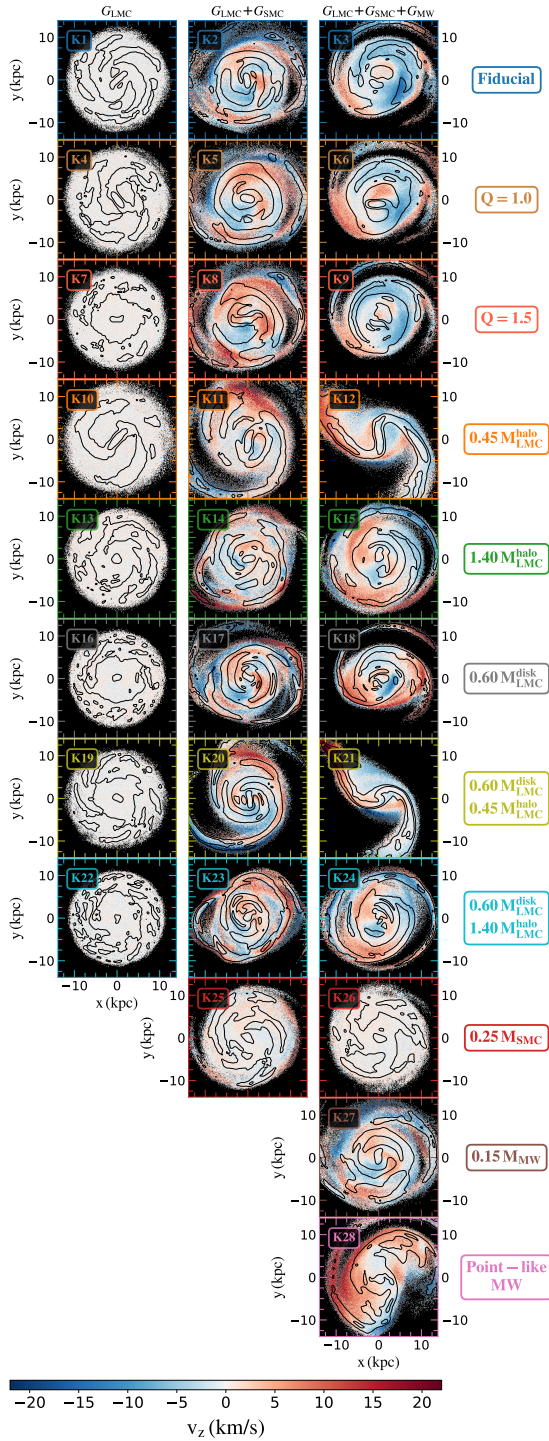
Fig. 5: Vertical velocity maps of the G_{LMC} disc as seen face-on at $t = 0$. Each row corresponds to a different set of simulations. We have the G_{LMC}, $G_{LMC}+G_{SMC}$ and $G_{LMC}+G_{SMC}+G_{MW}$ models on the left, centre and right panels, respectively. Black and white contour lines highlight the G_{LMC} overdensities.

$t = 0$. On the contrary, increasing the G_{LMC} halo mass (green lines) makes the disc more stable, making it more difficult to form a bar in comparison to the fiducial model, for all configurations. This is in agreement with simulations in the literature (e.g. Roca-Fàbrega et al. 2013).

Regarding the models where the mass of the G_{LMC} disc is smaller (right panels), if we compare all the models of different G_{LMC} halo mass (grey, yellow and cyan lines) with their analogue models with a heavier G_{LMC} disc (blue, orange and green lines, on their left, respectively), we observe that the amplitude of the bar is larger in all cases. This is caused by the fact that, despite being more internally stable, the G_{LMC} disc is more sensitive to external perturbations because the stellar particles are less gravitationally bound.

In the models where the G_{SMC} is lighter (red lines), the G_{MW} mass is smaller (dark brown line) and the G_{MW} is considered point-like (pink like), the G_{LMC} shows no bar formation, with differences far from the stochastic variation of the second order Fourier mode with respect to the fiducial model.

The change of the Toomre parameter Q, i.e. the gravitational stability of the stellar disc, has a significant impact on the bar formation for the isolated G_{LMC} models, as expected. The more unstable the disc is (light brown dotted line), the stronger the bar is, independently of whether there is or not interaction with other galactic systems. However, for the $G_{LMC}+G_{SMC}$ model, we observe how the bar strength decreases after the second G_{LMC}-G_{SMC} pericenter, being the value close to the threshold of $\Sigma_2/\Sigma_0 = 0.2$ at $t = 0$. Otherwise, in a more stable disc (light red dotted line), bars are not formed by secular evolution, but we observe how the first G_{LMC}-G_{SMC} pericenter boosts the formation of a strong bar on the G_{LMC} galaxy $0.5 - 1$ Gyr after the interaction, for both interacting models.

6.2. The G_{LMC} bar length

In Fig. 8 we show the outer bar region R_1 of G_{LMC} given by the Dehnen method as function of time, when the relative $m = 2$ Fourier amplitude Σ_2/Σ_0 is above the 0.2 threshold value. Here and hereafter, the crosses, the empty circles and the filled circles represent the G_{LMC}, $G_{LMC}+G_{SMC}$ and $G_{LMC}+G_{SMC}+G_{MW}$ configurations, respectively. From the three bars created in isolation (fiducial, low mass G_{LMC} galaxy halo and unstable G_{LMC} disc, represented by the blue, orange and light brown crosses, respectively) the longest is the low mass G_{LMC} galaxy halo model. As happens in the fiducial model, both bars grow over time by a factor ~2 when comparing the end of the simulations with the time when the bar is formed. On the other hand, the model with unstable G_{LMC} disc has a constant bar length $R_{1,LMC} \sim 2.5$ kpc over time.

We have very complex behaviours on the G_{LMC} bar length for the interacting configurations (empty and filled circles). The shortest bars are of $\lesssim 1$ kpc length and are obtained for interacting models with and without the G_{MW} (see, for example, the grey and green circles). The largest bars are created in the lighter G_{LMC} halo model (orange circles) with a length of $\gtrsim 5$ kpc. Whereas for some models the G_{LMC}-G_{SMC} pericenters imply a change in the bar length, as for example in the fiducial and heavy G_{LMC} DM halo model (blue and green crosses and circles, respectively), for other models the interaction does not have an impact on the G_{LMC} bar length change, as in the unstable G_{LMC} disc model (light brown crosses and circles).
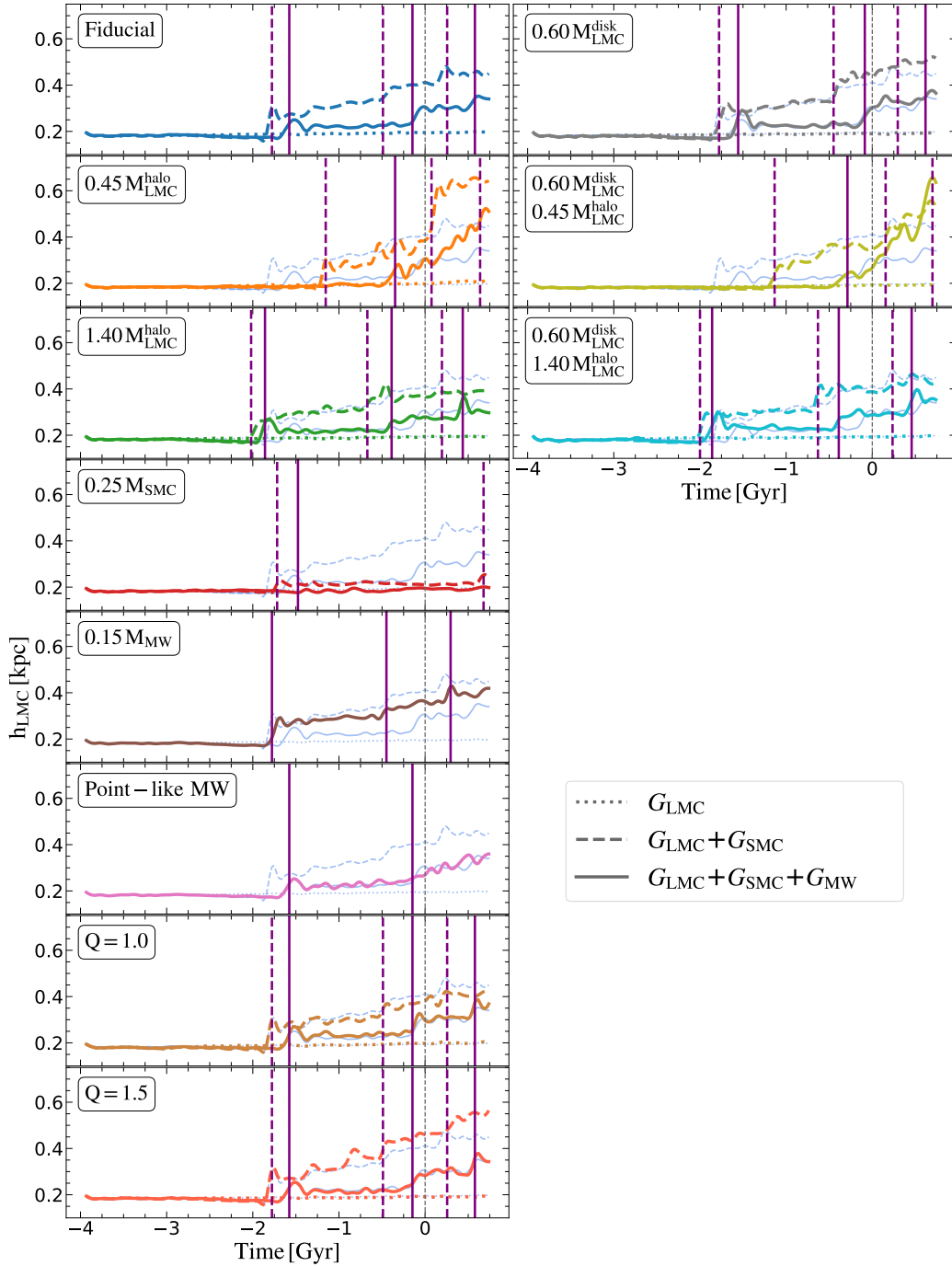
Fig. 6: Scale height evolution of the G_{LMC} disc. The dotted, dashed and solid lines show the G_{LMC}, $G_{LMC}+G_{SMC}$ and $G_{LMC}+G_{SMC}+G_{MW}$ models, respectively. The different panels represent a different set of simulations. The vertical purple solid (dashed) lines correspond to the G_{LMC}-G_{SMC} pericenters of the $G_{LMC}+G_{SMC}+G_{MW}$ ($G_{LMC}+G_{SMC}$) models. The vertical grey dashed line corresponds to the present time $t = 0$. For the sake of comparison, in shadowed blue lines it is plotted the scale height evolution of the G_{LMC} disc for the models of the fiducial set.

6.3. Analysis of the G_{LMC} bar off-centeredness

Besla et al. (2012) demonstrated that the off-center stellar bar of the LMC (and its one-armed spiral) can be naturally explained by a recent direct collision with the SMC. Here we analyse how the interaction of the G_{SMC} with the G_{LMC} can affect the position of the center of the stellar bar of the G_{LMC}.
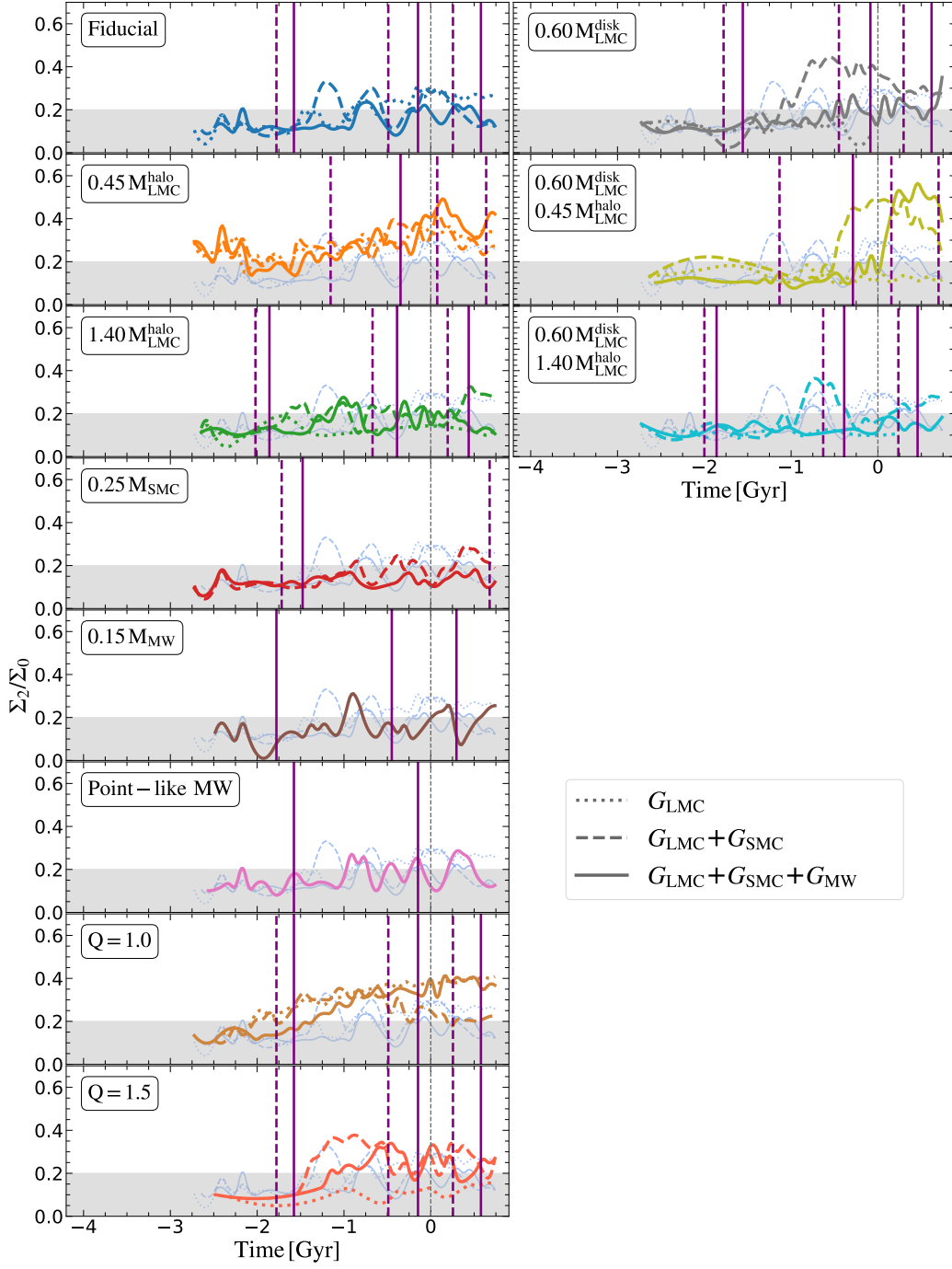
Fig. 7: Same as Fig. 6 but for the relative $m = 2$ Fourier amplitude of the G_{LMC} bar region. The grey area corresponds to $\Sigma_2/\Sigma_0 = 0.2$, which is the threshold used to consider if the G_{LMC} disc has a bar or not. The first 1.25 Gyr are not shown since it is when the G_{LMC} disc is being relaxed, which corresponds to two times the disc rotation.

Figure 9 shows the analysis of how off-centered the bar of the G_{LMC} is, determined by the distance between the G_{LMC} centre-of-mass and its bar center (obtained using a KDE of 3.0 kpc-bandwidth, as explained in Sect. 2.3), when the relative $m = 2$ Fourier amplitude Σ_2/Σ_0 is above the 0.2 threshold value. The three bars created in isolation (fiducial, low mass G_{LMC} galaxy

halo and unstable G_{LMC} disc, represented by the blue, orange and light brown crosses, respectively) share their center with the center-of-mass, as expected, leading to an $\sim$ 0 kpc bar off-center.

We observe how the G_{LMC}-G_{SMC} pericenters in the interacting models produce an increase in the bar off-center. In the full configurations of the light G_{LMC} halo (orange filled circles) and
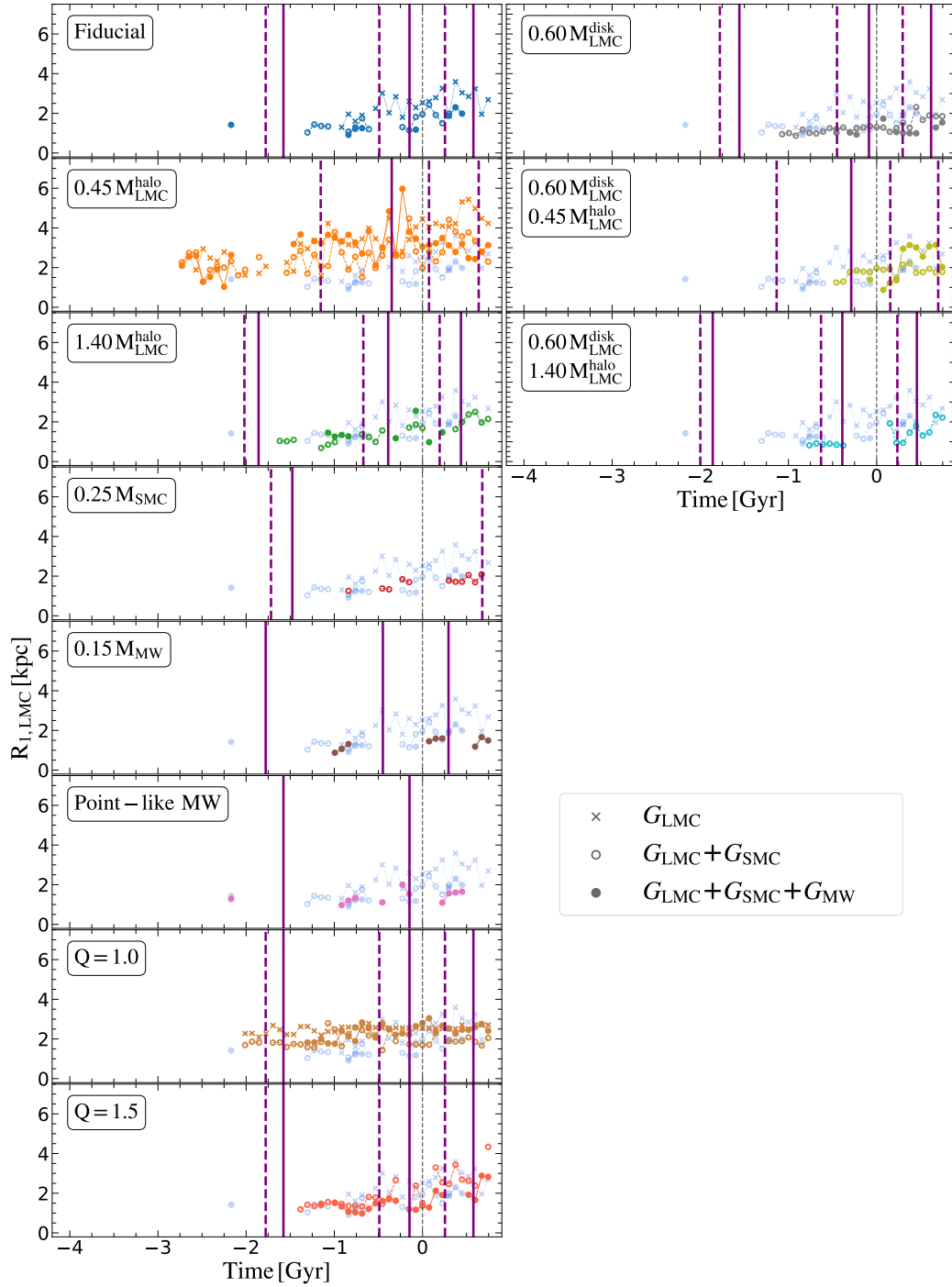
Fig. 8: Evolution of the G_{LMC} bar length, given by the outer bar radius R_1 from the Dehnen method. The crosses corresponds to the isolated G_{LMC} model, whereas the empty and fill dots show the $G_{LMC}+G_{SMC}$ and $G_{LMC}+G_{SMC}+G_{MW}$ models, respectively. The different panels represent a different set of simulations. The vertical purple solid (dashed) lines correspond to the MCs pericenters of the $G_{LMC}+G_{SMC}+G_{MW}$ ($G_{LMC}+G_{SMC}$) models. The vertical grey dashed line corresponds to the present time $t = 0$. For the sake of comparison, in shadowed blue lines it is plotted the evolution of the G_{LMC} bar length for the models of the fiducial set. We only show the obtained value when $\Sigma_2/\Sigma_0 > 0.2$, which is the threshold used to consider that the G_{LMC} disc has a bar.

the light G_{LMC} disc and halo (yellow filled circles) models are where the increased bar off-center is more readily apparent (up to

$\sim 2-3$ kpc) ~ 0.5 Gyr after the first pericenter and from then, it decreases where the bar tries to be located at the center-of-mass
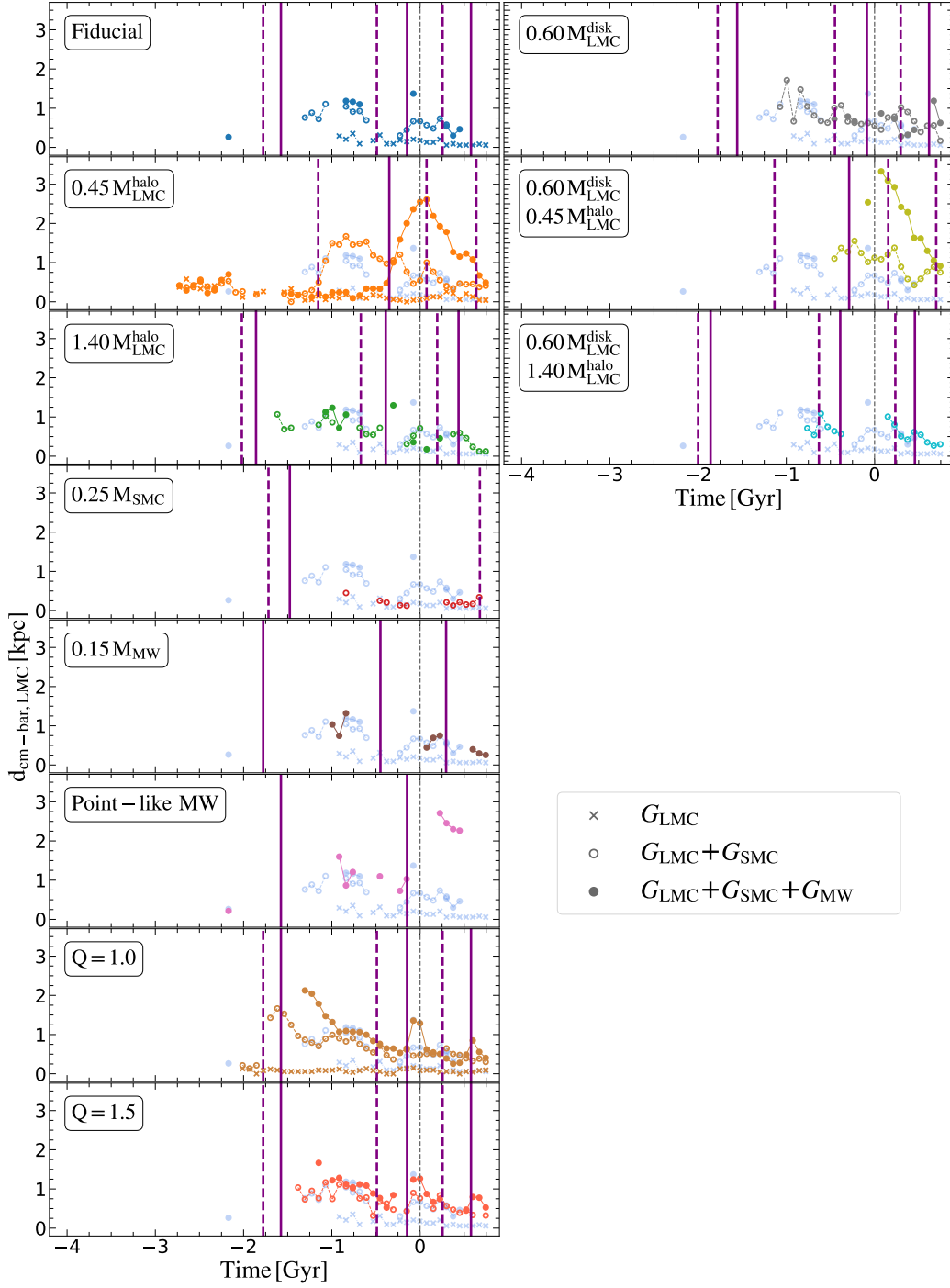
Fig. 9: Same as Fig. 8 but for the G_{LMC} bar off-center. It is given by the distance between the G_{LMC} centre-of-mass and the G_{LMC} bar center obtained using a KDE of 3.0 kpc-bandwidth as explained in Sect. 2.3.

of the host galaxy. In the majority of simulations we observe an off-center bar at a certain point of the temporal evolution.

6.4. The G_{LMC} bar pattern speed

Figure 10 shows the G_{LMC} bar pattern speed Ω_P given by the Dehnen method as function of time, when the relative $m = 2$ Fourier amplitude Σ_2/Σ_0 is above the 0.2 threshold value. The three bars created in the isolated configuration (fiducial, low

mass G_{LMC} galaxy halo and unstable G_{LMC} disc, represented by the blue, orange and light brown crosses, respectively) slow down over time (e.g. Athanassoula 2003; Widrow et al. 2008). In comparison to the fiducial model, the low mass G_{LMC} halo presents a stronger and slower bar, whereas the unstable G_{LMC} disc has a even stronger bar that roughly rotates at the same angular speed.

As in the case of the bar length, we have very complex behaviours for the interacting configurations (empty and filled circles). For the fiducial model, the interacting configurations have bars with smaller pattern speeds than in the isolated configuration. For the interacting configurations corresponding to the two models with more unstable discs (low mass G_{LMC} halo and G_{LMC} disc Q = 1.0 models, represented by orange and light brown empty and filled circles, respectively) we do not observe significant differences with respect to the decreasing pattern speed shown by the isolated models (crosses). For $t > 0$, the $G_{\mathrm{LMC}} + G_{\mathrm{SMC}}$ models show a bar $\sim$ 5 km s^{-1} slower (faster) for the low mass G_{LMC} halo (Q = 1.0) models in comparison to the isolated model.

7. Summary and discussion

In this paper we present KRATOS, a comprehensive suite of 28 pure N-body simulations of isolated and interacting LMC-like and SMC-mass galaxies. The 28 simulations are grouped in 11 sets of at most three simulations each containing: 1) a control model with an isolated LMC-like galactic system; 2) a model with both an LMC-like and a SMC-mass system; 3) a model that additionally includes a MW-mass system. For each of the three scenarios, we vary a set of the free parameters of the whole system (details on Sect. 2). The simulations have a spatial and temporal resolution of 10 pc and 5000 yr, respectively. The minimum mass per particle is $4 \times 10^3 M_\odot$.

The KRATOS suite is devoted to the analysis of the formation of substructures in an LMC-like disc after the interaction with an SMC-mass system and to compare it with the observations (see, for example, the kinematics maps of the LMC using *Gaia* data on Gaia Collaboration et al. 2021; Jiménez-Arranz et al. 2023b). The majority of the simulations by other authors on the interaction between the LMC, SMC and MW has been done to analyse and recreate the distribution and position of the gas components of these systems, like the Magellanic Stream and Leading Arm (Besla et al. 2010, 2012; Hammer et al. 2015; Pardy et al. 2018; Wang et al. 2019; Tepper-García et al. 2019; Lucchini et al. 2020, 2021). In the past, only the work by Besla et al. (2012) extensively explored the effect of this interaction on the internal structures of the LMC such as the off-centered bar and the single spiral arm. It may be possible to learn more about the interactions that took place between these two satellite galaxies and between them and the MW by comprehending the formation process of these LMC morphological features.

In Table 3 we compare the initial conditions of the fiducial model of KRATOS suite and the models presented in Besla et al. (2012, hereafter B12). The B12 models include hydrodynamics whereas the KRATOS suite contains pure N-body simulations. Differences can be found in both the amount of mass of the three galaxies and how it is distributed. For instance, in B12 the LMC is modelled with a disc of gas and a disc of stars surrounded by a DM halo with a Hernquist profile whereas in KRATOS the LMC is modelled as a disc of stars surrounded by a NFW DM halo. A significant difference lies on the modelling of the MW, where B12 models the Galaxy as a static NFW potential whereas in KRATOS simulates the MW as a live NFW DM

	KRATOS	B12
	(Pure N-body)	(Hydrodynam.)
[G_{LMC}]		
Stellar Distribution	Disc	Disc
Scale Length (kpc)	2.85	1.7
Stellar Mass ($M_\odot$)	5.0×10^9	2.5×10^9
DM Distribution	NFW	Hernquist
DM Concentration	9	9
DM Mass ($M_\odot$)	1.8×10^{11}	1.8×10^{11}
[G_{SMC}]		
Stellar Distribution	NFW	Disc
Stellar Mass ($M_\odot$)	2.6×10^8	2.6×10^8
DM Distribution	NFW	Hernquist
DM Concentration	15	15
DM Mass ($M_\odot$)	1.9×10^{10}	2.1×10^{10}
[G_{MW}]		
DM Distribution	NFW	Static NFW
DM Concentration	12	12
DM Mass ($M_\odot$)	1.0×10^{12}	1.5×10^{12}

Table 3: Comparison of the initial conditions of the G_{LMC}, G_{SMC} and G_{MW} galaxies for the the fiducial model presented in this work (KRATOS) and the model presented by Besla et al. (2012, B12).

halo. However, the authors of B12 claim that not considering dynamical friction from the MW halo is expected to have little impact on the orbit in a first passage scenario. Conversely, in both works it is analysed the effect of modelling the LMC and SMC as an isolated binary pair or in interaction with the MW potential. Finally, in terms of the resolution of both simulations, B12 and KRATOS simulations have of the order of $\sim 10^6$ stars particles in the G_{LMC} disc, but there are many more particles on the G_{LMC} DM halo in the KRATOS simulations than in B12 ($10 - 35$ vs 0.1×10^6). For the G_{SMC}, in KRATOS we have less star particles (0.6 vs 1×10^5) but a significant larger number of DM particles (0.01 vs $1 - 4.5 \times 10^6$). The minimum mass per particle is $2.5 \times 10^3 M_\odot$ for B12 and $4 \times 10^3 M_\odot$ for KRATOS. The spatial resolution of B12 and KRATOS are 100 and 10 pc, respectively. In Besla et al. (2012) no explicit information is given on the temporal resolution of B12, while it is of 5000 yr for KRATOS.

Looking at the bar fraction in the suite of 28 simulations in KRATOS, we quantify the number of bars (as used in this work, with Σ_2 / Σ_0 amplitude larger than 20%). We find that in 17 out of the 28 simulations, the disc develops either a weak and transient (less than 1.5 Gyr approx.) or strong bar. Only 11 of the models do not show a clear bar in any moment of the evolution of the galaxy. These numbers agree with the fraction of bars observed in nearby galaxies(e.g. Marinova et al. 2007; Menéndez-Delmestre et al. 2007; Barazza et al. 2008; Sheth et al. 2008; Nair & Abraham 2010; Masters et al. 2011), which is about 30%-60%. Out of
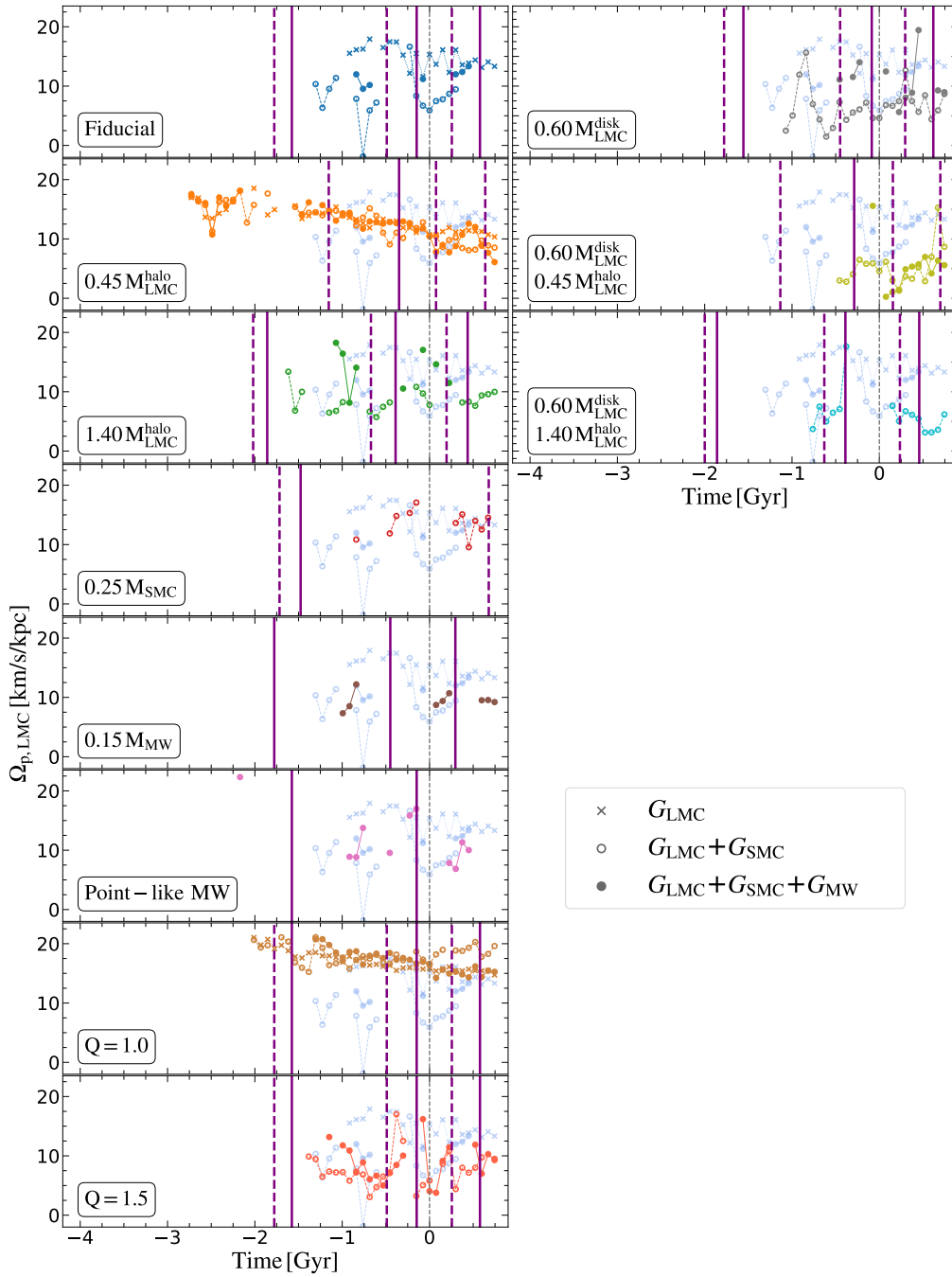
Fig. 10: Same as Fig. 8 but for the G_{LMC} bar pattern speed.

the barred galaxy models, 6 show a weak (below 20% or very transient in time bar structure), while 11 models show a strong and long-lived bar (more than 1.5 Gyr). These strong bars may have different origin: 3 of them lie in the control G_{LMC} models so they develop as internal disc instabilities; 4 of them are formed in models with G_{LMC} and G_{SMC} interaction or even with G_{MW} interaction. While 4 bars form in models of interacting galaxies, but the corresponding control G_{LMC} also develops a bar, so both mechanisms could create the bar structure.

As mentioned above, KRATOS simulations are designed to compare with the internal LMC disc kinematics (e.g. Gaia Collaboration et al. 2021; Jiménez-Arranz et al. 2023b). In Jiménez-Arranz et al. (2023a), the LMC bar pattern speed is studied using *Gaia* DR3 data. In this work, we use three different methods to evaluate the bar properties: the bar pattern speed is measured through the Tremaine-Weinberg (TW, Tremaine & Weinberg 1984) method, the Dehnen method (introduced in our Sect. 2.3) and a bisymmetric velocity (BV) model (Gaia Collabora-

tion et al. 2022). The work suggests that due to the significant variation with frame orientation, the TW method appears to be unable to determine which global value best represents an LMC bar pattern speed. The Dehnen method gives a pattern speed $\Omega_p = -1.0 \pm 0.5$ km s^{-1} kpc^{-1}, thus corresponding to a bar which barely rotates, slightly counter-rotating with respect to the LMC disc. This method does not take into account a possible strong and counter-rotating $m = 1$ disc component, which would balance the bar pattern speed. The BV method recovers a LMC bar corotation radius of $R_c = 4.20 \pm 0.25$ kpc, corresponding to a pattern speed $\Omega_p = 18.5^{+1.2}_{-1.1}$ km s^{-1} kpc^{-1}. This result is consistent with previous estimates and gives a bar corotation-to-length ratio of $R_c/R_{bar} = 1.8 \pm 0.1$, which makes the LMC hosting a slow bar, as most interacting bars found in nearby galaxies (e.g. Géron et al. 2023). The pattern speed of the bars in the KRATOS simulations also fall within this range of $\Omega_p = 10 - 20$ km s^{-1} kpc^{-1}, suggesting indeed that the LMC has a low rotating bar.

Regarding the disc scale height computed in the KRATOS simulations and comparing to recent values in the literature, Ripepi et al. (2022) find, using classical cepheids, that the LMC disc appears "flared" and thick, with a disc scale height of $h_{LMC} = 0.97$ kpc. The authors argued that strong tidal interactions with the MW and/or SMC, as well as previous mergers involving now-disrupted LMC satellites, can all be used to explain this feature. Since the present scale height is sensitive to the initial conditions of the G_{LMC} disc, we do not aim to replicate it in our paper. However, we state that interactions indeed lead to a significant increase in the G_{LMC} thickness.

8. Conclusions

In this paper we introduce a comprehensive suite of pure N-body and open access simulations named KRATOS with the goal to study the internal kinematics of the LMC disc. *Gaia* DR3 revealed a complex and rich velocity maps (e.g. Gaia Collaboration et al. 2021; Jiménez-Arranz et al. 2023b). The interpretation of these maps requires a range of simulated LMC models. In this work we generate models with three different configurations: a control G_{LMC} as an isolated LMC galaxy, another one with the G_{SMC} only interaction and, finally, the most realistic situation where both the G_{SMC} and G_{MW} may interact with the G_{LMC}. We take into account the uncertainties regarding structural parameters and orbital parameters by considering a different set of initial conditions, where we vary one of the parameters at a time (see Table 2).

Results shown in this paper from the KRATOS suite can be summarised as:

– Regarding the infall history between the G_{LMC} and the G_{SMC}, the effect of not including the G_{MW} makes the pericentric passages between the two galaxies to happen earlier than when the three galaxies are present (see Fig. 1).
– In relation to the infall history between the G_{MW} and the G_{LMC}, the higher the mass of the G_{MW}, the closer the two galaxies will become, as expected (see Fig. 2).
– The KRATOS simulations are suited to explore different G_{LMC} galaxy morphologies, having a large variety of spiral arm shapes, presence of bar, warped discs, etc. as seen in Fig. 3.
– Different galaxy morphologies also translate into different disc kinematic maps, suitable to perform a first interpretation of the LMC kinematic maps (e.g. Gaia Collaboration et al. 2021; Jiménez-Arranz et al. 2023b), as seen in Figs. 4 and 5.

– As Cepheids suggest (Ripepi et al. 2022), the G_{LMC} disc scale height is increased just after a pericentric passage of the G_{SMC} as seen in Fig. 6 for all models.
– Tidal interactions can not only destroy bars (when they are formed), but also create them, as seen in Fig. 7.
– As demonstrated in Besla et al. (2012), we also observe that the off-center stellar bar of the G_{LMC} can be naturally explained by a recent direct interaction with the G_{SMC}, as seen in Figs. 3 and 9.
– The G_{SMC} pericentric passages do not significantly change the bar length and pattern speed of long-lived bars, as seen in Figs. 8 and 10.
– As suggested by Géron et al. (2023), the longest bars are the ones with a lower pattern speed (see their Fig. 12.).

To sum up, KRATOS suite of N-body simulations are designed to study the internal kinematics of the G_{LMC} disc and to help interpreting the complex maps obtained using *Gaia* data. The high spatial, temporal and mass resolution used in the simulations are proven to be suitable for such purpose, as the preliminary scientific results presented in this work show. More specific analysis on the LMC-SMC interaction is left for successive papers of the series.

Acknowledgements

References

Athanassoula, E. 2003, MNRAS, 341, 1179
Bagheri, G., Cioni, M. R. L., & Napiwotzki, R. 2013, A&A, 551, A78
Barazza, F. D., Jogee, S., & Marinova, I. 2008, ApJ, 675, 1194
Besla, G., Kallivayalil, N., Hernquist, L., et al. 2007, ApJ, 668, 949
Besla, G., Kallivayalil, N., Hernquist, L., et al. 2010, ApJ, 721, L97
Besla, G., Kallivayalil, N., Hernquist, L., et al. 2012, MNRAS, 421, 2109
Binney, J. & Tremaine, S. 2008, Galactic Dynamics: Second Edition

Bland-Hawthorn, J., Tepper-Garcia, T., Agertz, O., & Freeman, K. 2023, ApJ, 947, 80

Carrera, R., Conn, B. C., Noël, N. E. D., Read, J. I., & López Sánchez, Á. R. 2017, MNRAS, 471, 4571

Chandrasekhar, S. 1943, ApJ, 97, 255

Choudhury, S., Subramaniam, A., Cole, A. A., & Sohn, Y. J. 2018, MNRAS, 475, 4279

Cioni, M. R. L., van der Marel, R. P., Loup, C., & Habing, H. J. 2000, A&A, 359, 601

de Vaucouleurs, G. & Freeman, K. 1972, Vistas in Astronomy, 14, 163

Dehnen, W., Semczuk, M., & Schönrich, R. 2023, MNRAS, 518, 2712

Diaz, J. D. & Bekki, K. 2012, ApJ, 750, 36

Duffy, A. R., Schaye, J., Kay, S. T., et al. 2010, MNRAS, 405, 2161

Elmegreen, D. M. & Elmegreen, B. G. 1980, AJ, 85, 1325

Fujii, M. S., Bédorf, J., Baba, J., & Portegies Zwart, S. 2019, MNRAS, 482, 1983

Gaia Collaboration, Drimmel, R., Romero-Gomez, M., et al. 2022, arXiv e-prints, arXiv:2206.06207

Gaia Collaboration, Luri, X., Chemin, L., et al. 2021, A&A, 649, A7

Gallagher, John S., I. & Hunter, D. A. 1984, ARA&A, 22, 37

Garavito-Camargo, N., Besla, G., Laporte, C. F. P., et al. 2019, ApJ, 884, 51

Gardiner, L. T. & Noguchi, M. 1996, MNRAS, 278, 191

Gardiner, L. T., Sawa, T., & Fujimoto, M. 1994, MNRAS, 266, 567

Géron, T., Smethurst, R. J., Lintott, C., et al. 2023, MNRAS, 521, 1775

Ghosh, S. & Di Matteo, P. 2023, arXiv e-prints, arXiv:2308.10948

Graczyk, D., Pietrzyński, G., Thompson, I. B., et al. 2014, ApJ, 780, 59

Grady, J., Belokurov, V., & Evans, N. W. 2021, ApJ, 909, 150

Hammer, F., Yang, Y. B., Flores, H., Puech, M., & Fouquet, S. 2015, ApJ, 813, 110

Harris, J. 2007, ApJ, 658, 345

Hilditch, R. W., Howarth, I. D., & Harries, T. J. 2005, MNRAS, 357, 304

Hindman, J. V., Kerr, F. J., & McGee, R. X. 1963, Australian Journal of Physics, 16, 570

Irwin, M. J., Kunkel, W. E., & Demers, S. 1985, Nature, 318, 160

Jiménez-Arranz, Ó., Chemin, L., Romero-Gómez, M., et al. 2023a, arXiv e-prints, arXiv:2312.11192

Jiménez-Arranz, Ó., Romero-Gómez, M., Luri, X., et al. 2023b, A&A, 669, A91

Kallivayalil, N., van der Marel, R. P., & Alcock, C. 2006a, ApJ, 652, 1213

Kallivayalil, N., van der Marel, R. P., Alcock, C., et al. 2006b, ApJ, 638, 772

Kallivayalil, N., van der Marel, R. P., Besla, G., Anderson, J., & Alcock, C. 2013, ApJ, 764, 161

Kerr, F. J., Hindman, J. F., & Robinson, B. J. 1954, Australian Journal of Physics, 7, 297

Kim, S., Staveley-Smith, L., Dopita, M. A., et al. 1998, ApJ, 503, 674

Kravtsov, A. V., Klypin, A. A., & Khokhlov, A. M. 1997, ApJS, 111, 73

Lin, D. N. C. & Lynden-Bell, D. 1982, MNRAS, 198, 707

Łokas, E. L., Athanassoula, E., Debattista, V. P., et al. 2014, MNRAS, 445, 1339

Lucchini, S., D'Onghia, E., & Fox, A. J. 2021, ApJ, 921, L36

Lucchini, S., D'Onghia, E., Fox, A. J., et al. 2020, Nature, 585, 203

Luks, T. & Rohlfs, K. 1992, A&A, 263, 41

Marinova, I., Jogee, S., Bacon, D., et al. 2007, in American Astronomical Society Meeting Abstracts, Vol. 211, American Astronomical Society Meeting Abstracts, 97.12

Masters, K. L., Nichol, R. C., Hoyle, B., et al. 2011, MNRAS, 411, 2026

Menéndez-Delmestre, K., Sheth, K., Schinnerer, E., Jarrett, T. H., & Scoville, N. Z. 2007, ApJ, 657, 790

Misawa, T., Charlton, J. C., Kobulnicky, H. A., Wakker, B. P., & Bland-Hawthorn, J. 2009, ApJ, 695, 1382

Moetazedian, R. & Just, A. 2016, MNRAS, 459, 2905

Murai, T. & Fujimoto, M. 1980, PASJ, 32, 581

Nair, P. B. & Abraham, R. G. 2010, ApJ, 714, L260

Navarro, J. F., Frenk, C. S., & White, S. D. M. 1996, ApJ, 462, 563

Nikolaev, S., Drake, A. J., Keller, S. C., et al. 2004, ApJ, 601, 260

Noël, N. E. D., Conn, B. C., Carrera, R., et al. 2013, ApJ, 768, 109

Olsen, K. A. G. & Salyk, C. 2002, AJ, 124, 2045

Pardy, S. A., D'Onghia, E., & Fox, A. J. 2018, ApJ, 857, 101

Petersen, M. S. & Peñarrubia, J. 2021, Nature Astronomy, 5, 251

Pfenniger, D. & Friedli, D. 1991, A&A, 252, 75

Pietrzyński, G., Graczyk, D., Gallenne, A., et al. 2019, Nature, 567, 200

Quinn, P. J., Hernquist, L., & Fullagar, D. P. 1993, ApJ, 403, 74

Ripepi, V., Chemin, L., Molinaro, R., et al. 2022, MNRAS, 512, 563

Ripepi, V., Cioni, M.-R. L., Moretti, M. I., et al. 2017, MNRAS, 472, 808

Roca-Fàbrega, S., Valenzuela, O., Figueras, F., Romero-Gómez, M., & Antoja, T. 2012, in European Physical Journal Web of Conferences, Vol. 19, European Physical Journal Web of Conferences, 05011

Roca-Fàbrega, S., Valenzuela, O., Figueras, F., et al. 2013, MNRAS, 432, 2878

Rubio, M., Lequeux, J., & Boulanger, F. 1993, A&A, 271, 9

Schmidt, T., Cioni, M.-R. L., Niederhofer, F., et al. 2020, A&A, 641, A134

Sheth, K., Elmegreen, D. M., Elmegreen, B. G., et al. 2008, ApJ, 675, 1141

Skowron, D. M., Jacyszyn, A. M., Udalski, A., et al. 2014, ApJ, 795, 108

Staveley-Smith, L., Kim, S., Putman, M., & Stanimirović, S. 1998, Reviews in Modern Astronomy, 11, 117

Subramanian, S. & Subramaniam, A. 2012, ApJ, 744, 128

Tepper-García, T., Bland-Hawthorn, J., Pawlowski, M. S., & Fritz, T. K. 2019, MNRAS, 488, 918

Tremaine, S. & Weinberg, M. D. 1984, ApJ, 282, L5

Tremaine, S. D. 1976, ApJ, 203, 72

Valenzuela, O. & Klypin, A. 2003, MNRAS, 345, 406

van der Marel, R. P. 2001, AJ, 122, 1827

van der Marel, R. P., Alves, D. R., Hardy, E., & Suntzeff, N. B. 2002, AJ, 124, 2639

van der Marel, R. P. & Cioni, M.-R. L. 2001, AJ, 122, 1807

Vasiliev, E. 2023a, arXiv e-prints, arXiv:2306.04837

Vasiliev, E. 2023b, Galaxies, 11, 59

Wang, J., Hammer, F., Yang, Y., et al. 2019, MNRAS, 486, 5907

Widrow, L. M., Pym, B., & Dubinski, J. 2008, ApJ, 679, 1239

Yozin, C. & Bekki, K. 2014, MNRAS, 439, 1948

Zaritsky, D. 2004, ApJ, 614, L37

Zivick, P., Kallivayalil, N., Besla, G., et al. 2019, ApJ, 874, 78

Part III

SUMMARY OF RESULTS, DISCUSSION AND CONCLUSIONS

SUMMARY, DISCUSSION AND CONCLUSIONS

This last chapter is devoted to summarise the main results presented in this thesis. Here we also discuss the key features of this work and give some general conclusions. Additionally, we present future work prospects in the dynamical characterisation of the Magellanic Clouds (MCs).

6.1 GAIA DR3 CLEAN SAMPLES FOR THE LARGE AND SMALL MAGELLANIC CLOUD

The articles presented in the first two sections of Part i describe Large Magellanic Cloud (LMC) and Small Magellanic Cloud (SMC) clean samples of *Gaia* DR3 data (Jiménez-Arranz et al. 2023b,a, respectively). When looking at the MCs, an observer close to the Earth detects stars that can belong to the Milky Way (MW) or to the MCs. Then, in order to build a clean sample of LMC and SMC stars, we needed to define a selection criteria to separate them from the MW foreground. To do so, we implemented a selection method based on machine learning classifiers, in particular neural networks (NNs), using the full data available in the *Gaia* catalogue, namely the astrometric and photometric data.

Based on this classifier, three LMC and SMC star samples with different levels of completeness and purity were generated. We compare them with the outcome of the selection strategy used in the Gaia Collaboration papers (Gaia Collaboration et al. 2021), which was purely based on the proper motions. In this regard, a cross-matching of our more complete sample based on NNs and the proper motion selection sample of the Gaia Collaboration reveals that the former almost entirely contains the latter and the more complete sample contains nearly two million additional stars, showcasing the improvement of the selection criteria. Moreover, we externally validated our classification results using various test samples such as MCs RR Lyrae, MCs Cepheids and MCs-MW StarHorse (SH) samples with successful results.

The estimated MW contamination in each of the three LMC and SMC samples is in the 10-40% range; the "best case" is obtained for bright stars ($G < 16$), which are part of the line-of-sight velocity (V_{los}) sub-samples, and the "worst case" corresponds to the entire LMC and SMC samples determined by applying a strict criteria based on SH distances. A further check based on the comparison with a nearby area with uniform sky density indicates that the global contamination

in our samples is probably close to the low end of the range, around 10%.

Although these papers were published less than twelve months before the deposit of this thesis, some authors started to consider our MCs clean samples when using LMC and/or SMC samples with *Gaia* data (e.g. Li et al. 2023).

6.2   KINEMATICS OF THE LARGE MAGELLANIC CLOUD

With the LMC clean samples described in Section 6.1, in Jiménez-Arranz et al. 2023b we presented the first in-plane 3D velocity maps and profiles of the LMC by using *Gaia* Data Release 3 (DR3) proper motions and V_{los}. For the first time, an homogeneous data set of this type for a galaxy that is not the MW is presented with 3D velocity information, in our case using more than 20 thousand stars. This work was the natural follow up of the *Gaia* Early Data Release 3 (eDR3) performance verification paper (PVP) on the MCs (Gaia Collaboration et al. 2021), where we improved the deprojection formalism employed to allow inclusion of V_{los} data to get the LMC velocity components.

The detailed analysis of the LMC internal dynamics in 3D reveals the following findings: 1) the dynamics within the inner disc are primarily influenced by the presence of a bar; 2) kinematics within the spiral arm over-density indicate an inward motion and a faster rotation compared to the disc, particularly in the part connected to the bar; 3) the outer parts of the disc are notably impacted by the presence of MW stars, predominantly affecting older evolutionary stages; and 4) it is important to note that uncertainties related to assumed disc morphological parameters and the V_{los} of the LMC can, in certain instances, significantly influence the outcomes of the analysis.

In Jiménez-Arranz et al. 2023c, we aimed to constrain the LMC bar pattern speed using the velocity maps derived in Jiménez-Arranz et al. 2023b. We employed three techniques to assess the LMC bar pattern speed: the Tremaine-Weinberg (TW) method, the Dehnen method, and a bisymmetric velocity (BV) model. These methods yielded additional insights into the properties of the bar, such as the corotation radius and bar length and strength. We validated the methods through numerical simulations: an isolated MW-like galaxy and an interacting LMC-like galaxy (from the KRATOS suite, see Section 6.3).

For both simulations and data, the TW method showed a wide range of inferred pattern speeds, a consequence of its strong dependence on both the orientation of the galaxy frame and the viewing angle of the bar perturbation, making impossible to decide which global value best represents an LMC bar pattern speed. The bar pattern speeds and corotation radii of the simulations are well recovered by the Dehnen method and the BV model, respectively. The Dehnen method, when applied to the LMC data, recovers a bar pattern speed of

$\Omega_p = -1.0 \pm 0.5$ km s^{-1} kpc^{-1}, which barely rotates, slightly counter-rotating with respect to the LMC disc. This results would be at odds with the structure and kinematics of the LMC disc. The BV method determines a LMC bar corotation radius of $R_c = 4.20 \pm 0.25$ kpc, which corresponds to a pattern speed of $\Omega_p = 18.5^{+1.2}_{-1.1}$ km s^{-1} kpc^{-1}. This result is consistent with previous estimates and gives a bar corotation-to-length ratio of 1.8 ± 0.1, suggesting that the LMC is hosting a slow bar.

First, as shown with the simulations, the non-unique pattern speed found by the TW method cannot be representative of a global LMC bar pattern speed. This limitation of the method would be more pivotal than the ones already reported in the literature at the time of the deposit of this thesis (e.g. Debattista 2003; Zou et al. 2019; Cuomo et al. 2019). The reason of the failure of the TW method in giving a coherent LMC bar pattern speed is unclear. It could be that the tidal interaction with the SMC has broken the conditions of applicability of the method, the disc being no more in full equilibrium. However, both isolated and interacting discs in the simulations show similarities with the observations. It could also indicate that the impact of the spiral arms on the TW integrals is not as negligible as initially thought. More work will be necessary to investigate the origin of this issue with the TW method applied to the simulations and the LMC data.

Second, and in contrast to the TW method, we have shown that the Dehnen method performs well in both a simulation of an interacting and out-of-equilibrium disc and in a idealised well-defined rotationally supported stellar disc with no external perturbations, since it is by construction insensitive to the bar orientation and the outer spiral perturbation. It is surprising, then, that applying it to the LMC data yields a bar with null rotation, possibly slightly counter-rotating with respect to the disc. Is this discovery believable? Such peculiar bars can be found in numerical simulations. For example, a bar embedded in a counter-rotating dark matter halo has been demonstrated to decelerate, flip its pattern speed, and then decouple from the disc in terms of rotation (Collier and Madigan 2023). External interactions with the SMC and/or MW could be another source of the bar deceleration and counter-rotation. The KRATOS suite is one suitable numerical simulation that could be used to test this scenario (see Section 6.3).

Third, this work has introduced novel constraints on the corotation and pattern speed characteristics of the LMC stellar bar by using the BV method. Our aim is to continue this research with upcoming *Gaia* Data Releases that will provide better data quality. We anticipate that it will be simpler to establish an LMC clean sample with fewer restrictions, such as the crowding of stars at low radius or contamination from foreground MW stars, with improved angular resolution, more accurate proper motion measurements, and increased access to V_{los}. By doing this, we will be able to estimate the LMC pattern speed more

accurately and potentially alleviate the tensions that exist between the Dehnen and BV methods. Furthermore, we intend to investigate potential variations in the bar pattern speed across different stellar evolutionary phases within the LMC.

6.3   SIMULATIONS OF THE MAGELLANIC CLOUDS' INTERACTION

In Jiménez-Arranz et al. (submitted), we presented KRATOS, a comprehensive suite of 28 open access and pure N-body simulations of isolated and interacting LMC-like galaxies, to study the formation of substructures in their disc after the interaction with an SMC-mass galaxy. This was the first paper of a series that will be dedicated to the analysis of this complex interaction.

The 11 sets of simulations, each with a maximum of three configurations, contain: 1) a control model of an isolated LMC-like galaxy; 2) a model including the interaction with an SMC-mass galaxy; and 3) the most realistic configuration in which the LMC-like galaxy may interact with both an SMC-mass and MW-mass galaxy. By implementing these three scenarios, we aimed to distinguish the local instabilities in the LMC-like disc from the products of the interactions between these galaxies. For each of the three scenarios, we varied a set of the free parameters of the whole system. In order to better understand the effect of each of the free parameters on the LMC-SMC interaction and on the formation of LMC-like's disc structures, we varied one parameter at a time.

The following is an overview of the results obtained with the first exploration of the KRATOS suite. In relation to Section 6.2, a large sample of simulations with different initial conditions lead to different galaxy morphologies which also translates into different disc kinematic maps, suitable to perform a first interpretation of the LMC kinematic maps (Gaia Collaboration et al. 2021; Jiménez-Arranz et al. 2023b). We also quantified the number of bars in the KRATOS simulations. We found that the disc develops a weak and transient (less than 1.5 Gyr approx.) or strong bar in 17 out of the 28 simulations. Only 11 models lack a clear bar at any moment during the galaxy's evolution. These numbers agree with the fraction of bars observed in nearby galaxies, which is about 30%-60% (e.g. Marinova et al. 2007; Menéndez-Delmestre et al. 2007; Barazza et al. 2008; Sheth et al. 2008; Nair and Abraham 2010; Masters et al. 2011). When the bars in the KRATOS simulations form, their pattern speed falls within this range, $\Omega_p = 10 - 20 \text{ km s}^{-1} \text{ kpc}^{-1}$, indicating that the LMC may indeed have a low rotating bar (as proposed by the BV model in Jiménez-Arranz et al. 2023c). When the bars are long-lived (more than 1.5 Gyr approx.), the SMC-like galaxies pericentric passages do not significantly change the bar length and pattern speed. We also observed how tidal interactions can both create and destroy bars, and that the pericentric passage

of the SMC-mass galaxy boosts the LMC-like disc scale height (as suggested by Ripepi et al. 2022). Finally, a recent direct interaction with the SMC-mass galaxy can provide a natural explanation for the LMC-like galaxy's off-center stellar bar, as suggested by Besla et al. (2012).

Most of the KRATOS suite was run in virtual machines in the Google cloud provided by the Open Clouds for Research Environments (OCRE) project funded by the European Union's Horizon 2020 research and innovation program.

6.4 GENERAL CONCLUSIONS AND FUTURE WORK PROSPECTS

This thesis offers a new perspective on how we understand the internal movement of the MCs (in particular of the LMC), facilitated by the *Gaia* DR3 data. We also shared helpful resources with the scientific community: our LMC/SMC clean samples, and the KRATOS simulations are available for other researchers to use. The scientific community has already started using the MCs clean samples, carrying out diverse studies based on these datasets. The introduction of the KRATOS simulations offer new possibilities for future research on simulations that mirror the complex dynamics observed within the MCs, namely the origin of the asymmetry in the radial and residual tangential kinematic maps, the nature of the single spiral arm, and the characterisation of the warp, to name a few. We hope that making these resources available will inspire more studies and collaborations in the field.

Within this thesis, while significant progress has been made in understanding the dynamics of the LMC, there remains one pivotal project yet to be completed: unveiling the LMC's 3D structure only using *Gaia*'s positions and parallaxes. This project was originated from the *Gaia* eDR3 PVP on the MC (see Section 4 of Gaia Collaboration et al. 2021), and has continued throughout my thesis. Initial attempts employing the Approximate Bayesian computation (ABC) method proved unsuccessful. Subsequently, we shifted our approach to the Markov chain Monte Carlo (MCMC) method, which remains a work in progress as we continue our efforts to unveil the elusive LMC's 3D structure. On the other hand, a stellar bridge has been identified with a young evolutionary phase sample. We plan to provide a membership probability of the stars between the two Clouds of being part of the bridge.

To finish, the next *Gaia* Data Release (DR4) in 2025 is anticipated to serve as a significant validation and expansion of the conclusions outlined in this thesis. The forthcoming dataset carries the potential to delve deeper into the dynamics of the LMC, offering the possibility of uncovering additional insights that hold considerable promise for the scientific community.

LIST OF ACRONYMS

4MOST 4-meter Multi-Object Spectroscopic Telescope

ABC Approximate Bayesian computation

BHB blue horizontal branch

BV bisymmetric velocity

DECAM Dark Energy Camera

DM dark matter

DR2 Data Release 2

DR3 Data Release 3

EDR3 Early Data Release 3

ESA European Space Agency

ESO European Southern Observatory

HST Hubble Space Telescope

LMC Large Magellanic Cloud

MC Magellanic Cloud

MCELS Magellanic Cloud Emission Line Survey

MCMC Markov chain Monte Carlo

MCPS Magellanic Clouds Photometric Survey

MW Milky Way

NASA National Aeronautics and Space Administration

NN neural network

OCRE Open Clouds for Research Environments

PVP performance verification paper

RC red clump

RG red giant

SH StarHorse

SMASH Survey of the Magellanic Stellar History

SMC Small Magellanic Cloud

TW Tremaine-Weinberg

VISTA Visible and Infrared Survey Telescope for Astronomy

VMC VISTA Magellanic Survey YJKs Catalogue

v_{los} line-of-sight velocity

VLT Very Large Telescope

WISE Wide-field Infrared Survey Explorer

BIBLIOGRAPHY

Antoja, T. et al. (2020). "An all-sky proper-motion map of the Sagittarius stream using Gaia DR2." In: *A&A* 635, L3, p. L3.

Avner, E. S. and I. R. King (1967). "The influence of the Magellanic Clouds on the Milky Way." In: *AJ* 72, p. 650.

Bagheri, G., M. R. L. Cioni, and R. Napiwotzki (2013). "The detection of an older population in the Magellanic Bridge." In: *A&A* 551, A78, A78.

Bajaja, E. et al. (1985). "A new general survey of high-velocity neutral hydrogen in the southern hemisphere." In: *ApJS* 58, pp. 143–165.

Barazza, F. D., S. Jogee, and I. Marinova (2008). "Bars in Disk-dominated and Bulge-dominated Galaxies at z ⁓0: New Insights from ⁓3600 SDSS Galaxies." In: *ApJ* 675.2, pp. 1194–1212.

Bekki, K. and S. Stanimirović (2009). "The total mass and dark halo properties of the Small Magellanic Cloud." In: *MNRAS* 395.1, pp. 342–350.

Belokurov, V. et al. (2019). "The Pisces Plume and the Magellanic wake." In: *MNRAS* 488.1, pp. L47–L52.

Besla, G. et al. (2010). "Simulations of the Magellanic Stream in a First Infall Scenario." In: *ApJ* 721.2, pp. L97–L101.

Besla, G. et al. (2007). "Are the Magellanic Clouds on Their First Passage about the Milky Way?" In: *ApJ* 668.2, pp. 949–967.

Besla, G. et al. (2012). "The role of dwarf galaxy interactions in shaping the Magellanic System and implications for Magellanic Irregulars." In: *MNRAS* 421.3, pp. 2109–2138.

Brueck, M. T. and M. R. S. Hawkins (1983). "An investigation of faint stars in a region of the Magellanic Clouds." In: *A&A* 124, pp. 216–222.

Carrera, R. et al. (2017). "The Magellanic Inter-Cloud Project (MAGIC) III: first spectroscopic evidence of a dwarf stripping a dwarf." In: *MNRAS* 471.4, pp. 4571–4578.

Chandra, V. et al. (2022). "Distant Echoes of the Milky Way's Last Major Merger." In: *arXiv e-prints*, arXiv:2212.00806, arXiv:2212.00806.

Choi, Y. et al. (2018a). "SMASHing the LMC: A Tidally Induced Warp in the Outer LMC and a Large-scale Reddening Map." In: *ApJ* 866.2, 90, p. 90.

Choi, Y. et al. (2018b). "SMASHing the LMC: Mapping a Ring-like Stellar Overdensity in the LMC Disk." In: *ApJ* 869.2, 125, p. 125.

Choudhury, S. et al. (2018). "Photometric metallicity map of the Small Magellanic Cloud." In: *MNRAS* 475.4, pp. 4279–4297.

Cioni, M. R. L., H. J. Habing, and F. P. Israel (2000a). "The morphology of the Magellanic Clouds revealed by stars of different age: results from the DENIS survey." In: *A&A* 358, pp. L9–L12.

Cioni, M. R. L. et al. (2000b). "The tip of the red giant branch and distance of the Magellanic Clouds: results from the DENIS survey." In: *A&A* 359, pp. 601–614.

Cioni, M. R. L. et al. (2011). "The VMC survey. I. Strategy and first data." In: *A&A* 527, A116, A116.

Cioni, M.-R. L. et al. (2016). "The VMC survey. XVII. Proper motions of the Small Magellanic Cloud and the Milky Way globular cluster 47 Tucanae." In: *A&A* 586, A77, A77.

Collier, A. and A.-M. Madigan (2023). "How to Flip a Bar." In: *arXiv e-prints*, arXiv:2305.06383, arXiv:2305.06383.

Conroy, C. et al. (2021). "All-sky dynamical response of the Galactic halo to the Large Magellanic Cloud." In: *Nature* 592.7855, pp. 534–536.

Cuomo, V. et al. (2019). "Bar pattern speeds in CALIFA galaxies. II. The case of weakly barred galaxies." In: *A&A* 632, A51, A51.

D'Onghia, E. and A. J. Fox (2016). "The Magellanic Stream: Circumnavigating the Galaxy." In: *ARA&A* 54, pp. 363–400.

Debattista, V. P. (2003). "On position angle errors in the Tremaine-Weinberg method." In: *MNRAS* 342.4, pp. 1194–1204.

Demers, S. and M. J. Irwin (1991). "Catalogue of blue stars between the Magellanic Clouds." In: *A&AS* 91, p. 171.

Di Teodoro, E. M. et al. (2019). "On the dynamics of the Small Magellanic Cloud through high-resolution ASKAP H I observations." In: *MNRAS* 483.1, pp. 392–406.

Diaz, J. D. and K. Bekki (2012). "The Tidal Origin of the Magellanic Stream and the Possibility of a Stellar Counterpart." In: *ApJ* 750.1, 36, p. 36.

El Youssoufi, D. et al. (2019). "The VMC survey - XXXIV. Morphology of stellar populations in the Magellanic Clouds." In: *MNRAS* 490.1, pp. 1076–1093.

Elmegreen, D. M. and B. G. Elmegreen (1980). "The location of star-forming regions in barred Magellanic-type galaxies." In: *AJ* 85, pp. 1325–1327.

Erkal, D. et al. (2019). "The total mass of the Large Magellanic Cloud from its perturbation on the Orphan stream." In: *MNRAS* 487.2, pp. 2685–2700.

Gaia Collaboration et al. (2016). "The Gaia mission." In: *A&A* 595, A1, A1.

Gaia Collaboration et al. (2021). "Gaia Early Data Release 3. Structure and properties of the Magellanic Clouds." In: *A&A* 649, A7, A7.

Gaia Collaboration et al. (2022a). "Gaia Data Release 3: Reflectance spectra of Solar System small bodies." In: *arXiv e-prints*, arXiv:2206.12174, arXiv:2206.12174.

Gaia Collaboration et al. (2022b). "Gaia Data Release 3: The extragalactic content." In: *arXiv e-prints*, arXiv:2206.05681, arXiv:2206.05681.

Gallagher John S., I. and D. A. Hunter (1984). "Structure and Evolution of Irregular Galaxies." In: *ARA&A* 22, pp. 37–74.

Garavito-Camargo, N. et al. (2019). "Hunting for the Dark Matter Wake Induced by the Large Magellanic Cloud." In: *ApJ* 884.1, 51, p. 51.

Gardiner, L. T., T. Sawa, and M. Fujimoto (1994). "Numerical simulations of the Magellanic system - I. Orbits of the Magellanic Cloufs and the global gas distribution." In: *MNRAS* 266, pp. 567–582.

Gómez, F. A. et al. (2012). "Signatures of minor mergers in the Milky Way disc - I. The SEGUE stellar sample." In: *MNRAS* 423.4, pp. 3727–3739.

Graczyk, D. et al. (2014). "The Araucaria Project. The Distance to the Small Magellanic Cloud from Late-type Eclipsing Binaries." In: *ApJ* 780.1, 59, p. 59.

Grady, J., V. Belokurov, and N. W. Evans (2021). "Magellanic Mayhem: Metallicities and Motions." In: *ApJ* 909.2, 150, p. 150.

Guhathakurta, P. and D. B. Reitzel (1998). "Local Group Suburbia: Red Giants in M31's Outer Spheroid and a Search for Stars in the Magellanic Stream." In: *Galactic Halos*. Ed. by D. Zaritsky. Vol. 136. Astronomical Society of the Pacific Conference Series, p. 22.

Halbwachs, J.-L. et al. (2022). "Gaia Data Release 3. Astrometric binary star processing." In: *arXiv e-prints*, arXiv:2206.05726, arXiv:2206.05726.

Hammer, F. et al. (2015). "The Magellanic Stream System. I. Ram-Pressure Tails and the Relics of the Collision Between the Magellanic Clouds." In: *ApJ* 813.2, 110, p. 110.

Harris, J. (2007). "The Magellanic Bridge: The Nearest Purely Tidal Stellar Population." In: *ApJ* 658.1, pp. 345–357.

Harris, J. and D. Zaritsky (2009). "The Star Formation History of the Large Magellanic Cloud." In: *AJ* 138.5, pp. 1243–1260.

Haschke, R., E. K. Grebel, and S. Duffau (2012). "Three-dimensional Maps of the Magellanic Clouds using RR Lyrae Stars and Cepheids. I. The Large Magellanic Cloud." In: *AJ* 144.4, 106, p. 106.

Hasselquist, S. et al. (2021). "APOGEE Chemical Abundance Patterns of the Massive Milky Way Satellites." In: *ApJ* 923.2, 172, p. 172.

Hilditch, R. W., I. D. Howarth, and T. J. Harries (2005). "Forty eclipsing binaries in the Small Magellanic Cloud: fundamental parameters and Cloud distance." In: *MNRAS* 357.1, pp. 304–324.

Hindman, J. V., F. J. Kerr, and R. X. McGee (1963). "A Low Resolution Hydrogen-line Survey of the Magellanic System. II. Interpretation of Results." In: *Australian Journal of Physics* 16, p. 570.

Ibata, R. A., G. Gilmore, and M. J. Irwin (1994). "A dwarf satellite galaxy in Sagittarius." In: *Nature* 370.6486, pp. 194–196.

Irwin, M. J., S. Demers, and W. E. Kunkel (1990). "A Blue Stellar Link Between the Magellanic Clouds." In: *AJ* 99, p. 191.

Irwin, M. J., W. E. Kunkel, and S. Demers (1985). "A blue stellar population in the HI bridge between the two Magellanic Clouds." In: *Nature* 318.6042, pp. 160–161.

Jacyszyn-Dobrzeniecka, A. M. et al. (2016). "OGLE-ing the Magellanic System: Three-Dimensional Structure of the Clouds and the Bridge Using Classical Cepheids." In: *Acta Astron.* 66.2, pp. 149–196.

Jiménez-Arranz, Ó. et al. (2023a). "Application of a neural network classifier for the generation of clean Small Magellanic Cloud stellar samples." In: *A&A* 672, A65, A65.

Jiménez-Arranz, Ó. et al. (2023b). "Kinematic analysis of the Large Magellanic Cloud using Gaia DR3." In: *A&A* 669, A91, A91.

Jiménez-Arranz, Ó. et al. (2023c). "The bar pattern speed of the Large Magellanic Cloud." In: *arXiv e-prints*, arXiv:2312.11192, arXiv:2312.11192.

Kallivayalil, N. et al. (2013). "Third-epoch Magellanic Cloud Proper Motions. I. Hubble Space Telescope/WFC3 Data and Orbit Implications." In: *ApJ* 764.2, 161, p. 161.

Katz, D. et al. (2022). "Gaia Data Release 3 Properties and validation of the radial velocities." In: *arXiv e-prints*, arXiv:2206.05902, arXiv:2206.05902.

Kerr, F. J., J. F. Hindman, and B. J. Robinson (1954). "Observations of the 21 cm Line from the Magellanic Clouds." In: *Australian Journal of Physics* 7, p. 297.

Kim, S. et al. (1998). "An H I Aperture Synthesis Mosaic of the Large Magellanic Cloud." In: *ApJ* 503.2, pp. 674–688.

Li, J. et al. (2023). "AspGap: Augmented Stellar Parameters and Abundances for 23 million RGB stars from Gaia XP low-resolution spectra." In: *arXiv e-prints*, arXiv:2309.14294, arXiv:2309.14294.

Lin, D. N. C. and D. Lynden-Bell (1982). "On the proper motion of the Magellanic Clouds and the halo mass of our galaxy." In: *MNRAS* 198, pp. 707–721.

Lindegren, L. et al. (2016). "Gaia Data Release 1. Astrometry: one billion positions, two million proper motions and parallaxes." In: *A&A* 595, A4, A4.

Lucchini, S. et al. (2020). "The Magellanic Corona as the key to the formation of the Magellanic Stream." In: *Nature* 585, pp. 203–206.

Lucchini, S., E. D'Onghia, and A. J. Fox (2021). "The Magellanic Stream at 20 kpc: A New Orbital History for the Magellanic Clouds." In: *ApJ* 921.2, L36, p. L36.

Luks, T. and K. Rohlfs (1992). "Structure and kinematics of neutral hydrogen gas in the Large Magellanic Cloud." In: *A&A* 263, pp. 41–53.

Marinova, I. et al. (2007). "The Evolution of Bars and Disks as a Function of Environment in STAGES." In: *American Astronomical Society Meeting Abstracts*. Vol. 211. American Astronomical Society Meeting Abstracts, p. 97.12.

Massana, P. et al. (2022). "The synchronized dance of the magellanic clouds' star formation history." In: *MNRAS* 513.1, pp. L40–L45.

Masters, K. L. et al. (2011). "Galaxy Zoo: bars in disc galaxies." In: *MNRAS* 411.3, pp. 2026–2034.

Mathewson, D. S., M. N. Cleary, and J. D. Murray (1974). "The Magellanic Stream." In: *ApJ* 190, pp. 291–296.

Mazzi, A. et al. (2021). "The VMC survey - XLIII. The spatially resolved star formation history across the Large Magellanic Cloud." In: *MNRAS* 508.1, pp. 245–266.

Menéndez-Delmestre, K. et al. (2007). "A Near-Infrared Study of 2MASS Bars in Local Galaxies: An Anchor for High-Redshift Studies." In: *ApJ* 657.2, pp. 790–804.

Meschin, I. et al. (2014). "Spatially resolved LMC star formation history - I. Outside in evolution of the outer LMC disc." In: *MNRAS* 438.2, pp. 1067–1080.

Misawa, T. et al. (2009). "The Magellanic Bridge as a Damped Lyman Alpha System: Physical Properties of Cold Gas Toward PKS 0312-770." In: *ApJ* 695.2, pp. 1382–1398.

Murai, T. and M. Fujimoto (1980). "The Magellanic stream and the galaxy with a massive halo." In: *PASJ* 32, pp. 581–603.

Nair, P. B. and R. G. Abraham (2010). "On the Fraction of Barred Spiral Galaxies." In: *ApJ* 714.2, pp. L260–L264.

Nidever, D. L., S. R. Majewski, and W. Butler Burton (2008). "The Origin of the Magellanic Stream and Its Leading Arm." In: *ApJ* 679.1, pp. 432–459.

Nidever, D. L. et al. (2010). "The 200° Long Magellanic Stream System." In: *ApJ* 723.2, pp. 1618–1631.

Nidever, D. L. et al. (2017). "SMASH: Survey of the MAgellanic Stellar History." In: *AJ* 154.5, 199, p. 199.

Niederhofer, F. et al. (2022). "The VMC survey - XLVI. Stellar proper motions in the centre of the Large Magellanic Cloud." In: *MNRAS* 512.4, pp. 5423–5439.

Nikolaev, S. et al. (2004). "Geometry of the Large Magellanic Cloud Disk: Results from MACHO and the Two Micron All Sky Survey." In: *ApJ* 601.1, pp. 260–276.

Noël, N. E. D. et al. (2013). "The MAGellanic Inter-Cloud Project (MAGIC). I. Evidence for Intermediate-age Stellar Populations in between the Magellanic Clouds." In: *ApJ* 768.2, 109, p. 109.

Olsen, K. A. G. and C. Salyk (2002). "A Warp in the Large Magellanic Cloud Disk?" In: *AJ* 124.4, pp. 2045–2053.

Pardy, S. A., E. D'Onghia, and A. J. Fox (2018). "Models of Tidally Induced Gas Filaments in the Magellanic Stream." In: *ApJ* 857.2, 101, p. 101.

Peñarrubia, J. et al. (2016). "A timing constraint on the (total) mass of the Large Magellanic Cloud." In: *MNRAS* 456.1, pp. L54–L58.

Petersen, M. S. and J. Peñarrubia (2021). "Detection of the Milky Way reflex motion due to the Large Magellanic Cloud infall." In: *Nature Astronomy* 5, pp. 251–255.

Pietrzyński, G. et al. (2019). "A distance to the Large Magellanic Cloud that is precise to one per cent." In: *Nature* 567.7747, pp. 200–203.

Putman, M. E. (2000). "The Magellanic System's Interactive Formations." In: *PASA* 17.1, pp. 1–5.

Putman, M. E. et al. (2003). "The Magellanic Stream, High-Velocity Clouds, and the Sculptor Group." In: *ApJ* 586.1, pp. 170–194.

Ramos, P. et al. (2022). "The Sagittarius stream in Gaia Early Data Release 3 and the origin of the bifurcations." In: *A&A* 666, A64, A64.

Recillas-Cruz, E. (1982). "Spectral types in the direction of the Magellanic Stream." In: *MNRAS* 201, pp. 473–478.

Ripepi, V. et al. (2012). "The VMC survey - V. First results for classical Cepheids." In: *MNRAS* 424.3, pp. 1807–1816.

Ripepi, V. et al. (2014). "The VMC Survey - VIII. First results for anomalous Cepheids." In: *MNRAS* 437.3, pp. 2307–2319.

Ripepi, V. et al. (2015). "The VMC Survey - XIII. Type II Cepheids in the Large Magellanic Cloud." In: *MNRAS* 446.3, pp. 3034–3061.

Ripepi, V. et al. (2016). "The VMC Survey. XIX. Classical Cepheids in the Small Magellanic Cloud." In: *ApJS* 224.2, 21, p. 21.

Ripepi, V. et al. (2017). "The VMC survey - XXV. The 3D structure of the Small Magellanic Cloud from Classical Cepheids." In: *MNRAS* 472.1, pp. 808–827.

Ripepi, V. et al. (2022). "The VMC survey - XLVIII. Classical cepheids unveil the 3D geometry of the LMC." In: *MNRAS* 512.1, pp. 563–582.

Rubele, S. et al. (2015). "The VMC survey - XIV. First results on the look-back time star formation rate tomography of the Small Magellanic Cloud." In: *MNRAS* 449.1, pp. 639–661.

Rubio, M., J. Lequeux, and F. Boulanger (1993). "Results of the ESO-SEST key programme: CO in the Magellanic clouds. III. Molecular gas in the small Magellanic Cloud." In: *A&A* 271, pp. 9–17.

Schmidt, T. et al. (2020). "The VMC survey. XXXVIII. Proper motion of the Magellanic Bridge." In: *A&A* 641, A134, A134.

Schmidt, T. et al. (2022). "The VMC survey – XLV. Proper motion of the outer LMC and the impact of the SMC." In: *arXiv e-prints*, arXiv:2201.10018, arXiv:2201.10018.

Scowcroft, V. et al. (2016). "The Carnegie Hubble Program: The Distance and Structure of the SMC as Revealed by Mid-infrared Observations of Cepheids." In: *ApJ* 816.2, 49, p. 49.

Shapley, H. (1940). "An Extension of the Small Magellanic Cloud." In: *Harvard College Observatory Bulletin* 914, pp. 8–9.

Sheth, K. et al. (2008). "Evolution of the Bar Fraction in COSMOS: Quantifying the Assembly of the Hubble Sequence." In: *ApJ* 675.2, pp. 1141–1155.

Skowron, D. M. et al. (2014). "OGLE-ING the Magellanic System: Stellar Populations in the Magellanic Bridge." In: *ApJ* 795.2, 108, p. 108.

Smith, R. C. et al. (2005). "The Magellanic Emission Line Survey (MCELS)." In: *American Astronomical Society Meeting Abstracts*. Vol. 207. American Astronomical Society Meeting Abstracts, p. 25.07.

Sparke, L. S. and I. Gallagher John S. (2000). *Galaxies in the universe : an introduction*.

Stanimirović, S., L. Staveley-Smith, and P. A. Jones (2004). "A New Look at the Kinematics of Neutral Hydrogen in the Small Magellanic Cloud." In: *ApJ* 604.1, pp. 176–186.

Staveley-Smith, L. et al. (1998). "Neutral Hydrogen in the Magellanic System." In: *Reviews in Modern Astronomy* 11, p. 117.

Subramanian, S. and A. Subramaniam (2012). "The Three-dimensional Structure of the Small Magellanic Cloud." In: *ApJ* 744.2, 128, p. 128.

Tanga, P. et al. (2022). "Data Release 3: the Solar System survey." In: *arXiv e-prints*, arXiv:2206.05561, arXiv:2206.05561.

Tatton, B. L. et al. (2021). "The VMC Survey - XL. Three-dimensional structure of the Small Magellanic Cloud as derived from red clump stars." In: *MNRAS* 504.2, pp. 2983–2997.

Tepper-García, T. et al. (2019). "The Magellanic System: the puzzle of the leading gas stream." In: *MNRAS* 488.1, pp. 918–938.

Tremaine, S. D. (1976). "The effect of dynamical friction on the orbit of the Magellanic Clouds." In: *ApJ* 203, pp. 72–74.

Vasiliev, E. (2023a). "Dear Magellanic Clouds, welcome back!" In: *arXiv e-prints*, arXiv:2306.04837, arXiv:2306.04837.

Vasiliev, E. (2023b). "The Effect of the LMC on the Milky Way System." In: *Galaxies* 11.2, p. 59.

Wan, Z. et al. (2020). "A SkyMapper view of the Large Magellanic Cloud: the dynamics of stellar populations." In: *MNRAS* 492.1, pp. 782–795.

Yoshizawa, A. M. and M. Noguchi (2003). "The dynamical evolution and star formation history of the Small Magellanic Cloud: effects of interactions with the Galaxy and the Large Magellanic Cloud." In: *MNRAS* 339.4, pp. 1135–1154.

Yozin, C. and K. Bekki (2014). "Tidal-induced lopsidedness in Magellanic-type galaxies." In: *MNRAS* 439.2, pp. 1948–1958.

Zaritsky, D. (2004). "The Case of the Off-Center, Levitating Bar in the Large Magellanic Cloud." In: *ApJ* 614.1, pp. L37–L40.

Zaritsky, D., J. Harris, and I. Thompson (1997). "A digital photometric survey of the magellanic clouds: First results from one million stars." In: *AJ* 114, pp. 1002–1013.

Zaritsky, D. et al. (2000). "The Morphologies of the Small Magellanic Cloud." In: *ApJ* 534.1, pp. L53–L56.

Zivick, P. et al. (2019). "The Proper-motion Field along the Magellanic Bridge: A New Probe of the LMC-SMC Interaction." In: *ApJ* 874.1, 78, p. 78.

Zou, Y. et al. (2019). "Testing the Tremaine-Weinberg Method Applied to Integral-field Spectroscopic Data Using a Simulated Barred Galaxy." In: *ApJ* 884.1, 23, p. 23.

de Jong, R. S. et al. (2019). "4MOST: Project overview and information for the First Call for Proposals." In: *The Messenger* 175, pp. 3–11.

de Vaucouleurs, G. and K. C. Freeman (1972). "Structure and dynamics of barred spiral galaxies, in particular of the Magellanic type." In: *Vistas in Astronomy* 14.1, pp. 163–294.

van der Marel, R. P. (2001). "Magellanic Cloud Structure from Near-Infrared Surveys. II. Star Count Maps and the Intrinsic Elongation of the Large Magellanic Cloud." In: *AJ* 122.4, pp. 1827–1843.

van der Marel, R. P. and M.-R. L. Cioni (2001). "Magellanic Cloud Structure from Near-Infrared Surveys. I. The Viewing Angles of the Large Magellanic Cloud." In: *AJ* 122.4, pp. 1807–1826.

van der Marel, R. P. and N. Kallivayalil (2014). "Third-epoch Magellanic Cloud Proper Motions. II. The Large Magellanic Cloud Rotation Field in Three Dimensions." In: *ApJ* 781.2, 121, p. 121.

The bibliography above refers to citations in Chapter 1, the individual introductions of Chapters 2, 4, 3 and 5 and Chapter 6. Citations of the individual publications are listed within the corresponding manuscript.